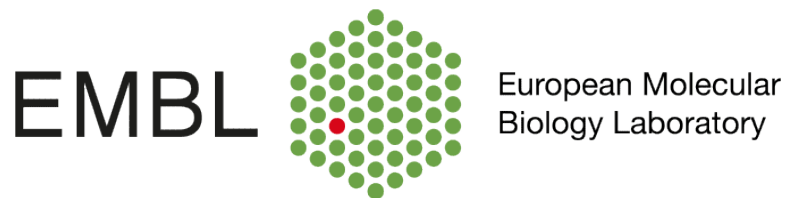


Structural and biophysical studies of mid-coat endocytic adaptors



Dissertation submitted to the University of Hamburg
Universität Hamburg
Fakultät für Mathematik, Informatik und Naturwissenschaft
Fachbereich Chemie
Institut für Biochemie und Molekularbiologie

Javier Lizarrondo Diaz de Cerio

Hamburg, October 2022
Defense date: 16th of December 2022

Thesis evaluators:

Dr. Maria M. Garcia-Alai

Team leader at the European Molecular Biology Laboratory (EMBL) and the Centre of Structural Systems Biology (CSSB)

Prof. Dr. Daniel Wilson

Professor at the Institute of Biochemistry and Molecular Biology (University of Hamburg)

The work presented in this dissertation was carried out in between September 2018 and September 2022 in the Team of Dr. Maria M. Garcia-Alai at the European Molecular Biology Laboratory (EMBL) in Hamburg, Germany.

Para Felix y Rosa

*"No dejes apagar el entusiasmo,
virtud tan valiosa como necesaria;
trabaja, aspira, tiende siempre hacia la altura."*

Rubén Darío

Table of Contents

I	Scientific publications	1
II	List of Abbreviations	2
III	List of Tables	5
IV	List of Figures	7
1	German Abstract	10
2	English Abstract	12
3	Introduction	13
3.1	Cells communicate with their environment	13
3.1.1	The plasma membrane, the interface for communication with the environment	13
3.2	Endocytosis	14
3.3	Clathrin-mediated endocytosis	16
3.3.1	Clathrin: an essential component of the protein machinery for membrane internalization	18
3.3.2	Adaptor proteins: essential players in clathrin mediated endocytosis in yeast	20
3.3.3	The AP-2 adaptor complex	22
3.3.4	Mid-coat endocytic adaptors in yeast: Ent1 and Sla2	23
3.3.5	Phospholipids trigger the assembly of the endocytic coat	25
3.3.6	Membrane binding domains during clathrin-mediated endocytosis	26
3.3.7	Membrane remodeling during clathrin mediated endocytosis	27
3.3.8	Cooperative molecular bridging by Sla2 and Ent1	29
4	Objectives of this work	31
5	Results	32
5.1	Structural basis of ANTH-ENTH cooperation for membrane binding and remodelling during clathrin-mediated endocytosis	32
5.1.1	Sample preparation of the ANTH:ENTH: PIP ₂ complex	32
5.1.2	Protein-lipid ratios govern ANTH-ENTH- PIP ₂ complex formation and its oligomeric diversity	39
5.1.3	cryoEM structure of the ANTH-ENTH- PIP ₂ complex	44
5.1.3.1	The final di-octameric ANTH-ENTH- PIP ₂ map	45
5.1.4	The PIP ₂ molecules act as a glue between different ANTH and ENTH domains	46
5.1.5	Dissecting the role of protein-protein interfaces over complex formation of ANTH-ENTH complexes	49
5.1.5.1	Effect of mutations over domain stability and aggregation	52

5.1.5.2	Effect of interface residue mutations over complex formation	53
5.1.6	The ANTH-ENTH Interface 1	54
5.1.7	The ANTH-ENTH interface 2: a novel oligomerization interface	56
5.1.8	The ANTH-ANTH interface	57
5.1.9	A conserved Sla2 ANTH loop	59
5.1.10	Beyond A ₈ E ₈ assemblies, other types of assemblies	61
5.1.11	Further oligomeric states of the ANTH-ENTH system	61
5.1.12	The ANTH-ENTH complex can assemble into larger oligomeric assemblies capable of deforming membranes	63
5.1.13	Time resolved SAXS studies of the interaction of ANTH and ENTH domains	68
5.2	Biophysical characterization and structural studies of mid-coat adaptors Sla2 and Ent1	71
5.2.1	Expression test of Sla2 and Ent1 full length proteins from <i>S. cerevisiae</i>	71
5.2.2	Expression and Purification of mid-coat adaptors Sla2 and Ent1 from <i>C. thermophilum</i>	71
5.2.3	Biophysical characterization of mid-coat adaptors CtSla2 and CtEnt1	72
5.2.4	Full length adaptor complex formation experiments	74
5.2.5	Structural studies of CtSla2 by Single Particle Analysis cryoEM	77
5.2.6	Expression and purification of Sla2ΔTHATCH	81
5.2.7	Characterization of the coiled-coil of Sla2	82
5.2.8	Crystallization trials of Sla2 coiled coil	84
5.2.9	SAXS of coiled-coil constructs and SEC-SAXS with the CLC	88
5.2.10	Studying the interaction between Sla2 and Clathrin light chain	90
5.3	Structural characterization of clathrin selectivity for endocytic adaptors	95
5.3.1	Introduction	95
5.3.2	Crystal structure and AlphaFold prediction with CHC NTD	96
5.3.3	Binding studies of CHC NTD to adaptors	99
6	Discussion	105
6.1	Sla2 and Ent1 cooperate for efficient internalization of the plasma membrane	105
6.2	Full length endocytic adaptors	109
6.2.1	Fitting of experimental data to predicted models	109
6.2.2	Sla2: A flexible and dynamic actin regulator	111
6.2.3	Sla2 and CLC binding	112
6.3	Interactions of clathrin with SLiMs across species	113
7	Outlook	115
8	Materials and Methods	117
8.1	Materials	117
8.1.1	Chemicals used in this work	117
8.1.2	Lipids used in this work	118
8.1.3	Molecular Biology Reagents	118
8.1.4	Enzymes used in this work	119
8.1.5	Enzymes used in this work	119
8.1.6	Consumables used in this work	120
8.1.7	Equipment used in this work	122

8.1.8	Cell strains used in this work	122
8.1.9	Media used in this work	124
8.1.10	Buffers used in this work	124
8.1.11	Computational resources used in this work	125
8.2	Methods	127
8.2.1	Molecular biology	127
8.2.1.1	PCR and site directed mutagenesis	127
8.2.1.2	Site-directed mutagenesis (Quickchange)	127
8.2.1.3	Plasmid Transformation	128
8.2.2	Protein Production	128
8.2.3	Protein Purification	131
8.2.4	Protein Characterization	132
8.2.4.1	nano Differential scanning fluorimetry (nanoDSF)	132
8.2.4.2	Circular Dichroism	133
8.2.4.3	Dynamic Light Scattering	134
8.2.4.4	Mass Photometry	135
8.2.5	Binding Assays	135
8.2.5.1	Biolayer interferometry	135
8.2.5.2	Isothermal titration Calorimetry (ITC)	136
8.2.5.3	Microscale thermophoresis	137
8.2.6	Small Angle X-ray Scattering	137
8.2.6.1	SAXS batch measurements	138
8.2.6.2	SEC-SAXS	138
8.2.6.3	Stopped-flow time-resolved SAXS (SF-TR-SAXS) data collection and analysis	139
8.2.7	Mass Spectrometry	139
8.2.7.1	MALDI-ToF	139
8.2.7.2	Native Mass Spectrometry	140
8.2.8	Cryogenic Electron Microscopy	141
8.2.8.1	Negative Staining	141
8.2.8.2	Single Particle Analysis cryoEM	141
8.2.8.3	Grid preparation	141
8.2.8.4	Data processing	141
8.2.8.5	ANTH-ENTH complex	141
8.2.8.6	Model building of the ANTH-ENTH-PIP ₂ complex	142
8.2.8.7	Sla2 C-terminus	143
8.2.9	X-ray crystallography	145
8.2.10	Membrane deformation assays	145
8.2.10.1	LUVs preparation	145
8.2.10.2	GUVs preparation	146
8.2.10.3	Fluorescence Microscopy	146
9	References	147
10	Appendix	163
10.1	Appendix 1	163
10.1.1	ANTH-ENTH system	163
10.1.2	Full lengths chapter	174
10.1.3	Ct CHC NTD structure	179
10.1.4	List of hazardous substances	181
11	Acknowledgements	183

I. Scientific publications

- Niebling, S., Veith, K., Vollmer, B., Lizarrondo, J., Burastero, O., Schiller, J., Struve García, A., Lewe, P., Seuring, C., Witt, S., García-Alai, M. (2022). Biophysical Screening Pipeline for Cryo-EM Grid Preparation of Membrane Proteins. *Frontiers in molecular biosciences*, 9, 882288.

<https://doi.org/10.3389/fmolb.2022.882288>

- Lizarrondo, J., Klebl, D. P., Niebling, S., Abella, M., Schroer, M. A., Mertens, H., Veith, K., Thuenauer, R., Svergun, D. I., Skruzny, M., Sobott, F., Muench, S. P., Garcia-Alai, M. M. (2021). Structure of the endocytic adaptor complex reveals the basis for efficient membrane anchoring during clathrin-mediated endocytosis. *Nature communications*, 12(1), 2889.

<https://doi.org/10.1038/s41467-021-23151-7>

II. List of Abbreviations

Table II.1: Abbreviations

Abbreviation	
°C	Degree celsius
µg	Microgram
µL	Microliter
µM	Micromolar
2D	Two-dimensional
3D	Three-dimensional
Å	Ångström
AF2	AlphaFold2
ANTH	AP180 N-terminal Homology
APs	Adaptor Proteins
BAR	Bin/Amphiphysin/Rsv
Bis-Tris	Bis(2-hydroxyethyl)amino-tris(hydroxymethyl)methane
CALM	Clathrin assembly lymphoid myeloid leukemia
CCPs	Clathrin-coated pits
CCS	Clathrin-coated sites
CCVs	Clathrin-coated vesicles
CD	Circular dichroism
CHC	Clathrin Heavy Chain
CLC	Clathrin Light Chain
CMC	Critical micelle concentration
CME	Clathrin-mediated endocytosis
CLEM	Correlative Light-Electron microscopy
Cryo-EM	Cryogenic electron microscopy
cryo-ET	Cryogenic Electron Tomography
cv	Column volume
ddH ₂ O	Double-distilled water
DDM	n-Dodecyl-β-D-maltopyranoside
DLS	Dynamic light scattering
DNA	Deoxyribonucleic acid
dNTP	Deoxyribonucleoside triphosphate
DTT	1,4-dithiothreitol
ENTH	Epsin N-terminal Homology
EM	Electron Microscopy
FRET	Förster resonance energy transfer
g	Gram
GUVs	Giant Unilamellar Vesicles
h	Hours
HEPES	4-(2-hydroxyethyl)-1-piperazineethanesulfonic acid
IDRs	Intrinsically disordered regions
IMAC	Immobilized metal affinity chromatography
IMPs	Integral Membrane proteins

Table II.2: Add caption - continued

IPTG	Isopropyl β -d-1-thiogalactopyranoside
ITC	Isothermal Titration Calorimetry
KD	Dissociation constant
kDa	Kilodalton
L	Liter
LB	Lysogeny broth medium
LDL	Low density lipoprotein
LUVs	Large Unilamellar Vesicles
mAU	Milli absorption units
MX	Macromolecular crystallography
MES	2-(N-Morpholino)ethansulfonsäure
mg	Milligram
min	Minutes
mL	Milliliter
mM	Millimolar
MP	Mass Photometry
ms	Milliseconds
MS	Mass Spectrometry
MST	Microscale thermophoresis
MWCO	Molecular weight cut-off
nanoDSF	Nano differential scanning fluorometry
ng	Nanogram
Ni-NTA	Nickel nitrilotriacetic acid
nL	Nanoliter
nM	Nanomolar
nm	Nanometer
No.	Number
NPF	Asn-Pro-Phe
ns	Nanoseconds
OD600 nm	Optical density at 600 nm
PC	Phosphatidylcholine
PCR	Polymerase chain reaction
PDB	Protein data bank
PE	Phosphatidylethanolamine
PEG	Polyethylene glycol
PI	Phosphatidylinositol
PIP ₂	phosphatidyl-inositol (4,5) bis-phosphate
PM	Plasma Membrane
PS	Phosphatidylserine
psi	Pound-force per square inch
r	Radius
RT	Room temperature
s	Seconds
SAXS	Small angle X-ray scattering
SDS-PAGE	Sodium dodecyl sulfate polyacrylamide gel electrophoresis
SEC	Size exclusion chromatography
SLiMs	Short Linear Motifs
SPA	Single Particle Analysis
SUMO	Small Ubiquitin-Related Modifier

Table II.2: Add caption - continued

TAE	Tris-acetate-EDTA
TB	Terrific broth medium
TBE	Tris-borate-EDTA
TCEP	Tris(2-carboxyethyl)phosphin
THATCH	talin-HIP1/R/Sla2p actin-tethering C-terminal homology
T _m	Melting temperature
Tris	Tris(hydroxymethyl)aminomethane
UIMs	Ubiquitin interaction motifs
V	Volt
w/v	Weight per volume
w/w	Weight per weight
WT	Wildtype
xg	Times gravity
ΔT_m	Melting temperature difference
λ	Wavelength

III List of Tables

II.1	Abbreviations	2
II.2	Add caption - continued	3
II.2	Add caption - continued	4
3.1	List of structural models deposited in the Protein Data Bank for ANTH and ENTH membrane binding domains of adaptor proteins.	30
5.1	Parameters obtained from the DLS AC functions of the ANTH-ENTH-PIP ₂ sample	37
5.2	SAXS parameters derived from different ANTH-ENTH assemblies in solution in presence of PIP ₂	42
5.3	Fitting of different oligomeric states using OLIGOMER to SAXS data from different ANTH-ENTH1/2 assemblies in solution in presence of PIP ₂	42
5.4	Native MS parameters obtained for the PIP ₂ titration over ANTH and ENTH	43
5.5	Cryo-EM data collection, refinement and validation statistics of the ANTH-ENTH 16-mer structure	45
5.6	Mutations inserted in the ANTH domain of Sla2 and the ENTH domain of Ent1	52
5.7	DLS parameters obtained for ANTH and ENTH mutants	54
5.8	DLS measurements of ANTH-ENTH- <i>PIP</i> ₂ complexes containing point mutations in the different interface	58
5.9	Experimental and theoretical masses for ANTH, ENTH, PIP ₂ and adducts/complexes observed by native MS.	59
5.10	Fitting for the binding kinetics determined by BLI	70
5.11	Structural parameters derived from SAXS curves	84
5.12	Crystallization conditions that yield crystals for Sla2 coil-coil constructs	87
5.13	Crystal structures available for CHC NTD in the Protein Data Bank with different peptides	103
5.14	Data collection and refinement statistics (molecular replacement) for CtCHC	104
8.1	Chemicals used in this work	117
8.2	Chemicals used in this work- continued	118
8.3	Lipids used in this work	118
8.4	Molecular Biology Reagents used in this work	118
8.5	Consumables used in this work	120
8.6	Consumables used in this work - continued	121
8.7	Equipment used in this work	122
8.8	Equipment used in this work - continued	123
8.9	Cell strains used in this work	123
8.10	Primers used to generate different constructs	128
8.11	Primers used to generate ANTH and ENTH mutants	129

8.12	Primers used to generate ANTH and ENTH mutants - continued	130
8.13	Expression conditions of different proteins	131
10.1	Data collection and processing parameters for the ANTH-ENTH 12-mer assembly (ANTH WT, ENTH F5A/L12A/V13A).	164
10.2	Native MS of ANTH and ENTH mutants	172
10.3	Oligomeric states with different number of PIP ₂ molecules bound. The cells marked in black are species detectable for the corresponding mutants	173
10.4	Secondary structure content derived from the CD data	174
10.5	Data collection and processing parameters for the C-terminus of CtSla2	174
10.6	Summary of proteins used in this work	180
10.7	List of hazardous substances. For more information, check the ‘Regulation (EC)No 1272/2008’ of the European Agency for Safety and Health at Work.	181

IV List of Figures

3.1	Different mechanism of endocytosis.	15
3.2	Schematic of the clathrin mediated endocytosis process.	17
3.3	Clathrin, the main player in clathrin mediated endocytosis.	21
3.4	Domain organization of endocytic adaptors from <i>S. cerevisiae</i>	22
3.5	Domain organization of Sla2 and Ent1.	25
3.6	PIP ₂ binding mechanism of ANTH and ENTH domains.	28
5.1	nanoDSF of the ANTH domain of Sla2 and ENTH domain of Ent1.	32
5.2	DLS of SEC Buffer containing diC8-PI(4,5)P ₂	33
5.3	DLS of the ANTH and ENTH domains in presence of PIP ₂	34
5.4	Sample preparation of the ANTH-ENTH- PIP ₂ complexes.	35
5.5	Sample preparation of ANTH-PIP ₂ and ENTH-PIP ₂ samples.	36
5.6	DLS comparison between ANTH-ENTH- PIP ₂ samples using high and low concentration of protein.	37
5.7	Sample preparation of ANTH-ENTH- PIP ₂ complexes from ANTH- PIP ₂ and ENTH- PIP ₂ complexes.	38
5.8	Mass Photometry histogram of ANTH-ENTH- PIP ₂ complexes.	38
5.9	SAXS data for ANTH, ENTH and ANTH-ENTH- PIP ₂ complexes.	40
5.10	SAXS data of several ANTH-ENTH1/2- PIP ₂ complexes.	41
5.11	SAXS derived parameters of ANTH-ENTH1/2- PIP ₂ complexes in solution.	41
5.12	Mass-charge distributions for ANTH-ENTH- PIP ₂ complexes present at different concentrations.	43
5.13	Processing flowchart for a 16-mer ANTH-ENTH complex.	44
5.14	Cryo-EM structure of a 16-mer AENTH complex.	46
5.15	PIP ₂ binding sites in the ANTH-ENTH tetramer.	48
5.16	The ANTH-ENTH tetramer interfaces.	49
5.17	Schematic of the workflow used for testing the effects over ANTH-ENTH complex formation in the mutagenesis study.	50
5.18	nanoDSF for the ANTH and ENTH point-mutants.	51
5.19	Different interfaces present in the ANTH-ENTH tetramer.	55
5.20	The Sla2-specific Y247-L248 insertion is not part of the ANTH-ENTH interface.	60
5.21	ANTH-ENTH 12-mer assembly (A ₆ E ₆) obtained by mutation of residues F5A/L12A/V13A of the amphipatic α0 helix of the ENTH domain.	62
5.22	Smaller intermediates of AENTH oligomers.	63
5.23	Protein-lipid interactions of the AENTH 16-mer complex structure and of the ANTH-ENTH assembly on GUVs.	64
5.24	Effect of AENTH tetramer and mutants on GUVs by fluorescence microscopy.	66
5.25	Effect of AENTH tetramer mutants on LUVs by negative stain.	67
5.26	Time-resolved SAXS data demonstrate a fast assembly of ANTH and ENTH domains in solution.	69

5.27	ANTH-ENTH complex formation is a reversible process.	70
5.28	Expression test of Ent1 and Sla2 full length from <i>S. cerevisiae</i>	72
5.29	Purification of CtSla2 and CtEnt1.	73
5.30	Biophysical characterization of full length mid-coat adaptors CtSla2 and CtEnt1.	75
5.31	SAXS data corresponding to CtSla2 and CtEnt1 full length.	76
5.32	DLS data for formation of the full length adaptor complex.	77
5.33	SAXS data of CtSla2-CtENTH in presence of PIP ₂	78
5.34	Low-resolution cryoEM map of the C-terminus of CtSla2.	79
5.35	cryoEM map of an oligomer of CtSla2 C-terminus.	80
5.36	Comparison between the AlphaFold model of Sla2 C-terminus	82
5.37	Purification of Sla2 Δ THATCH.	83
5.38	Biophysical characterization of Sla2 coil-coil constructs.	85
5.39	SAXS data for Sla2 296-767 (yellow) and Sla2 432-767 (blue).	86
5.40	Mass Photometry for crystals obtained using Sla2 432-767 and Sla2 296-767.	87
5.41	Purification from CLC from <i>S. cerevisiae</i>	88
5.42	Quality Control report for CLC of <i>S. cerevisiae</i>	89
5.43	SAXS experiments of yeast CLC.	91
5.44	Binding affinity of Sla2 and CLC measured by ITC.	92
5.45	SEC and SEC-SAXS studies of the interaction between Sla2 and CLC.	94
5.46	Purification of CtCHC NTD	96
5.47	Crystal structure of Ct CHC NTD	97
5.48	Structures of CtCHC NTD	98
5.49	AlphaFold2 predictions of CtCHC NTD with 1, 2, 3 and 4 CtEnt1 peptides	100
5.50	Binding studies of clathrin-box containing peptide to CHC NTD analysed by nanoDSF	101
5.51	Binding studies of CtEnt1 full length to CHC NTD analysed by MST	102
7.1	Sla2 constructs that will be used for biophysical binding studies to actin.	116
8.1	Processing pipeline for the structure of the C-terminus of Sla2	144
10.1	Cryo-EM reconstruction parameters for the 16-mer ANTH-ENTH complex.	163
10.2	Symmetry of the 16-mer ANTH-ENTH complex.	164
10.3	Representative EM densities in the cryoEM model of the 16-mer.	165
10.4	DLS data for the ANTH/ENTH mutants and complexes.	166
10.5	Native MS of the ANTH-ENTH WT complex in the presence of 60 μ M PIP ₂	167
10.6	SEC profiles from different ANTH and ENTH mutants	168
10.7	SEC profiles from different ANTH and ENTH mutants	169
10.8	SDS-PAGE analysis of ANTH and ENTH mutants purified.	170
10.9	Growth defects of selected mutants affecting the ANTH-ENTH interface 2 and the ANTH-ANTH interface.	171
10.10	SVD analysis of SF-TR-SAXS.	171
10.11	Intensity profiles from SEC-SAXS for CtSla2 and CtEnt1	174
10.12	AlphaFold predictions of CtSla2 dimer (a), CtEnt1 (b) and yeast CLC (c).	175
10.13	Multiple sequence alignment of Sla2 binding residues.	175
10.14	Intensity plots of SEC-SAXS runs for CLC, Sla2 coil-coil and the complex between the two.	176
10.15	Purification of Sla2 coil-coil constructs	177

10.16SEC runs of Sla2 coil-coil, CLC and the complex between the two. . . .	178
10.17AlphaFold prediction of an W-box peptide into Ct CHC NTD	179
10.18GSH symbols	182

1. German Abstract

Clathrin-vermittelte Endozytose ist ein konservierter Prozess in Eukaryoten, der für verschiedene Funktionen wie Ernährung und synaptische Kommunikation von großer Bedeutung ist. Während der Clathrin-vermittelten Endozytose baut sich eine große Proteinmaschinerie selektiv in einem Bereich der Plasmamembran auf und erzeugt Clathrin-beschichtete Vertiefungen (CCPs: clathrin-coated pits). Innerhalb dieses komplexen und dynamischen Netzwerks von Protein-Protein- und Protein-Membran- Wechselwirkungen müssen die endozytische Hülladaptoren Sla2 und Ent1 an der Plasmamembran befestigt bleiben, um Kraft vom Aktin-Zytoskelett zu übertragen, die für eine erfolgreiche Membraninvagination in Hefe erforderlich ist. Diese Arbeit präsentiert eine Kryo-EM-Struktur eines 16-mer-Komplexes der ANTH- und ENTH- Membranbindungsdomänen von Sla2 und Ent1, die an das Phospholipid PIP2 gebunden sind. Die Baueinheit dieses Oligomers ist ein Heterotetramer, das PIP2-Moleküle an den ANTH-ENTH-Grenzflächen bindet. Von der Struktur abgeleitete Mutationen von Resten, die in den neu identifizierten Proteinschnittstellen dieses Komplexes vorhanden sind, wurden mit einem breiten Spektrum biophysikalischer und struktureller Techniken untersucht. Die Ergebnisse der Komplexbildungsexperimente beschreiben die entscheidenden Wechselwirkungen die für die Komplexbildung verantwortlich sind, und mangelhafte Zellwachstumsphänotypen demonstrieren ihre biologische Relevanz. Wichtig ist, dass die ANTH-ENTH-Kooperation und größere Baugruppen bilden können, um zum Membranumbau beizutragen. Darüber hinaus legen zeitaufgelöste Kleinwinkel-Röntgenstreuung-Messungen (SAXS) der Wechselwirkung dieser Adapterdomänen *in vitro* nahe, dass sich ANTH- und ENTH-Domänen entwickelt haben, um in Gegenwart von PIP2 eine schnelle Assemblierung im Zeitbereich von weniger als einer Sekunde zu erreichen, und dass weitere Proteine nicht zur Ausbildung eines stabilen Komplexes erforderlich sind. Über die Membranbindungsdomänen von Mid-Coat-Adaptoren hinaus präsentiert diese Arbeit auch die biophysikalische Charakterisierung der Wildtypen von Sla2 und Ent1 von *C. thermophilum*. Die Charakterisierung des C-Terminus von Sla2 mittels CryoEM und Strukturvorhersagen offenbart unterschiedliche Oligomer- und Konformationszustände, die für die Interaktion mit dem Aktin-Zytoskelett relevant sein könnten. Darüber hinaus wird die Wechselwirkung von Sla2 mit der leichten Kette von Clathrin (CLC: clathrin light chain) in Lösung gezeigt und unter Verwendung von SEC-SAXS charakterisiert. Bindungsstudien zeigen darüber hinaus eine Protein-Protein-Wechselwirkung mit geringer Affinität. Es ist bekannt, dass Ent1 über seine Clathrin-Box-Motive an die N-terminale Domäne der schweren Kette von Clathrin (NTD: N-terminal domain) bindet. Die Kristallstruktur der schweren Clathrin-Kette NTD von *C. thermophilum* gegenüber anderen Eukaryoten hoch konserviert, und die Bindung zwischen WT-Ent1 und einem Peptid, das die Sequenz enthält, liefert Informationen bezüglich des Mechanismus der Bindung dieses Adapters an die Clathrin-Hülle.

Zusammen liefern diese Ergebnisse ein molekulares Verständnis dafür, wie Mid-Coat-Adaptoren zum molekularen Puzzle von Clathrin-beschichteten endozytischen Stellen beitragen.

2. English Abstract

Clathrin-mediated endocytosis is a conserved process in eukaryotes essential for several functions such as nutrition and synaptic communication. During clathrin-mediated endocytosis, a large protein machinery selectively assembles in a region of the plasma membrane, creating clathrin-coated pits (CCPs). Within this complex and dynamic network protein-protein and protein-membrane interactions, endocytic midcoat adaptors, Sla2 and Ent1, must remain attached to the plasma membrane to transmit force from the actin cytoskeleton required for successful membrane invagination in yeast.

This work presents a cryo-EM structure of a 16-mer complex of the ANTH and ENTH membrane-binding domains from Sla2 and Ent1 bound to PIP₂. The building unit from this oligomer is a hetero-tetramer that binds PIP₂ molecules at the ANTH-ENTH interfaces. Structure-derived mutations of residues present in the newly identified protein interfaces of this complex were studied by a wide-range of biophysical and structural techniques. Complex formation experiments delineate the key interactions for complex formation and deficient cell growth phenotypes demonstrate its biological relevance. Importantly, the ANTH-ENTH cooperate to form larger assemblies to contribute to membrane remodelling, promoting the formation of CCPs. Furthermore, a time-resolved small-angle X-ray scattering (TR-SAXS) study of the interaction of these adaptor domains *in vitro* suggests that ANTH and ENTH domains have evolved to achieve a fast sub-second timescale assembly in the presence of PIP₂ and do not require further proteins to form a stable complex.

Beyond the membrane binding domains of mid coat adaptors, biophysical characterization of full length Sla2 and Ent1 from *C. thermophilum* was also performed. cryoEM Single Particle Analysis of Sla2 together with structural predictions reveals different oligomeric and conformational states which could be relevant for its interaction with the actin cytoskeleton, an essential component required for membrane internalization. Furthermore, interaction of adaptors with clathrin is also studied here: the complex between Sla2 and clathrin light chain (CLC) is characterised in solution using SEC-SAXS and binding studies reveal a low affinity protein-protein interaction which affects the flexibility of clathrin. The crystal structure of the clathrin heavy chain N-Terminal domain (NTD) from *C. thermophilum* shows a high conservation from other eukaryotes, and binding studies of this domain with adaptors shed some light regarding the specificity of the binding of these adaptors to the clathrin coat.

Together, these findings provide a molecular understanding of how mid-coat adaptors contribute to the molecular puzzle assembled for building clathrin-coated vesicles.

3. Introduction

3.1 Cells communicate with their environment

Living beings are defined as any organism or form of life able to perform three essential functions: nutrition (through metabolism and growth), relation (response to stimuli and adaptation to the environment) and reproduction. While being able to communicate with their environment, cells have a defined structure and are delimited by large biological membrane that surrounds the cell: the plasma membrane. Cells also have several internal compartments involved in different functions, designated as organelles, which are usually separated by internal membranes.

3.1.1 The plasma membrane, the interface for communication with the environment

The plasma membrane (PM), like most biological membranes, is created by a bilayer of lipids, with stacking of the hydrophobic acyl chains of the lipids inside the membrane surrounded by the polar head groups, which are exposed to the aqueous environment. The composition of the PM comprises an elaborated mixture of lipids, decorated by several different types of proteins, including Integral Membrane Proteins (IMPs) and membrane associated proteins with distinct topologies that fulfil different roles required by the cell for responding to the environmental cues. The wide diversity of lipids with different polar head groups and different levels of insaturations on their acyl chains allow a fine regulation of membrane fluidity and tension properties to different types of membranes, and also to certain specific regions within the same membrane.

The plasma membrane is also usually referred as a semi-permeable barrier, since it separates the cell from its environment but it is not completely sealed, letting water, gases and other small hydrophobic molecules flow through so cells receive signals and nutrients from their surroundings, but remain isolated from the exterior. To allow the transport of nutrients and signalling molecules that are incapable of diffusing through the plasma membrane (mostly due to their size and chemical composition), different transporters, pumps, channels and receptors are present in the plasma membrane.

Different types of membrane proteins present in the surface can diffuse within the plasma membrane and cluster together in certain regions of the cell. However, the availability of these receptors needs to be tightly regulated depending on the internal status of the cell to regulate the amount of target molecules that should be captured from the environment (e.g. sugar transporters should be internalised when enough sugars are present within the cell).

3.2 Endocytosis

To regulate the protein and lipid composition of the cell surface and for the internalization of materials from the exterior, evolution has carefully selected a protein machinery in charge of internalization of a specific region of the plasma membrane. The internalization of a portion of the plasma membrane containing cargo of interest into the cell is known as endocytosis (which can be directly translated from Greek as “brought into the cell”). This process is the opposite of exocytosis, where a portion of internal membrane fuses to the plasma membrane and releases contents of such vesicles into the cell surface and the environment.

Given the broad range of signals and nutrients that cells receive from their environment, endocytosis is involved in many fundamental cellular processes besides just regulation of the composition of the plasma membrane. The most widely-studied ones are nutrient uptake and cell signaling, since the availability of several receptors (such as the GLUT4 transporter (Foley et al., 2011) is regulated using this process. Beyond that, endocytosis has also a role in cell adhesion and polarity. The internalization of certain regions of the plasma membrane designated for endocytosis naturally contributes as well to the control of plasma membrane homeostasis by regulating different types of lipids available in the plasma membrane. In neurons, clathrin-mediated endocytosis (a subtype of endocytosis) is relevant during synaptic receptor recycling, once the signal fired by the neurotransmitter binding to their receptors has been triggered (Saheki, De Camilli, 2012). Endocytosis also plays an important role in viral infection, since many viruses, such as SARS-CoV-2, hijack surface receptors present in eukaryotic cells and trigger their internalization using the endocytic mechanism of these receptors (Kaksonen, Roux, 2018; Lu et al., 2016; Smith et al., 2017).

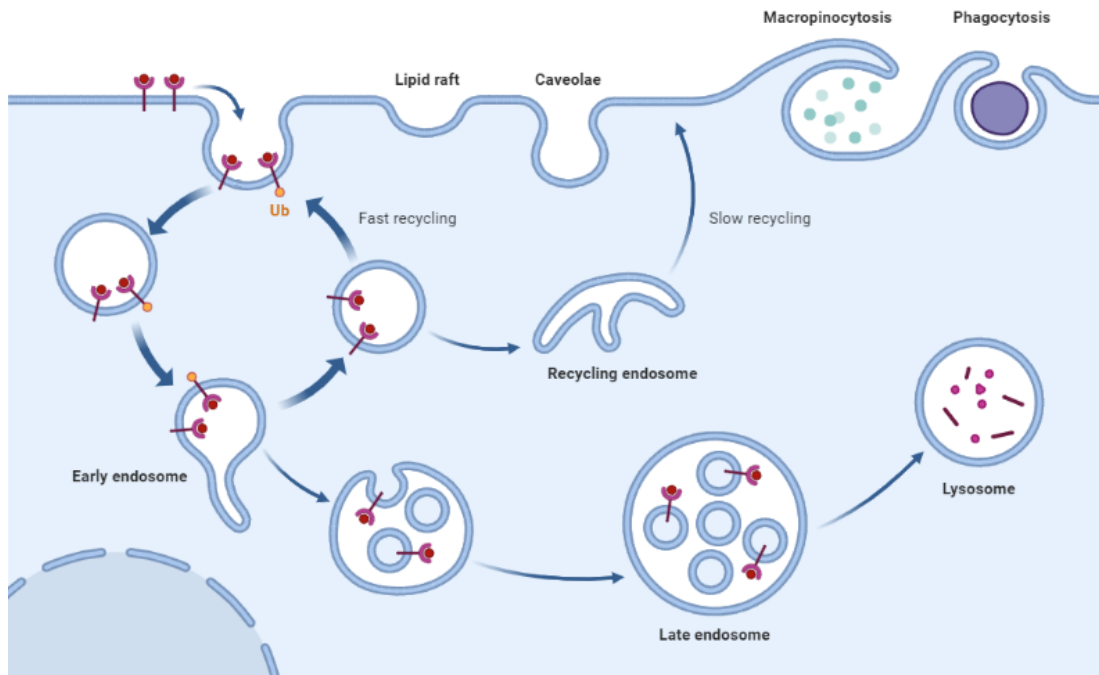


Figure 3.1: **Different mechanism of endocytosis.**

(left to right) Clathrin mediated-endocytosis takes place when receptor or cargoes are targeted/activated with molecules such as Ubiquitin. These receptors are internalising into a vesicle and fuse with the endosomes where they can be recycled back to the surface of the cell or proceed towards internal trafficking in the endo-lysosomal pathway. Changes in the lipid composition in the plasma membrane that change the fluidity of the membrane in certain regions, known as lipid rafts, which promote the internalization of smaller regions of the plasma membranes known as Caveolae. The cell can also internalise larger materials from the environment such as liquids or entire pathogens by micropinocytosis and phagocytosis, respectively. Created with [BioRender.com](https://www.biorender.com)

Given endocytosis is essential for the communication of cells with their environment, it is conserved from low to high eukaryotes (e.g. from yeast to mammals). There are different sub-classes of endocytosis according to the different types of cargoes selected to be internalised into the cell (Figure 3.1). Some cargoes can play a role in the activation of the formation of protein coats around the plasma membrane, such as in clathrin-mediated endocytosis or fast-endophilin mediated endocytosis (FEME). Other processes do not require specific cargoes, but depend on the formation of lipid rafts, highly fluid portions of the plasma membrane enriched in lipids such as cholesterol. This process, which yields smaller vesicles than those of clathrin-mediated endocytosis, is used for the internalization of lipids into the plasma membrane, and it has been shown to be involved in several physiological functions. Besides these, endocytosis also exists in many other flavours such as pinocytosis and phagocytosis are used for the internalization of liquids from the environment or of pathogens and apoptotic debris,

respectively (Doherty, McMahon, 2009; Rennick et al., 2021).

3.3 Clathrin-mediated endocytosis

One of the most extensively studied endocytic processes is receptor-mediated endocytosis, also known as clathrin-mediated endocytosis (CME). As its name indicates, receptor-mediated endocytosis is responsible for the internalization of membrane receptors as cargoes into the cell. Upon their activation, these receptors usually activate a cascade of events that trigger the assembly of the endocytic machinery to build the protein coat around the region of the plasma membrane that needs to be internalised. An essential component of this protein coat is clathrin, which plays a major structural role for building the protein coat around endocytic sites (Kirchhausen et al., 2014). Many years of research around clathrin mediated endocytosis in budding yeast have allowed a very detailed understanding of its timeline and components (with more than 60 proteins involved), which have been described in several genetic and microscopy studies (Figure 3.2) (Kaksonen, Roux, 2018; Merrifield, Kaksonen, 2014; Lu et al., 2016; Mund et al., 2018).

The components of the endocytic machinery have been well characterised over time, and their arrival and function within the endocytic site has been shown to be heavily regulated by several different factors, including post-translational modifications such as phosphorylation and ubiquitination (Mettlen et al., 2018). Based on their function performed within the endocytic coat, proteins have been assigned into different modules: early arriving proteins (such as Ede1), coat proteins (such as clathrin), WASP/Myo proteins, actin module proteins and scission proteins (such as Dynamin) (Mund et al., 2018).

CME occurs in a sequential way and can be divided in the following stages: (1) initiation, where pioneering proteins bind cargo and the plasma membrane after the increase of the local concentration of PI(4,5)P₂, a phospholipid enriched in regions of the plasma membranes where endocytosis occurs; (2) maturation, where curvature starts being generated and the clathrin coat grows around the endocytic site forming clathrin-coated pits (CCPs); (3) membrane invagination, enabled by the force from actin polymerization against the plasma membrane; and (4) membrane scission, catal-

used by the GTPase dynamin by constriction of the membrane at the neck of the invagination. Finally, once CCPs are cleaved off from the plasma membrane, clathrin coated vesicles are directed towards the internal trafficking systems of the cell, where coat disassembly and recycling of components takes place with the help of chaperones such as Hsp70 and Auxilin (Kang et al., 2009; Xing et al., 2010).

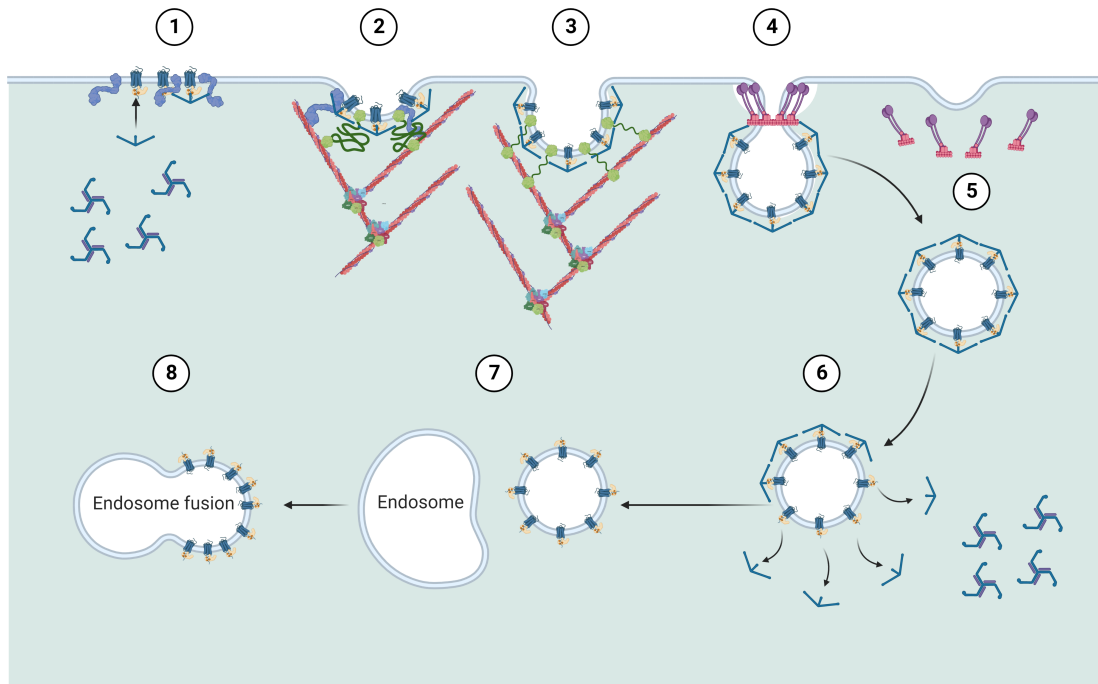


Figure 3.2: **Schematic of the clathrin mediated endocytosis process.**

1. Initiation stage. Adaptor proteins bind to the receptors and the plasma membrane via interactions with cargoes containing certain motifs or with PIP₂, respectively, and initiate the formation of the endocytic coat by recruitment of clathrin. 2. Clathrin coated pit (CCP) formation takes place with further recruitment of molecules to the clathrin coat. In yeast, adaptors start the recruitment of the actin cytoskeleton. 3. Membrane invagination process takes place driven by actin polymerization and branching together with further coating of the endocytic site by clathrin. 4. The scission machinery binds to the neck of the CCP and cleaves it from the plasma membrane. 5. Clathrin-coated vesicles (CCVs) containing cargoes are internalised into the cell. 6. The endocytic coat components are recycled with the help of Auxilin and Hsp70 chaperones for coat disassembly. 7. Uncoated vesicles containing cargo proceed into the internal membrane trafficking system. 8. Vesicles fuse with the endosome. Created with [BioRender.com](https://www.biorender.com)

CME has been conserved through evolution from yeast to higher eukaryotes, such as mammalian cells, where it is essential in organism-wide processes such as synaptic receptor recycling. However, in spite of the large similarities and the large proportion of shared components, there are remarkable differences between yeast and mammalian cells endocytosis. The most remarkable difference is probably the size and shape of the vesicles (in yeast they are smaller and oval-shaped compared to round larger vesicles

in higher eukaryotes), and the dependence of the actin cytoskeleton for membrane invagination, required in yeast and dispensable in higher eukaryotes (Kaksonen, Roux, 2018).

3.3.1 Clathrin: an essential component of the protein machinery for membrane internalization

Clathrin was firstly identified in the 1970s as a protein involved in the internalization of vesicles in cells, and was initially isolated from brain pig tissue, where is very abundant due to the large amount of synaptic connections with neurotransmitter receptors that are internalised using clathrin-mediated endocytosis. Its characterization using Electron Microscopy (EM) and the observation of its ability to form cage-like assemblies gave clathrin its name (Pearse, 1976, 1975). One of the first cargoes that were studied to be internalised by means of clathrin coated vesicles was Low Density Lipoprotein (LDL), which showed a dependence for clathrin for its internalization through its specific receptor and gave rise to the term “clathrin-mediated” endocytosis (Goldstein et al., 1979).

Clathrin is composed by a heavy and a light chain, and it is a trimer, known as triskelion, in its native state. Each triskelion is composed by three heavy chains (CHC, 180 kDa) and three light chains (CLC, 20 kDa) (Ungewickell, Branton, 1981). CHC consists of an N-terminal domain, a 7-blade β -propeller, followed by a long stretch of repetitive domains which by means of an α -helical zig-zag form a curled elongated structure, known as the leg of clathrin (with two different segments, an angle, and a knee) and a final C-terminal domain containing the tripod helix, involved in clathrin multimerization (Figure 3.3). In mammals, there are two splicing variants of CHC, and they have been proposed to differentially form coated pits or plaques, influencing cell adhesion and muscle development and maintenance (Moulay et al., 2020). CLC contains a single long helix that binds to CHC (Figure 3.3), along with intrinsically disordered regions, which were attributed some regulatory roles in the regulation of the clathrin coat assembly and its interactions with other adaptor proteins present in endocytosis. Also in mammals light chains (CLCa and CLCb) have been shown to be tissue specific and display different properties of interactions with other endocytic proteins (Biancospino et al., 2019; Redlingshöfer et al., 2019).

Clathrin triskelia can assemble into different types of cage-shape structures and contribute to the formation of CCPs. Clathrin's ability to trimerize depends on pH, indicating that coat formation relies on electrostatic interactions (Ybe et al., 1998). Clathrin coated structures in the cell vary in diameter (700 – 1000 Å) as well as in shape, with several types of assembly reported in literature to this date (Fotin et al., 2004a; Morris et al., 2019; Paraan et al., 2020). Furthermore, the advances in the field of cryo-electron tomography (cryoET) along with the regularity on the clathrin cages assemblies have allowed the determination of *in situ* clathrin coat structures (Serwas et al., 2022). The standard cages reported in literature describe an assembly in which hexagons and pentagons assemble adjacently, with two types of contacts between triskelia that stabilise the coat. Additionally, clathrin plaques in the periphery of the cell have been studied for their relation with other processes such as cell adhesion and migration (Sochacki, Taraska, 2019).

Since the early days of single particle analysis EM (SPA-EM), structures of different clathrin cages and coats from purified samples or reconstituted systems have shed light into the mechanism of assembly of the coat and its structural role as a platform for the recruitment of other endocytic proteins and cargo at the plasma membrane in clathrin-coated sites (CCS) (Fotin et al., 2004a,b; Marsh, 2002; Morris et al., 2019; Vigers et al., 1986; Bucher et al., 2018; Kukulski et al., 2012; Scott et al., 2018). Importantly, even though clathrin is present in yeast endocytic sites and it qualifies as an abundant coat protein, it is not an absolute prerequisite for endocytosis (Payne et al., 1988). In addition, correlative light and electron microscopy (CLEM) has revealed that clathrin does not shape the membrane during invagination, but is instead required to determine the correct size and regularity of the invagination of emerging endocytic vesicles (Avinoam et al., 2015; Kukulski et al., 2016).

The role of clathrin during membrane remodeling has been a long standing debate in the CME field, with two prevalent models: the constant curvature vs the constant surface model (Scott et al., 2018; Sochacki, Taraska, 2019). Clathrin has been shown to sense membrane curvature (Zeno et al., 2021), and its interactions with adaptors regulate the transition from flat to curved during CME (Bucher et al., 2018). Recently, super-resolution and Simultaneous Two-wavelength Axial Ratiometry (STAR) microscopy studies manifest the capability of clathrin to assemble both as a flat and

curved coat in the endocytic sites (Mund et al., 2022; Nawara et al., 2022).

3.3.2 Adaptor proteins: essential players in clathrin mediated endocytosis in yeast

Clathrin mediates endocytosis through the formation of a protein coat around the endocytic site but it does not interact directly with the plasma membrane. Instead, adaptor proteins connect the clathrin coat with the plasma membrane. Initially referred as the 50-100 kDa accessory proteins, these adaptor proteins are a diverse set of proteins with different topologies and functions, which include the AP-2 complex, proteins of the clathrin assembly lymphoid myeloid leukemia (CALM) family and epsins, connect the clathrin coat with the plasma membrane (Merrifield, Kaksonen, 2014; Edeling et al., 2006; Ford et al., 2001, 2002; Kalthoff et al., 2002; Miller et al., 2015).

Adaptor Proteins (APs) are in charge of cargo recognition, and of connecting the cargo and the plasma membrane with the clathrin coat surrounding the endocytic pit and with the actin cytoskeleton, indispensable for CME in yeast. APs can be classified according to their arrival times into the endocytic site into early, middle and late arriving proteins. Early proteins have been shown to be dispensable in yeast, with endocytosis taking place in just a few seconds (compared to the standard 2 minutes process) by fast internalization of the plasma membrane (Brach et al., 2014). The redundancy of the role of some endocytic proteins provides the endocytic system with robustness needed for this essential cellular process. For example, two genes encoding epsins present in yeast (Ent-1 and Ent-2) fulfil a similar role, and a deletion of both genes was shown to be lethal, making loss of function phenotypes only achievable by controlled expression of at least one copy (Skruzny et al., 2012; Wendland et al., 1999). Another layer of endocytosis where the variety of adaptors becomes relevant is cargo recognition. The recognition of different cargoes by the endocytic machinery is accomplished by adaptor proteins, which target different endocytic signals in the forms of Short Linear Motifs (SLiMs), conformational determinants (e.g. the SNARE domain of VAMP8) or covalent modifications (such as Ubiquitination or phosphorylation) in the cytosolic domains of the membrane receptors that will need to be internalised (Traub, Bonifacino, 2013). This variety of mechanisms together with the large diversity of adaptors allows the endocytic machinery to bind selectively receptors that need to be

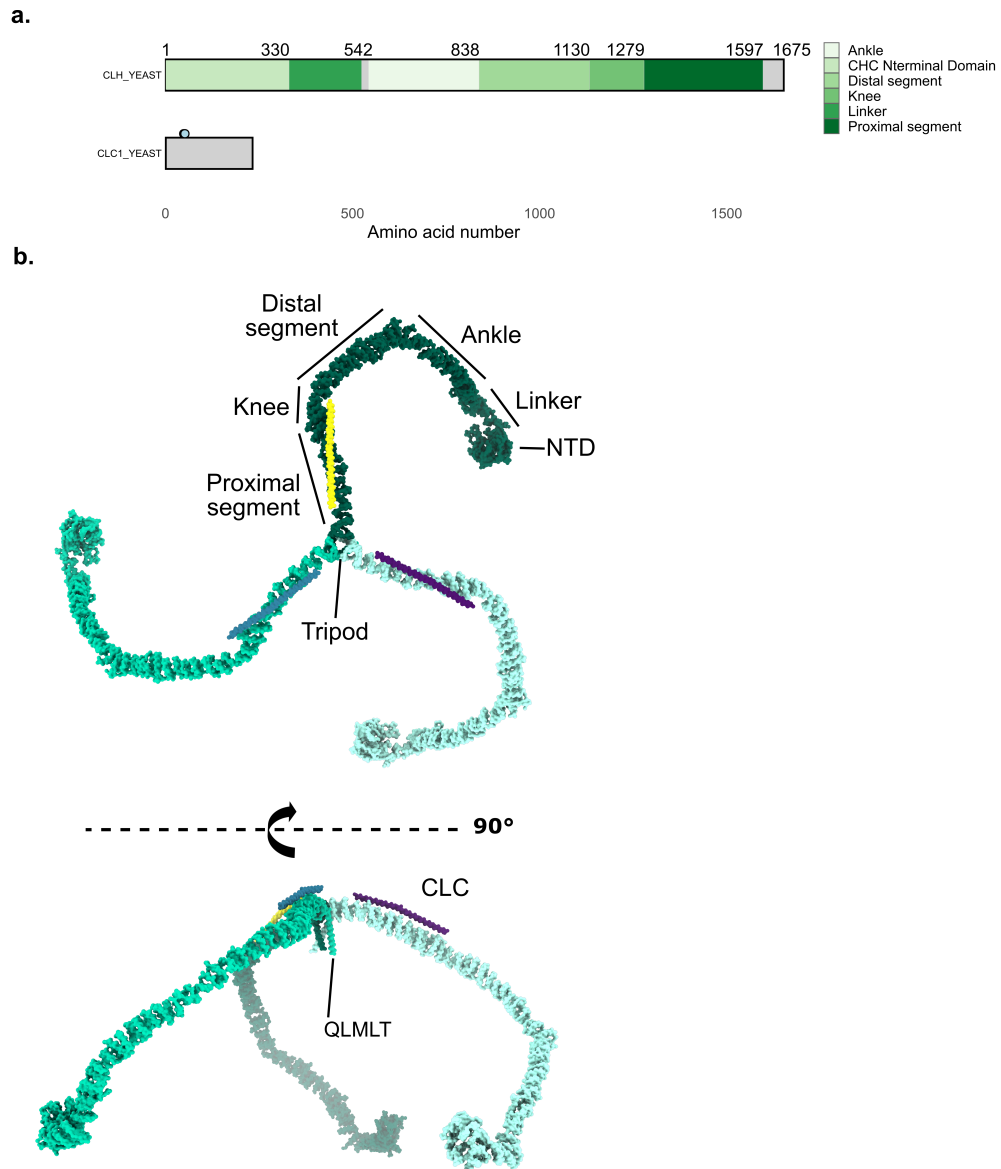


Figure 3.3: Clathrin, the main player in clathrin mediated endocytosis.

a. Domain arrangement of clathrin heavy chain (CHC) and clathrin light chain (CLC). **b.** Structural model of a clathrin triskelion, composed by three molecules of CHC and three molecules of CLC. The different domains of CHC composing the clathrin leg are indicated (adapted from (Xing et al., 2010)).

internalised.

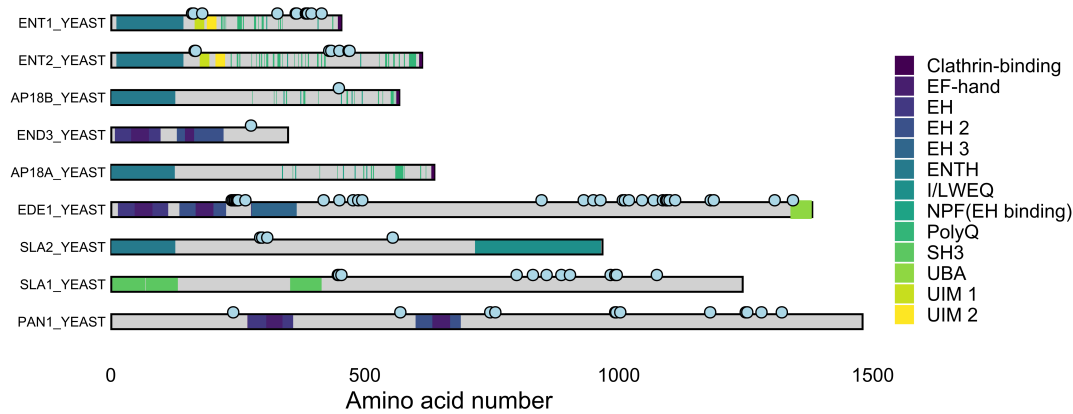


Figure 3.4: **Domain organization of endocytic adaptors from *S. cerevisiae*.**

3.3.3 The AP-2 adaptor complex

One of the most important adaptor complexes during CME is the AP-2 complex. The AP-2 complex belongs to a family of membrane trafficking hetero-tetrameric adaptor complexes, classified from AP-1 to AP-5, involved in different membrane trafficking pathways such as the trans-Golgi network and the endo-lysosomal system (Park, Guo, 2014). The AP-2 complex has been extensively studied given its relevance during cargo selection and its relation with the initiation of the formation of the clathrin coat (Cocucci et al., 2012; Graham et al., 2014).

This hetero-tetrameric complex is composed by 2 large homologous subunits (β and δ), a medium chain (μ) and a small chain (σ). The topology of the AP-2 complex comprises a compact core built by the four subunits, with two peripheral appendage domains connected to the large subunits by flexible linkers. Several structural studies using X-ray crystallography and cryoEM have revealed the different conformations of the complex upon membrane and cargo binding, and its contribution of the recruitment of further components of the endocytic coat (Kovtun et al., 2020; Muenzner et al., 2017; Partlow et al., 2022). The core of the AP-2 complex has been shown to adopt (at least) two different conformations, a closed state and an open state, the latter exposing the cargo binding sites for binding. In the close state, larger contacts are established between the two large subunits, and the intermediate μ subunit rests in between the two, while opening of the core leads to large movement of the intermediate μ subunit for cargo binding. Through its different subunits, the AP-2 complex contains (1) motifs for

binding PIP₂ in the plasma membrane, (2) cargo binding domains that bind motifs in receptors and (3) clathrin binding motifs, located in the β 2 subunit which have shown to promote clathrin assembly (Edeling et al., 2006), and that bind to the NTD domain of CHC (Muenzner et al., 2017). Finally, AP-2 recruits other adaptors such as Eps15 to the endocytic site by binding sites present on its appendage domains (Schmid et al., 2006).

3.3.4 Mid-coat endocytic adaptors in yeast: Ent1 and Sla2

Besides the AP-2 complex, adaptor proteins usually contain membrane binding domains that keep the endocytic coat bound to the plasma membrane (such as ANTH and ENTH domains), and intrinsically disordered regions (IDRs) that contain Short Linear Motifs (SLiMs) that bind to clathrin, other adaptors and cargo. Some adaptors, such as Epsins, also contain Ubiquitin Interaction motifs (UIMs) for interacting with Ubiquitinated cargoes (Szymanska et al., 2016)(Figure 3.4).

Mid coat adaptors, Sla2 (also known as End4 in literature) and Ent1 (Hip1R and Epsin-1 in higher eukaryotes) have been studied in yeast and in higher eukaryotes with some differences. These two adaptors have the topology of elongated knot and string proteins, with globular domains connected by coiled-coil or intrinsically disordered regions (IDRs) (Figure 3.5). Sla2 and Ent1 interact also with the clathrin coat.

Sla2 was initially assigned as cortical actin binding protein involved in clathrin mediated endocytosis and known to exist as a dimer (Yang et al., 1999). Later, its connection with the clathrin coat by its coiled coil domain and its string and knots topology was described using microscopy, together with its role in connecting the plasma membrane (Engqvist-goldstein et al., 2001). The N-terminal ANTH domain binds to the plasma membrane by interactions with PIP₂ and other phospholipids (Ford et al., 2001). The C-terminal domain of Sla2 was defined as an actin binding domain in the 90s as a conserved region of this protein and other actin binding proteins (McCann, Craig, 1997). The actin binding domain of the mammalian homologue, Hip1R, termed talin-HIP1/R/Sla2p actin-tethering C-terminal homology (THATCH) domain, was characterized using X-ray crystallography and the residues relevant for actin binding were described (Brett et al., 2006). Recent *in situ* cellular studies have been able to localize the actin binding domains of Hip1R in the proximity of actin filaments at

the endocytic site, where this actin regulator is present (Serwas et al., 2022). Hip1R and the related protein Hip1 (a close homologue) were found to interact directly *in vivo* with Clathrin Light Chain (CLC). This interaction takes place on the coil-coil region of this adaptor, as it can be seen from the crystal structure of Hip1R, which lays down a platform for CLC binding (Legendre-Guillemain et al., 2005; Wilbur et al., 2008; Ybe et al., 2007). In yeast, the interaction between CLC and Sla2 has been proposed to have a regulatory role of clathrin over Sla2, controlling the internalization of the plasma membrane (Boettner et al., 2011).

Epsin-1 (Ent1 in yeast) was firstly identified as an endocytic protein associated with clathrin (Chen et al., 1998; Wendland et al., 1999). As many other adaptor proteins, Ent1 has an N-terminal membrane binding domain, termed ENTH, followed by a highly flexible and disordered region that contains Ubiquitin-Interacting Motifs (UIMs) and short SLiMs, that bind to clathrin and to other adaptors such as AP-2 and Eps15 (Kalthoff et al., 2002). A key component of the interactions of Ent-1 with the plasma membrane is its N-terminal amphipathic helix, which bends the plasma membrane by insertion into the inner bilayer (Ford et al., 2002; Itoh et al., 2001; Kweon et al., 2006; Lai et al., 2012; Yoon et al., 2010). The intrinsically disordered region of Ent-1 also contributes to membrane remodeling, by crowding effect and it was proved to be key for the reconstitution of a minimal endocytic system (Dannhauser, Ungewickell, 2012). Differently than Sla2, Ent1 does not contain a folded C-terminal domain that binds to actin, however, a conserved region in its intrinsically disordered region has been shown perform an actin binding role similar to the actin binding domain of Sla2. Interestingly, phosphorylation sites present in this region of the IDR of Ent1 targeted by Prk1 kinase were shown to negatively regulate the actin binding of Ent1 (Skruzny et al., 2012). Ent1 contains at least one “Clathrin Box” SLiM in its C-terminal IDR, defined in the Eukaryotic Linear Motif database as: L [IVLMF].[IVLMF][DE] (Kumar et al., 2022). This SLiM has been shown to interact with the N-terminal Domain of CHC, by specifically binding some sites of the β -propeller. Even though there is a lot of structural information about the binding of this motifs to CHC, there are several open questions regarding how these different motifs can regulate the assembly of the coat.

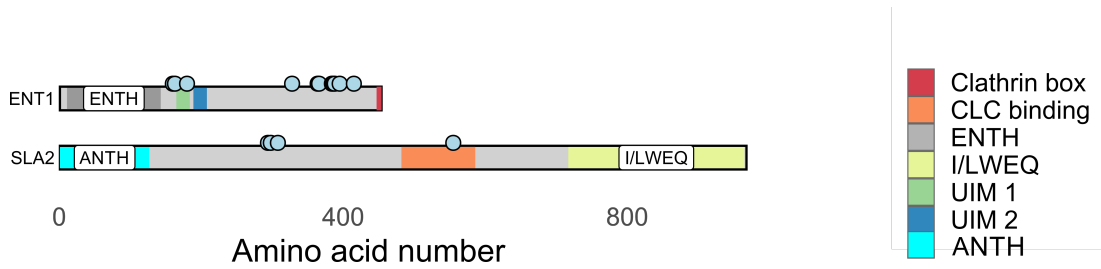


Figure 3.5: **Domain organization of Sla2 and Ent1.**
The clathrin interaction regions are also shown. Phosphorylation sites are represented with blue circles.

3.3.5 Phospholipids trigger the assembly of the endocytic coat

Beyond the variety of proteins involved in CME, the composition of the plasma membrane also plays an important role in the regulation and control of this essential biological process, in particular phosphoinositides (PIPs). It is known that the PIP_2 local concentration is increased in regions of the plasma membrane targeted for endocytosis promoting the binding of adaptors, by phosphorylation of $\text{PI}(4)\text{P}$ by PI 4-kinase III (Baskin et al., 2016) and type I PI 4-phosphate 5-kinases (PIP5Ks) (Di Paolo, De Camilli, 2006; He et al., 2017). The enhanced affinity of the membrane binding domains of these adaptors for this specific phospholipid compared to other lipids present in this regions of the plasma membrane triggers the assembly of the endocytic coat via the multiple interactions of adaptor domains containing membrane binding domains (such as ANTH and ENTH) and AP-2 complex (Ford et al., 2002; Itoh et al., 2001). The direct activation of kinases that phosphorylate $\text{PI}(4)\text{P}$ to convert it into $\text{PI}(4,5)\text{P}_2$ by the AP-2 complex creates a forward feedback loop that promotes the endocytic coat in regions of the plasma membrane designated to be internalized by CME (Thieman et al., 2009). As the endocytic pits mature, the recruitment of 5-phosphatases (such as synaptojanin and SHIP2) that hydrolyze the $\text{PI}(4,5)\text{P}_2$ and $\text{PI}(3,4,5)\text{P}_3$ leads to the progression of CCP internalization. Disruption of this process leads to the accumulation of abortive CCPs in the membrane (Nakatsu et al., 2010). Towards the mature stages of CCPs, $\text{PI}(3,4)\text{P}_2$ is synthesized from $\text{PI}(4,5)\text{P}_2$ by the phosphatidylinositol 3-kinase $\text{C}2\alpha$. This change in the lipid composition of the CCP favours the recruitment of BAR containing proteins, such as sorting nexin 9 (SNX9), which contribute to membrane constriction of the neck of the CCP (Schöneberg et al., 2017).

3.3.6 Membrane binding domains during clathrin-mediated endocytosis

In the plasma membrane, PI(4,5)P₂ becomes the triggering factor the ANTH-ENTH interaction of Sla2 and Ent1. Ent1 and Sla2 bind to the plasma membrane in regions where the endocytic coat is assembled through their membrane binding domains, epsin N-terminal homology (ENTH) and AP180 N-terminal homology (ANTH) domains, respectively (Ford et al., 2001, 2002; Garcia-Alai et al., 2018; Skruzny et al., 2015). They bind specifically to the polar group of PI(4,5)P₂, a lipid enriched at the endocytic sites. ANTH and ENTH domains from these adaptors and other homologues have been previously extensively studied, with several structures of both domains from different domains available in the Protein Data Bank (Table 3.1). The structures of ENTH and ANTH domains in complex with PIP₂ and other phospholipids reveal their different lipid binding mechanisms (Figure 3.6).

ANTH domains have a conserved PIP₂ binding motif (³⁷KKKH⁴⁰, residue numbering for CALM) that creates a positively charged patch that coordinates the polar head group of PIP₂ (negatively charged, Figure 3.6a). As an electrostatic interaction, this interaction has been shown to be dependent on pH (Hom et al., 2007). The ANTH domain of Sla2 shows two specific features distinguish it from the ANTH domain of the CALM family: the absence of an N-terminal amphipathic helix in Sla2 and the presence of an extended loop between the $\alpha 8$ and $\alpha 9$ helices of the ANTH domain, as it can be observed from crystal structure of the ANTH domain of Sla2 from *C. thermophilum* (Garcia-Alai et al., 2018).

ENTH is a small globular domain that contains an N-terminal amphipathic helix, usually termed as $\alpha 0$. Several studies have shown the flexible and disordered nature of this $\alpha 0$ helix in absence of lipids or a membrane environment (Kweon et al., 2006). ENTH in complex with I(1,4,5)P₃, a similar phosphatidylinositol shows a binding pocket comprising the conserved residues R7, R8, R25, N30, R63, K69, and H73 (residue numbering from *R. norvegicus*) that coordinate the head of the phospholipid in the core of its domain by the contribution of the charged residues of its amphipathic helix (Figure 3.6b). A crystal structure of a complex of two ENTH domains bound to a single molecule of PI(4,5)P₂ highlighted the structural cooperativity in the binding of

epsins to the phospholipids in the plasma membrane (Figure 3.6c) (Garcia-Alai et al., 2018).

3.3.7 Membrane remodeling during clathrin mediated endocytosis

During clathrin mediated endocytosis, the plasma membrane needs to be remodeled into a high-curvature endocytic pit from which a vesicle will emerge from the plasma membrane (Figure 3.2). There are several mechanisms of membrane remodelling and curvature generation, including changes in the lipid composition in one side of the membrane bilayer, protein crowding, insertion of hydrophobic protein domains, membrane scaffolding of the curvature and cytoskeletal forces such as actin polymerization which deform the membrane (Haucke, Kozlov, 2018; McMahon, Boucrot, 2015).

One mechanism performed by epsins among other adaptor proteins, is the insertion of an amphipathic α -helix into the plasma membrane. This helix, usually that is known to refold upon interaction with the plasma membrane (Lai et al., 2012). By insertion of this helix only into the inner leaflet of the lipid bilayer of the plasma membrane, these proteins are able to generate negative curvature that promotes membrane invagination towards the interior (Campelo et al., 2008).

Another mechanism to promote membrane bending is the presence of domains with intrinsic curvature that stabilize the curvature generated during membrane remodeling for invagination (Kozlov, Taraska, 2022). BAR (Bin/Amphiphysin/Rvs) domain containing proteins, bind to membranes by coordination of the polar head groups of phospholipids in the membrane. The oligomerization of BAR domains in the plasma membrane imposes intrinsic curvature in the plasma membrane (Frost et al., 2008).

Finally, several endocytic adaptors, including Epsin1 and AP180, contain intrinsically disordered regions (IDRs), which have been shown to contribute to membrane remodeling by steric pressure that drives membrane bending (Busch et al., 2015; Stachowiak et al., 2012). Recent work has also unveiled the mechanism of generation of the steric pressure by large disordered regions using FRET (Houser et al., 2022). The pressure of the plasma membrane and the force needed for membrane remodeling has been object of several studies, with several models for the force production for membrane invagination have been proposed (Lacy et al., 2018).

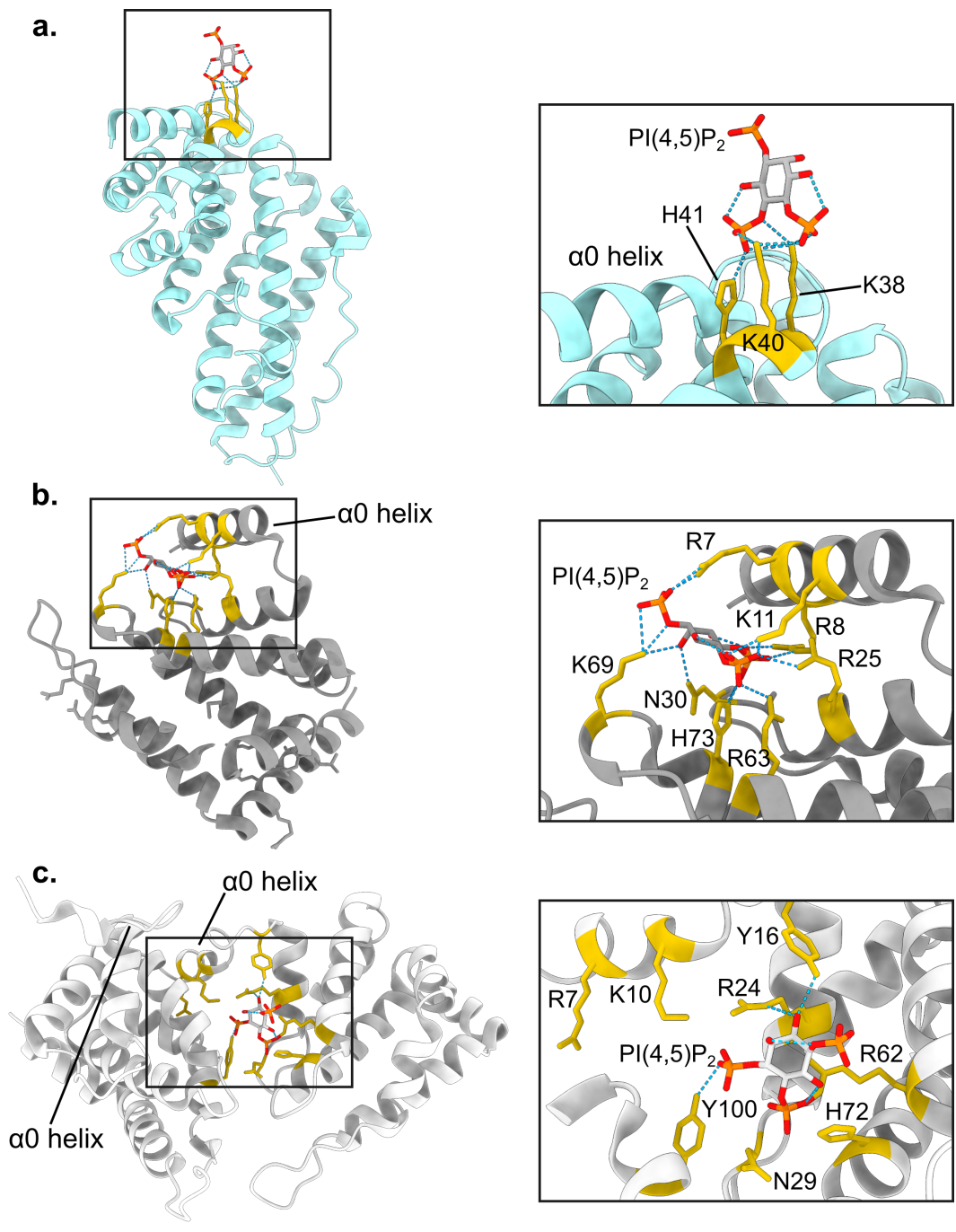


Figure 3.6: PIP₂ binding mechanism of ANTH and ENTH domains.
a. CALM ANTH domain from *R. norvegicus* (PDB ID = 1HFA, (Ford et al., 2001)). The conserved PIP₂-binding motif KRKH is located in the proximity of the amphipathic alpha helix. **b.** ENTH domain from Ent-1 from *R. norvegicus* bound to IP₃ (PDB ID = 1H0A, from (Ford et al., 2002)). The phospholipid binding site is located in the pocket between the amphipathic alpha0 helix and the core of the domain. **c.** ENTH domain of Ent2 from *S. cerevisiae* (PDB ID = 5ON7, from (Garcia-Alai et al., 2018)). The crystal structure shows that the PIP₂ is located between the two domains, with residue Y100 coordinating the PIP₂ from the binding pocket. For the three structures, the domains are shown in a cartoon representation and the phospholipids are shown in stick representation. The residues coordinating the polar head of the phospholipids are shown in stick representation and coloured in gold, and the hydrogen bonds are shown as dashed blue lines.

3.3.8 Cooperative molecular bridging by Sla2 and Ent1

In yeast, high turgor pressure makes actin polymerization forces indispensable for membrane internalization, where mammalian cells do not require of these forces in order to be able to invaginate the plasma membrane (Kaksonen, Roux, 2018; Smith, Smith, 2022). The cooperation between Sla2 and Ent1 during clathrin mediated endocytosis and their role as essential connectors between the plasma membrane and the actin cytoskeleton has been shown in previous studies.

Disturbance of the connection between the plasma membrane and the actin cytoskeleton by deletion of Sla2 generated a characteristic phenotype with defects over internalization, revealing actin tails during CME (Kaksonen et al., 2003). Interestingly, controlled removal of both Epsin genes in yeast (EPN1 and EPN2) yielded a similar result, indicating epsins also play a role in the attachment of the plasma membrane with the actin cytoskeleton, with evidence for the concerted action of Sla2 and Ent1 in membrane-actin cytoskeleton coupling (Skruzny et al., 2012). Both proteins connect the plasma membrane and the actin cytoskeleton (through their C-terminal actin-binding domains), which allows them to gather the forces provided by actin for successful membrane invagination of the plasma membrane (Messa et al., 2014). A recent quantification of the forces exerted for membrane invagination by Sla2 using FRET-based sensors report this affinity around 8 pN per Sla2 molecule (Abella et al., 2021). Molecular studies of the ANTH-ENTH interactions have shown that the coordinated action of both domains is capable of deforming membranes into regular protein-coated tubules and Electron Microscopy studies of these tubules revealed a regular lattice of ANTH and ENTH domains that cover the plasma membrane. However, the interpretation of this data was limited by the resolution achieved, and the cooperative mechanism of the two adaptor proteins could not be described (Skruzny et al., 2015). Further *in vitro* studies using ANTH and ENTH domains from yeast and humans demonstrated the existence cooperativity in the binding of PIP₂ by the concerted action of the two domains, and the formation of hetero-oligomers of ANTH and ENTH domains by Native Mass Spectrometry (Native MS). Following these findings, a model for the assembly of the two domains in the plasma membrane over time was proposed (Garcia-Alai et al., 2018; Heidemann et al., 2020).

Table 3.1: List of structural models deposited in the Protein Data Bank for ANTH and ENTH membrane binding domains of adaptor proteins.

Protein	Domain	Species	PDB code	Reference
Ent-1	ENTH	<i>R. norvegicus</i>	1EDU	Hyman et al., 2000
Ent-1	ENTH	<i>S. cerevisiae</i>	5LOZ	Tanner et al., 2016
Ent-1	ENTH-IP ₃	<i>R. norvegicus</i>	1H0A	Ford et al., 2002
Ent-1	ENTH	<i>D. rerio</i>	5LP0	Levin Kravets et al. 2016
Ent-2	ENTH-PIP ₂	<i>S. cerevisiae</i>	5ON7	Garcia-Alai et al 2018
Ent-2	ENTH	<i>S. cerevisiae</i>	4GZC	Costakes et al., 2013
Ent-1	ENTH	<i>S. cerevisiae</i>	5ONF	Garcia-Alai et al., 2018
Ent-1	ENTH	<i>S. cerevisiae</i>	5AHV	Skruzny et al., 2015
CLINT1	ENTH	<i>H. sapiens</i>	2QY7	Miller et al., 2007
Ent-3	ENTH	<i>S. cerevisiae</i>	3ONK	Wang et al., 2011
Ent-5	ENTH	<i>S. cerevisiae</i>	5J08	Zhang et al., 2016
Ent-2	ENTH	<i>S. cerevisiae</i>	6ENR	Garcia-Alai et al., 2018
Ent-2	ENTH N112D/ S114E/ E118Q	<i>S. cerevisiae</i>	4GZD	Costakes et al., 2013
AP180	ANTH	<i>D. melanogaster</i>	1HX8	Mao et al., 2001
Sla2	ANTH	<i>C. thermophilum</i>	5OO7	Garcia-Alai et al., 2018
CALM	ANTH	<i>R. norvegicus</i>	1HF8	Ford et al., 2001
CALM	ANTH-PIP ₂	<i>R. norvegicus</i>	1HFA	Ford et al., 2001
CALM	ANTH-IP ₂	<i>R. norvegicus</i>	1HG2	Ford et al., 2001
CALM	ANTH-IP ₆	<i>R. norvegicus</i>	1HG5	Ford et al., 2001
CALM	ANTH-Ub	<i>H. sapiens</i>	7JXV	Pashkova et al., 2021
PICALM	ANTH	<i>R. norvegicus</i>	3ZYK	Miller et al., 2011
Hip1R	ANTH	<i>R. norvegicus</i>	7OST	Ford et al., TBP

4. Objectives of this work

The endocytic coat relies on several transient protein-protein and protein-lipid interactions throughout the constant deformation of the plasma membrane. It is intriguing how the weak protein-membrane interactions so far described can hold the plasma membrane during its remodeling without detaching from the membrane (Ford et al., 2001, 2002; Smith et al., 2017). Several mechanisms for membrane remodeling have been studied and models have been proposed (Campelo et al., 2008; Di Paolo, De Camilli, 2006; Haucke, Kozlov, 2018; Kozlov et al., 2014; Sun, Drubin, 2012), yet the structural role of PIP₂ during membrane remodeling is still under debate, and our understanding of the nature and dynamics of membrane phospholipids and their associations with endocytic proteins during endocytosis remains limited.

Here, the following questions regarding adaptors are addressed:

- What is the structural basis for the high-affinity of adaptors for the plasma membrane?
- How is membrane remodeling affected by multimeric complex protein scaffolds in addition to the mechanism studied for individual adaptors?
- What are the time-scales of formation of multimeric mid-coat complexes?

Beyond these questions, midcoat adaptors connect the plasma membrane with the clathrin coat and with the actin cytoskeleton. In the second part of this work, characterization of adaptors addresses the following questions:

- What is the conformational landscape of adaptors in solution, and how are those influenced by clathrin binding?
- Are there structural changes in Sla2 upon binding to clathrin and to the membrane?
- What elements regulate the binding of mid-coat adaptors to clathrin?

5. Results

5.1 Structural basis of ANTH-ENTH cooperation for membrane binding and remodelling during clathrin-mediated endocytosis

5.1.1 Sample preparation of the ANTH:ENTH:PIP₂ complex

The ANTH domain from Sla2 and the ENTH domain from Ent1 from *S. cerevisiae* were produced recombinantly and purified. ANTH and ENTH domains have been previously described as globular domains of 33 and 18 kDa respectively (PDB ID 5ONF, 5ON7, 5OO7, 7OST, 3ZYK, and Table 3.1) (Garcia-Alai et al., 2018; Miller et al., 2015). The first step after protein purification is to verify that the recombinant proteins are folded and that sample quality is adequate for structural studies. nanoDSF showed that ANTH and ENTH domains are thermally stable, with melting temperatures (T_m) of 61 °C and 53 °C, respectively (Figure 5.1).

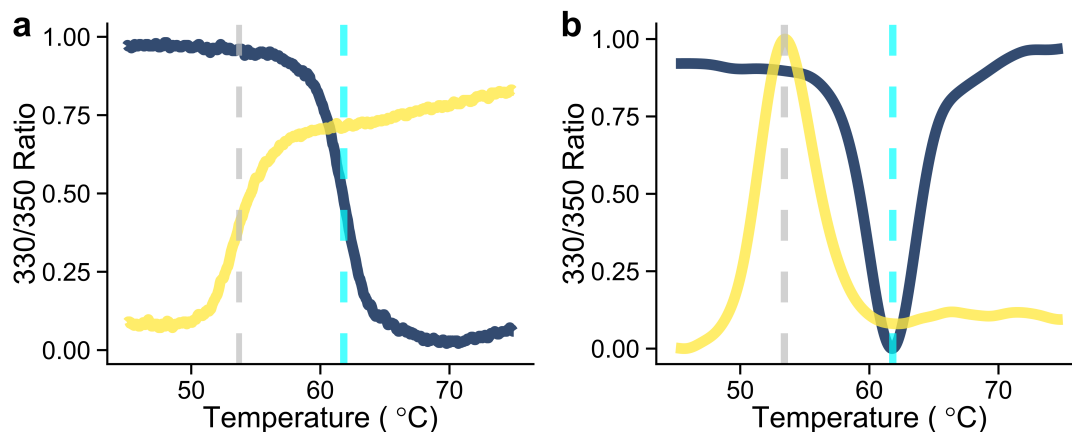


Figure 5.1: **nanoDSF of the ANTH domain of Sla2 and ENTH domain of Ent1.** ANTH (blue) and ENTH (yellow) show a transition upon thermal denaturation due to the change of the environment of the Trp residues **a**. Signal from the Ratio of the fluorescence at 330 and 350 nm. The (T_m) calculated from the transitions is shown as a dashed line (grey for ENTH and cyan for ANTH). **b**. First derivative of the data from which the T_m is calculated.

Dynamic Light Scattering (DLS) experiments were performed to characterise the behaviour of ANTH and ENTH samples in different conditions. At high concentrations (10 mg/ml), DLS showed that the ANTH domain of Sla2 displayed a small shoulder

on its auto-correlation (AC) function, indicating that this domain might be prone to produce some aggregates at high concentrations (Figure 5.3a). Lowering the concentration of ANTH domain removed the aggregates present in the sample (see below). On the other hand, the ENTH domain of Ent1 behaved as a monodisperse sample even at high concentrations. (Figure 5.3b)

After characterization of the small domains, screening to obtain a sample of a hetero-complex of ANTH and ENTH in presence of PIP₂ was performed using DLS. For ANTH-ENTH-PIP₂ complex reconstitution experiments, a soluble variant of the lipid was chosen in order to be able to perform biophysical techniques based on previous work (Garcia-Alai et al., 2018). Measurements of SEC buffer containing either 200 and 400 μM of soluble PIP₂ (diC8-PI(4,5)P₂, from now on referred only as PIP₂) showed an auto-correlation function of comparable slope at both concentrations (Figure 5.2). Typically, buffers used for DLS experiments should not contain components with significant contribution to the scattering, however this is not the case when the sample contains detergents or lipids above their Critical Micellar Concentration (CMC) (Meyer et al. (2015)). In these cases, the DLS auto-correlation function reports the presence of the lipid micelles in solution as these concentrations are above the CMC of the PIP₂.

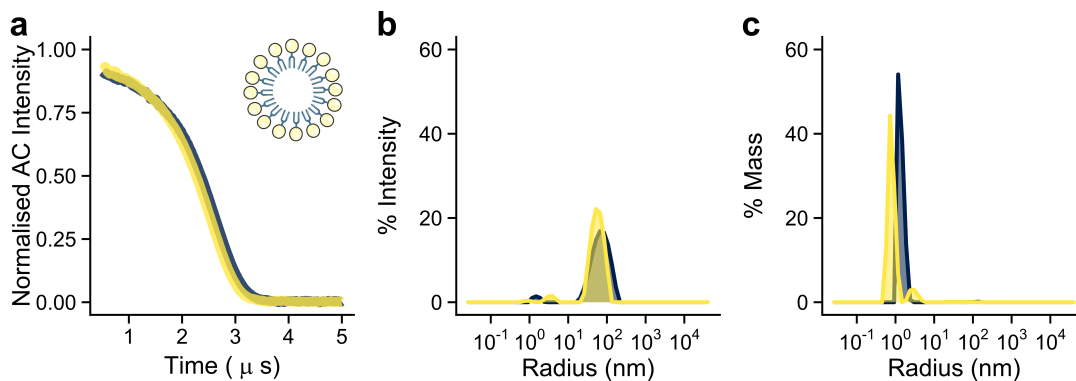


Figure 5.2: **DLS of SEC Buffer containing diC8-PI(4,5)P₂.**

a. The buffer with 200 μM (yellow) and 400 μM (blue) shows an auto-correlation function due to the presence of the PIP₂ micelles (showed as a schematic on top). **b and c.** Intensity and mass plots derived from the auto-correlation function using the Cumulants method for analysis (see Methods). The overall size of the PIP₂ micelles is around 1 nm.

Upon mixing of the ANTH and ENTH domains at high concentrations (approx. 10 mg/ml) with PIP₂, large aggregates were formed in the samples, reported by the DLS AC functions (Figure 5.3, yellow curves). Structural techniques, including X-ray crystallography, cryo-EM and particularly SAXS, which were intended to be used for

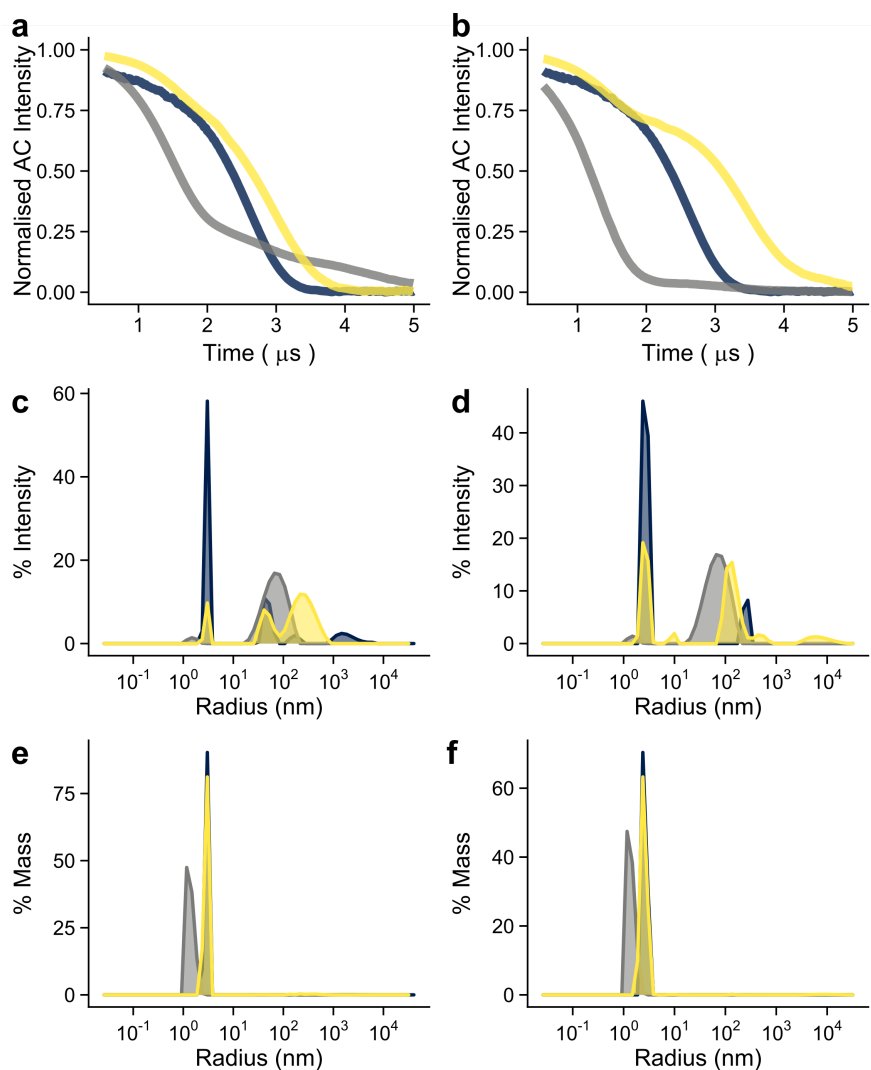


Figure 5.3: **DLS of the ANTH and ENTH domains in presence of PIP₂.**

a. Auto-correlation curves for the ANTH at 10 mg/ml (grey), 200 μ M PIP₂ (blue) and ANTH at 10 mg/ml in presence of 200 μ M PIP₂ (yellow). **b.** Auto-correlation curves for the ENTH at 10 mg/ml (grey), 200 μ M PIP₂ (blue) and ENTH at 10 mg/ml in presence of 200 μ M PIP₂ (yellow). **c and d.** Intensity plots for the different populations detected in solution. **e and f.** Mass plots for the different populations detected in solution.

studying ANTH-ENTH-PIP₂ hetero-complexes, do not tolerate the presence of significant amounts of aggregates. Therefore, sample optimization was required in order to find conditions that render a sample amenable for structural studies.

There are a few reasons to explain the large aggregation events present in these samples. It is known from literature that the refolding of the ENTH α 0 (disordered in the absence of a membrane/lipids) allows its insertion into the plasma membrane (Ford et al., 2002; Lai et al., 2012). For this reason, it is likely that the sample becomes more unstable and prone to aggregation upon addition of PIP₂ due to these conformational changes.

To overcome this effect and improve the quality of samples containing ANTH-ENTH-PIP₂ complexes, the sample preparation protocol was modified (Figure 5.4). First, the concentration of ANTH/ENTH was decreased to around 20 μ M. This was done in order to decrease amount of aggregates observed for ANTH domain (even in the absence of lipid, Figure 5.3a). Secondly, the ANTH and ENTH were incubated with the lipid separately at Room Temperature for 3 hours. The reason for the long incubation time is due to the fact that aggregation of the domains upon addition of PIP₂ might be transient/reversible, and therefore this incubation step could potentially allow for some aggregates to be brought back into solution in the presence of PIP₂. After incubation, the sample was centrifuged in order to remove the aggregates that are not soluble after incubation. The protein concentrations were then re-adjusted by re-measuring the Absorbance at 280 nm (to account for the fraction of protein that became insoluble upon mixing it with the PIP₂). Finally, the ANTH and ENTH domains in presence of PIP₂ were mixed at equimolar ratios.

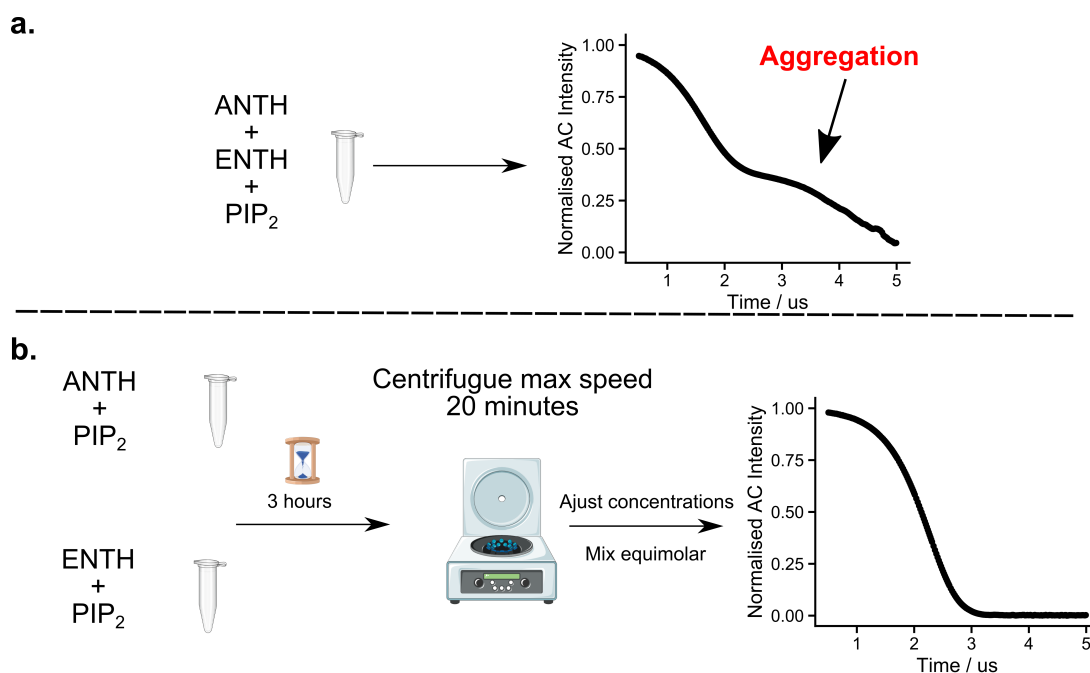


Figure 5.4: **Sample preparation of the ANTH-ENTH-PIP₂ complexes.**

a. Mixing and incubation of ANTH and ENTH domains together with PIP₂ results in aggregated samples, as it can be appreciated in the auto-correlation function from the DLS. **b.** incubation of each domain separately with PIP₂ and centrifugation renders monodisperse samples that can be further used for structural studies.

As expected the samples of ANTH-PIP₂ and ENTH-PIP₂ with lower protein concentration showed AC functions with a higher degree of monodispersity than the ones prepared at high concentrations (Figure 5.5). However, their auto-correlation func-

tions shifted towards longer auto-correlation times that corresponded to larger soluble species present in the sample. This indicates that ANTH and ENTH individually are also capable of larger oligomerization into large soluble species in presence of PIP₂.

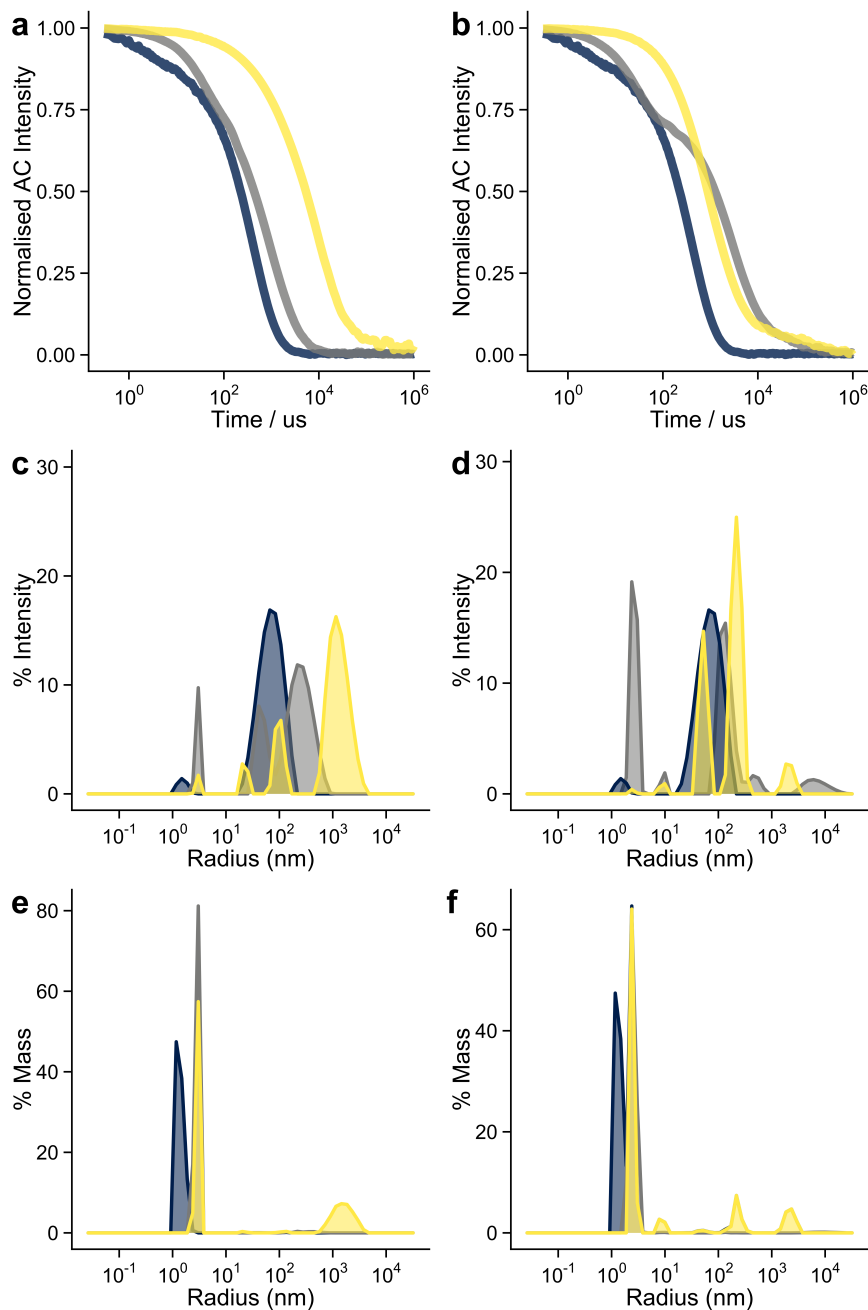


Figure 5.5: **Sample preparation of ANTH-PIP₂ and ENTH-PIP₂ samples.**
a and b. Auto-correlation functions for ANTH (**a**) and ENTH (**b**) domains at high (grey) or low (yellow) protein concentrations. The auto-correlation function of the buffer is shown in blue for comparison with both samples. **c and d.** Intensity plots for the ANTH-PIP₂ (**c**) and ENTH-PIP₂ (**d**) samples. **e and f.** Mass plots for the ANTH-PIP₂ (**e**) and ENTH-PIP₂ (**f**) samples.

In contrast with the initial sample prepared just by mixing the different components of the ANTH-ENTH-PIP₂ complex, the sample corresponding to the ANTH-ENTH-

PIP₂ complexes prepared using the optimized protocol displays a monodisperse DLS auto-correlation function that corresponds with particles of a size around 9 nm (Figure 5.7). These particles yield a molecular weight and dimensions in agreement with the previously identified oligomeric states by Native MS (Garcia-Alai et al., 2018). Strikingly, upon mixing of the ANTH-PIP₂ and ENTH-PIP₂ samples at equimolar ratios, the auto-correlation function shifted towards shorter times, corresponding to smaller particles dominating the scattering signal of the sample (Figure 5.7, and Table 5.1). This shows that mostly likely hetero-oligomers of ANTH-ENTH domains are smaller than the larger ones created by just either ANTH or ENTH with PIP₂ in solution *in vitro*.

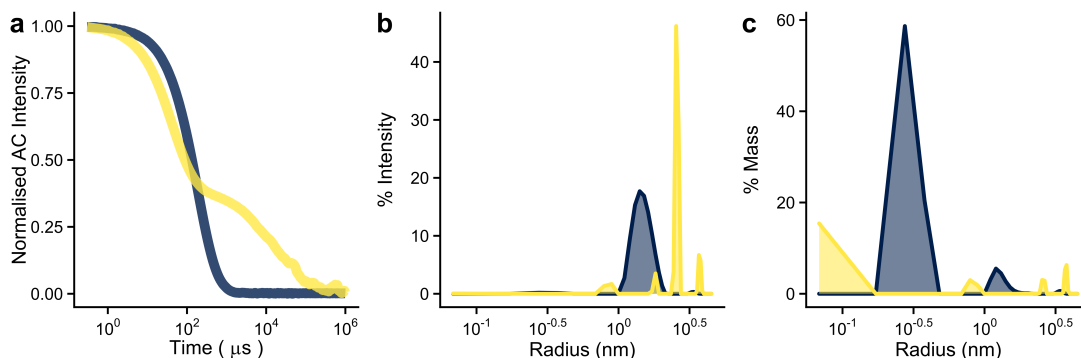


Figure 5.6: **DLS comparison between ANTH-ENTH-PIP₂ samples using high and low concentration of protein.**

a. Auto-correlation function. The sample prepared at high concentration (yellow) presents a large component of aggregates that make the sample non-suitable for structural studies, while the low concentration sample (blue) shows a monodisperse curve. **b and c.** Intensity and Mass plots derived from the AC function for these samples. The sample at low concentration of protein displays a large peak at the expected radius for particles of ANTH-ENTH-PIP₂ oligomers.

Table 5.1: Parameters obtained from the DLS AC functions of the ANTH-ENTH-PIP₂ sample

Peak	Radius (nm)	% Pde	MW (kDa)	% Intensity	% Intensity	% Number
Peak 1 (True)	1.6	7.88	9.9	0.7	50.4	99.2
Peak 2 (True)	7.9	11.55	419.3	81.8	48.5	0.8
Peak 3 (True)	257.6	14.96	1473226.6	8.7	0.2	0.0
Peak 4 (True)	1176.1	27.61	51449180.4	8.8	0.9	0.0

Once the sample preparation for ANTH-ENTH-PIP₂ complexes was optimised as described, Mass Photometry (MP) was used to explore the heterogeneity of the sample in terms of different oligomeric states, given its higher resolution when compared to techniques such as DLS for the accurate determination of the MW of protein complexes (Figure 5.8). MP showed a heterogeneous distribution with a large proportion of the sample corresponding to species of lower MW, including ANTH-dimers (peak at 55

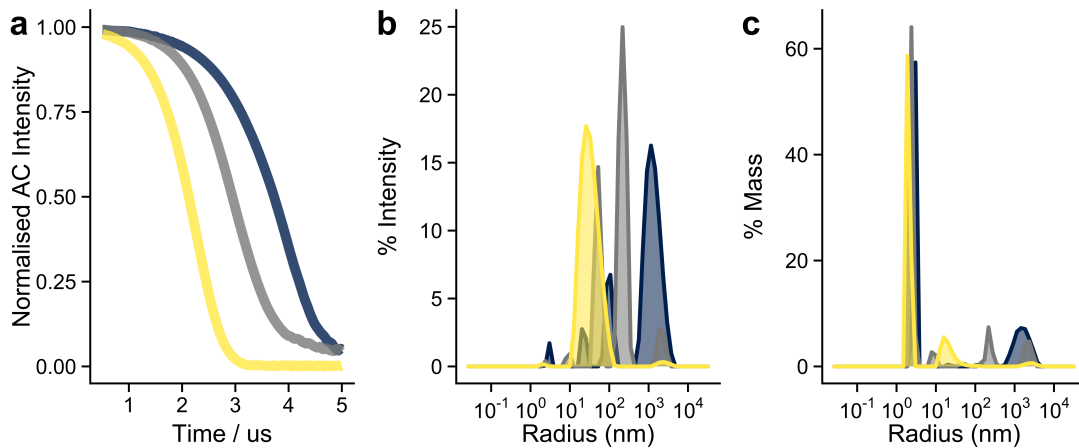


Figure 5.7: **Sample preparation of ANTH-ENTH-PIP₂ complexes from ANTH-PIP₂ and ENTH-PIP₂ complexes.**

a. Auto-correlation function of the ANTH-ENTH-PIP₂ sample (yellow), the ANTH-PIP₂ sample (blue) and the ENTH-PIP₂ sample (grey). **b and c** show the corresponding Intensity and Mass plots calculated from these samples.

KDa). Two peaks at 315 and 415 kDa could also be reliably detected, whose masses could be assigned to ANTH-ENTH-PIP₂ assemblies previously reported (Garcia-Alai et al., 2018; Heidemann et al., 2020) and that were solved using single particle cryoEM in this work (A₆E₆ and A₈E₈ assemblies, see below).

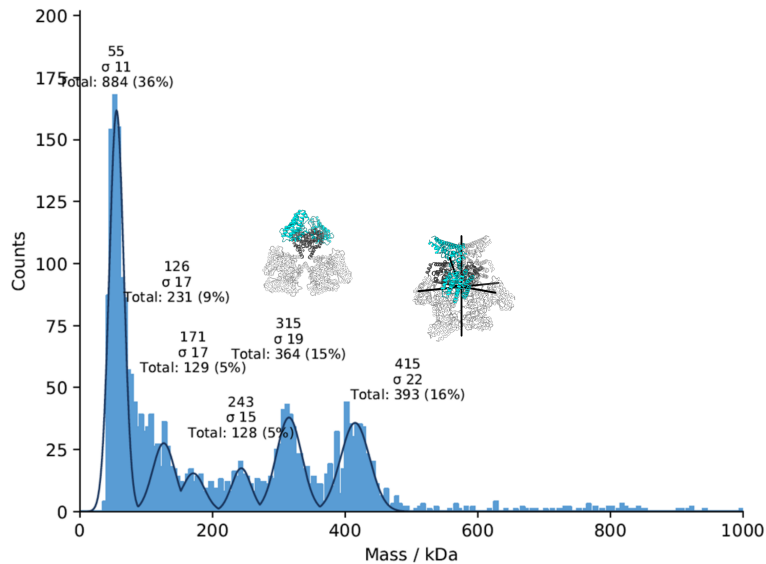


Figure 5.8: **Mass Photometry histogram of ANTH-ENTH-PIP₂ complexes.**

The sample at 100 nM contains a large proportion of ANTH dimers (at 55 kDa), and two main oligomeric populations at 315 and 415 kDa, which correspond with A₆E₆ and A₈E₈ assemblies of ANTH and ENTH domains in presence of PIP₂. There are other intermediates present in the sample for which the resolution is not as good therefore preventing its accurate assignment.

5.1.2 Protein-lipid ratios govern ANTH-ENTH-PIP₂ complex formation and its oligomeric diversity

Small Angle X-ray Scattering (SAXS) is a powerful tool to study the structural parameters of biological samples in solution without restraints imposed by other structural methods that provide information at higher resolution such as crystallography or cryoEM. SAXS curves of ANTH and ENTH in presence of PIP₂ and of the ANTH-ENTH-PIP₂ complexes were collected (Figure 5.9). ANTH-PIP₂ and ENTH-PIP₂ samples showed small R_G values in agreement with their known domain structure, and present a globular structure in spite of the addition of PIP₂. These data contradict the large particles observed by DLS upon the addition of PIP₂, since the contribution of these large particles to the scattering profile of the sample should be much larger than the one from the small globular domains.

Interestingly, ANTH showed a larger radius of gyration (R_G) than expected from its monomeric shape, but this could be due to its tendency to oligomerise, as we saw by DLS and the ANTH dimers observed in MP measurements (and also native MS, see below). In the case of the ANTH-ENTH-PIP₂ complex, the shape of the SAXS profile shows a remarkable change with respect to the samples corresponding each of the domains separately. A notable change is also reported in the overall dimensions derived from the R_G derived from the Guinier region and D_{max} (Table 5.2). This is in agreement with the fact that hetero-oligomers of both domains are being formed and constitute larger assemblies than the overall dimensions of these small globular domains. The overall shape of these oligomers in solution is still rather globular, as it can be appreciated in the dimensionless Kratky plot, where the maximum for the profile falls into the expected value for globular particles (Figure 5.9). Furthermore, we can see that the ANTH-ENTH-PIP₂ oligomers constitute a more “diverse” and flexible sample, as the Kratky plot does not completely return to the baseline towards higher qR_G values, indicating the presence of flexibility (and most likely heterogeneity) in the sample (Figure 5.9h).

To explore relevant factors that contribute to complex formation in solution, a titration of different protein concentrations into buffer containing either 200 or 400 μ M of PIP₂ using ENTH1 (ENTH domain of Ent1) and ENTH2 (ENTH domain of Ent2,

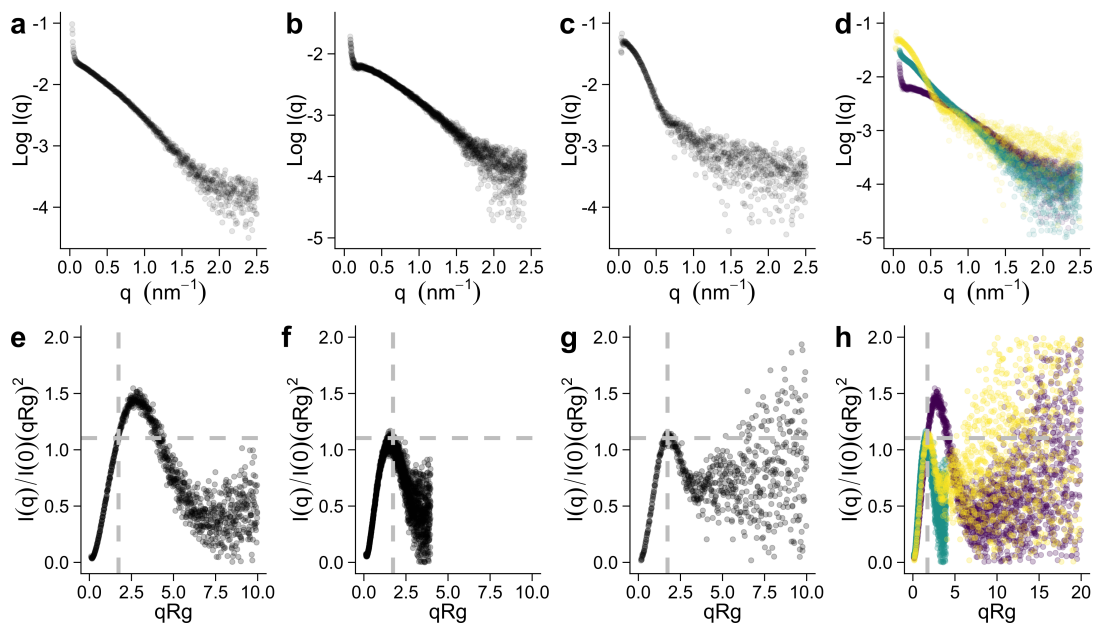


Figure 5.9: **SAXS data for ANTH, ENTH and ANTH-ENTH-PIP₂ complexes.**

The curves obtained for ANTH **a**, ENTH **b** are significantly different than the one obtained after mixing them **c**. **d**. Shows an overlay of the three different samples (ANTH in green, ENTH in purple and ANTH-ENTH-PIP₂ in yellow). **e - g** Dimensionless Kratky plots for each sample. **h**. Dimensionless Kratky plot for the three samples

a member of the Epsin family with high homology) was performed and SAXS data of these sample were recorded (Figure 5.10). Although the overall shape of the curves did not change massively, close inspection of the curves by comparison revealed small changes that indicate that the samples are different from each other, most probably due to the change on protein:lipid ratios. Looking at the overall sample parameters derived from the curves, a trend can be observed for the R_G , the D_{max} and for the Porod Volume (V_{POROD}) derived from the curves. All these parameters decrease upon decreasing the concentration of ANTH and ENTH domains (Figure 5.11). These trends indicate that upon increasing the amount of protein available, the equilibrium is shifting towards higher oligomeric states as the amount of lipid available decreases.

Using OLIGOMER (Konarev et al., 2003), which allows to fit several oligomeric states to the data, it could be seen how the monomer component increases in detriment of the complex components upon decrease in the protein:lipid ratios (Table 5.3). In conclusion, multiple oligomeric states of ANTH-ENTH-PIP₂ complexes are co-existing in solution and their abundance depends on the amount of lipids present for binding to ANTH and ENTH.

Finally, in addition to the titration and analysis performed using SAXS, native

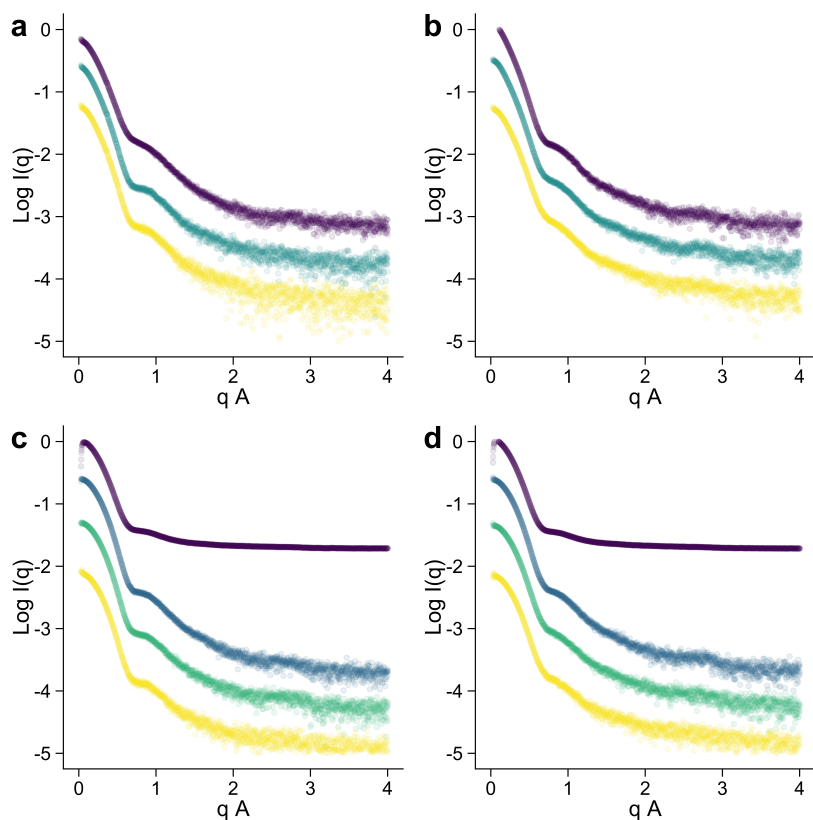


Figure 5.10: **SAXS data of several ANTH-ENTH1/2-PIP₂ complexes.**
a. ANTH and ENTH1 at 200 μM PIP₂. **b.** ANTH and ENTH1 at 400 μM PIP₂. **c.** ANTH and ENTH2 at 200 μM PIP₂. **d.** ANTH and ENTH2 at 400 μM PIP₂. The protein concentrations are indicated in Table 5.2

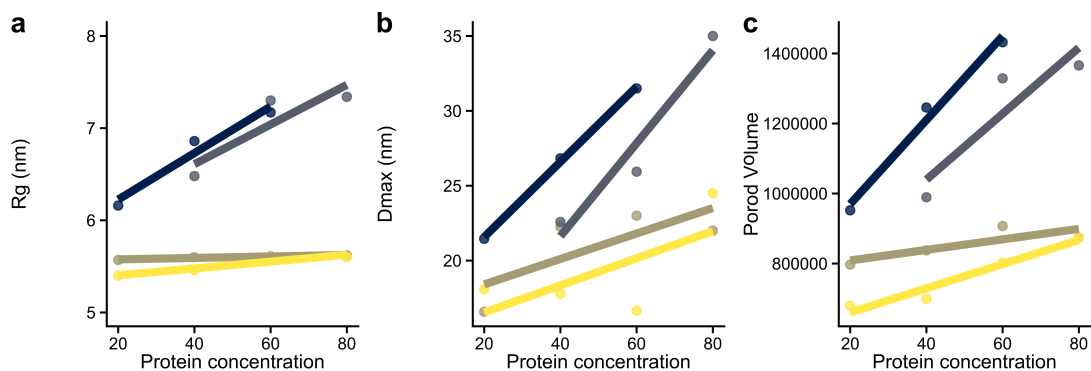


Figure 5.11: **SAXS derived parameters of ANTH-ENTH1/2-PIP₂ complexes in solution.**
 R_G (a), D_{max} (b) and V_{POROD} (c) are shown for ANTH-ENTH1 with 200 μM PIP₂ (blue), ANTH-ENTH1 with 400 μM PIP₂ (grey), ANTH-ENTH2 with 200 PIP₂ (brown) and ANTH-ENTH2 with 400 μM PIP₂ (yellow). All of them increase upon increasing the protein concentration.

Table 5.2: SAXS parameters derived from different ANTH-ENTH assemblies in solution in presence of **PIP₂**.

Protein (μM)	ENTH1				ENTH2				
	80	60	40	20	80	60	40	20	
	PIP ₂ (μM)								
R _G	200		7.17	6.86	6.16	5.62	5.61	5.6	5.57
	400	7.34	7.3	6.48		5.6	5.6	5.46	5.4
D _{MAX}	200		31.5	26.83	21.46	22	23	22.26	16.58
	400	35	25.94	22.58		24.5	16.65	17.77	18.09
V _{POROD}	200		1432020	1245630	952101	874109	907193	837671	797120
	400	1365910	1328900	989333		874893	802079	698845	679323

Table 5.3: Fitting of different oligomeric states using OLIGOMER to SAXS data from different ANTH-ENTH1/2 assemblies in solution in presence of **PIP₂**.

PIP ₂ (μM)	Protein (μM)	ENTH1				ENTH2			
		80	60	40	20	80	60	40	20
200	32-mer	m0.278	0.526	0.454	0.27	0.176	0.195	0.165	0.144
	16-mer	0.338	0.387	0.473	0.579	0.597	0.694	0.711	0.719
	Monomer	0.384	0.086	0.072	0.151	0.226	0.11	0.124	0.137
	χ^2	3.27	1.60	1.32	15.40	4.67	2.76	1.53	
400	32-mer	0.523	0.506	0.301		0.164	0.13	0.08	0.064
	16-mer	0.363	0.373	0.482		0.665	0.683	0.687	0.664
	Monomer	0.114	0.121	0.217		0.169	0.187	0.233	0.272
	χ^2	2.41	2.27	1.60		14.31	5.59	1.76	1.01

mass spectrometry was employed to look at the distribution of different oligomeric states present in the sample at different lipid concentrations. The main advantage of this titration is the higher resolution of the technique, whose accuracy allows the identification of several types of complexes and also to distinguish between complexes with the same oligomeric state but with different numbers of lipids bound. Interestingly, a wider variety of assemblies arised upon increase of the lipid concentration (Table 5.4, Figure 5.12). There is a clear signal shift from the signal corresponding to ANTH-ENTH assemblies of stoichiometry A₈E₈ (with several sub-populations with different number of PIP₂ molecules bound) towards the smaller assemblies previously reported to have A₆E₆ ANTH:ENTH stoichiometry (with a lower number of PIP₂ molecules bound, Table 5.4). In any case, the signal for the A₈E₈ assemblies does not disappear completely, indicating that in spite of the shift towards A₈E₈ assemblies both of them co-exist. Together, these data indicate that the ANTH-ENTH system is able of recruiting the different amounts of lipids to form different assemblies and that lowering the protein:lipid ratios may

result in a wider variety of smaller assemblies.

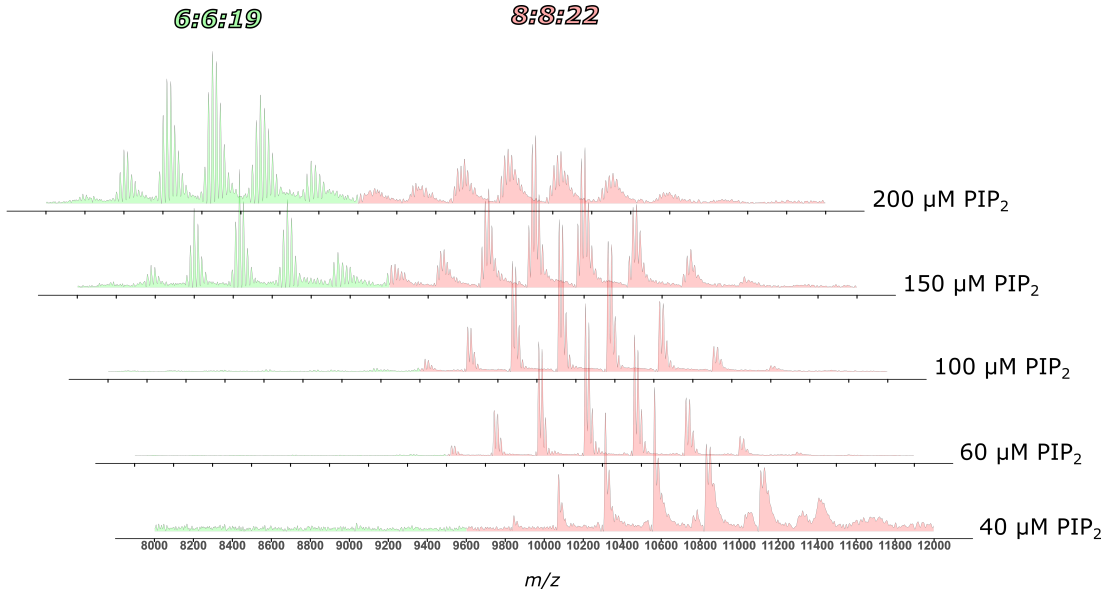


Figure 5.12: **Mass-charge distributions for ANTH-ENTH-PIP₂ complexes present at different concentrations.**

The part of the spectra corresponding to A₈E₈ assemblies is shadowed in red and the part corresponding to A₆E₆ is shadowed in green. The different number of PIP₂ bound are indicated in Table 5.4

Table 5.4: Native MS parameters obtained for the **PIP₂** titration over ANTH and ENTH

Sample	m/z range	MWs (Da)	Species	Number of PIP ₂ bound
WT 20 μM PIP ₂	2000-6000	33210	only monomer	
WT 40 μM PIP ₂	9000-13000	433160	A ₈ E ₈	22
		433940		23
WT 60 μM PIP ₂	9000-12000	433110	A ₈ E ₈	22
		433850		23
WT 100 μM PIP ₂	9000-12000	433170	A ₈ E ₈	22
		433890		23
		326020		18
		326730	A ₆ E ₆	19
WT 150 μM PIP ₂	8000-12000	327490		20
		433260		22
		433970	A ₈ E ₈	23
		434720		24
		435460		25
		326800		19
		327540		20
WT 200 μM PIP ₂	8000-12000	328290	A ₆ E ₆	21
		329060		22
		329810		23
		434790		24
		435550	A ₈ E ₈	25
		436290		26

5.1.3 cryoEM structure of the ANTH-ENTH-PIP₂ complex

After sample optimization to reduce aggregation and increase monodispersity using DLS, sample preparation for cryoEM was performed (Figure 5.7). The ANTH-ENTH-PIP₂ sample was vitrified and the structure of an ANTH-ENTH-PIP₂ oligomeric assembly was solved using single particle analysis (Figure 5.13).

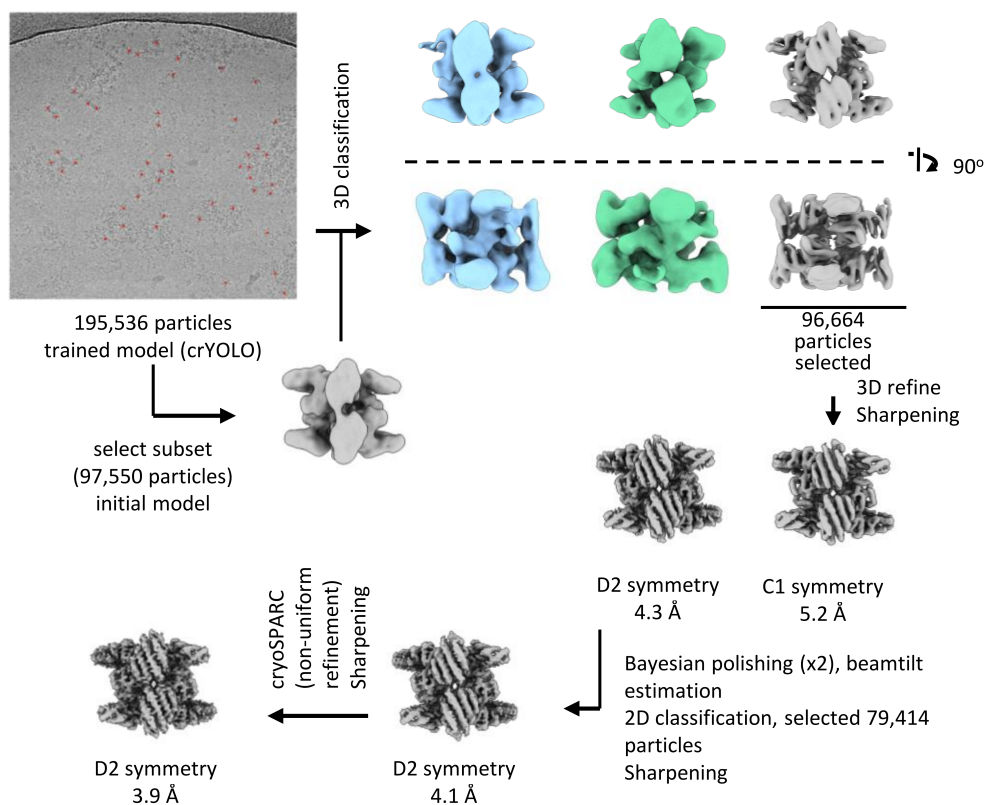


Figure 5.13: **Processing flowchart for a 16-mer ANTH-ENTH complex.**

An initial ab-initio model was used for 3D classification, revealing different classes with different numbers of sub-units (in blue, green and grey). The most complete class (grey) was selected for downstream processing as indicated in the Materials and Methods section. *Adapted from (Lizarrondo et al., 2021).*

2D classification of automatically picked particles gave some good 2D classes that were used for an initial 3D reconstruction (ab-initio model). From this reconstruction, a 3D classification procedure yielded different low-resolution maps which could be assigned to different types of ANTH-ENTH oligomers missing 1 or 2 sub-units, revealing large levels of heterogeneity present in the sample. The most complete map was selected for downstream processing (Figure 5.13 and Table 5.5).

Table 5.5: Cryo-EM data collection, refinement and validation statistics of the ANTH-ENTH 16-mer structure

Data collection and processing	
Magnification	×75,000
Voltage (kV)	300
Electron exposure (e-/Å ²)	75.2
Defocus range (µm)	-1 to -3
Pixel size (Å)	1.065
Symmetry imposed	D2
Initial particle images (no.)	195,536
Final particle images (no.)	79,414
Map resolution (Å)	3.9
FSC threshold	0.143
Map resolution range (Å)	3.7 to 5.7
Refinement	
Initial model used	5ONE, 5O07
Model resolution (Å)	3.9
FSC threshold	0.5
Model resolution range (Å)	-
Map sharpening B factor (Å ²)	200
Model composition	
Non-hydrogen atoms	26,192
Protein residues	3152
Ligand	s 20
B factors (Å ²)	
Protein	70
Ligand	-
r.m.s. deviations	
Bond lengths (Å)	0.012
Bond angles (°)	2.037
Validation	
MolProbity score	1.91
Clashscore	2.60
Poor rotamers (%)	3.78
Ramachandran plot	
Favoured (%)	93.56
Allowed (%)	5.80
Disallowed (%)	0.64

5.1.3.1 The final di-octameric ANTH-ENTH-PIP₂ map

The final map obtained corresponds to a di-octameric assembly of ANTH and ENTH domains (8 ANTH domains and 8 ENTH domains, also referred as A₈E₈). In the A₈E₈ di-octameric assemblies, the ENTH domains are located towards the core of the structure while the ANTH domains lay around them in the periphery of the map (Figure 5.14). The map is symmetric, with D2 symmetry, and the repeating unit is a tetramer of ANTH and ENTH molecules (2 of each domain, Figure 5.14b and Appendix Figure 10.2). As in every cryoEM 3D reconstruction, the resolution of the map varies in different regions, with the core of the map being at higher resolution than the overall reported resolution by the FSC curve (Appendix Figure 10.1). The resolution obtained

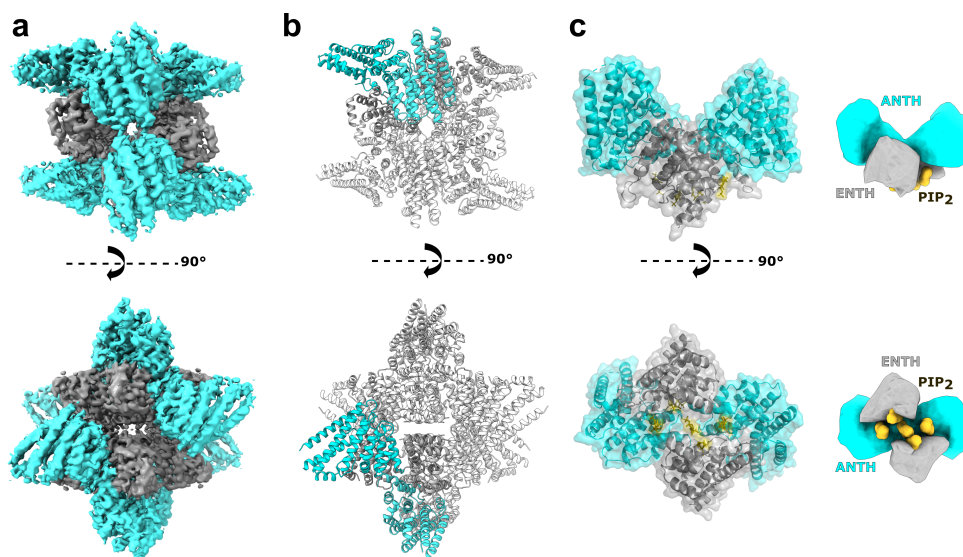


Figure 5.14: **Cryo-EM structure of a 16-mer AENTH complex.**

a. Cryo-EM reconstruction obtained for the 16-mer complex formed by 8 ANTH and 8 ENTH units (A_8E_8). The density corresponding to ANTH and ENTH is coloured correspondingly in cyan and grey. **b.** Model of the A_8E_8 complex built based on the EM density shown in cartoon representation. One tetramer is coloured with the ANTH domains in cyan and ENTH domains in grey (see Appendix Figure 10.2 for symmetry axes). **c.** The building unit is the AENTH tetramer (A_2E_2) shown in cartoon and surface representation, with the ENTH domains in grey and the ANTH domains in cyan. The PIP_2 polar heads bound to the tetramer are shown in stick representation (gold). A schematic of the tetramer is shown next to the structure. *Adapted from (Lizarrondo et al., 2021).*

allowed to build a model for the ANTH and ENTH domains within the map with high confidence in the core of the map. However, it should be noted that the regions of the model in the periphery are not reliable at the side chain level, as the resolution is only good enough to place the backbone from the last helix from the ANTH domains, but not their side chains (Appendix Figure 10.3).

5.1.4 The PIP_2 molecules act as a glue between different ANTH and ENTH domains

At the resolution in the core of the di-octameric cryo-EM map, three distinct lipid-binding sites could be identified in each A_2E_2 tetramer, harbouring 5 lipids per A_2E_2 (Figure 5.15) with a total of 20 PIP_2 lipids resolved in the entire 16-mer complex. The first binding site is located close to the ANTH KRKH motif, previously reported as a PIP_2 binding site, involving K24, K26 and H27 and in close proximity to K14 (Ford et al., 2001). Density present at this site could be assigned to the polar head of PIP_2 used for sample preparation (di- C_8 -PI(4,5) P_2). Interestingly, the polar head of PIP_2 seems to also interact with residues K66 and K68 on the ENTH domain adjacent

to this site (Figure 5.15a). There are 8 PIP₂ molecules shared in this way between the ANTH and ENTH domains in our 16-mer structure, one per AENTH interface. In addition, density was present in the previously described lipid-binding pocket of the ENTH domain (Ford et al., 2002). This binding site involves residues K3 and K10 on the ENTH $\alpha 0$ helix, the amphipathic helix involved in membrane bending, and residues R24, N29, K61 and R62 in proximity to a PIP₂ molecule (Figure 5.15b). Each ENTH domain contains one PIP₂ in its binding pocket, adding 8 PIP₂ bound to the 16-mer structure. Next to the PIP₂ binding site in the ENTH, there is another PIP₂ molecule (one per tetramer) located in the space between the two $\alpha 0$ helices of the ENTH domains in between their binding sites. In this case, the polar head of PIP₂ is coordinated by residues K10 and K14 of each of the two ENTH domains, establishing a total of 4 interactions that coordinate PIP₂ in this interface (Figure 5.15c). Noteworthy to mention is that K10 coordinates both the PIP₂ molecules bound to the ENTH binding pocket and those shared between the two ENTH domains in the tetramer. Each tetramer contains one molecule of PIP₂ between the two ENTH domains adding a further four in the structure. In summary, our 16-mer structure shows 20 PIP₂ molecules, all of them clustered close to the core of the structure. Within each tetramer, the PIP₂ are located in between the different ANTH and ENTH domains which by sharing different residues achieve the high affinity for the lipid previously reported.

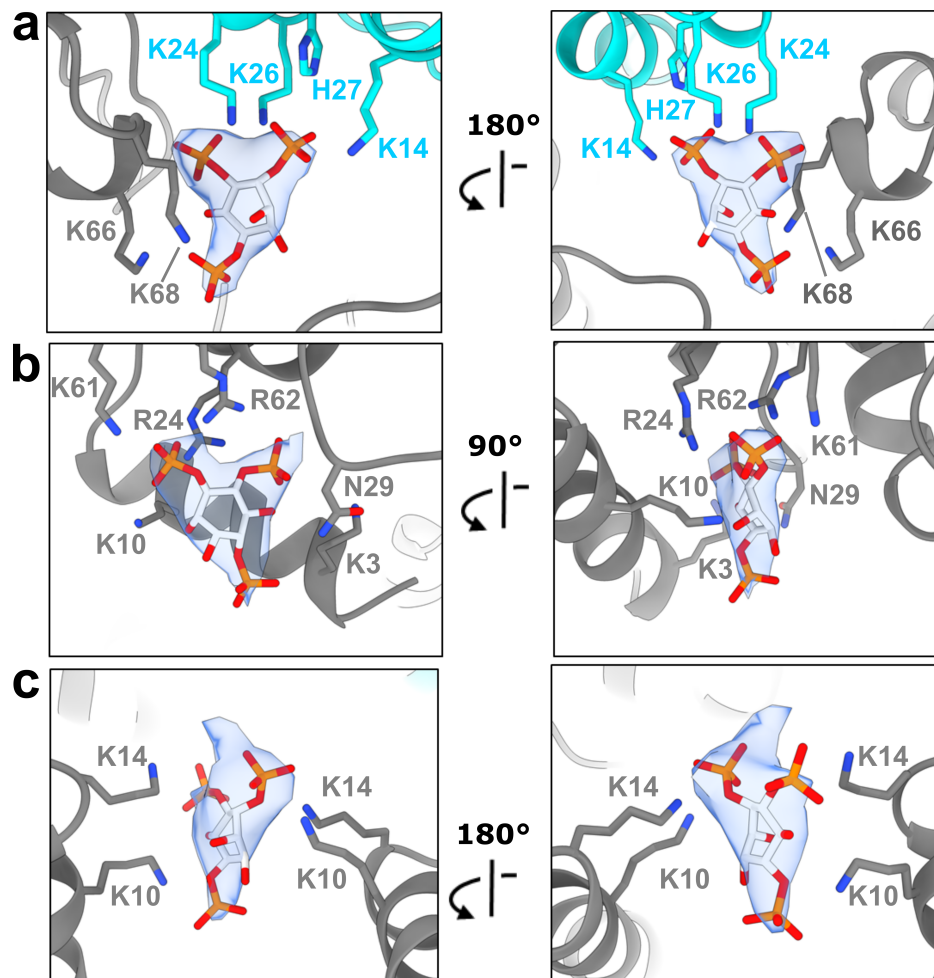


Figure 5.15: **PIP₂ binding sites in the ANTH-ENTH tetramer.**

a. PIP₂ binding site shared by the ANTH and ENTH domains. **b.** PIP₂ binding site within the ENTH domain. **c.** PIP₂ binding site in the interface between two ENTH domains. The residues involved in PIP₂ binding are shown in sticks and coloured blue for nitrogen and grey and cyan for carbon in ENTH and ANTH, respectively. The polar head of the PIP₂ is shown in stick format and coloured red, orange and light grey for oxygen, phosphate and carbon, respectively with the corresponding density shown as a transparent surface. *Adapted from (Lizarrondo et al., 2021).*

5.1.5 Dissecting the role of protein-protein interfaces over complex formation of ANTH-ENTH complexes

The building unit of the ANTH-ENTH complexes is a hetero-tetramer. Once bound to PIP₂, protein-protein interactions between the ANTH and ENTH domains are established through two main hetero-dimerization interfaces, and one homo-dimerization ANTH-ANTH interface. Thus, each AENTH tetramer contains a total of 5 interfaces (Figure 5.16). To test the structural relevance over complex formation of residues present in different interfaces, point mutations were performed on these residues of ANTH and ENTH. The full list of mutations is shown in Table 5.6. The experimental design for the mutational study is shown in Figure 5.17.

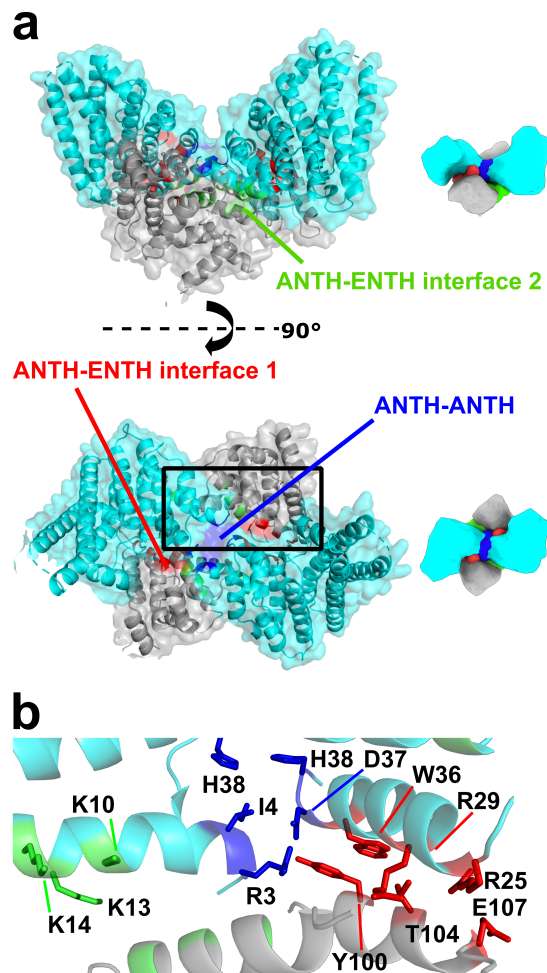


Figure 5.16: The ANTH-ENTH tetramer interfaces.

a. Surface representation of the A₂E₂ tetramer, with ANTH subunits in cyan and ENTH subunits in grey. The different interfaces are coloured: ANTH-ENTH interface 1 in red, ANTH-ENTH interface 2 in green and ANTH-ANTH interface in blue. **b.** Cartoon representation of the tetramer area within the black rectangle in **a** showing the different interfacial residues as sticks (same color code as in **a**). Adapted from (Lizarrondo *et al.*, 2021).

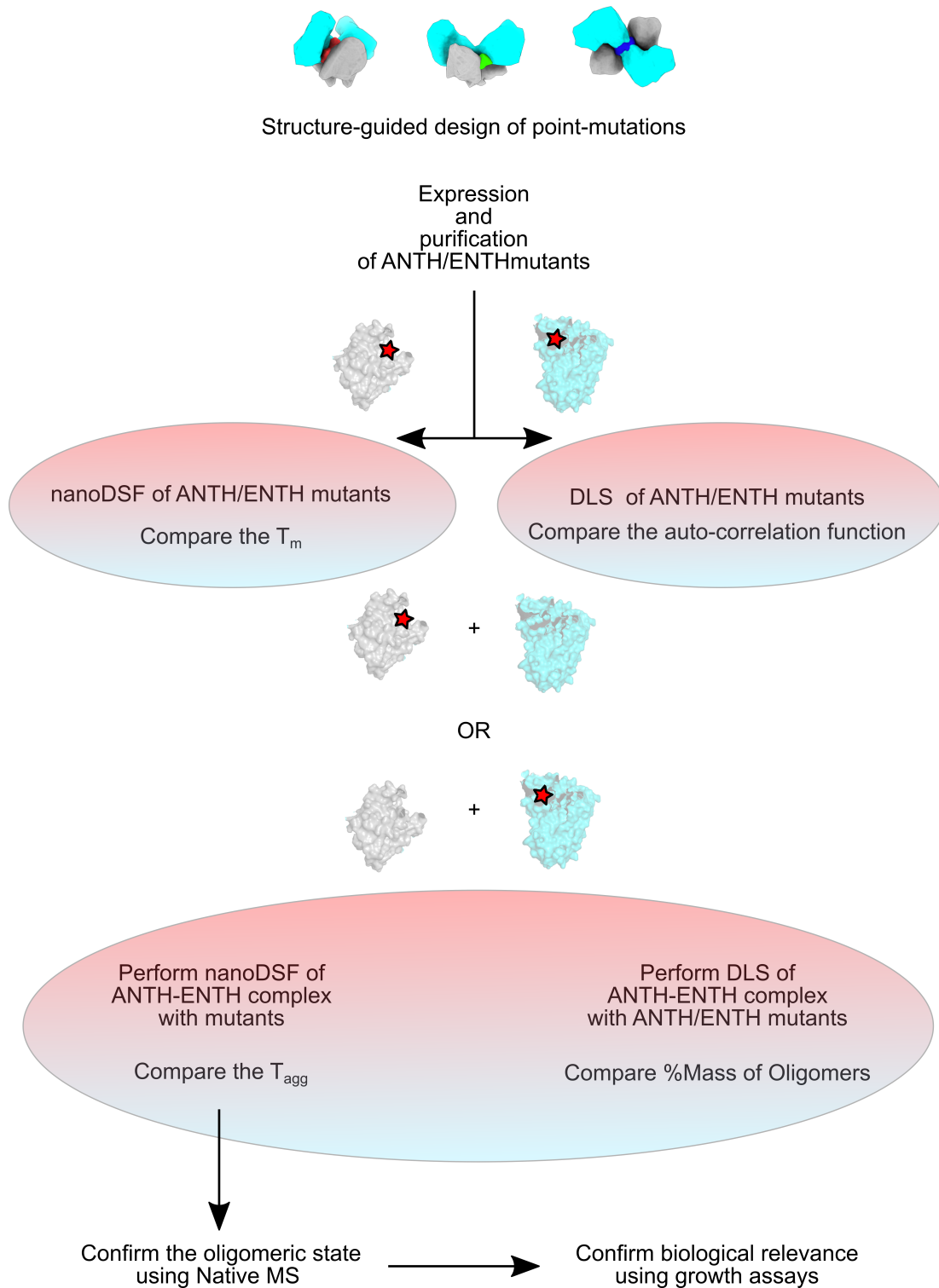


Figure 5.17: Schematic of the workflow used for testing the effects over ANTH-ENTH complex formation in the mutagenesis study.

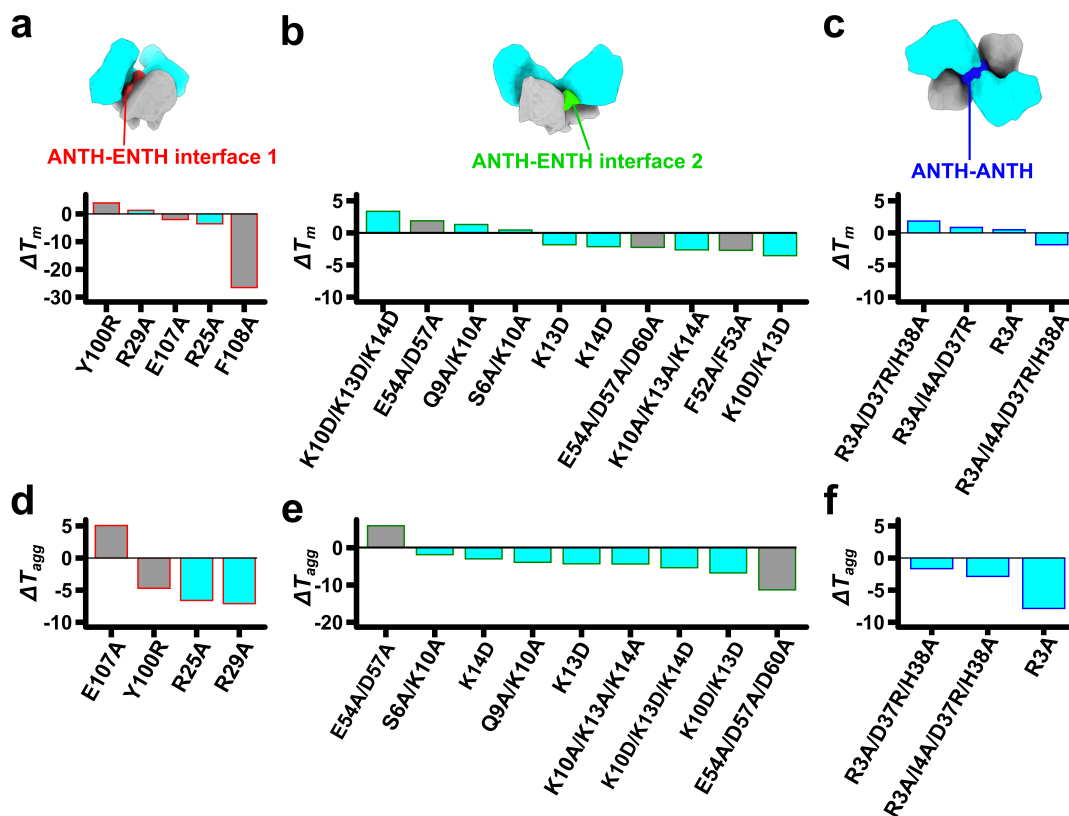


Figure 5.18: nanoDSF for the ANTH and ENTH point-mutants.

a.-c. The melting temperature (T_m) of the ANTH (cyan) and ENTH (grey) domains was compared with the one of ANTH and ENTH WT and the difference is reported. **d.-f.** The selected mutants were used for nanoDSF experiments and the aggregation temperature (T_{agg}) of ANTH-ENTH complexes was studied following the static scattering and compared with that of the wild-type. Adapted from (Lizarrondo *et al.*, 2021).

Table 5.6: Mutations inserted in the ANTH domain of Sla2 and the ENTH domain of Ent1

Domain	Mutation	Interface
ANTH	S6A/K10A	Oligomerization
	K10A/K13A/K14A	Oligomerization
	K10D/K13D/K14D	Oligomerization
	K10D/K13D	Oligomerization
	K14D	Oligomerization
	K13A	Oligomerization
	A15A	Oligomerization
	Q9A/K10A	Oligomerization
	R3A/I4A/D37A/H38A	ANTH-ANTH
	R3A	ANTH-ANTH
	R3A/I4A/D37A/H38A	ANTH-ANTH
	M1A	ANTH-ANTH
	R3A/I4A/D37R	ANTH-ANTH
	R3A D37A H38A	ANTH-ANTH
	Δ Y247/L248	Conserved Sla2 ANTH Loop
	R177E R178E	Inter-tetramer contacts
	S100A R177E R178E	Inter-tetramer contacts
	E57R S100A R177E R178E	Inter-tetramer contacts
	E57R R177E R178E	Inter-tetramer contacts
	ENTH	F5A/I12A
Y100R		Hotspot
E107A		Hotspot
F108A		Hotspot
Q20A		Oligomerization*
F52A/F53A		Oligomerization
ENTH E54A D57A		Oligomerization
N98A		Oligomerization*
E97A		Oligomerization*

* These residues were not considered part of this interface in the final model

From all mutations, expression of the double mutant ENTH E97A/N98A was not possible as the bacterial cells did not grow in presence of this plasmid. The strategy was then to mutate these two residues separately and trying to obtain single mutants. ENTH E97A showed similar expression to the wild-type protein, while ENTH N98A showed little expression, which prevented purification of this mutant for complex formation experiments, possibly hinting to an essential function for this residue during protein folding that hampers its production.

5.1.1.5.1 Effect of mutations over domain stability and aggregation

After expression and purification of the mutants, nanoDSF was used to test whether all mutant domains retained stability upon mutation. Figure 5.18a-c summarizes the results obtained for the thermal stability of the domains obtained from the Fluorescence Ratio between 350 and 330 nm. Some of the mutants showed a significant decrease thermal stability with respect to their wild-type counterparts. Given mutation of these residues affect the stability of the ANTH and ENTH domains by themselves, these

mutants were not further considered for ANTH-ENTH complex formation assays.

Prior to ANTH-ENTH complex reconstitution experiments, the monodispersity and sample quality of the mutants were tested by DLS, specially given that the ANTH domain seems to aggregate at high concentrations and this property could be further stimulated upon point-mutation of certain residues. DLS auto-correlation curves showed that most of the mutants had a consistent radius of around 3.2 nm for the ANTH domain and around 2.5 nm for the ENTH domain (Table 5.7). Interestingly, mutants ANTH A15D and ENTH E54A/D57A/E60A showed large aggregates present in the sample, possibly pointing to a destabilization of the domain by these mutations. Aggregation properties and melting temperatures are two properties that are usually liked in proteins, and DLS data showed that this is the case of the mutants with compromised stability (Appendix Figure 10.4). For the ENTH domains, mutants F5A/I12/L12A, E54A/D57A and E97A show a higher melting temperature than ENTH WT (+ 2 °C), and mutant ENTH Y100R and ENTH Q20A show an even higher melting temperature (+ 5 °C), indicating these mutations stabilize further the ENTH domain. On the other hand, mutant ENTH F52A/F53A seems affected by more than 2 °C, indicating that these two hydrophobic residues affect the thermal sensitivity of the domain. Therefore, this mutant was not considered for further complex formation assays. The rest of the mutants were considered for complex formation experiments.

5.1.5.2 Effect of interface residue mutations over complex formation

To assess the impact of the mutations on complex assembly, ANTH-ENTH complexes were assembled in the presence of PIP₂ *in vitro* (as done for the cryo-EM sample preparation) using mutants for one of the domains and its wild-type counterpart. The stability of the complexes reconstituted using mutants was evaluated by looking at the scattering signal that reports the aggregation temperature (T_{agg}) upon thermal denaturation by nanoDSF. Most mutant complexes showed a lower aggregation temperature when compared with ANTH-ENTH wild-type (WT) (Figure 5.18d-f).

Next, the effect over complex formation was monitored using DLS. ANTH and ENTH domains in the presence of PIP₂ form structures around 8 to 10 nm of average hydrodynamic radius (Figure 5.19d, black dot). Mutation of ANTH or ENTH residues involved in ANTH-ENTH complex formation showed less particles corresponding to 16-

Table 5.7: DLS parameters obtained for ANTH and ENTH mutants

Domain	Mutation	Radius (nm)	% Pde	MW (kDa)	% Intensity	% Intensity	% Number
ANTH	M1A	3.1	23.68	46.9	96	100	100
	R3A/I4A/D37R	3.2	9.27	51.6	86.5	99.8	100
	S6A/K10A	3.2	8.95	52.1	84.8	99.9	100
	K13A	3.3	11.08	56	94.5	100	100
	A15D	3.2	15.64	49.8	69.2	100	100
	Δ Y247/L248	3.5	11.87	62.5	99.2	99.9	100
	K10A/K13A/K14A	3.3	11.26	54.9	97.1	100	100
	K10D/K13D/K14D	3.5	11.89	62.4	96.3	100	100
ENTH	F5A/I12A	2.5	10.31	28.5	71.1	99.9	100
	E54A/D57A	2.7	17.76	34.1	47	100	100
	F52A/F53A	2.8	16.78	36.7	95.5	100	100
	Y100R	3	21.6	42.7	96	100	100
	Q20A	2.9	10.71	39.2	24.2	99.8	100
	E97A	2.7	13.26	34.5	76.3	100	100
	AAAA*	4	25.44	87.5	22.4	99	100

*Mutant of the PIP2 binding residues

mer assemblies *in vitro* when compared with ANTH-ENTH WT complexes, which can be observed as a shift in the auto-correlation function and a decrease in the proportion of particles at the hydrodynamic radius corresponding to the complex (Figure 5.19-f, Table 5.8, Appendix Figure 10.4).

5.1.6 The ANTH-ENTH Interface 1

Previous mutagenesis work on these domains described ENTH T104 and ANTH R29 as important residues for the functionality of Ent1 and Sla2 proteins in yeast (Skruzny et al., 2012, 2015). These two residues were selected as the centre of an ANTH-ENTH hetero-dimer fitted into a 13.6 Å resolution EM map of GUVs arranged as tubular structures coated by these domains (Skruzny et al., 2015). In the newly solved A₂E₂ structure, ENTH T104 and ANTH R29 are located in one of the observed interfaces, defined as “ANTH-ENTH interface 1” (Figure 5.19a). Other residues present in this interface are ENTH Y100, E107 and ANTH R25, W36. ANTH R25 is in close contact with ENTH E107 and ENTH Y100 is oriented parallel to ANTH W36, establishing a stacking interaction by the coordination of their aromatic rings (Figure 5.19a). The ENTH Y100R mutant did not show 16-mer ANTH-ENTH assemblies *in vitro* by DLS and native MS (Figure 5.19c and 5.19g, Table 5.8). *In vivo*, the growth-

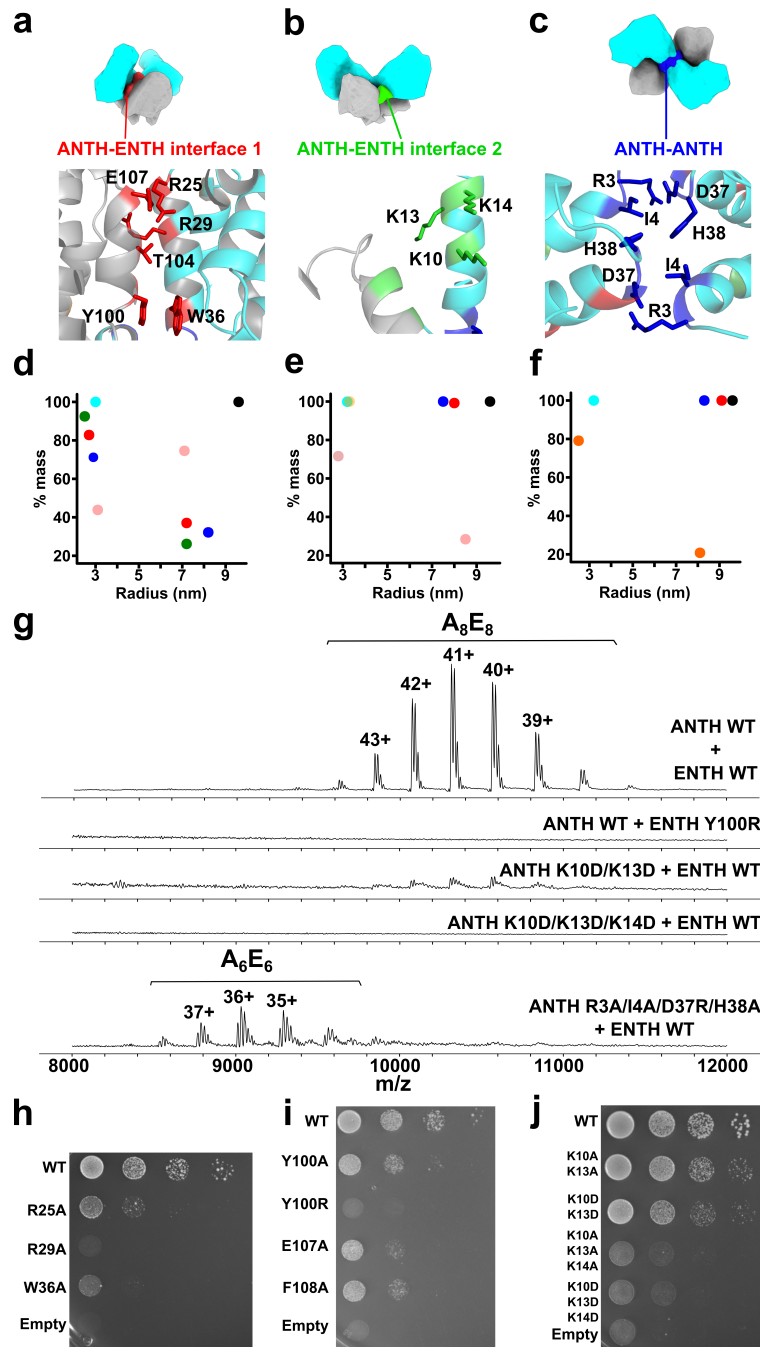


Figure 5.19: Different interfaces present in the ANTH-ENTH tetramer.

a-c. Schematic representation of the ANTH-ENTH model showing the different interfaces present, designated as ENTH-ANTH interface 1 (**a**), ANTH-ENTH interface 2 (**b**) and ANTH-ANTH interface (**c**). In the lower panels, the residues involved in each of the interfaces are shown in stick representation and coloured using the color scheme for each of the interfaces. **d-e.** Intensity mass plot from DLS data showing the hydrodynamic radius of particles in solution for wild type AENTH (black) and different mutants. As a reference the ANTH domain is shown in cyan (see Table 5.8 for DLS parameters). (**d**) ENTH-ANTH interface 1 showing mutations ANTH Y100R (red) ANTH R25A (blue), ANTH R29A (green) and ENTH E107A (pink); (**e**) ENTH-ANTH interface 2 with mutations ANTH K10A/K13A/K14A (pink) ANTH K10D/K13D/K14D (yellow), ENTH E54A/D57A/D60A (blue) and ANTH Q9A/K10A (red). (**f**) ANTH-ANTH interface with mutations ANTH R3A (orange), ANTH R3A/I4A/D37R/H38A (blue) and ANTH R3A/I4A/D37R (red). **g.** Summary of the native mass spectrometry results obtained for the mutants of the tetramer interfaces. **h.-j.** Growth defects of mutants of ANTH (**h.**) and ENTH (**i.**) ANTH-ENTH interface 1, and ANTH-ENTH interface 2. (**j.**) Interface mutants were expressed after depletion or deletion of endogenous Ent1 and Sla2 proteins, respectively. Cell growth was analysed after plating 10-fold serial dilution of cells on SD-Ura plates and incubation for 3 days at 37 °C. Adapted from (Lizarrondo et al., 2021).

defect phenotype of ENTH Y100R mutant has been previously attributed to a possible role of Ent1 in binding GTP-activating proteins for Cdc42, a critical regulator of cell polarity (Aguilar et al., 2006). Here we show that this residue plays a crucial role in the formation of the ANTH-ENTH complex. In addition, mutation *in vivo* of ANTH R25, R29 and W36 and ENTH Y100 and E107 showed strong or intermediate growth deficiency phenotypes in yeast, confirming an essential role of this interface for proper endocytic function (Figure 5.19h and 5.19i). ENTH F108A also introduced a growth defect phenotype *in vivo* (Figure 5.19i), but our *in vitro* data showed that the stability of the protein is compromised by this mutation (Figure 5.18a).

5.1.7 The ANTH-ENTH interface 2: a novel oligomerization interface

A second interface in the ANTH-ENTH tetramer involves residues K10, K13 and K14 of ANTH (Figure 5.19b). ANTH K14 is involved in the interaction with PIP₂, indicating synergy in PIP₂ binding and function of this ANTH-ENTH interface 2. After testing that mutations of the lysine residues in this interface did not affect stability of ANTH domain (Figure 5.18b), these mutants display ANTH-ENTH complexes with a lower aggregation temperature (T_{agg}) by nanoDSF, indicating that the stability of these complexes is partially compromised (Figure 5.18e). Apart from this destabilization effect, some mutants also showed a clear effect on complex assembly reported by DLS (Figure 5.19e and Table 5.8) when compared with ANTH-ENTH WT complex. Specifically, triple mutant ANTH K10A/K13A/K14A showed a smaller proportion of 16-mer assemblies in solution, while mutant ANTH K10D/K13D/K14D completely abolished complex formation (Figure 5.19e).

The DLS experiments provided us with evidence that ANTH-ENTH complexes were not able to form upon mutation of certain residues given their expected hydrodynamic radius. However, the molecular weight obtained and therefore oligomeric state derived from the analysis (e.g. in the case of a slightly smaller radius than wild-type) are not extremely precise. To explore with a greater level of detail the effect of these mutations on the assembly of ANTH-ENTH complexes, non-denaturing electrospray ionization mass spectrometry (native MS) was used to analyse the assembly when mutant domains were used to reconstitute complexes (Figure 5.19g). Native MS allowed the identification of charge state distributions corresponding to A₈E₈ complexes at high

m/z, with 22-24 PIP₂ molecules bound (Appendix Figure 10.5 and Table 5.9).

Moreover, ANTH K10D/K13D displays a large destabilization of the complex observed by nanoDSF (Figure 5.18e) and only a weak native MS signal corresponding to the 16-mer assembly when compared to the wild-type (Figure 5.19g). Together, these results indicate that K10 and K13 residues are important for oligomerization. Beyond that, ANTH K10D/K13D/K14D completely abolished complex formation, and no signal for larger assemblies other than monomeric species was observed by native MS in agreement with the DLS data (Fig. 5.19g).

In vivo, mutations of these residues caused growth defect phenotypes in yeast strains lacking Sla2 WT (5.19j and Appendix Figure 10.9). Mutation of ANTH K10/K13 to alanine caused an intermediate growth defect phenotype which was enhanced when these residues were mutated to aspartic acid. The tripe mutant K10/K13/K14 present in this interface caused a severe growth defect phenotype when mutated to alanine, further enhanced when replaced by aspartic acid. Furthermore, each of the three lysine residues has an important role in complex formation, as individual mutations of these lysines also caused growth defect phenotypes *in vivo* (Appendix Figure 10.9). Altogether, these results indicate that lysines of the ANTH-ENTH interface 2 are essential for the assembly of the tetrameric lipid-binding ANTH-ENTH unit and for the ANTH-ENTH function *in vivo*. On the ENTH domain, E54A/D57A/D60A showed the largest destabilization in the nanoDSF data (Figure 5.18e). However, mutation of these residues did not show any complex disruption by DLS *in vitro* nor introduced a growth defect in yeast cells, most likely ruling out a major role in the ANTH-ENTH assembly and function (Appendix Figure 10.9a).

5.1.8 The ANTH-ANTH interface

Finally, ANTH-ANTH interface mutants (Figure 5.18c) did not show a large destabilization effect over the complex *in vitro* with the exception of ANTH R3A (Figure 5.18f) which also generated a larger amount of monomeric species upon complex formation when compared to ANTH-ENTH wild type by DLS (Figure 5.19f and Table 5.8). ANTH R3A/I4A/D37A-ENTH WT complexes showed a slightly smaller complex in solution than the one by wild-type complex (7.5 nm vs 9.6 nm of WT). Together with the similar stability of these complexes with respect to the wild-type, we concluded this

Table 5.8: DLS measurements of ANTH-ENTH-*PIP*₂ complexes containing point mutations in the different interface

ANTH	ENTH	Radius (nm)	% Pde	MW (kDa)	% Intensity	% Mass	% Number
WT	WT	9.6	11.85	664.6	100	100	0
R25A	WT	2.9	8.85	41.9	1.8	64.0	99.0
R29A	WT	8.2	8.56	468.1	9.7	15.2	1.0
		2.5	15.06	29.3	11.1	90.6	99.6
WT	Y100R	7.2	14.29	343.9	22.2	7.7	0.4
		2.7	0	33.3	15.2	78.5	98.1
WT	E107A	7.2	14.81	344.4	71.3	21.3	1.9
		3.1	4.61	47.2	3.2	29.8	78.0
WT	E54A/ D57A/ D60A	7.1	16.06	331.7	76.6	68.2	22.0
		7.5	26.06	374	100	100	100
S6A/ K10A	WT	6.7	6.86	287.7	93.8	99.4	100
K13D	WT	7.2	10.19	344.6	100	100	100
Q9A/ K10A	WT	8	11.18	433.9	96.8	99.2	100
K10A/ K13A/ K14A	WT	8.5	16.31	508	90.7	28.4	1.6
WT	E54A/ D57A	3.3	11.49	55.8	3.5	73.1	99.5
		9.7	8.91	684.9	9.5	8.2	0.5
K10D/ K13D/ K14D	WT	3.2	12.67	51.4	39.8	99.9	100
R3A	WT	2.5	9.08	28.9	9.9	79.1	99.3
		8.1	6.85	454.0	89.0	20.8	0.7
R3A/ I4A/ D37A	WT	8.3	9.15	479.8	100	100	100
R3A/ D37R/ H38A	WT	7.5	9.83	380.4	94.8	99.2	100.0
K10D/ K13D	WT	7.5	40.8	381.3	100	100	100
K14D	WT	7.4	24.5	358.9	89	99	100
WT	F5A/ I12A/ V13A	8	11.62	436	100	100	100
Δ Y247/ L248	WT	9	36.27	571.8	100	100	100

Table 5.9: Experimental and theoretical masses for ANTH, ENTH, PIP₂ and adducts/complexes observed by native MS.

Species	Theoretical mass (Da)	Experimental mass (Da)	Main charge state	FWHM*
diC ₈ -PI(4,5)P ₂	747.5	-	-	-
ENTH	18847.9	18847.8	8 ⁺ **	1.2
ENTH + Na	18870.9	18871.4	8 ⁺ **	1.1
ENTH + PIP ₂	19594.4	19593.2	8 ⁺ **	1.1
ANTH	33210.0	33209.6	11 ⁺	1.2
ANTH + Na	33233.0	33230.3	11 ⁺	1.3
ANTH + PIP ₂	33956.5	33959.4	11 ⁺	1.3
ANTH ₈ ENTH ₈ + 22 PIP ₂	433181	432887	41 ⁺	9.7
ANTH ₈ ENTH ₈ + 23 PIP ₂	433892	433633	41 ⁺	10.5
ANTH ₈ ENTH ₈ + 24 PIP ₂	434627	434380	41 ⁺	9.2
ANTH ₆ ENTH ₆ + 17 PIP ₂	324125	324382	36 ⁺	8.5
ANTH ₆ ENTH ₆ + 18 PIP ₂	324872	325141	36 ⁺	10.7
ANTH ₆ ENTH ₆ + 19 PIP ₂	325618	325902	36 ⁺	12.2

*FWHM (full width at half maximum) is given for the predominant charge state peak to indicate the experimental error.

**Sensitivity for the Orbitrap UHMR instrument used here is reduced at low m/z (< 2500), so higher charge states of free ENTH may be attenuated.

ANTH₆ENTH₆ was obtained using ANTH R3A/I4/ D37R/H38A and ANTH₈ENTH₈ was assembled using WT domains

mutant was able to form other intermediate versions of the ANTH/ENTH complex. Interestingly, native MS for the R3A/I4A/D37R/H38A mutant showed a shift in the signal of the complexes obtained to lower m/z, corresponding to 12-mers (Figure 5.19g and Table 5.9), in agreement with the DLS data that showed particles of slightly smaller hydrodynamic radius. Assemblies of 12-mers have been previously reported as lower abundance species (Garcia-Alai et al., 2018; Heidemann et al., 2020) and are formed by 6 ANTH and 6 ENTH molecules (also termed A₆E₆). However, in spite of these effect over oligomeric state, mutation of the ANTH-ANTH interface did not cause growth defect phenotype *in vivo* (Appendix Figure 10.9c).

5.1.9 A conserved Sla2 ANTH loop

Apart from mutations on the newly discovered interface, the ANTH domain also has loop with residues Y247 and L248 that is conserved specifically in ANTH domains

of the Sla2 family. Deletion of this loop caused an endocytosis-linked growth defect in yeast, previously attributed to a possible interface in the protein complex with epsin (Garcia-Alai et al., 2018). The DLS results show that the ANTH Δ Y247L248-ENTH WT complex can form perfectly (Table 5.8), and nanoDSF confirms that the stability of this complex is similar to the one of the wild type, most likely ruling out a role of this specific loop in the oligomerization properties of the ANTH domain. The cryoEM structure shows that these residues are not involved in any interface of the assembly, but instead that their deletion leads to an unstable protein when looking at the thermal stability of the protein *in vitro*, suggesting that they are crucial for the correct folding of ANTH (Figure 5.20) and explaining the deleterious effect found in yeast.

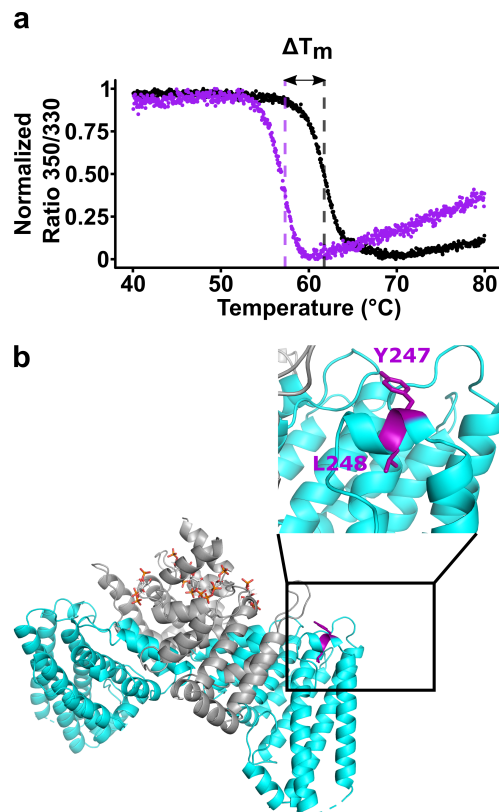


Figure 5.20: The Sla2-specific Y247-L248 insertion is not part of the ANTH-ENTH interface.

a. nanoDSF data for ANTH wt (black, $T_m = 61.7$ °C) and ANTH Δ Y247/L248 (violet, $T_m = 57.7$ °C). The shift in the transition of the nanoDSF signal can be clearly observed and is indicated as ΔT_m , indicating that this mutation destabilizes the protein. The T_m was obtained from the fluorescence signal ratio 350/330 nm. **b.** Residues Y247 and L248 of ANTH domain did not establish any contacts in the ANTH-ENTH complex. Cartoon representation of the ANTH-ENTH tetramer and the PIP₂ molecules bound to it, with the YL residues colored in violet. The insert shows the detailed orientation of these residues, which do not establish any protein-protein contacts. Deletion of these residues disrupts helix α_{12} .

5.1.10 Beyond A_8E_8 assemblies, other types of assemblies

Intriguingly, DLS reported slightly smaller complexes than for the wild-type complex for ENTH $\alpha 0$ helix mutant F5A/I12A/V13A (Table 5.8), similarly than the assemblies detected by Native MS with other mutations such as the ones for the ANTH-ANTH interface (Table 5.9). Furthermore, ENTH $\alpha 0$ helix mutant F5A/L12A/V13A produced a native MS spectrum with signal only corresponding to 12-mers ANTH-ENTH (Figure 5.21a). Given this mutant is not present in one of the ANTH-ENTH tetramer interfaces, a question arises regarding whether this type of assemblies would also have composed using A_2E_2 tetramers as building units, or whether the mutation on these residues in the amphipathic helix would impose a different arrangement of the domains different from the one we had demonstrated with the mutagenesis study.

Single particle cryo-EM data for ANTH-ENTH complexes formed with ENTH F5A/L12A/V13A showed a structure distinct from the A_8E_8 assembly (Figure 5.21 and Appendix Table 10.1). The density was unambiguously assigned to three A_2E_2 tetramers arranged around a central core of PIP₂ (Figure 5.21d). The position of the ANTH and ENTH domains within the A_2E_2 tetramer is remarkably similar to the A_8E_8 complex, indicating that mutation of hydrophobic residues on the amphipathic helix does not disrupt the ability of the ENTH domains to assemble into the functional hetero-tetramer with the ANTH domains. The difference in the capability of forming 16-mers vs 12-mers does not rely on mutations on the ANTH-ENTH tetramer in this case (as for the ANTH-ANTH mutants), but in an alteration of the amphipathic helix of ENTH. However, the tetramer is still the building blocks of these assemblies, indicating that other factors such as membrane curvature can affect the assembly of the ANTH-ENTH into membranes. All these observations support the hypothesis that the building units of AENTH complexes are hetero-tetramers that can form different higher order assemblies.

5.1.11 Further oligomeric states of the ANTH-ENTH system

The oligomeric states of ANTH-ENTH-PIP₂ complexes corresponding with di-octameric or di-hexameric assemblies of the adaptor membrane binding domains seem to be the most prominent ones as they have been observed in cryoEM and native MS.

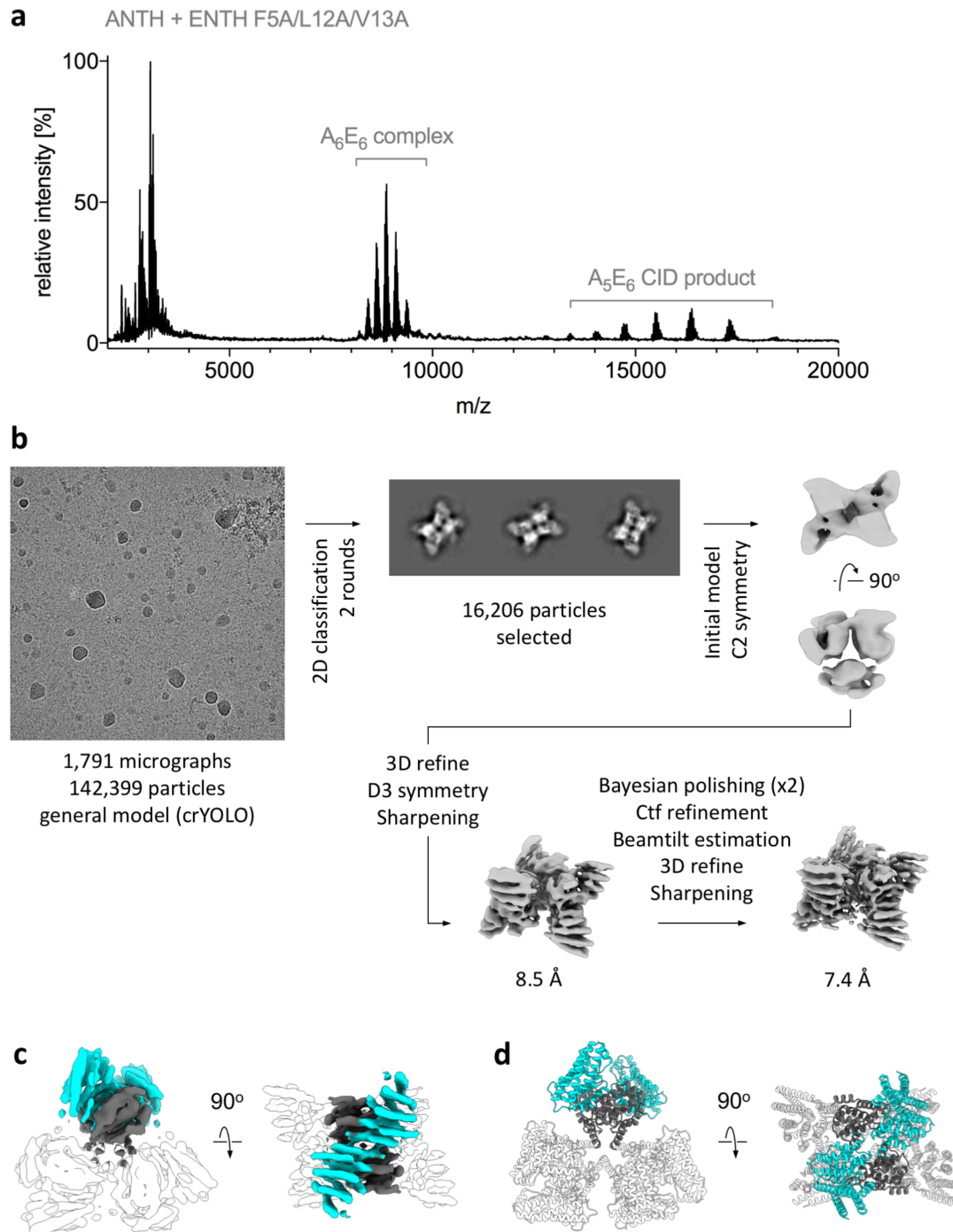


Figure 5.21: **ANTH-ENTH 12-mer assembly (A_6E_6) obtained by mutation of residues F5A/L12A/V13A of the amphipatic $\alpha 0$ helix of the ENTH domain.**

a. Native MS of ANTH in complex with ENTH F5A/L12A/V13A at 200 μM PIP₂. The main oligomeric species is the 6:6 AENTH complex. At high m/z, a 5:6 ANTH-ENTH complex is present, resulting from collision induced dissociation (CID) of the 6:6 complex. **b.** Processing flowchart for the 12-mer ANTH-ENTH complex. **c.** Final density map obtained for the 12-mer assembly with one tetramer coloured in cyan for the ANTH domain and in grey for the ENTH domain. **d.** Structural model for the 12-mer assembly. The tetramer structure (A_2E_2) was fitted into the EM density map for each of the three tetramers. The ANTH and ENTH domains are coloured for one of the three tetramers in the same colour code as in **c.** Adapted from (Lizarrondo *et al.*, 2021).

However, there are further assembly intermediates before reaching the di-octameric and di-hexameric assemblies.

Some mutations gave rise to smaller intermediates that became more and more prominent upon combinations of some mutants (Figure 5.22). Some of those oligomeric states could be identified and reliably assigned (Appendix Table 10.7). However, it is not entirely clear why those assemblies occur on those particular mutations and what factors change the preferred oligomerization states of the ANTH-ENTH system: is oligomerization stalled because of the mutations or is it a kinetic effect?

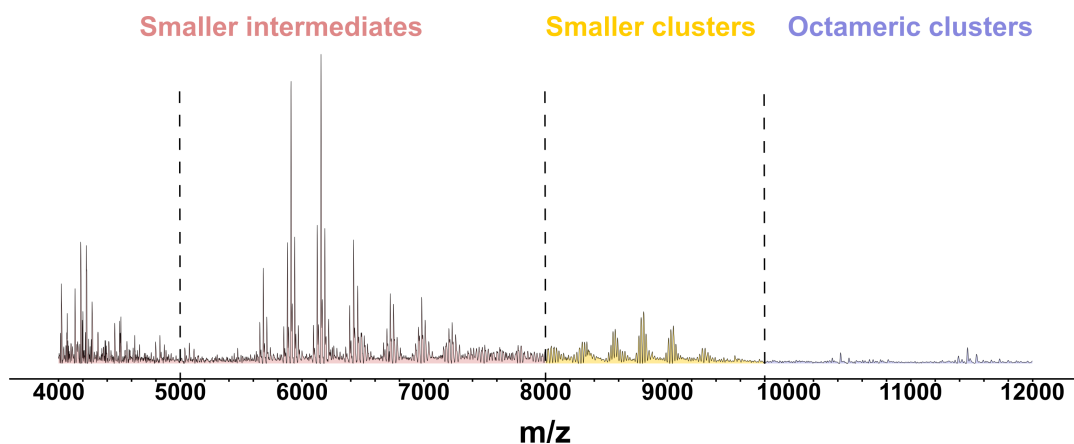


Figure 5.22: Smaller intermediates of AENTH oligomers.

5.1.12 The ANTH-ENTH complex can assemble into larger oligomeric assemblies capable of deforming membranes

Previous work showed that the ANTH and ENTH domains together tubulate and coat GUVs with regular helical assemblies, as determined by cryo-EM to 13.6 Å resolution (Skruzny et al., 2015). The 16-mer structure solved by single particle EM showed that, instead of the heterodimer previously proposed, the ANTH-ENTH tetramer constitutes the building unit of larger clusters and assemblies.

To support this notion, the ANTH-ENTH tetramer was used for flexible fitting into the electron density map of ANTH-ENTH coat on GUVs using adaptive distance restraints in ISOLDE (Figure 5.23). Overall, the fitting agrees with the previous assignment of the domains to the larger and smaller densities present on the surface of the tubules for the ANTH and ENTH domains respectively. The fitted model places the two ENTH $\alpha 0$ helices pointing towards the core of the tubules (Figure 5.23c), consistent with the membrane bending mechanism of the ENTH domain by insertion of the $\alpha 0$

helix and displacement of the lipids in the inner layer of the plasma membrane (McMahon, Boucrot, 2015). Similarly, the fit also shows that the ANTH domains have their conserved lysine patch exposed towards the direction of the membrane, and therefore available to bind the polar heads of the PIP₂ at the membrane (Figure 5.23e). Thus, the combined synergy between the membrane binding mechanism of both domains confers the ANTH-ENTH tetramer the capability to act as a membrane anchor in a membrane environment as well, in agreement with its biological function.

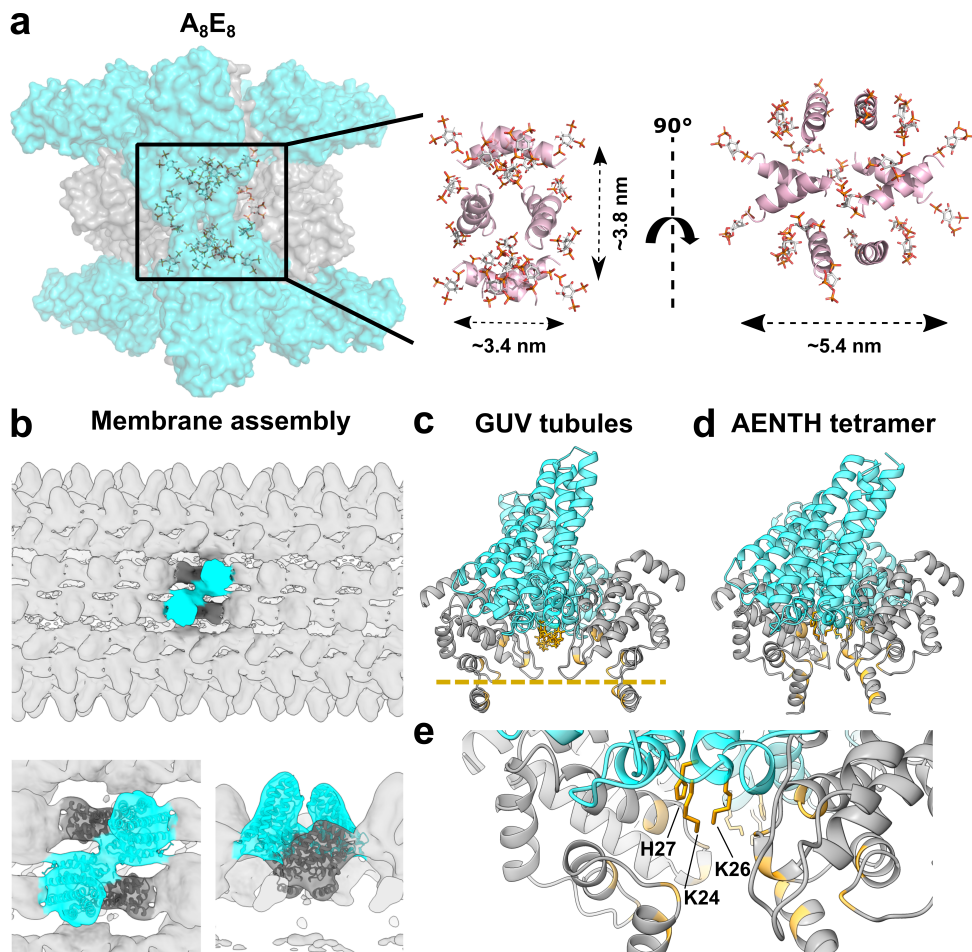


Figure 5.23: **Protein-lipid interactions of the AENTH 16-mer complex structure and of the ANTH-ENTH assembly on GUVs.**

a. (left) All the polar heads from the PIP₂ placed in the structure (shown in sticks) are contained in the region near to the core of the structure (shown in surface representation), indicating the presence of a PIP₂ micelle in the center of the map. (right) Only the $\alpha 0$ helices from ENTH subunits are shown in cartoon representation (in pink) together with the PIP₂ shown in stick (coloured by atom), all of them are pointing towards the interior of the structure. **b-e.** Flexible fitting of the tetrameric model to the previously obtained cryo-EM map of ANTH-ENTH coat on GUV tubules (Skruzny et al., 2015). **b.** Overview of the GUVs tubular coat structure with the tetramer fitting inside the lobes of the structure (EM-DB entry: EM-2896). (bottom) Close-up view of the tetramer fitted into the EM density of the GUV structure. **c.** AENTH tetramer structure fitted to the GUVs coat structure. The regions involved in PIP₂ contacts are coloured in gold in the cartoon representation. The bilayer plane is indicated as a gold dashed line. **d.** AENTH tetramer in the 16-mer ANTH-ENTH complex, with the lipid binding regions highlighted in gold in the cartoon representation. **e.** Close-up for the ANTH lysine patch residues involved in coordination of the polar head of PIP₂ lipid. Adapted from (Lizarrondo et al., 2021).

To address the relevance of the ANTH-ENTH tetramer in membrane binding and remodeling, the effects of protein interface mutations were studied in presence of **in vitro** model membranes. Giant unilamellar vesicles (GUVs) containing PIP₂ were prepared and mixed them with WT ANTH-GFP or ENTH-GFP fusions and interface mutants, respectively, and observed them by confocal fluorescence microscopy. Addition of wild type ANTH and ENTH domains led to membrane remodeling and resulted into elongated hairy structures protruding from GUVs, while the individual domains did not cause any major membrane re-shaping phenotype (Figure 5.24a-f). Those interface mutants that were not able to assemble the A₈E₈ complex: ENTH Y100R, ANTH R29A, ANTH K10D/ K13D and ANTH K10D/K13D/K14D did also not introduce membrane remodeling (Figure 5.24i, k, l and m), while the mutant E54A/D57A/D60A, which still enabled complex formation, elicited similar hairy membrane structures as wt ENTH (Figure 5.24h).

Higher curvature liposomes (LUVs) containing PIP₂ were prepared by extrusion and their interactions with ANTH and ENTH visualized by negative stain EM. Addition of ANTH alone did not deform LUVs containing PIP₂, whereas ENTH caused their aggregation (Figure 5.25b and c). Corroborating what was already observed for GUVs, addition of wild-type ANTH and ENTH domains together caused tubulation of liposomes (Figure 5.25d). Mutations on the “ANTH ENTH interface 1” had a strong effect on membrane remodeling with ANTH R29A and ENTH Y100R displaying aggregation of LUVs without causing tubulation (Figure 5.25f and g). “ANTH ENTH interface 2” ANTH lysine mutants (K10D/K13D/K14D and K10D/K13D), incapable of oligomerization with ENTH, induced a strong aggregation of LUVs (Figure 5.25i and j). Similar to what was observed for GUVs, ENTH E54A/D57A/D60A was able to tubulate LUVs, in agreement with our observations for complex assembly followed by DLS and native MS.

The ANTH R25A mutant was shown to partially impair complex assembly *in vitro* and exhibits an intermediate growth defective phenotype *in vivo* (Figure 5.19d and h). However, the mixture of ANTH R25A and ENTH was sufficient to induce tubulation of both GUVs and LUVs (Figure 5.24g and Figure 5.25e). Similarly, ENTH E107A, which introduced a mild growth defect phenotype *in vivo* (Figure 5.19i) did not show a clear effect on membrane remodeling *in vitro*, capable to tubulate GUVs and LUVs

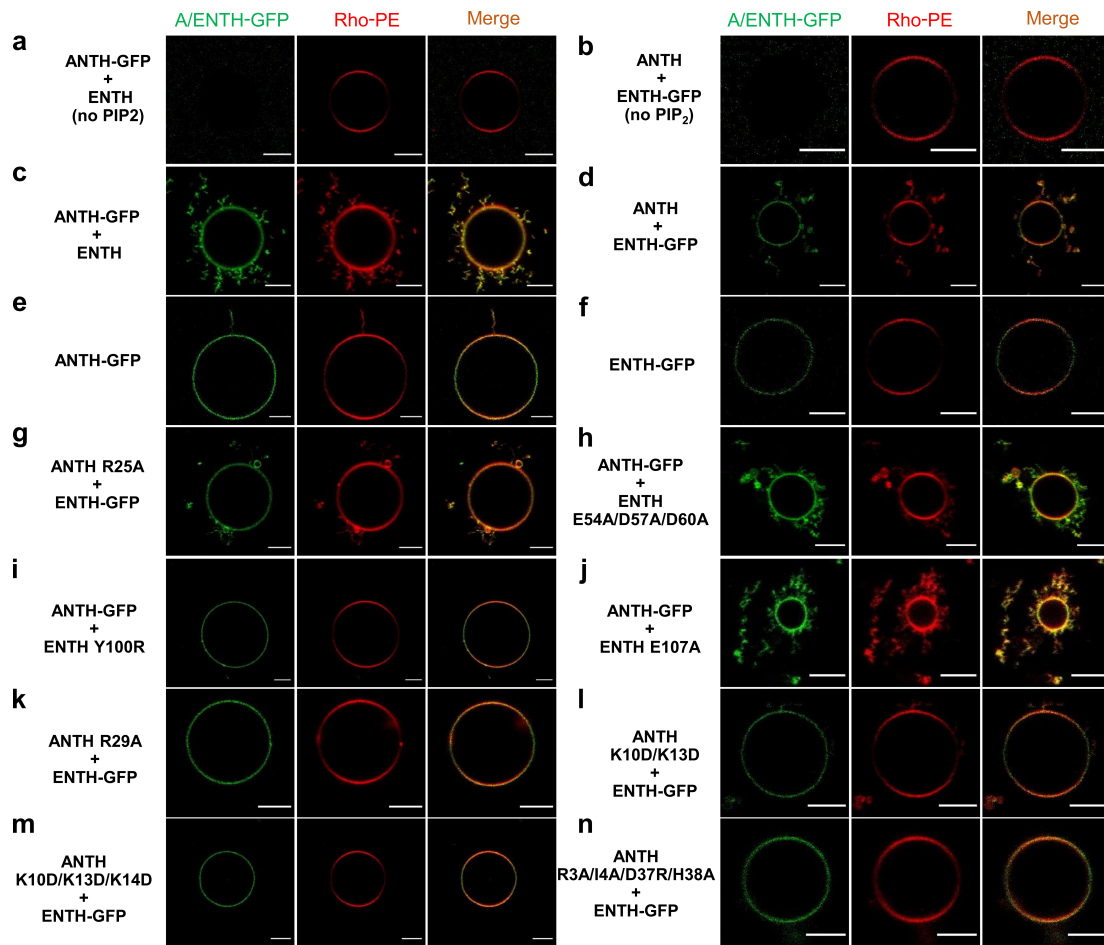


Figure 5.24: **Effect of AENTH tetramer and mutants on GUVs by fluorescence microscopy.** **a-b.** ANTH-GFP and ENTH-GFP do not bind GUVs without PIP₂. **c-d.** ANTH-GFP or ENTH-GFP mixed with ENTH or ANTH, respectively, caused membrane deformation as seen by the numerous membrane protrusions around GUVs. **e-f.** ANTH-GFP or ENTH-GFP did not cause a remodelling effect on the GUV membrane. **g-n.** ANTH and ENTH mutants mixed with ENTH-GFP and ANTH-GFP, respectively, showed different membrane deformation capabilities. Each experiment was repeated independently 3 times with similar results. All scale bars are 5 μm. *Adapted from (Lizarrondo et al., 2021).*

(see Figure 5.24j and Fig. 5.25h). Finally, “ANTH-ANTH interface” mutant ANTH R3A/I4A/D37R/H38A, that introduced intermediate effects on complex destabilization (Figure 5.19f-g) and no growth defect phenotypes *in vivo* (Appendix Fig. 10.9c) was capable of tubulating LUVs but not GUVs (Figure 5.24n and Fig. 5.25l). In case of ANTH R3A/I4A/D37R/H38A, the typical 16-mer AENTH complex was not observed for this mutant, but a 12-mer assembly (Figure 5.19g and Table 5.8) was sufficient to introduce membrane reshaping *in vitro*.

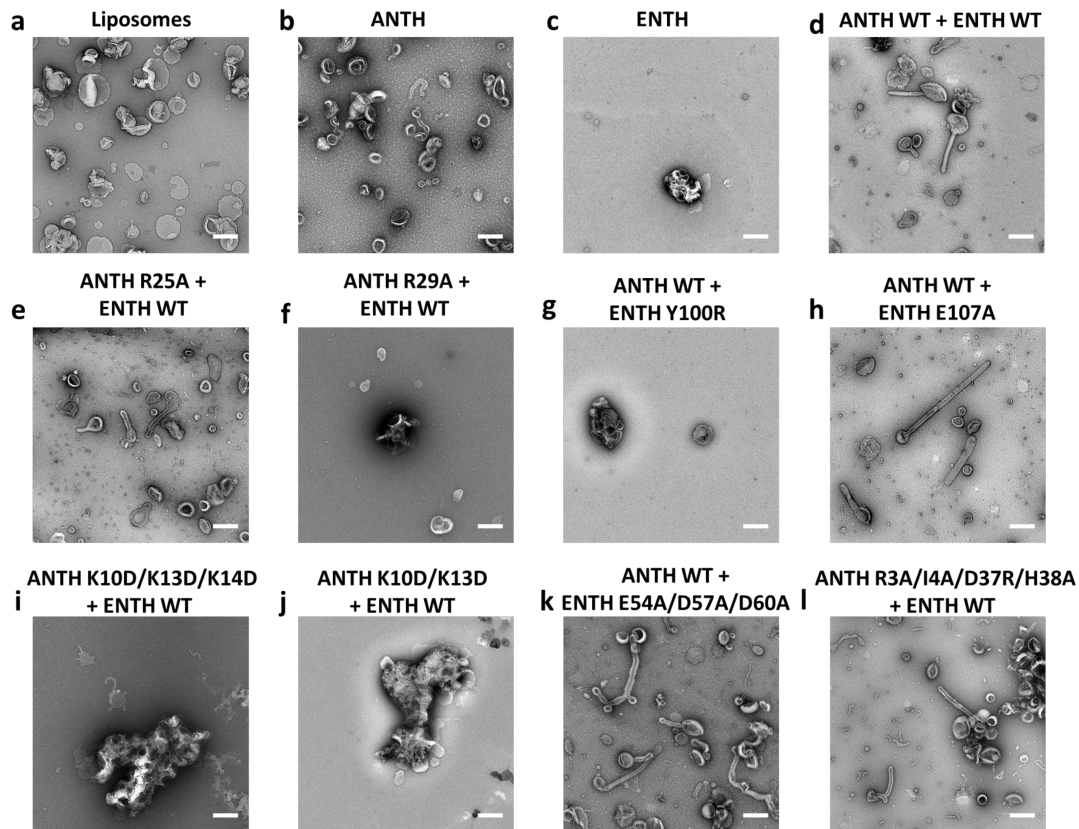


Figure 5.25: **Effect of AENTH tetramer mutants on LUVs by negative stain.**

a. LUVs observed by negative staining. **b.** ANTH does not deform LUVs notably. **c.** ENTH causes LUVs to become aggregated and to adopt irregular shapes. **d.** ANTH together with ENTH reshapes LUVs into tubular structures as previously reported¹⁸. **e-l.** ANTH and ENTH mutants show different effects on LUVs. ANTH R25A (**e**), ENTH E54A/D57A/D60A (**k**) and ANTH R3A/I4A/D37A/H38A (**l**) mutants (mixed with its wild type partner domain) display a AENTH wt phenotype reshaping LUVs into tubular structures ANTH R29A (**f**) and ENTH Y100R (**g**) ANTH K10D/K13D/K14D (**i**) and ANTH K10D/K13D (**j**) mutants (mixed with its wild type partner domain) display an ENTH wt phenotype being unable to tubulate LUVs. Each experiment was repeated independently 3 times with similar results. All scale bars are 200 nm. *Adapted from (Lizarrondo et al., 2021).*

5.1.13 Time resolved SAXS studies of the interaction of ANTH and ENTH domains

In equilibrium, ENTH and ANTH form protein-lipid clusters in the presence of PIP₂, whose major component is the A₈E₈ ANTH-ENTH complex determined by SPA cryo-EM. All the biophysical techniques in our mutation study provided information regarding the end-point of oligomerization given the time-scales of the experiments performed, but the growth assays showed the biological relevance of the ANTH-ENTH tetramer.

In order to study the compatibility with cellular timescales of the ANTH-ENTH assembly, we performed stopped-flow SAXS (SF-TR-SAXS) studies of the interaction upon fast mixing of its constituents in the P12 beamline at Petra III in DESY. A stopped-flow device enabled rapid mixing of the ANTH and ENTH domains followed by immediate exposure to X-ray radiation and the scattering signal followed over time. The buffer-subtracted SAXS curves obtained over the first 400 ms are shown in Figure 5.26a. We observed a very fast change of the SAXS curves, particularly in the q-region between 0.02 to 0.6 nm⁻¹ over this period of time, after which the curves remained relatively unchanged.). The R_G extracted from the Guinier region of the curves for all timepoints showed a fast increase and then remained stable over time, indicating that the formation of larger oligomers takes place immediately after mixing (Figure 5.26b). As the assembly was started from monomers and evolved into 16-mers, the ab initio program DAMMIX (Konarev, Svergun, 2018) was employed to determine the shape and fraction of the intermediate component of AENTH. The resulting monomer component (first curve) decreased over time, while the volume fraction of the complex (last curve of our dataset) together with the intermediate component, increased with time until around 400 ms, similar to the observed R_G increase (Figure 5.26c). The low resolution model of the intermediate component showed similar dimensions to the ANTH-ENTH tetramer (Figure 5.26d). However, given the heterogeneity present in solution, this structural model should be considered just as a representative average of the oligomeric states in solution during millisecond timescale. In conclusion, the SF-TR-SAXS data indicate that the association of the domains takes place very rapidly and even faster than the fast oligomerization occurring during endocytic coat assembly *in vivo*, where

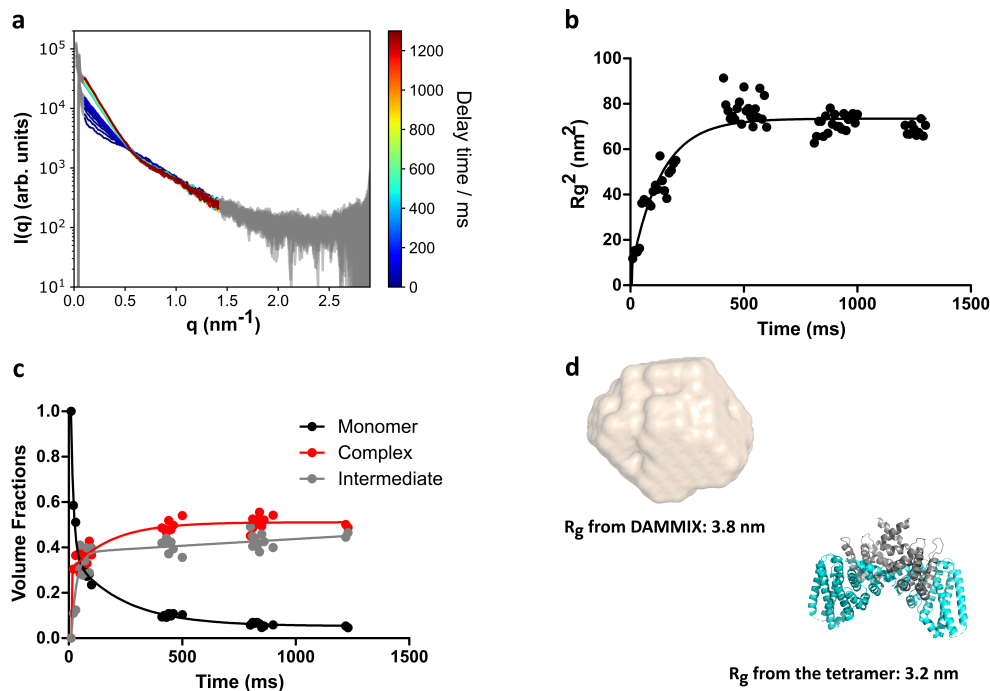


Figure 5.26: **Time-resolved SAXS data demonstrate a fast assembly of ANTH and ENTH domains in solution.**

a. Buffer-subtracted SAXS curves for the time-resolved measurements of the complex formation between ANTH and ENTH in presence of 200 μM PIP₂. For better visibility, the data were smoothed with a Savitzky-Golay filter (51-point window, 2nd order polynomial). Delay times are color coded from 0 ms in blue to 1200 ms in dark red. The shape of the curve changes dramatically from the initial time points after 400 ms, when the curve stabilizes. **b.** Evolution of the R_g^2 data of the time-resolved SAXS data set overtime. After 500 ms the R_G is relatively constant in all curves. A single exponential fitting was performed and the half-time obtained was 91 ms. **c.** Volume fractions of DAMMIX obtained using the SAXS curves. The contribution of the unknown component is labelled as “Intermediate”. The volume fractions were fitted to a bi-exponential function to obtain the time-constants (fast constant 8 ms, slow constant around 150 ms). **d.** DAMMIX ab initio model obtained for the intermediate component vs AENTH tetramer structure from the 16-mer cryoEM map solved. The dimensions of the tetramer and the DAMMIX ab initio model are rather similar, which could indicate that the unknown component of the SAXS data could be tetramers forming in solution that later on assemble further into larger oligomeric states. Adapted from (Lizarrondo et al., 2021).

it happens in the range of seconds (Brach et al., 2014; Kaksonen, Roux, 2018; Lu et al., 2016). Interestingly, the TR-SAXS reveal a mixture of (largely) tetramers and 16-mers at the end of the time range probed (1.4 s). This result further corroborates the finding that much longer incubation times (minutes) are needed for the formation of (nearly) monodisperse 16-mer solution.

Finally, once endocytosis has been accomplished, the endocytic coat has to be disassembled and its components recycled. We performed biolayer interferometry (BLI) experiments to obtain information regarding the reversibility of complex formation. Our results indicate that complex formation is fully reversible upon decreased concentrations of any of the two adaptor domains, as the signal decreases exponentially back to the baseline upon removal of their interaction partner (Figure 5.27 and Table 5.10).

This indicates that these domains are able to disassemble while the endocytic coat is being dismantled and the local concentration of one of their partner decreases.

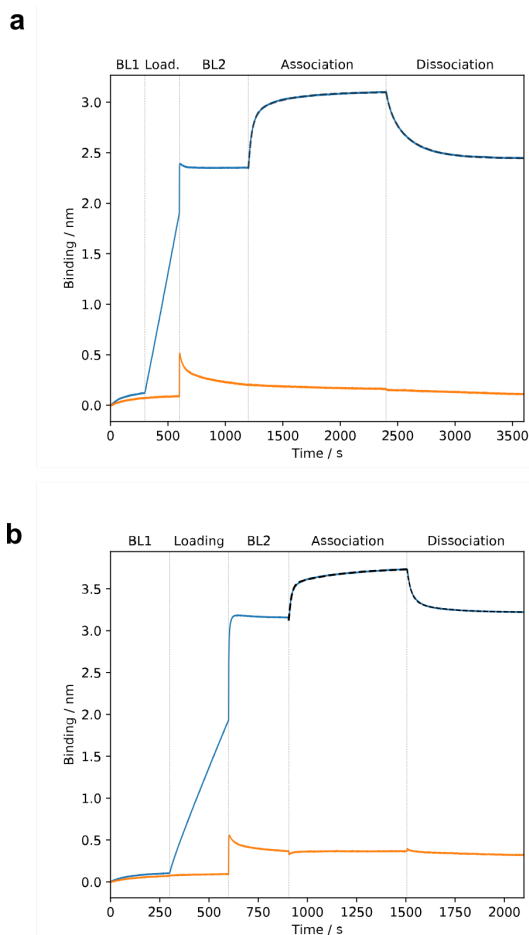


Figure 5.27: **ANTH-ENTH complex formation is a reversible process.**

Binding kinetics measured by biolayer interferometry (BLI) between His-tagged ANTH (a) or ENTH (b) immobilized on a Ni-NTA Octet sensor (load stage performed at 3.7 $\mu\text{g}/\text{ml}$ monomeric protein) in the presence of 0.25 μM free ENTH (a) or ANTH (b) (blue curves) and without ligand (orange curves). All steps were done in 50 mM Tris HCl pH 8.0, 125 mM NaCl and 0.05% BSA. For baseline 2 (BL2), association and dissociation stages the buffer additionally contained 170 μM DDM and 50 μM PIP₂. See Table 5.10 for the kinetic constants.

Table 5.10: Fitting for the binding kinetics determined by BLI

Figure 5.27A		
Fit rise	Fit decay	
$k_{\text{obs}1}$: 3.06E-02 1/s	$k_{\text{diss}1}$: 4.40E-03 1/s	K_{D1} : 31.4 nM
$k_{\text{obs}2}$: 3.45E-03 1/s	$k_{\text{diss}2}$: 1.91E-02 1/s	K_{D2} : 212 nM
R^2 : 0.9989	R^2 : 0.9995	
Figure 5.27B		
Fit rise	Fit decay	
$k_{\text{obs}1}$: 7.45E-02 1/s	$k_{\text{diss}1}$: 6.23E-03 1/s	K_{D1} : 19.3 nM
$k_{\text{obs}2}$: 3.87E-03 1/s	$k_{\text{diss}2}$: 4.56E-02 1/s	K_{D2} : 230 nM
R^2 : 0.9980	R^2 : 0.9981	

5.2 Biophysical characterization and structural studies of mid-coat adaptors Sla2 and Ent1

5.2.1 Expression test of Sla2 and Ent1 full length proteins from *S. cerevisiae*

Beyond the ANTH and ENTH domains, mid-coat adaptors Sla2 and Ent1 contain other domains/regions, involved in their interactions with actin and with clathrin, which are essential for the adaptors to perform their biological function. In order to understand the mechanism of membrane invagination driven by adaptors, the full length sequences of Sla2 and Ent1 were cloned into a expression vector for production in *E. coli*. Initial expression tests for both GST-fusion constructs did not yield significant amounts of protein produced or the proteins were degraded after pull-down using His-tag (Figure 5.28). Sla2 full length could not be expressed in *E. coli* as a GST fusion, trying different strains of cells and expression conditions (such as temperature, IPTG concentrations, and time).

5.2.2 Expression and Purification of mid-coat adaptors Sla2 and Ent1 from *C. thermophilum*

Given the challenges to express Sla2 and Ent1 from *S. cerevisiae* in bacterial systems, the sequences from the thermophilic fungi *Chaetomium thermophilum*, whose genome has been sequenced before (Amlacher et al., 2011), were cloned in an attempt to obtain more thermally stable homologues. This strategy has been widely used in X-ray crystallography since enhanced stability of constructs usually leads to a higher number of hits during crystal trials. Also, thermally stable proteins are commonly easier to produce and purify, as they survive cell disruption methods and can cope with the high concentrations at which they are produced recombinantly.

The two adaptors, Sla2 and Ent1, from *C. thermophilum* (CtSla2 and CtEnt1, 118 kDa and 66 kDa respectively) were successfully produced recombinantly and purified (Figure 5.29). Sla2 was expressed as a GST-fusion, and GST was removed through purification with a second IMAC step before SEC. Ent1 was expressed with just a His-tag in the C-terminus that was also removed using the same strategy.

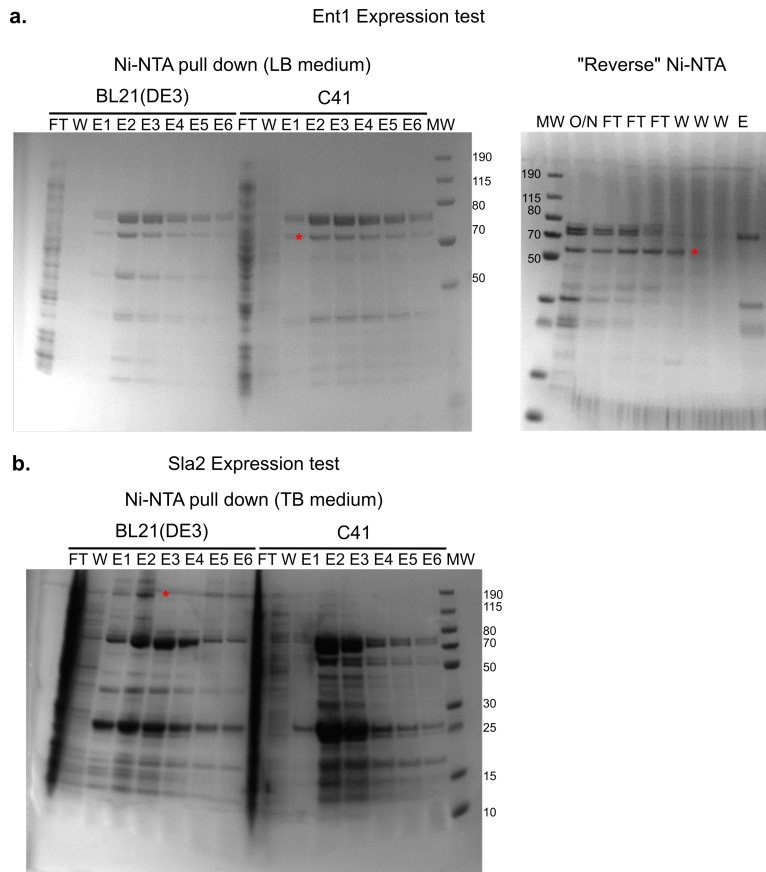


Figure 5.28: **Expression test of Ent1 and Sla2 full length from *S. cerevisiae*.** For both proteins, the His-GST construct was pulled using Ni-NTA beads where proteins were bound to and eluted with imidazole. For Ent1 (**a**), a “Reverse” Ni-NTA was used to separate the His-GST tag from Ent1. In all gels the bands of interest are marked with a red asterisk.

5.2.3 Biophysical characterization of mid-coat adaptors CtSla2 and CtEnt1

After protein purification, biophysical characterization of both adaptors was performed as part of the quality control pipeline prior to structural studies. CtSla2 shows two transitions upon thermal denaturation on nanoDSF (Figure 5.30a), one around at around 40 °C and the main one taking place around 59 °C, a similar T_m of the ANTH domain. On the other hand, CtEnt1 showed a single transition at ca. 53 °C, which compared to just the ENTH domain from the same protein is lower (53 °C° vs 60 °C). This indicates that the full-length Ent1 is more thermally unstable, due to the large IDR present in its C-terminus. For both CtEnt and CtSla2, most Tryptophan residues are located in the folded domains of the proteins (for Sla2, 3 out of 7 are in the ANTH domain and for Ent1, 4 out of 5 are in the ENTH domain), hence the contribution for the reported melting temperatures comes mostly from the ANTH/ENTH domains.

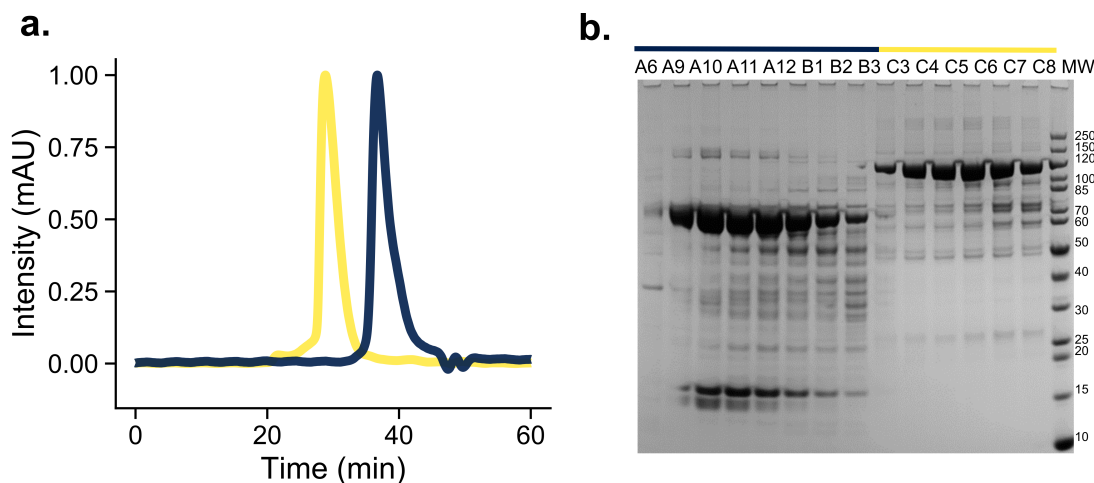


Figure 5.29: **Purification of CtSla2 and CtEnt1.**

a. Size Exclusion Chromatography profiles of CtSla2 (yellow) and CtEnt1 (blue) after IMAC and Reverse IMAC purifications. **b.** SDS-PAGE analysis of the fractions corresponding to the peaks indicated in **a.** The Molecular weights markers units are kDa. D: Dialysis. FT: Flow-through, W: wash. E: Elution.

Initial biophysical characterization using DLS showed that CtSla2 and CtEnt1 are monodisperse (Figure 5.30c-e); however, the AC function of CtEnt1 showed a small bump at high correlation times, indicating that there is some aggregation in the sample, which was not unexpected given the large proportion of intrinsically disordered regions that the protein contains. Circular Dichroism (CD) confirmed the presence of a large proportion of disordered regions in CtEnt1 together with some alpha-helical content, as can be seen from the deconvolution of the signal from the CD spectra (Figure 5.30f and Appendix Table 1). Finally, Mass Photometry shows that CtSla2 and CtEnt1 display a single mass distribution that correspond with the molecular weight calculated from their sequence, a monomer for CtEnt1 and a dimer from CtSla2, as expected from literature (Figure 5.30g and h).

Given the expected heterogeneity and the nature of the sample to aggregate shown by DLS (Figure 5.30c and d) and the disordered tendency of CtSla2 and CtEnt1, in-line SEC-SAXS measurements were performed (Figure 5.31). The intensity profiles showed a main peak for both samples, with more heterogeneity present in the measurements of CtSla2 (Appendix Figure 10.11a and b). CtSla2 shows a high slope at low q values, a trend usually observed for aggregated samples (Figure 5.31a). However, it is known from literature that the overall expected topology of Sla2 extremely elongated, which explains the shape of its SAXS curve. SAXS also reveals certain level of flexibility for CtSla2, as the curve does not return to the baseline on the normalised Kratky

plot. Furthermore, a second maximum in this plot points towards a dumb-bell shape, which is expected from a topology with two globular domains connected by a linker (Figure 5.31b). CtEnt1 shows a more globular SAXS profile, and its overall dimensions are smaller than the ones from CtSla2 (Figure 5.31a and Table 5.11). As expected, the normalised Kratky plot shows that CtEnt1 is extremely flexible, as the curve increases towards higher values of qR_G (Figure 5.31d). Figure 5.31c shows the distance distribution function for CtSla2 and CtEnt1. Similar to the Kratky plot, the distance distribution plot for CtSla2 contains a second maximum that accounts for the dumbbell shape that the ab-initio model generated shows in 3D (Figure 5.31d). Finally, a poor fitting of the structural prediction generated by AlphaFold (Appendix Figure 10.12) and the experimental data collected for these proteins demonstrates that the static structures do not represent the array of conformations mid-coat adaptors adopt in solution (Figure 5.31 e and f). In conclusion, SAXS allows to explore the conformational space of full-length adaptors and paves the way for tackling its structural characterization.

5.2.4 Full length adaptor complex formation experiments

Attempts to reconstitute a full-length adaptor complex using PIP₂ in a similar fashion as it was done for the ANTH and ENTH domains were performed using the same protocol as described in Figure 5.17. The DLS auto-correlation function corresponding to the complex shows a large proportion of the sample in the same dimensions (hydrodynamic radius) of Sla2, along with some particles or higher dimensions that were also present in the sample of Sla2 alone (Figure 5.32, compare yellow and blue in panel c). This indicates that no obvious multimerization takes place using the full length proteins in a similar way than when just using ANTH and ENTH domains (Figure 5.7). A potential drawback of detecting large changes in the oligomeric state of full-length adaptor complex by DLS comes from the extremely elongated and flexible shape of Sla2, which hinders an accurate deconvolution of the molecular weight and overall radius by DLS since the method used is often based on assumption of globular-like particles. Furthermore, compared with the large size of the Sla2 full length (ca. 236 kDa), the addition of the small ENTH domains (18 kDa) would not cause a significant change in the overall shift of the sample's molecular weight to be appreciated in the

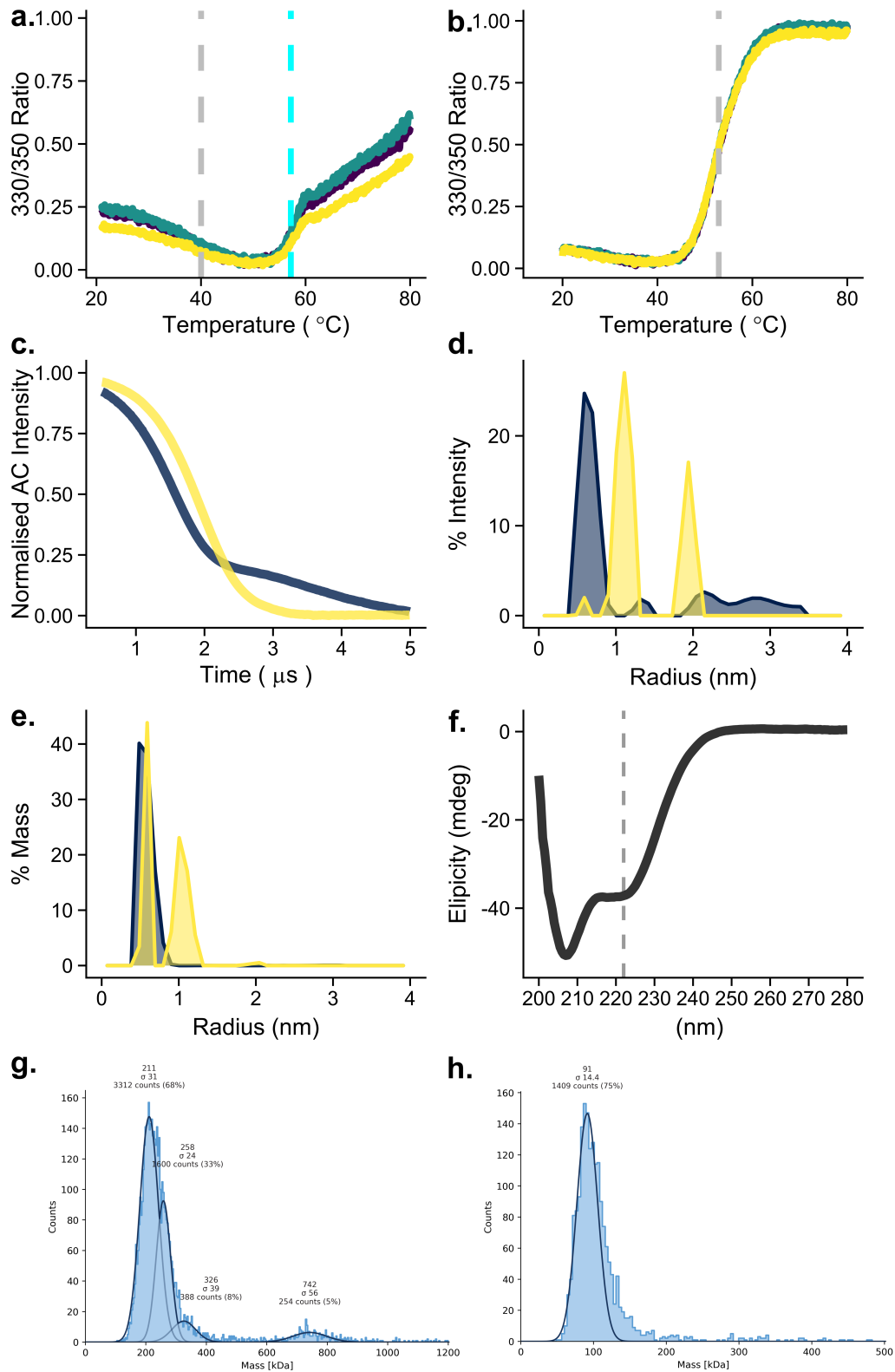


Figure 5.30: **Biophysical characterization of full length mid-coat adaptors CtSla2 and CtEnt1.**

a and b. nanoDSF of CtSla2 (a) and CtEnt1(b). The signal for the Ratio at 330/350 is shown. **c.** DLS auto-correlation function of CtSla2 (yellow) and CtEnt1 (blue). **d.** Intensity plot of CtSla2 and CtEnt1 in the same colour scheme as in c. **e.** Mass plot of CtSla2 and CtEnt1 in the same colour scheme as in c. **f.** Buffer subtracted CD spectrum of CtEnt1 showing a combination of random coil and alpha-helical content. **g and h.** Mass Photometry data of CtSla2 (g) and CtEnt1 (h) showing their expected molecular weights from sequence and confirming the oligomeric state of CtSla2 as a dimer.

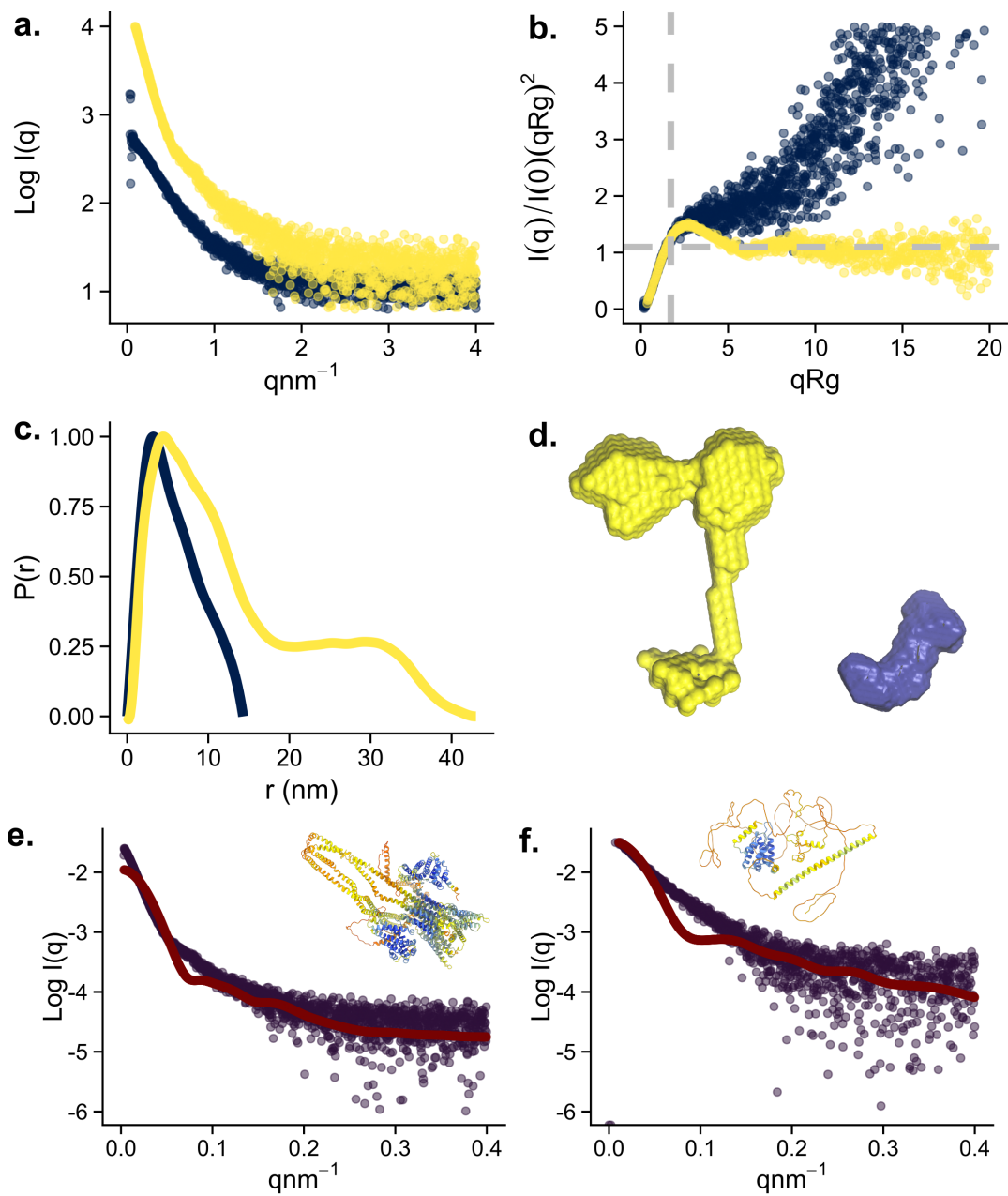


Figure 5.31: **SAXS data corresponding to CtSla2 and CtEnt1 full length.**
a. SAXS curves for CtSla2 (yellow) and CtEnt1 (blue). **b.** Normalised Kratky plot for CtSla2 (yellow) and CtEnt1 (blue). **c.** Distance distribution functions for CtSla2 (yellow) and CtEnt1 (blue). **d.** Ab-initio 3D models generated using DAMMIF for CtSla2 (yellow) and CtEnt1 (blue). **e and f.** Fittings of the AlphaFold structural prediction (Shown as an insert and in Appendix Figure 10.12) for CtSla2 (**g**) and CtEnt1 (**h**). The fitting is shown in red and the experimental data in deep purple. The χ^2 values for the fittings are 39.27 and 7.12 for CtSla2 and CtEnt1 respectively.

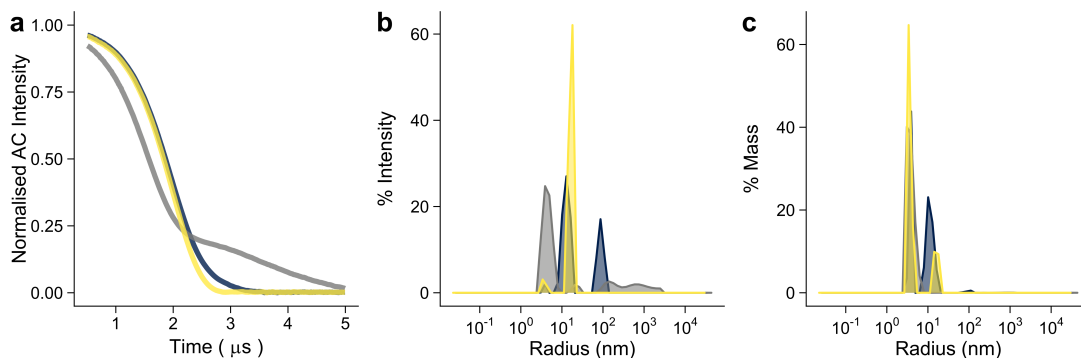


Figure 5.32: **DLS data for formation of the full length adaptor complex.**

CtSla2 and CtEnt1 were incubated in presence of 200 μM **PIP₂** (blue) in the same way than ANTH-ENTH-**PIP₂** complexes. **a.** Auto-correlation functions of CtSla2 (yellow), CtEnt1 (grey) and CtSla2-CtEnt1-**PIP₂** (blue) (blue). There is a small shift in the autocorrelation function, however no obvious multimerization is observed in the similar fashion than for the ANTH-ENTH complexes. **b and c.** Intensity and mass plots for these samples in the same color scheme.

auto-correlation function.

In view of the apparent lack of multimerization observed by DLS and its limitations, the change on CtSla2 oligomeric state was studied using SAXS. Upon mixing of the full length CtSla2 with the ENTH domain of CtEnt1 (CtENTH), the SAXS curve showed a noticeable change. However, this was not in line with a large multimerization event in a similar fashion as it happened with ANTH and ENTH domains (Figure 5.33a). Most likely, the change in the signal corresponds to the mixing effect with ENTH. On the normalised Kratky plot, the sample becomes slightly more elongated, since its maximum gets further away from the canonical maximum for globular proteins (Figure 5.33b). Interestingly, the distance distribution function also show that the sample becomes more elongated and the second maximum fades away, indicating that the overall conformation of the protein has changed in solution (Figure 5.33c). It could either be that the complex formation is not taking place at the conditions where the measurements were performed, or that the oligomerization mechanism for CtSla2 is not the same as for the individual ANTH domains (e.g. a 16-mer is not being formed and instead there is a smaller oligomer whose shape does not differ much from the large CtSla2, given the large difference in size from CtSla2 and CtENTH).

5.2.5 Structural studies of CtSla2 by Single Particle Analysis cryoEM

Attempting to determine the structure of Sla2, sample preparation for SPA cryoEM was performed. Given the large molecular weight of CtSla2, Sla2 in its native dimer

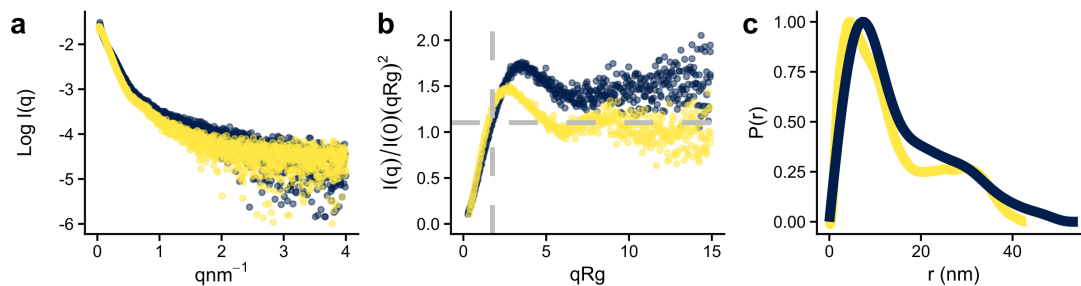


Figure 5.33: **SAXS data of CtSla2-CtENTH in presence of PIP_2 .**

a. SAXS curves for CtSla2 (yellow) and CtSla2-CtENTH in presence of 200 μM of PIP_2 (blue). **b.** Normalised Kratky plot of CtSla2 (yellow) and CtSla2-CtENTH in presence of 200 μM of PIP_2 (blue). **c.** Distance distribution function of CtSla2 (yellow) and CtSla2-CtENTH in presence of 200 μM of PIP_2 (blue).

state or any further oligomerization states would be observable in cryoEM. Initially, SPA cryoEM (performed in collaboration with the Muench group from the University of Leeds) yielded a low resolution map of Sla2, which could be assigned to the C-terminus of the protein (Figure 5.34).

The AlphaFold2 prediction for a dimer of CtSla2 shows an overall high confidence, except for the region between the ANTH and the coil-coil domain, which is annotated as a disordered and flexible region (Appendix Figure 10.12). Taking the last 400 amino acids of the dimer, the predicted model yields a visually good fit into the map (Figure 5.34). This confirms that this part of the protein can be resolved to a certain resolution. However, the rest of the protein is not present in the map. There are a few reasons why this could happen: (1) the protein is too flexible and the particle alignment on the C-terminus region which is resolved averages out the signal for the rest of the protein; (2) the box size chosen for processing is too small, and the rest of the protein is not included during the image reconstruction pipeline; (3) the protein is being degraded during sample preparation (vitrification) in its flexible region due to harsh and recurrent interactions with the air-water interface (AWI), which has been shown to be a bottleneck for sample preparation in some cases (Carragher et al., 2019). Since processing was attempted using a larger box to exclude hypothesis 2, probably the rest of the protein signal is not present in the 3D reconstruction due to other reasons. Sample preparation was attempted using a spray deposition technique instead of using the conventional blotting strategy, with the advance of the shorter vitrification times that allow to monitor reactions in the milliseconds timescales (Klebl et al., 2021). The drawback of this sample deposition system is the need of higher protein concentrations

(10x) compared with blotting systems. This results in a lower number of particles that limits the possibilities for the analysis using data acquired from grids prepared using this set up (data not shown).

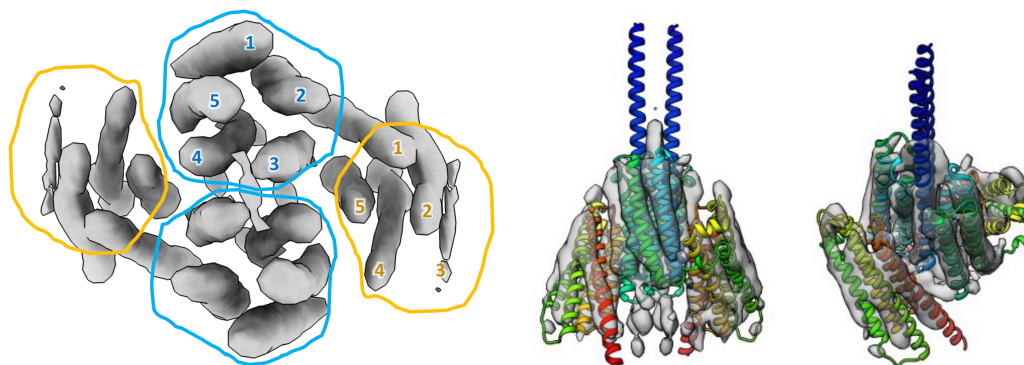


Figure 5.34: **Low-resolution cryoEM map of the C-terminus of CtSla2.**

The map corresponds to a dimer of Sla2, and each dimer contains two 5- α -helical bundles, circled in yellow and blue. The helix number is annotated. A side view of the map can be seen in the right with the AlphaFold prediction of this region of CtSla2 fitted into the density. *In collaboration with Stephen Muench, University of Leeds*

In some cases, ligands, additives or detergents can be used to stabilised the sample in an attempt to obtain better quality particles that provide with 3D information during the SPA analysis pipeline. In a second sample preparation, CtSla2 was put in presence of CtENTH and PIP₂ with the aim to (1) observe possible oligomers that could not be ascertained by SAXS and (2) test whether particles for CtSla2 would become more stable in presence of its ligand (PIP₂) and of its binding partner (CtENTH). The processing pipeline followed for this sample is shown in Figure 8.1. In this case, a map was obtained that corresponded to an oligomer of CtSla2 (Figure 5.35). The oligomer is formed by 3 subunits of CtSla2. Similarly, to the map obtain for CtSla2, this map only corresponds to the last 400 C-terminus residues of the protein, independently of the addition of CtENTH or PIP₂. This probably indicates that the inherent flexibility of CtSla2 is too high (even in presence of its ligands) to be solved by SPA, and that further strategies will need to be applied in order to resolve the structure.

Focusing on the CtSla2 oligomeric map, the main oligomeric state of the protein is a trimer of dimers, which can be clearly observed in the map (Figure 5.35b and c). The oligomer map corresponds to three subunits of CtSla2, which fit within the map. Interestingly, the last helix of the protein, predicted as disordered by some

prediction servers and therefore not included in the initial models, seems to connect the different oligomers (Figure 5.35d). The C-terminus latch helix has been shown to regulate dimerization of the related protein TALIN, and its dimerization has been shown to be a mechanism for regulating its binding to actin (Gingras et al., 2008). It could be therefore relevant that the oligomerization state of CtSla2 changes upon PIP₂ addition, regulating its actin binding properties. Future work will be required to ascertain the oligomeric state of Sla2 bound to actin.

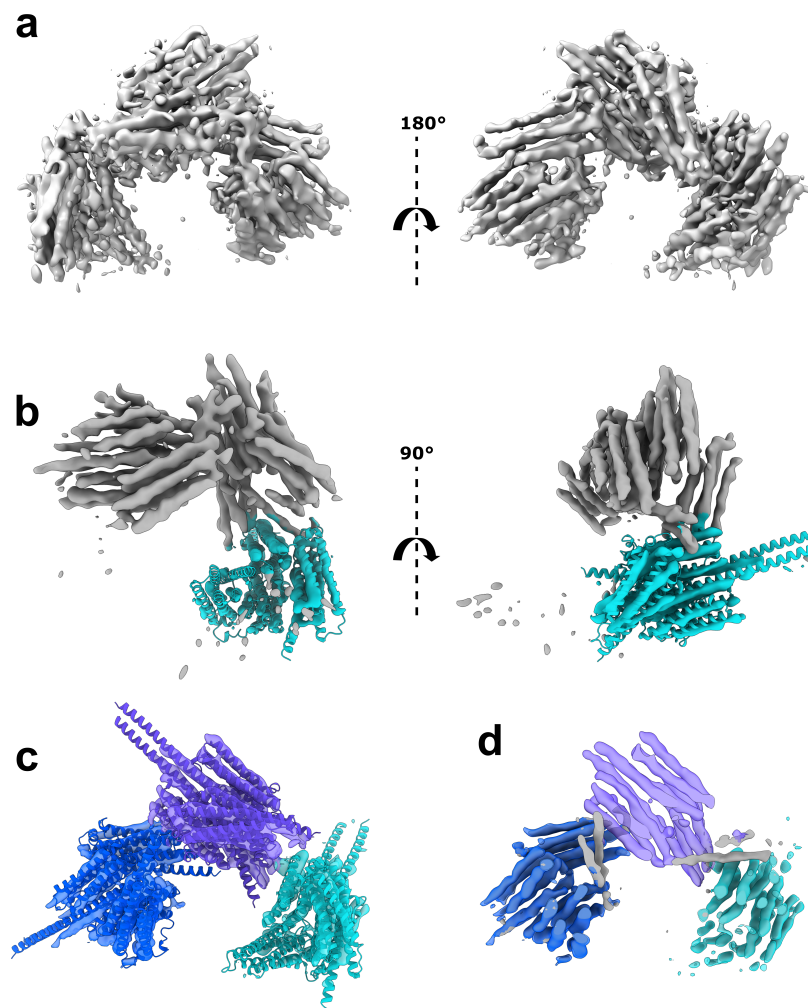


Figure 5.35: **cryoEM map of an oligomer of CtSla2 C-terminus.**

a. cryoEM map of Sla2. b. cryoEM map with one model of the last 400 amino acids of CtSla2 in cyan fitted into the map. The density corresponding to the model is coloured in cyan. c. Three subunits of CtSla2 C-terminus fitted into the EM map shown in cyan, purple, and blue. d. cryoEM map of the oligomer of CtSla2 C-terminus with the density corresponding to the model coloured. The C-terminal latch helices (not included in the model) can be appreciated.

Focusing on the cryoEM map and the AlphaFold2 prediction for a Sla2 dimer (they are highly similar), both show the last region of the coiled-coil domain, a 5 α -helical

bundle domain, which to date had not been annotated, and the THATCH domain of Sla2, and a C-terminus helix, which in the homologue TALIN is known as the latch helix. Interestingly, the conformation of the C-terminus of CtSla2 changes depending on the presence of this C-terminal helix in the input sequence (Figure 5.36). The actin binding residues of the THATCH domains of the mammalian homologue of Sla2, Hip1R, have been previously described (Brett et al., 2006) and are conserved between yeast and mammals (Appendix Figure 10.13). In the AlphaFold2 prediction confirmed by the cryoEM map, these residues are located in the context of the C-terminus part of Sla2, not considered in the previous crystallographic and biophysical studies. The actin binding residues are located in the interface between the THATCH domain and the domain between the 5 α -helical bundle next to the coil-coil domain and the THATCH domain (Figure 5.36). Theoretically, these residues need to be exposed and ready to bind to F-actin, however, the model fitting the cryoEM map places them in a more enclosed conformation that what could be allowed sterically for actin filament binding. Therefore, there has to be a conformational change of CtSla2 whereby the THATCH domain can open from the C-terminus core and bind to F-actin. A CtSla2 C-terminus model containing the last latch helix also places the THATCH domains more open, in a conformation that allows for these residues to be exposed for binding, which could potentially be the conformation of Sla2 in its active-bound state. However, further experiments and the determination of an actin-bound structure are required in order to validate this hypothesis.

5.2.6 Expression and purification of Sla2 Δ THATCH

During attempts of expression Sla2 from *S. cerevisiae*, it was possible to produce and purify a construct of *S. cerevisiae* Sla2 missing the C-terminal THATCH domain (Sla2 Δ THATCH, 87 kDa) (Figure Figure 5.37). SDS-PAGE analysis of the fractions corresponding to the peak from the SEC column containing the right molecular weight band revealed other bands at lower molecular weight (Figure 5.37, panel C). In spite of performing the expression at low temperature and the purification at 4 °C and in the presence of protease inhibitors, Mass Spec fingerprinting analysis confirmed that the lower molecular weight products correspond to degradation products of Sla2 Δ THATCH that were cleaved in the sequence the ANTH domain and in the middle of the coiled

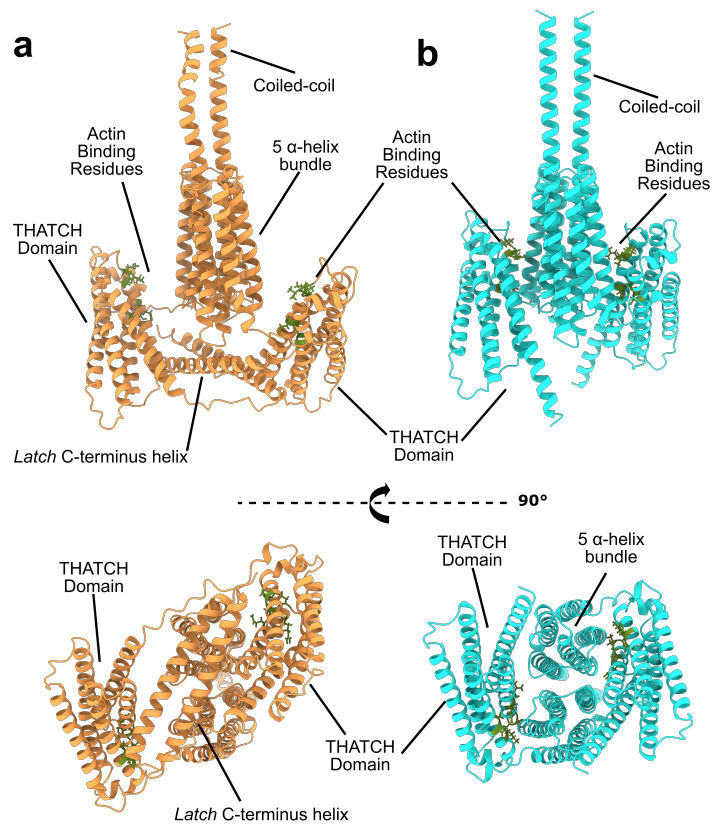


Figure 5.36: **Comparison between the AlphaFold model of Sla2 C-terminus** with (a) or without (b) the last latch α -helix. In the prediction accounting for the last latch helix, the THATCH domain is more open compared to the prediction where this last helix is absent, and consequently the actin binding residues become more open.

coil domain (data not shown). Looking at the disorder prediction by IUPred and the structural prediction by AlphaFold (Appendix Figure 10.12), it is not surprising the degradation happens at this point of the sequence given the high disorder level present in this region.

5.2.7 Characterization of the coiled-coil of Sla2

Given the large proportion of degradation present in Sla2dTHATCH confirmed by the MS fingerprinting analysis, the coiled coil domain of Sla2 was cloned in order to study this domain of the protein in isolation. To determine the structure of the coiled coil region of Sla2, three constructs spanning the coiled coil region of Sla2 were cloned as GST-fusion proteins into the pETM30 vector. Out of these three, two were possible to express in *E. coli* (Appendix Figure 10.15).

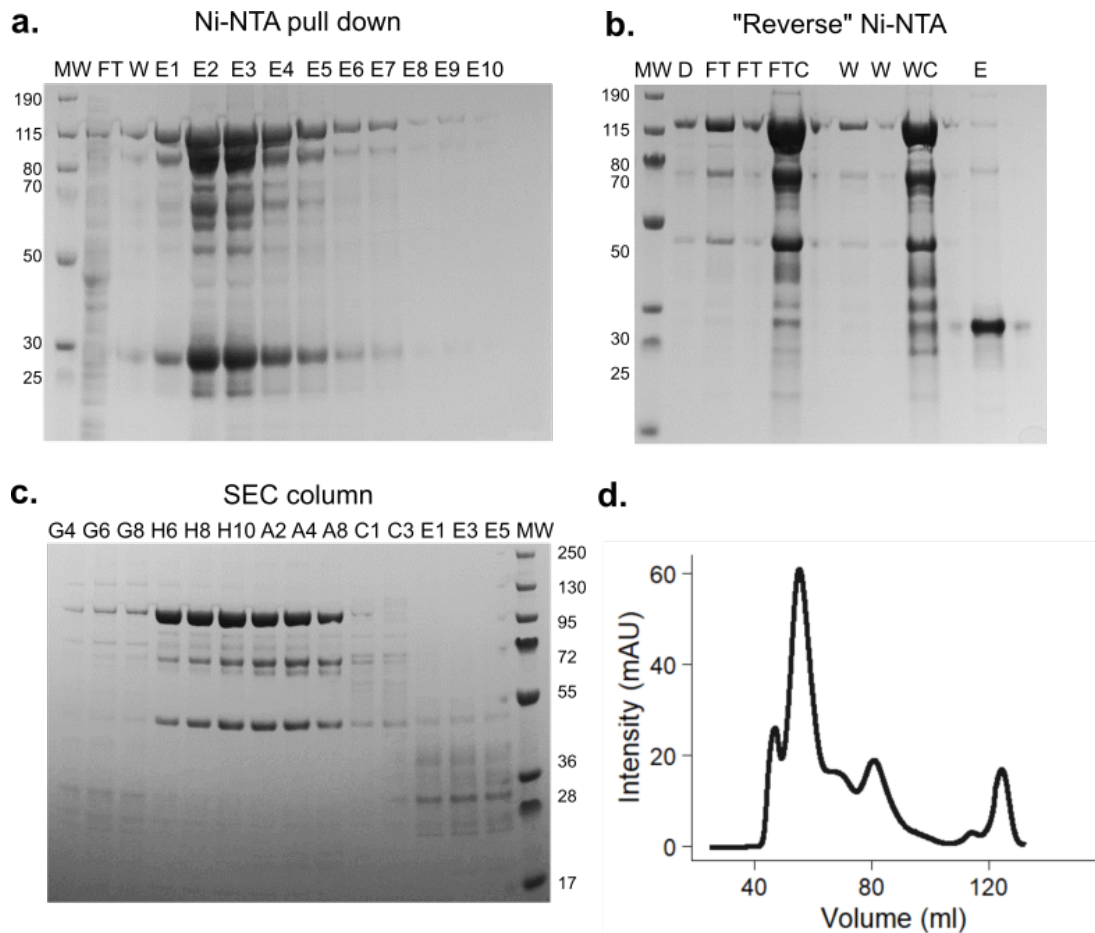


Figure 5.37: **Purification of Sla2 Δ THATCH.**

a. SDS-PAGE analysis of the fractions from a Ni-NTA pull down of His-GST-Sla2 Δ THACTH (ca. 100 kDa). FT = flow-through, W = Wash and E = Elution. The protein comes in the elution. **b.** SDS-PAGE analysis of the fractions from a “reverse” Ni-NTA pull down. D = dialysis. The protein after removal of the His-GST tag comes in the Flow-through (FTC= Concentrated Flow-thought) and in the Wash (WC = Concentrated Wash). **c.** SDS-PAGE analysis of the fractions corresponding to a Size Exclusion Chromatography using HiLoad 16/600 Superdex 200 column. MW of Sla2 Δ THATCH = 87 kDa. **d.** Chromatogram of the Absorbance at 280 of the SEC column. MW=Molecular weight ladder.

nanoDSF of these constructs showed two transitions, one very early at 25 °C and a later one at ca. 44 °C (Figure 5.38a-d). There was no apparent signal in the scattering channel, indicating that the protein does not aggregate upon thermal denaturation. To rule out the possibility that the protein might be denatured from the start given the weak transitions present in the sample, CD experiments were performed. The spectra (Figure 5.38e-f) show the characteristic shape of an alpha helical protein whose signal weakens upon thermal denaturation. Following the signal at 222 nm over thermal denaturation, a large loss of secondary structure could be observed, with a transition point at 44 °C (Figure 5.38g-h). The unfolding of the protein was not fully reversible for both constructs, as the spectrum at 20 °C after the thermal ramp is not identical

to the initial one, indicating that a fraction of the protein aggregated upon thermal denaturation. Interestingly there was a small fraction of beta sheet signal present in the sample and little amount of disorder (Appendix Table 10.4).

SAXS data for these two Sla2 coil-coil constructs confirmed that both constructs constitute an elongated coil-coil domain and that they are relatively flexible, as it can be seen in the normalised Kratky plot (Figure 5.39 and Table 5.11). The molecular weight calculations confirm that both constructs are a dimer in solution and the ab-initio model and distance distribution functions show that both Sla2 coil-coil constructs are elongated. The fitting between the predicted structure with AlphaFold and the protein does not yield a good fit with the SAXS data (Figure 5.39 e-f), probably due to the inherent flexibility of the constructs.

Table 5.11: Structural parameters derived from SAXS curves

Sample	I_0	R_G	D_{max}	V_{POROD}	R_G (Pr)	I_0 (Pr)	MW (kDa)	MW_{seq} (kDa)
Sla2 432-767	0.062 ± 0.00017	6.11 ± 0.03	21.05	182555	6.07	0.06	91	38.6
Sla2 296-767	0.075 ± 0.00028	6.95 ± 0.03	25.69	293458	7.41	0.08	118	53.9
CLC	169270.2 ± 38.54	4.96 ± 0.02	16.99	92722.8	5.18	17030	62	26.5
Sla2 - CLC	757.17 ± 2.18	5.92 ± 0.02	20.88	208142	6.31	770	94	65.1
CtSla2	28659.90 ± 177.12	11.20 ± 0.10	36.13	2610.53	11.16	27940	318	118
CtEnt1	0.034 ± 0.00026	5.07 ± 0.06	15.84	119076	5.08	0.03	74	65.90
CtSla2 + CtENTH + PIP ₂	0.021 ± 0.00028	11.04 ± 0.18	54.25	1350.05	13.35	0.02	318	254
Sla2 Δ THATCH	177556.40 ± 92.51	7.52 ± 0.06	26.43	347744	7.90	17690	130	87

5.2.8 Crystallization trials of Sla2 coiled coil

In spite of the inherent flexibility of the Sla2 coil-coil constructs observed by SAXS, crystal trials were set up in order to try to determine the atomic structure of this domain of Sla2 using MX. Commercial and custom screens were set for both soluble constructs

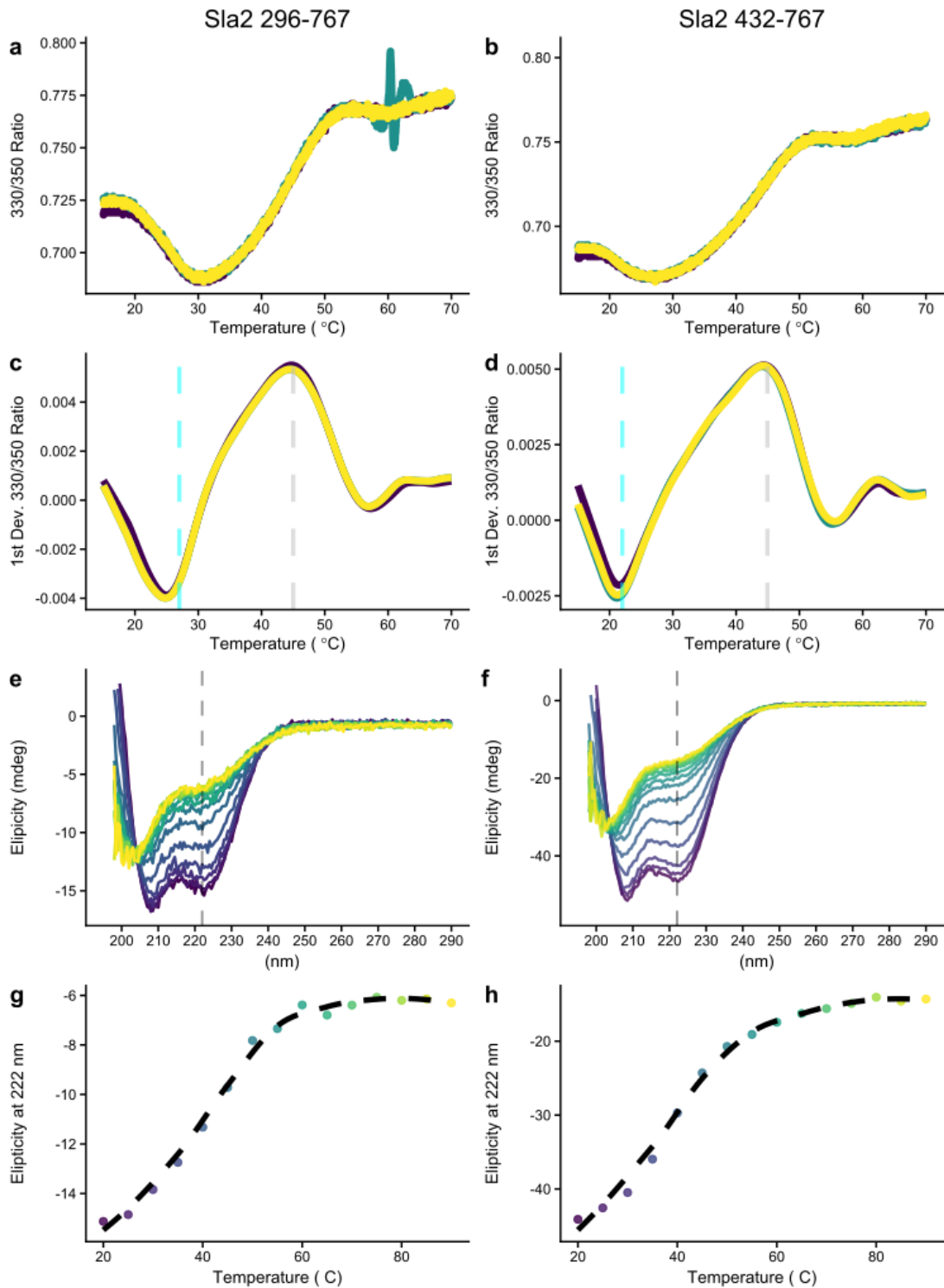


Figure 5.38: **Biophysical characterization of Sla2 coil-coil constructs.**

a-d. nanoDSF of Sla2 coil-coil constructs. **a** and **b** show the signal for the 330/350 Ratio. The transitions for the two proteins are shown as a dashed line. **c** and **d** show the first derivative of the ratio. **e-f.** CD spectra of Sla2 coil-coil constructs. **e** (Sla2 296-767) and **f** (Sla2 435-767) show the spectra in temperatures ranging from 20 to 90 °C (from blue to yellow). The wavelength at 222 nm was selected to see the loss of secondary structure upon thermal denaturation and the signal is plotted in **g** and **h**.

(Table 5.12). Crystals were obtained for both constructs in several conditions and their identity was confirmed by UV fluorescence (to discard they would correspond to salt

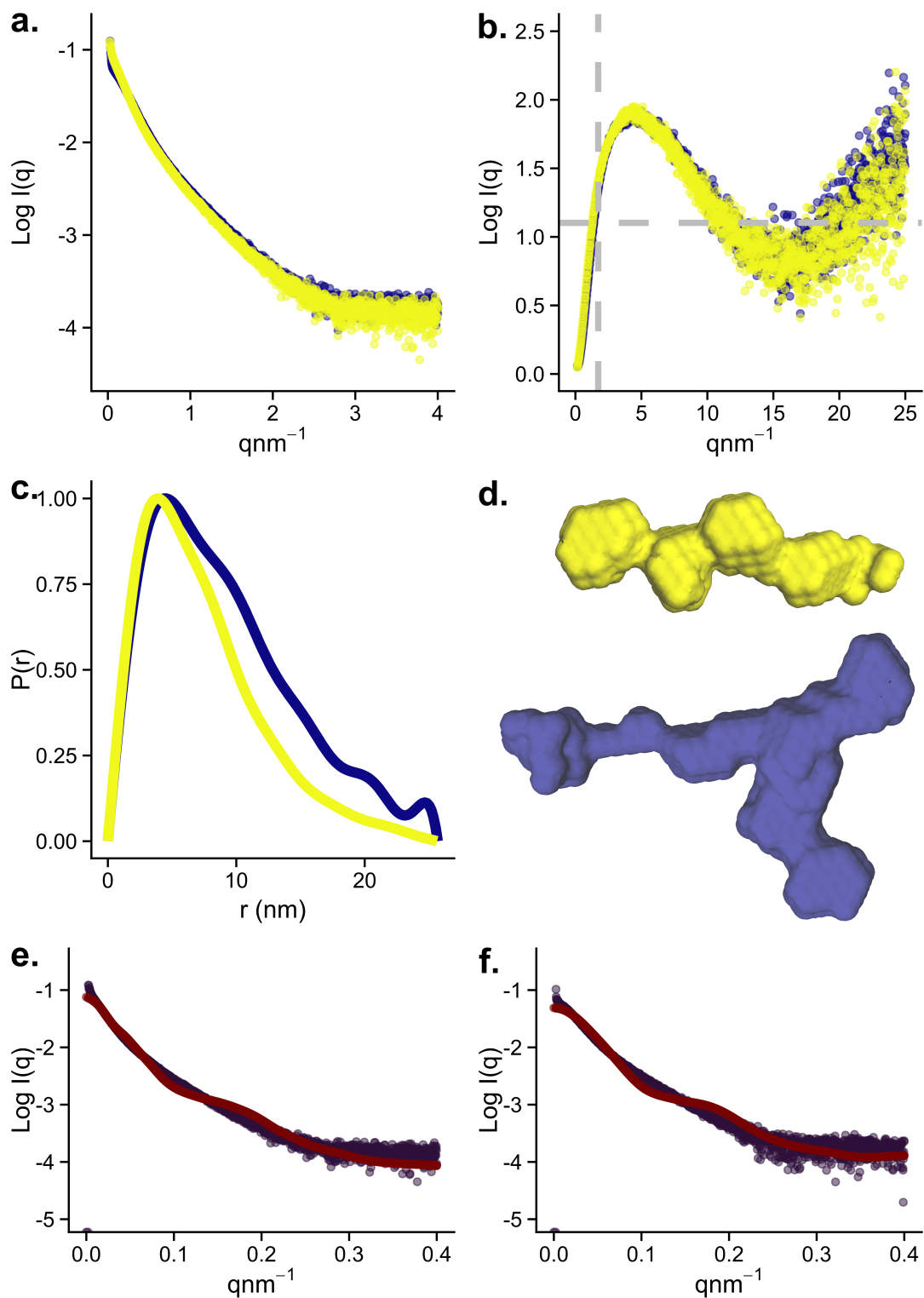


Figure 5.39: SAXS data for Sla2 296-767 (yellow) and Sla2 432-767 (blue). **a.** SAXS curves. **b.** Normalised Kratky plot. **c.** Distance distribution function. **d.** 3D ab initio models for both constructs. **e and f.** CRYSOLO fittings of the AlphaFold predictions for Sla2 296-767 (e) and Sla2 432-767 (f). The χ^2 values are 24.48 and 20.02, respectively.

crystals) and also using Mass Photometry, by fishing one crystal and dissolving it in buffer and measuring the molecular weight of crystal components (Figure 5.40).

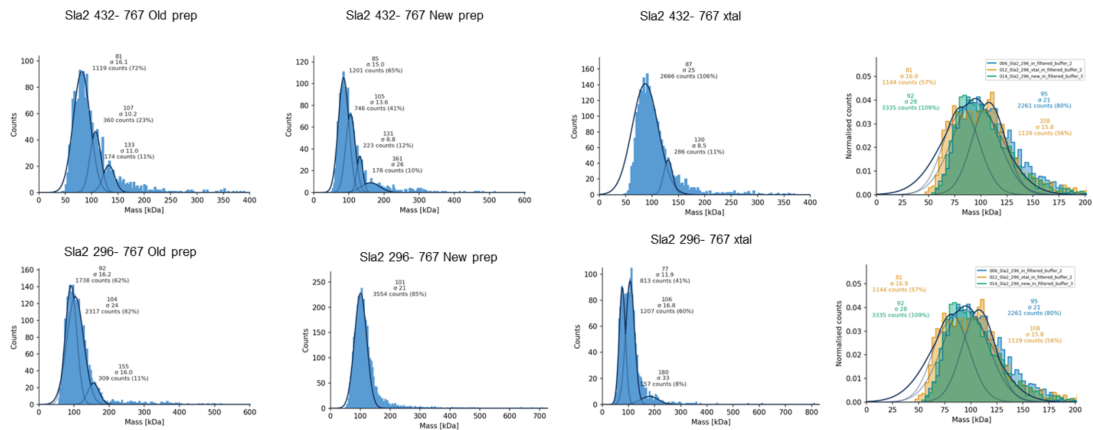


Figure 5.40: Mass Photometry for crystals obtained using Sla2 432-767 and Sla2 296-767. The molecular weights correspond to dimers of Sla2 coil-coil domain in all cases. Most sample show a single Gaussian distribution and the overlay between different preparations of protein confirms the identity of the protein crystallized.

Table 5.12: Crystallization conditions that yield crystals for Sla2 coil-coil constructs

Construct	Screen	Condition	Diffraction
Sla2 296-767	Solubility Stability Screen 2	A10, F5, F10, F6, E1, D3, H1	Best to 6 Å
	Hampton additive	B3, B5, B6, B12, D2, D3, D4, F11, G12	Best to 7.5 Å
	Custom 000933	A2, A6, B2, B6, C5, D1, D3,	Best to 5 Å
	MD LMB screen	E2, E7, G1, G6	No diffraction
Sla2 432-767	Custom 000934	B10, B12, C9, G3, H1, H2, H9	Best to 4.7 Å
	MD SG1 Screen2	E6	V LOW
	QIAGEN Classics-I	D1, E2	5 Å
	QIAGEN JCSG-Plus	B8	Low diffraction
	MD LMB screen	H2,H11, C1, C3, C8	4.5 Å
	MD MemGold HT-96	C4, C9, F2	Very Low diffraction
	QIAGEN ProComplex	G9, H2	Ice rings

Crystals were fished and tested at beamline P13 in Petra-III at DESY. Some datasets were collected for both datasets, with the highest diffraction at 4.5 Å. Attempts of solving the structure by molecular replacement using the AlphaFold2 prediction of Sla2 were unsuccessful most likely due to the lack of diffraction to high-enough resolutions for solving the phase problem. Given the flexibility observed by SAXS, it was surprising to obtain crystals of these constructs of Sla2, but the diffraction data highlight that even single crystals present a level of disorder that leads to weakening of the signal towards higher resolutions. Another possibility for the low diffraction could

be a high solvent content of the crystals. Given the topology of the protein, when just a few crystal contacts are present across the coiled-coil domain, the large water channels present in the crystal could have a deleterious effect over the resolution achievable with this sample. Changing the crystal packing, using dehydration protocols to remove solvent, or growing larger crystals that could yield more signal could be possible approaches used in future work in order to determine the precise atomic structure of this region of Sla2.

5.2.9 SAXS of coiled-coil constructs and SEC-SAXS with the CLC

Sla2 and its mammalian homologue, Hip1R are known to interact with CLC and contribute to the formation of the clathrin coat (Boettner et al., 2011; Ybe et al., 2007). In order to characterize the interaction with the full length Sla2, we cloned and expressed CLC from yeast.

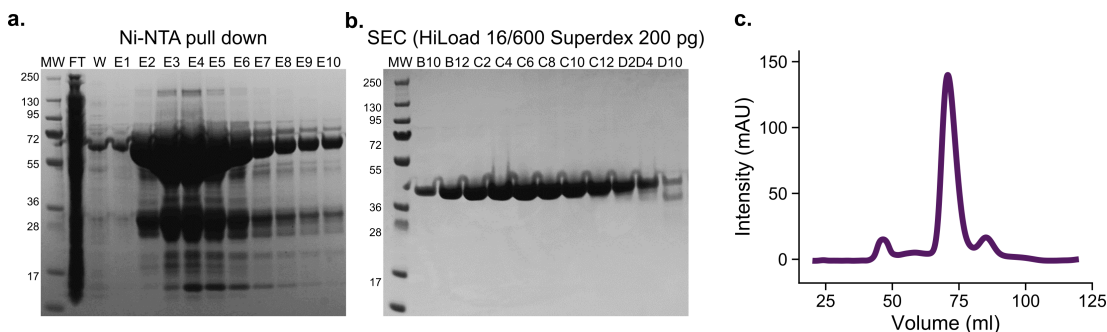


Figure 5.41: **Purification from CLC from *S. cerevisiae*.**

a. SDS-PAGE analysis of the fractions from a Ni-NTA pull down of His-GST-CLC. FT = flow-through, W = Wash and E = Elution. MW=Molecular weight ladder. The protein is present in the elution fractions. **b.** SDS-PAGE analysis of the fractions corresponding to a Size Exclusion Chromatography using HiLoad 16/600 Superdex S200 column after His GST cleavage. **c.** Chromatogram of the Absorbance at 280 nm of the SEC column.

After protein purification (Figure 5.41), biophysical characterization of the sample was performed. MALDI-TOF experiments were performed to confirm the sample identity. CLC showed the expected molecular weight from the sequence of a monomer with the standard detector (Figure 5.42a). Interestingly, even when the sample is predominantly a monomer, higher oligomeric species, namely dimers, trimers and tetramers, could be detected in the sample (Figure 5.42b). Pentamers and hexamers are also observed in the sample but to a lower abundance. This result indicates that probably the CLC can oligomerise in solution into different types of assemblies found by MS.

DLS experiments showed that the protein is monodisperse with an R_G of 4.5 nm,

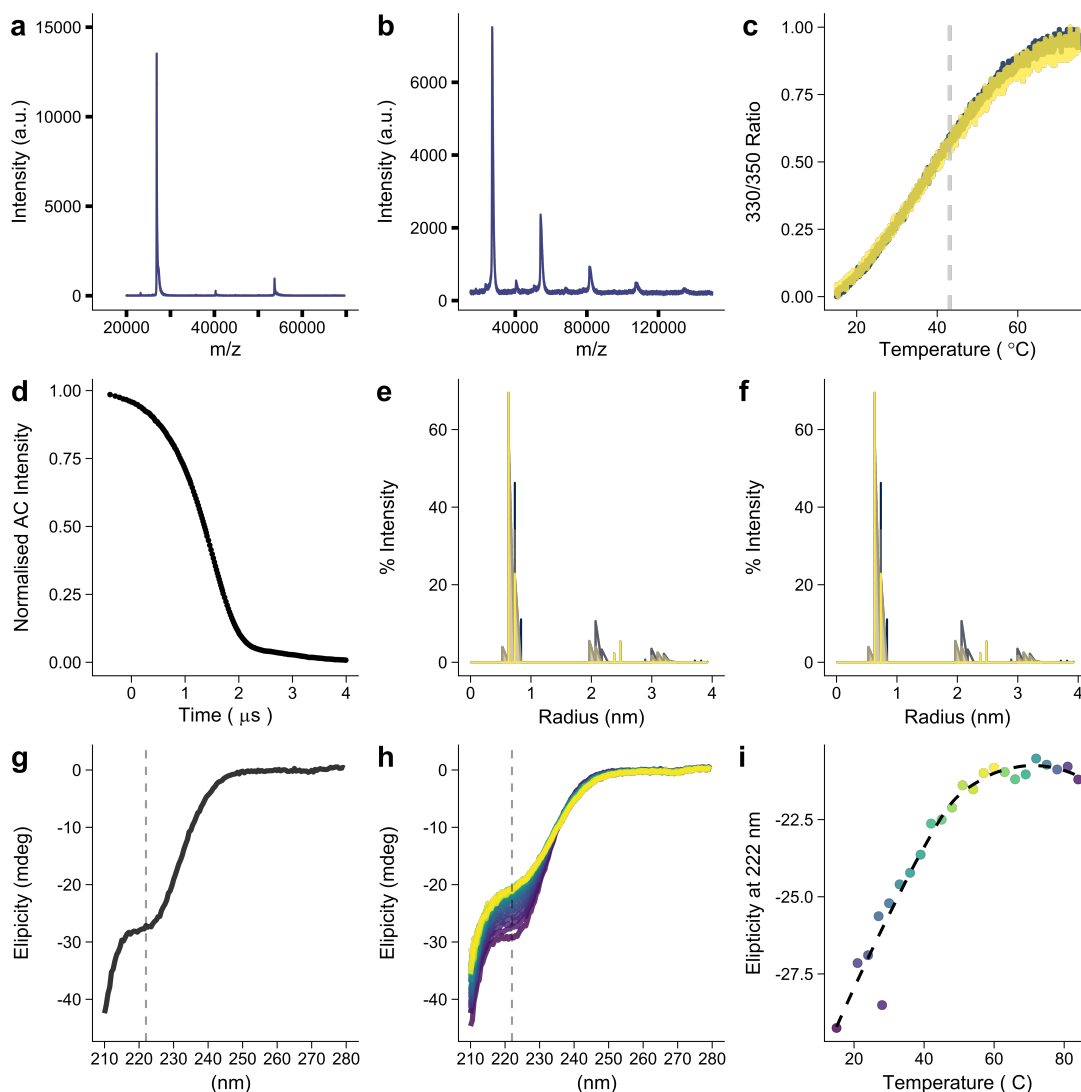


Figure 5.42: **Quality Control report for CLC of *S. cerevisiae*.**

a. MALDI-TOF using the standard detector shows monomer and dimer of CLC and that the sample is pure. **b.** Using the CoValX detector for higher masses, several further oligomeric states can be detected for CLC. **c.** nanoDSF curve obtained for CLC. **d.** DLS auto-correlation curve for CLC. **e and f.** Intensity and Mass plots derived from the DLS data. **g.** CD spectrum of CLC at 20 °C. **h.** CD spectra for CLC during a temperature ramp from 20 to 95 °C (from purple to yellow). **i.** Ellipticity at 222 nm at different temperatures.

and an estimated MW of around 120 KDa, which is much larger than expected from the sequence (Figure 5.42d-f). This supports the notion that CLC can be a multimer in solution. Another reason for the exacerbated R_G and MW is the fact that the protein is supposed to be elongated/disordered, instead of globular, which is assumed in the DLS analysis for deriving the MW of the sample (Figure 5.42e-f).

nanoDSF does not report any known transition since the two Trp residues are exposed to the solvent most likely so there is no change on their environment upon thermal denaturation. Analysis of the Ratio 350/330 curve yields an onset point at

15°C, which is the starting temperature of the experiment. The transition observed is very weak, nonetheless it yields a T_m 41 °C. There are several reasons that could account for such a low value: (1) CLC is either aggregated or misfolded, therefore it is partly denatured from the beginning due to a bad sample preparation that gives low quality sample; (2) Trp residues of CLC are (mostly) exposed towards the solvent even in its native state, therefore the shift in fluorescence of the protein upon denaturation is very weak and the DSF data not robust; (3) CLC is unstable under the conditions measured. To discard a folding/aggregation problem with the sample measured by nanoDSF, CD experiments were performed (Figure 5.42g). According to the shape of the spectra the protein is alpha helical and part of random disordered. From the thermal-denaturation following the CD signal, a loss of signal is observed from the beginning of the experiment, and a loss of signal which yields a T_m lower than 40 °C. This could mean the alpha helical content from the protein is not very significant in isolation, either by the intrinsic nature of CLC by itself or because the sample quality was not good enough. Probably, CLC needs of a binding partner, such as CHC, in order to adopt a stable helical conformation. SAXS measurements of CLC however, agree with its predictive flexible nature. The SAXS curves of CLC do not show any aggregation and therefore support the fact of a soluble protein together with the DLS measurements (Figure 5.43a). Furthermore, the Kratky plot show how the protein is extremely disordered, with the flow increasing towards higher values of qR_G and the porod plot indicates its elongated nature (Figure 5.43b and c). The distance distribution function and the ab-initio model generated from the data also show a mostly elongated flexible sample (Figure 5.43d and f). The poor fitting between the structural prediction by AlphaFold2 of CLC and the experimental data further reinforces the high degree of flexibility of CLC (Figure 5.43e).

5.2.10 Studying the interaction between Sla2 and Clathrin light chain

Previous studies have studied the interaction between Hip1R and Clathrin light chain (CLC), unravelling different preference for two isoforms of CLC which are differentially expressed in different tissues. Similar than in the mammalian system, yeast Sla2 is known to interact with CLC, and its interaction has been previously characterise in a cellular level (Newpher, Lemmon, 2006). The binding affinity between Sla2 Δ THATCH

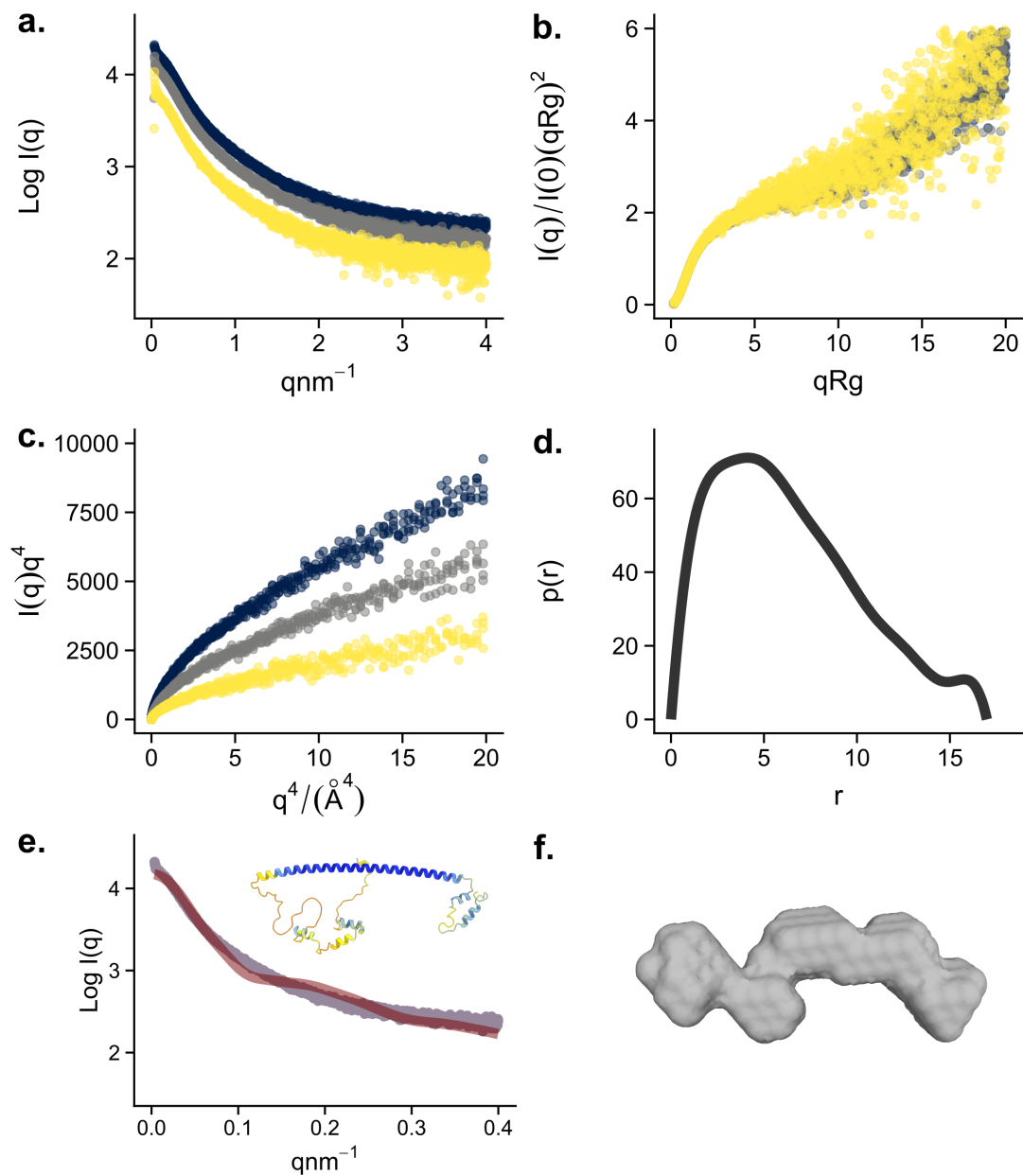


Figure 5.43: **SAXS experiments of yeast CLC.**

a. SAXS curves of three serial dilutions of CLC. **b.** Normalised Kratky plot for CLC. **c.** Porod plot of CLC. **d.** Distance distribution function of CLC. **e.** Fitting between the predicted structure of CLC by AlphaFold (red) and the experimental data (purple). The AF2 model is shown as an insert and in Appendix Figure 10.12. The χ^2 value is 25.71 **f.** 3D ab-initio model of CLC.

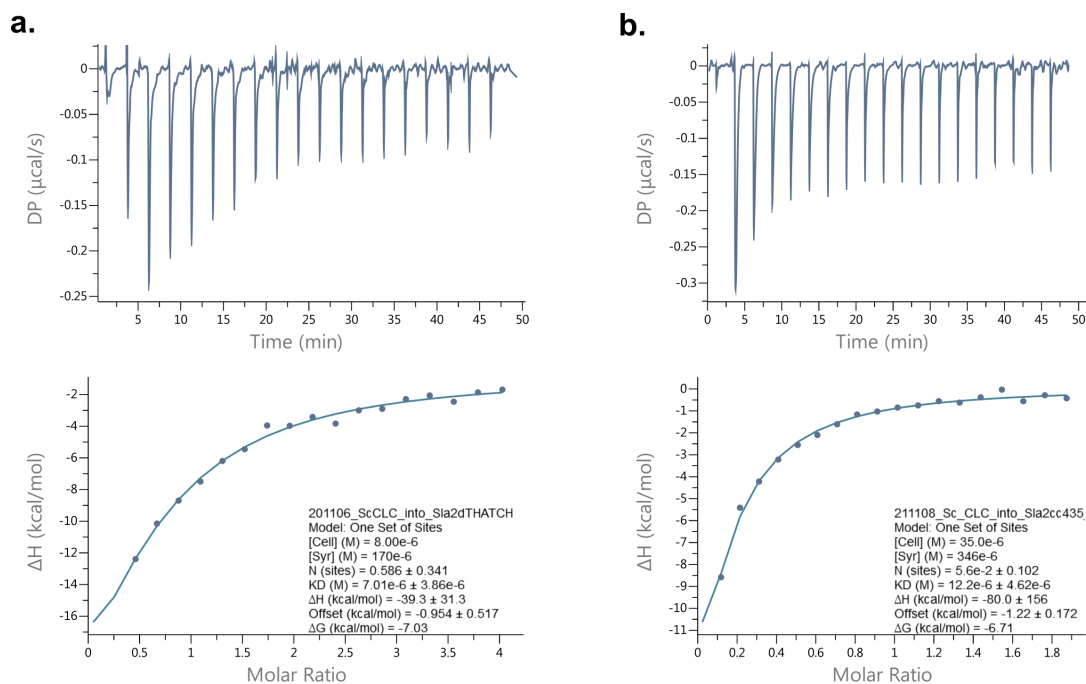


Figure 5.44: **Binding affinity of Sla2 and CLC measured by ITC.**

(a) Titration of yeast CLC into Sla2 Δ THATCH. (b) Titration of yeast CLC into Sla2 coil-coil 432-767.

and CLC was measured *in vitro* using ITC. The K_D measured is within the order of magnitude than the K_D s reported for the mammalian system (Biancospino et al., 2019). Using a shorter construct of Sla2, Sla2 432-767 (comprising just the coiled coil region of Sla2), the binding affinity is similar than with Sla2 Δ THATCH (Figure 5.44), in agreement with the cell biology data indicating that binding happens in this coiled-coil domain, and that the ANTH domain has no influence over the binding affinity of Sla2 to CLC.

In order to further characterise the Sla2-CLC complex, size exclusion chromatography was performed. Upon loading the two proteins together in SEC, a small shift in the retention time compared with the one of Sla2 coil-coil indicates that complex formation is taking place, since two bands appear on SDS-PAGE gel (Appendix Figure 10.16) or that the conformation of Sla2 is being altered in the presence of CLC, which also shows a peak at its usual retention time (Figure 5.45a). The intensity recorded for SAXS signal during SEC-SAXS experiments shows a similar profile than the SEC profiles, together with a shift towards slightly higher R_G values (Figure 5.45b, Appendix Figure 10.14 and Table 5.11). The intensity of the SAXS curve for the complex is also higher (Figure 5.45c), but the average SAXS profile of the Sla2 coil-coil-CLC complex is relatively similar to the one of Sla2. Interestingly, the normalised Kratky plot for

the three samples shows that the large flexibility present in the CLC sample is significantly reduced compared to Sla2 coil-coil-CLC complex, which could indicate that the fraction of CLC bound to Sla2 does so in a more rigid state (Figure 5.45d). Similarly to the increase in the R_G value of the complex sample, the distance distribution of the complex is also larger, and the maximum distance of this sample is significantly increased when compared to either CLC or Sla2 coil-coil (Figure 5.45e). This can be appreciated graphically in the 3D ab initio models generated from the distance distribution functions (Figure 5.45f). Finally, the availability of SAXS data from complex components (Sla2 coil-coil and CLC) allowed the analysis of the complex data using MONSA, which allows the allocation of the individual components within the complex data (Figure 5.45g). These data further confirms the elongated conformation of the CLC and Sla2-coil coil complex, and pin-points towards a model in where the two proteins just have a few interaction points, as it has been suggested in the mammalian homologue Hip1R with the crystal structure of its coil-coil domain (Niu, Ybe, 2008).

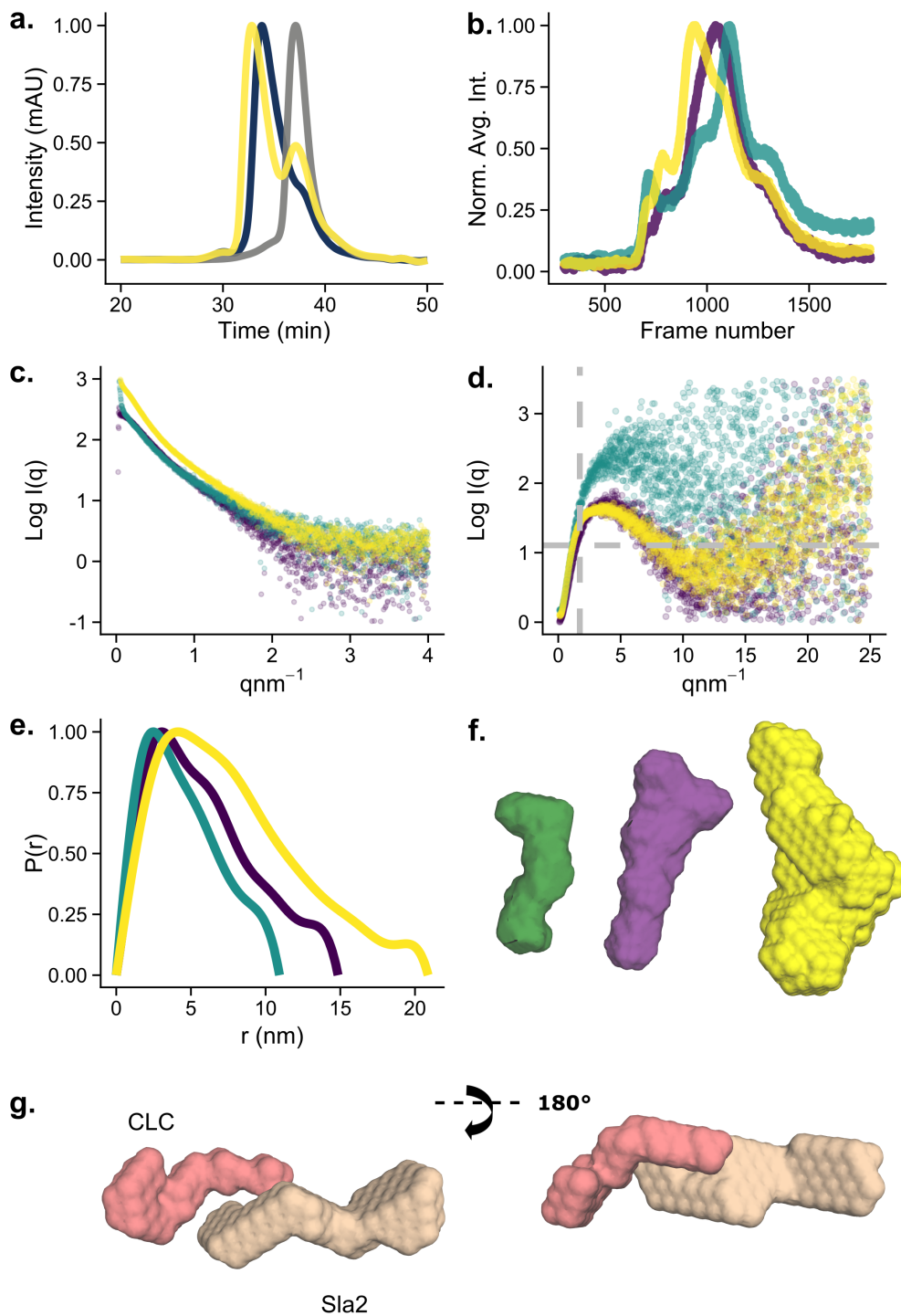


Figure 5.45: **SEC and SEC-SAXS studies of the interaction between Sla2 and CLC.** **a.** SEC profiles of CLC (grey), Sla2 coil-coil 432-767 (blue) and Sla2 coil-coil-CLC (yellow). **b.** Intensity profiles for SEC-SAXS runs for CLC (green), Sla2 coil-coil (purple) and the complex between Sla2 and CLC (yellow). **c.** SAXS curves generated from the frames in the top of the peaks in the same colour scheme as in **b.** **d.** Normalised Kratky plot for CLC, Sla2 coil-coil and the complex in the same colour scheme as in **b.** **e.** Distance distribution function for CLC, Sla2 coil coil and the complex in the same colour scheme as in **b.** **f.** 3D ab-initio models for CLC, Sla2 coil-coil and the complex in the same colour scheme as in **b.** **g.** Composite model generated by MONSA of the interaction between CLC and Sla2 coil-coil. The fractions of the model corresponding to Sla2 coil-coil and CLC is shown in wheat and red, respectively.

5.3 Structural characterization of clathrin selectivity for endocytic adaptors

5.3.1 Introduction

During its formation, the clathrin coat binds different adaptor proteins that connect it with the region of plasma membrane where cargo is being recruited, leading towards the formation of a clathrin-coated endocytic pit. The N-terminal domain of CHC (CHC NTD) has been known to mediate these interactions, and several studies have highlighted the importance of this domain of clathrin and its binding to adaptors as a crucial regulator of the endocytic coat progression (Mettlen et al., 2018; Partlow et al., 2022). As it can be seen in the multiple cage structures solved by cryoEM, CHC NTD does not form part of the triskelion interactions, but instead remains isolated towards the end of the cages connected to them by the leg domains (Fotin et al., 2004a; Paraan et al., 2020). There are several crystal structures of CHC NTD from mammals bound to different types of clathrin binding motifs which showcase the multiple interactions that clathrin establishes (Table 5.13).

CHC NTD is a β -propeller that consists of 7 blades that harbours 4 known binding sites for adaptors (in mammals). The first site, located between blades 1 and 2, is the so-called clathrin box, where adaptor proteins binding through the "Clathrin-box" motif, which consists of the consensus sequence of LØXØ[DE]. Some examples of proteins containing this sequence are Amphiphysin, β -Arrestin- 1, AP2 β 2 subunit, epsin, and AP180 (Haar ter et al., 2002). A second site, located between blades 4 and 5, is the Arrestin box, where β -Arrestin binds was found to bind through a [LI][LI]GXL motif. The third site was later characterized for binding a sequence containing W-box motifs, which have a consensus sequence of PWXXW. Different than the other two boxes, this adaptor binding box is located in the top side of the beta propeller (Miele et al., 2004). Finally, a fourth binding site was defined between blades 6 and 7 by (Wilcox, Royle, 2012) based on functional assays that demonstrated that cargo uptake requires of just a single functional adaptor binding site in CHC NTD.

5.3.2 Crystal structure and AlphaFold prediction with CHC NTD

Several studies have focused on the description of the different adaptor binding sites, and demonstrated that they are redundant to a certain extent. However, the possibility that the different boxes present in CHC NTD hide some hierarchical organization to sort out for different interactions present during clathrin coat formation has never been tested biophysically (e.g. is it a difference in affinity what drives this hierarchy?). Intriguingly, the sequence present in the Ent1 adaptor from *C. thermophilum* (whose characterization was also performed in this work) differs from the standard "Clathrin-box" SLiM defined for other organism such as *S. cerevisiae* and *H. sapiens*.

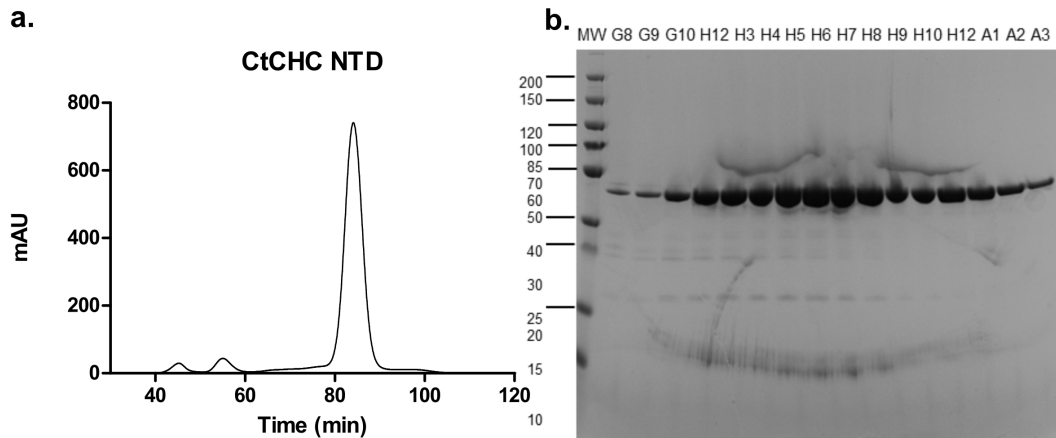


Figure 5.46: **Purification of CtCHC NTD**
a. SEC elution profile for CtCHC NTD using a HiLoad 16/600 Superdex S200 column. **b.** SDS-PAGE analysis of the fractions corresponding to the top of the peak.

To explore the possible differences driven by this sequence change observed in *C. thermophilum* system, the CHC NTD from this species was produced and purified (Figure 5.46). To compare possible differences in the binding of adaptors in *C. thermophilum* system and *H. sapiens*, the crystal structure of CHC NTD was determined to 1.6 Å resolution (Table 5.14, Figure 5.48b). This resolution, allowed a close inspection of the binding boxes in CHC NTD, where the position of the side-chains for the conserved Glutamine residues involved in binding to the peptides are clearly defined (Figure 5.47). The overall structure of CHC NTD from *C. thermophilum* is very similar to the one from *H. sapiens*, with RMSD values for C α of 1.453. The residues in the adaptor binding boxes are structurally conserved, as it can be seen by superimposing the crystal structures (Figure 5.48b). This remarkably structurally conserved binding pocket suggests that a similar mechanism of adaptor binding is conserved between *C.*

thermophilum and *H. sapiens*.

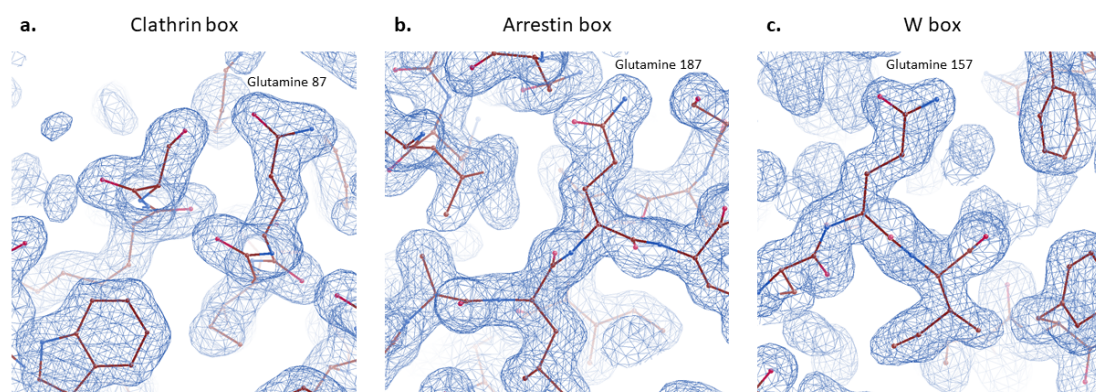


Figure 5.47: **Crystal structure of Ct CHC NTD**

Density in the different binding sites of Clathrin Heavy Chain N terminal domain, with relevant residues for binding indicated for each site. **a.** The Clathrin box site. **b.** The Arrestin box site. **c.** The W box site. 2Fo-Fc at 1 Sigma is shown around the model in blue wireframe representation.

Differently than in mammals, CtEnt1 does not contain the consensus sequence for the clathrin box (L[IVLMF].[IVLMF], defined in the ELM Database), but contains a LITF sequence instead. Interestingly, this peptide sequence shares some similarities with the sequence of the β -Arrestin motif crystalized previously in the Clathrin box from CHC NTD (Haar ter et al., 2002) (Figure 5.49c). This raises the question of whether binding of adaptors by clathrin is conserved across species, in spite of these sequences changes observed. To understand the differences in between the different motifs in *C. thermophilum*, two peptides, one corresponding to the C-terminus of Ent1 (GEAFTQQRGNLITF, from Uniprot ID G0SAK2), and one corresponding to another member of the epsin family which contained a clathrin box motif (GNGPDDLLG from Uniprot ID G0SBZ9), were designed and ought to be used for co-crystallization experiments. Unfortunately, the peptide from Ent1 was not soluble at concentrations required for co-crystallization experiments, probably because of the significant proportion of hydrophobic amino acids present in its sequence. Moreover, crystal trials to obtain peptide-bound structures using the Clathrin-box motif peptide were unsuccessful, yielding only the Apo- structures.

Given the lack of availability of structural information with peptide-bound structures from this species, AlphaFold2 was used to predict peptide bound models the C-terminus of Ent1 in complex with CHC NTD (Figure 5.48d). Interestingly, the prediction of AF2 places the motif sequence in the clathrin box binding site of the CHC NTD (Figure 5.48a). This prediction has a high pLDDT score for the motif sequence,

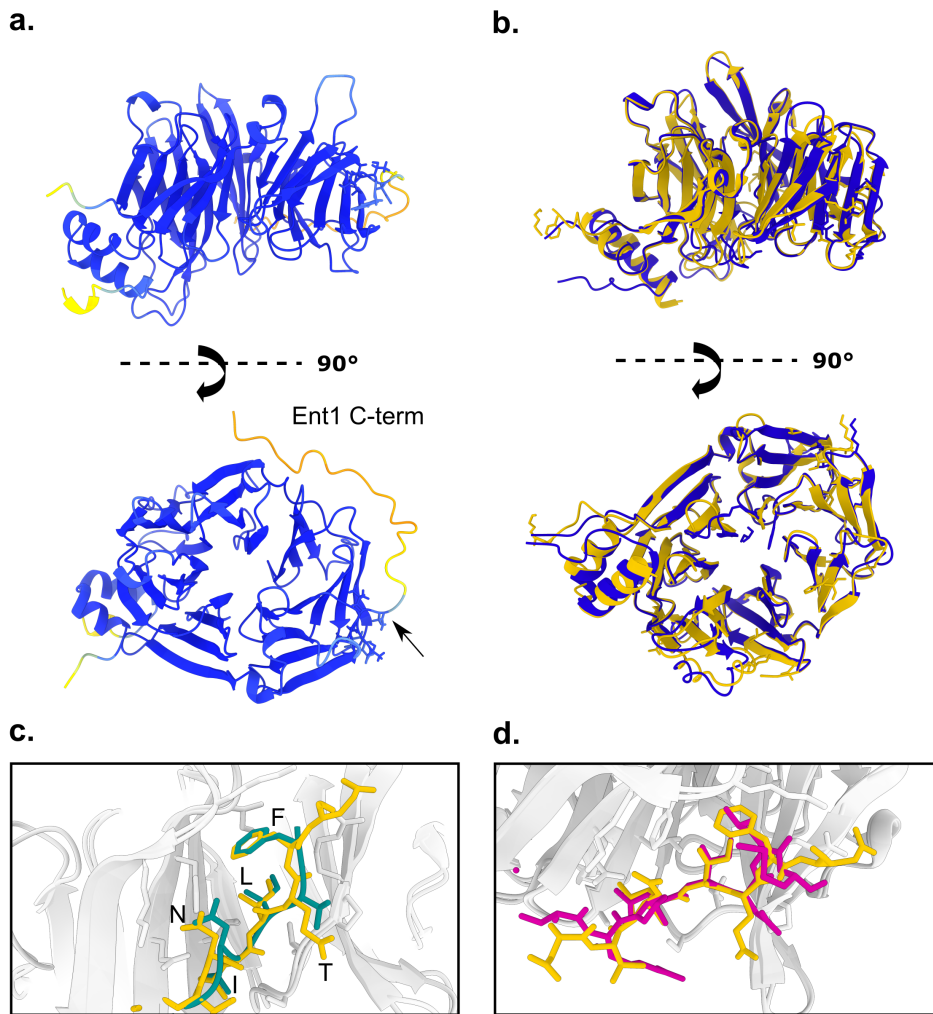


Figure 5.48: **Structures of CtCHC NTD**

a. AF2 prediction of the CHC NTD domain of *C. thermophilum* in complex with a peptide from CtEnt1 coloured according to its pLDDT score. The region of the peptide that binds to the Clathrin site has a higher score and it is indicated with an arrow. **b.** Overlay between the crystal structure of CtCHC NTD and the structure from *H. sapiens* (purple). **c.** Overlay between the AF-2 predicted peptide (orange) and the peptide from β -Arrestin (teal). The high similarity even at the side chain level between the two can be appreciated. **d.** Overlay between the peptide predicted by AF-2 (orange) and the peptide containing a "Clathrin box" SLiM (magenta).

which suggests that the location and structure assigned to this region of the peptide is reliable. This suggests that in spite of the difference in sequence, AF2 could predict the binding site of this motif to be the clathrin box. When comparing the AlphaFold prediction with other crystal structures available, the two peptides (β -Arrestin and *C. thermophilum* Ent1) share a short NLI sequence, and the overlay of both structures shows that both peptides fall with a very similar conformation into the clathrin box, including the Phe residue towards the end of the motif (Figure 5.48).

5.3.3 Binding studies of CHC NTD to adaptors

It has been reported in literature that yeast and human CHC NTDs bind more than 1 peptide per domain. AlphaFold2 predictions using two, three and four peptide sequences were performed (Figure 5.49). The confidence of the predictions (pLDDT score) drops down for the peptides as the number of peptides increases. Interestingly, in the prediction with two peptides, the second peptide falls right into the arrestin box, and the peptide has an “acceptable” score for the prediction, shown still in light blue (Figure 5.49b). On the other hand, using three and four peptides, AF2 place the peptides close to the binding site described by Willox and Royle; however, the peptides show several clashes with CHC NTD, and the score for the prediction is very low (orange). Therefore, these predictions are most likely not reliable to interpret, and no conclusions can be made about the binding of these peptides into this site. CHC NTD contains a “W-box”, which has been shown to bind peptides containing W motifs (Miele et al., 2004). None of the AlphaFold predictions showed peptides binding into the W box binding site, however, this could be due to the lack of sequence information from which this prediction algorithm nourishes. A prediction using peptide containing a sequence corresponding to the W motif (from human amphiphysin), placed the W-box motif peptide into the clathrin box instead of the W-box (Appendix Figure 10.17), suggesting that AF2 is limited in its capabilities to dissect these specific protein-protein interactions in the different boxes of CHC NTD.

Several studies have previously characterized the interaction between some SLiMs of adaptors and CHC NTD using different methods, such as ITC, NMR and Fluorescence techniques (Miele et al., 2004; Kang et al., 2009; Zhuo et al., 2015). Most of these studies address the interaction using short peptide motifs containing one of the sequences that binds to the corresponding box in the NTD of CHC. However, adaptor proteins, including epsins, contain other motifs that interact with other components of the endocytic coat, which potentially could modulate their affinity for clathrin. Since co-crystallization of the CHC NTD with a peptide containing the sequence of the C-terminus of Ent1 was not possible due to the solubility problems of the peptide, binding studies between CtCHC NTD and Ent1 full-length were performed using Microscale Thermophoresis (MST) (Figure 5.51). The results show that the binding between Ent1

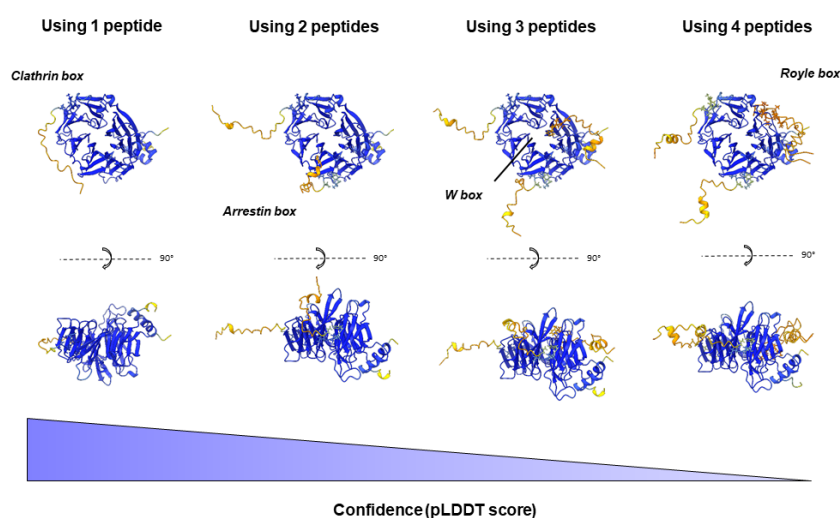


Figure 5.49: **AlphaFold2 predictions of CtCHC NTD with 1, 2, 3 and 4 CtEnt1 peptides**

and the CHC NTD has a K_D value of around $10 \mu\text{M}$. As commonly observed for MST, there was a small dependency between the dissociation constant obtained and the MST power used to stimulate the reporter dye. The K_D value, on the low micromolar range, falls into the expected affinities of protein-protein interactions present in the clathrin coat, usually of weak-affinity nature to provide with dynamics to the endocytic coat (Smith et al., 2017). Nevertheless, within the micromolar range at which these interactions have been characterized, this affinity is higher than those reported for the clathrin box, but lower than the one reported for the arrestin box. It could be that Ent1 is binding to the arrestin box in this case since the sequence for the motif is different and the CHC NTD is highly conserved. However, structural information will be needed to determine that with certainty.

To compare the results obtained with the Ent1 C-term peptide, the affinity between the peptide containing the clathrin box and CHC NTD was measured using nanoDSF and analyzed applying Isothermal Analysis (Figure 5.50). From the thermal denaturation in absence of peptide, the melting temperature of Ct CHC NTD without ligands is of $60 \text{ }^\circ\text{C}$. Upon a titration with the peptide, there is a progressive stabilization to higher temperature up to $65 \text{ }^\circ\text{C}$. Fitting of the T_m vs the concentration of CtCHC NTD yielded a K_D of $230 \mu\text{M}$. However, the limitation of this analysis is that the fraction unfolded of the sample at different temperatures is different and therefore the estimated

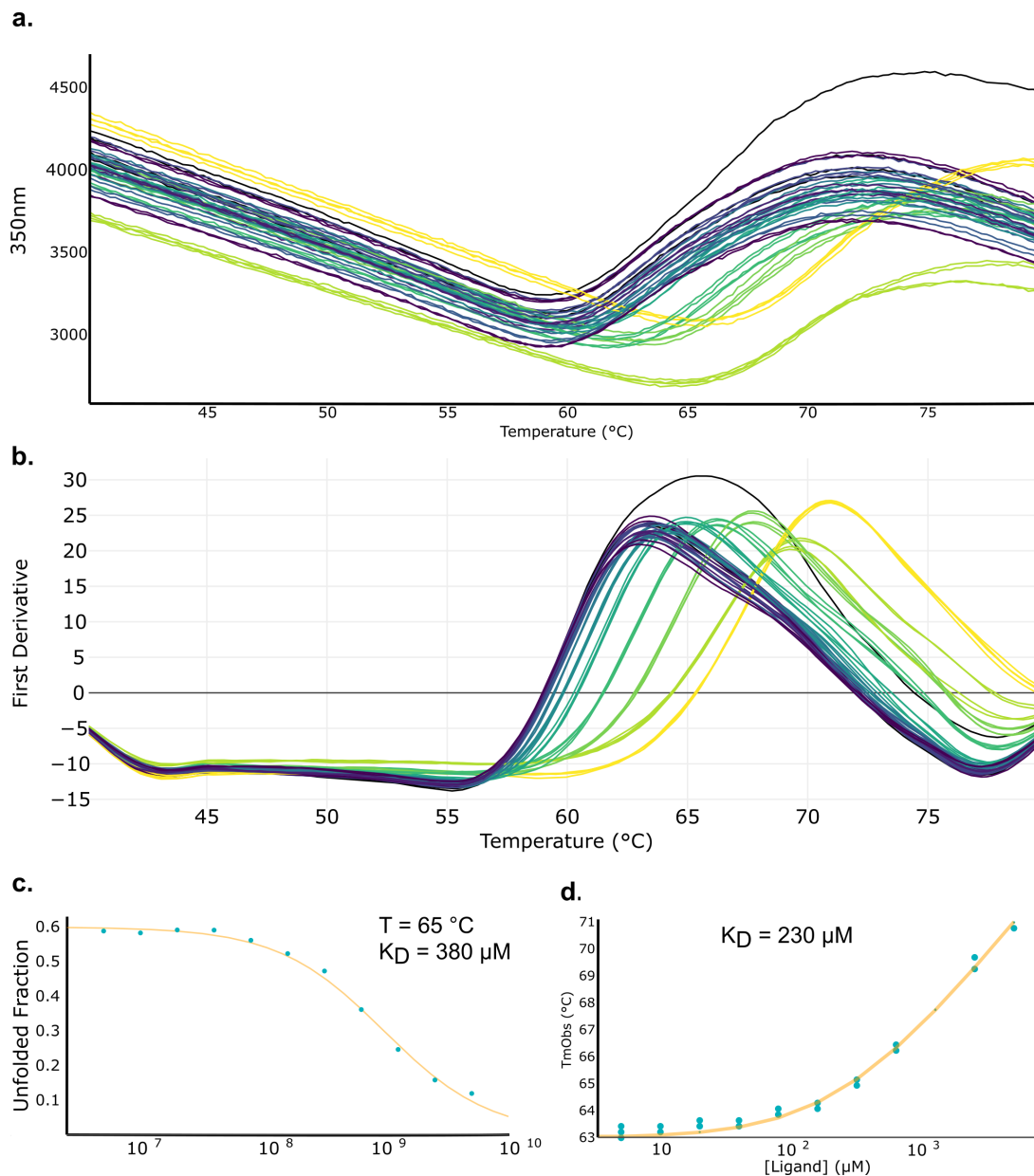


Figure 5.50: **Binding studies of clathrin-box containing peptide to CHC NTD analysed by nanoDSF**

a. nanoDSF denaturation curves followed at 350 nm with different concentrations of the peptide containing the Clathrin-box SLiM (blue to yellow, from 0 to 5 mM). **b.** First derivative of the data, it can be seen how the peptide shifts the maximum of the derivative, reporting an stabilization of around 5 °C upon binding to CtCHC NTD. **c.** Isothermal Analysis of the thermal denaturation curves. The fraction unfolded vs the peptide concentration are plotted together with the fitting used to obtain the K_D value. **d.** Fitting of the T_m to the ligand concentration.

K_D is not correct. For this reason, Isothermal Analysis was applied, and the analysis shows that the dissociation constant between CHC and this peptide has a K_D of 380 μM . This value is in line with other studies that have characterized clathrin box binding affinities. However, this K_D value needs to be interpreted carefully, since Isothermal analysis implies the calculation must be performed around the T_m of the protein, this is far from the temperatures of where other K_D s have been calculated and also of the

physiological temperature of this organism.

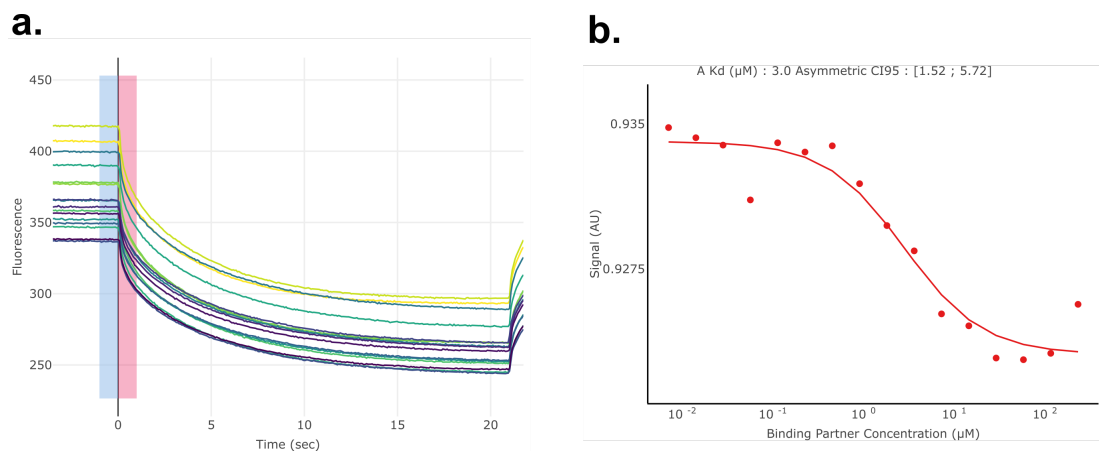


Figure 5.51: **Binding studies of CtEnt1 full length to CHC NTD analysed by MST**
a. MST traces obtained upon stimulation with high MST power. **b.** Binding curve obtained from the MST data.

Table 5.13: Crystal structures available for CHC NTD in the Protein Data Bank with different peptides

Species	Ligand	Species	Reference	PDB ID	Resolution (Å)	Motif
<i>B. taurus</i>	β 2 adaptin	<i>H. sapiens</i>	Muenzner et al 2017	5M5R	1.76	GDLL NLDLG
<i>B. taurus</i>	Amphiphysin	<i>H. sapiens</i>	Muenzner et al 2017	5M5S	1.88	ETLLD LDFDP
<i>B. taurus</i>	Amph4T1	<i>R. norvegicus</i>	Muenzner et al 2017	5M5T	1.70	ETLLDLD LDLE
<i>B. taurus</i>	Hep. D virus Large Antigen	Hepatitis delta virus genotype I (isolate Italian)	Muenzner et al 2017	5M5U	2.15	WDILFP ADP
<i>B. taurus</i>	Hep. D virus Large Antigen	Hepatitis delta virus genotype I (isolate Italian)	Muenzner et al 2017	5M5V	1.96	PPRLPLEC
<i>B. taurus</i>	Extended Amph peptide	<i>H. sapiens</i>	Muenzner et al 2017	5M61	1.84	ETLLDL DFDPFK
<i>B. taurus</i>	Amphiphysin	<i>H. sapiens</i>	Miele et al., 2005	1UTC	2.30	TLPWDL WTT
<i>R. norvegicus</i>	β 3 adaptin	<i>H. sapiens</i>	Ter Haar, 2000	1C9L	2.90	DTNLIEFE
<i>H. sapiens</i>	Pitstop	-	Bulut et al., 2011	4G55	1.69	-
<i>H. sapiens</i>	Pitstop-2	-	Bulut et al., 2011	2XZG	1.70	-
<i>H. sapiens</i>	GTSE1	<i>H. sapiens</i>	Perfetye et al., 2020	6QNN	2.03	VGQLIDL SSP and SRPL IDLML
<i>H. sapiens</i>	GTSE1	<i>H. sapiens</i>	Perfetye et al., 2020	6QNP	2.70	VGQLIDL SSP and SR- PLIDLML
<i>B. taurus</i>	B β -Arrestin-1	<i>Bos taurus</i>	Kang et al., 2009	3GC3	2.20	DTNLIEL DTNDD
<i>H. sapiens</i>	ES9	-	Djonghe et al., 2019	6E4L	1.60	-
<i>B. taurus</i>	β -arrestin	<i>Bos taurus</i>	Kang et al., 2009	3GD1	3.50	VDTNLIEL DTNDD

Table 5.14: Data collection and refinement statistics (molecular replacement) for CtCHC

Data collection	
Wavelength (Å)	0.976
Space group	P21 21 21
Cell dimensions	
a, b, c (Å)	0.41, 101.02, 154.64
$\alpha\beta\gamma$ (°)	90.00, 90.00, 90.00
Resolution (Å)	84.57 – 8.76 (1.63-1.6)
Rsym or Rmerge	0.073 (0.040-2.102)
I / I	16.0 (50.4-1.4)
Completeness (%)	99.4 (61.47-1.60)
Multiplicity	13.2 (11.2-13.5)
Refinement	
Resolution (Å)	1.60
No. reflections	1153807 (unique 87672)
Rwork / Rfree	0.197/0.222
No. atoms	11981
Protein	11981
Ligand/ion	6
Water	496
B-factors	
Protein	26
Ligand/ion	31,35,38,40
Water	37
R.m.s. deviations	
Bond lengths (Å)	0.90
Bond angles (°)	0.73

6. Discussion

Clathrin-mediated endocytosis is crucial for the internalization of several cargoes, including several transmembrane proteins considered as therapeutic targets in different diseases for their role during signaling processes, mechano-transduction and neuronal communication. Providing mechanistic understanding cellular processes at molecular resolution allows the manipulation of such processes in situations where this is of interest, particularly when such processes are involved in health and disease, such as in the case of clathrin-mediated endocytosis. The formation of the clathrin coat around the endocytic site is an energetically costly process for the cell, and as such, different check points that control the correct progression of this process have been described, for instance during cargo recruitment. All components from the endocytic coat need to be assembled properly and timely, to render the internalization of the plasma membrane for clathrin-coated pit formation. Several examples of deleterious effects of deletion of key components of the CME machinery prove this (e.g. deletion of both copies of Epsin genes in yeast is lethal (Aguilar et al., 2006)). Also, the apparent redundancy of the role that some proteins play during internalization makes the system with robust alterations of its components (Dannhauser, Ungewickell, 2012).

6.1 Sla2 and Ent1 cooperate for efficient internalization of the plasma membrane

The results presented in this work provide a mechanistic understanding of the cooperation of yeast mid-coat adaptors Sla2 and Ent1 to anchor to the plasma membrane and contribute to its internalization. The cryo-EM structure of the ANTH-ENTH-PIP₂ oligomer allows to describe the cooperative behaviour observed for mid-coat adaptors. The depiction of the ANTH-ENTH tetramer as the building block for ANTH-ENTH-PIP₂ oligomers previously detected, such as the 16-mer and 12-mer complexes (Garcia-Alai et al., 2018; Heidemann et al., 2020), unravels that these oligomers constitute higher order assemblies. The position of the lipids detected in the structure shows how

these assemblies are intrinsic in the samples prepared for the *in vitro* structural studies, since the structure reveals how the ANTH and ENTH warp around the PIP₂ micelles in solution.

The synergy between the ANTH domain of Sla2 and the ENTH domain of Ent1 allows the creation of a molecular anchor by the combination of several protein-lipid and protein-protein interactions described in this work. The combination of the cryoEM map of the 16-mer with the previously characterized PIP₂-binding sites of the individual domains allows to understand the mechanism whereby the combination of ANTH-ENTH domains achieves high affinity and specificity for PI(4,5)P₂, by multiple interactions that coordinate different lipid molecules. Several years of research have characterised a number of protein-protein and protein-lipid interactions present in the endocytic coat. Most of them appear to be weak molecular interactions which confer the dynamic nature that the coat needs throughout its progression and allow it to be finely tuned (Smith et al., 2017). The cooperative interaction of mid-coat adaptors with the plasma membrane via PIP₂ stands out from the usual spectrum of protein-protein and protein-lipid interactions that have been described for most components of the endocytic coat. Together with the specificity of the membrane binding domains by this particular type of phospholipid, the combination of all these factors creates a robust and specific membrane anchor. The mutational study presented here and carried out *in vitro* (and also *in vivo*) discerns the role of each interface to the residue level, characterizing the ANTH-ENTH system to an unprecedented level of detail.

Besides the tetramer protein-protein and protein-lipid interactions that this work allows to describe, mid-coat adaptors play a secondary essential role during CME, which is membrane remodelling. The experiments presented here where mutants defective for complex formation are also defective in their membrane remodeling activity, reinforce the idea that the tetramer constitutes the building block for this system. Nevertheless, it must be acknowledged that the correlation between complex formation defective mutants and those who were not able to deform membranes had some outliers (e.g. ANTH R25A, ENTH E107A, and the ANTH-ANTH interface mutant ANTH R3A/I4A/D37R/H38A), which were capable of membrane deformation. This suggests that disruption of perhaps weaker interactions in the ANTH-ENTH complex which do not tightly bind to the membrane are still capable of membrane deformation.

Within the ANTH-ENTH system, several of the experiments presented in this work, particularly SAXS and Native MS have highlighted the diversity of ANTH-ENTH assemblies present in samples containing PIP₂. Some dependence on the abundance of certain species was observed by Native MS and SAXS, suggesting the protein:lipid ratios govern the diversity of species possible in a certain sample. Moreover, native MS has the power to unravel different amount of lipids bound to the different assemblies (16-mer or 12-mers), which indicates that the binding sites are not fully occupied and that different lipids have different hierarchies in the binding (e.g., for each oligomeric state a minimum number of PIP₂ molecules is required to keep the ANTH-ENTH complex together). Intriguingly, the mutations measured by native MS in search for complex formation phenotypes revealed several smaller assemblies with different amounts of lipids bound. The cryoEM map of the 12-mer using the ENTH $\alpha 0$ mutant, together with the flexible fitting of the tetramer of the membrane bound ANTH/ENTH domains and with the mutational study performed demonstrates that the building block of the system is the ANTH-ENTH tetramer. These different and smaller intermediates, resulting upon mutation open the question of whether other arrangements different than the tetramer are possible or whether the species captured upon these mutations are just intermediates of tetramers towards the already known multi-tetramer species (12-mers and 16-mers). Some possible experiments to decipher that question could be performing kinetic experiments with high resolution methods, such as native MS, using these mutants to clarify whether this effect is kinetic, or to perform other time-resolved structural techniques, such as time-resolved EM, which could reveal the domain arrangement of these oligomers as it was done for the 12-mer ENTH $\alpha 0$ mutant.

Given the presence of PIP₂ in our sample preparation and that we solved the structure of the ENTH domain bound and in complex, its $\alpha 0$ helix is refolded compared to some previous crystal structures. In the whole assembly, all the $\alpha 0$ helixes inserted in between the PIP₂ polar heads assigned in the structure agree with the mechanism of membrane deformation of the ENTH domain, which consists of the insertion of this secondary structure element for the displacement of lipids in the inner layer of the plasma membrane. However, the cooperative binding of PIP₂ by just ENTH domains (Garcia-Alai et al., 2018), with their low micromolar affinity reported in literature (Itoh et al., 2001), is not sufficient for tight membrane anchoring. The concerted binding of

PIP₂ with ANTH is required to achieve high affinity for PIP₂-enriched membranes of endocytic sites (Skruzny et al., 2012, 2015). We can now describe how this is achieved by the concerted binding of ANTH and ENTH of two PIP₂ molecules at protein interfaces who create protein-protein interactions, and increasing thus the avidity of the ANTH-ENTH tetrameric complex to the membrane.

Membrane deformation by assembly of different protein machineries contributes to membrane invagination, and several theoretical models have addressed the force requirements for membrane invagination under different membrane tension conditions (Lacy et al., 2018; Day, Stachowiak, 2020). The tight attachment of the endocytic coat to the plasma membrane is particularly important for systems where membrane tension is increased, such as is the case of yeast and cells that undergo osmotic pressure changes. The force requirements of membrane invagination in yeast or in conditions where turgor pressure is increased in mammalian cells makes the role played by the cytoskeleton essential. The polymerization of actin in the endocytic sites is regulated by several factors, and the organization of the filaments and their branching points can weight differently the force produced (Akamatsu et al., 2020; Serwas et al., 2022). Mid coat adaptors are responsible for the transmission of this force from actin polymerization essential for membrane invagination, which for Sla2 has been particularly characterised at a molecular level (Abella et al., 2021). The ANTH-ENTH tight membrane anchor allows this force transmission and therefore membrane internalization.

The temporal control of endocytosis allows for optimal cargo recruitment and correct adaptor proteins and clathrin assembly for coat formation. In contrast with higher eukaryotes, in yeast membrane invagination takes place only in the last few seconds during the late stages of endocytosis. The steric pressure that the endocytic coat needs to be overcome may explain this difference, meaning that formation of an efficient membrane pulling machinery needs to take place during the initial coat formation process. The kinetic experiments performed using TR-SAXS and BLI suggest that the ANTH and ENTH domains are capable of performing fast assembly in solution and that these two domains do not require of any other endocytic components for the formation of a stable complex. According to the TR-SAXS data, the complex is able to assemble in just 100 ms in the dimensions of a tetramer. This timescale, much faster than the range of endocytic events, suggest that the assembly of the mid-coat in the plasma

membrane for membrane invagination is not the limiting step in coat formation, and that the assembly of Sla2 and Ent1 is immediately triggered once that PIP₂ is available for binding. Furthermore, the complex disassembles when one of the partner proteins is removed, as shown by the BLI experiments, revealing an equilibrium of a highly dynamic complex in solution. The PIP₂ is the lock that keeps the complex together, however, the action of phosphatases which are recruited towards the end of endocytosis which by reducing the local concentration of this lipid shift the equilibrium of the ANTH-ENTH complex towards the disassembly of this and other complex components that need to be recycled.

6.2 Full length endocytic adaptors

6.2.1 Fitting of experimental data to predicted models

With the advent of increasingly reliable prediction tools such as AlphaFold2 (AF2) (Jumper et al., 2021) and RosettaFold (Baek et al., 2021), looking into the 3D structure of a given protein sequence became easier than ever before. The structural biology community is witnessing a deeply transformative period where the opportunity arises for testing the boundaries of this recently improved tool. The availability of a large amount of structural predictions allows for new comparisons of the predicted models of the proteins of interest with experimental data from structural techniques.

SAXS is a structural technique often criticized because of its limited resolution. Nevertheless, it can be used to ascertain different types of questions relevant for protein structure. SAXS provides with the overall structural parameters of a sample at room temperature in solution, it informs about flexibility, oligomeric state, quality of the samples and whether aggregates are present at the selected experimental condition. Beyond that, it provides valious information regarding the 3D topology of the protein. For all the structures where SAXS data were collected in this work (the full adaptors Sla2 and Ent1 from *C. thermophilum*, the CLC of yeast, and the coiled-coil domain of Sla2 from *S. cerevisiae*), the comparison of the AF2 models with the experimental data CLC yields a poor fit. There are several factors that could contribute to these results.

First, the limitations of this structure prediction tools should be evaluated. The quality of the models is not always 100% accurate due to different factors, such as the

low complexity of certain regions of the sequence. Furthermore, this algorithm has been trained on the structural information available deposited in the PDB. The lack of previous similar structural models prevents proper training of these algorithms, an example which holds true for IDRs, where the conformational ensemble explored is much larger than for globular proteins. The presence of IDRs whose structure spans a wider ensemble of conformations than those sampled in the PDB often yields poor predictions (with a low pLDDT score) that are not reliable. Moreover, usually these IDRs are flexible, which in turn allows several different topologies for a protein containing such regions in solution. A poor fitting between the experimental data from a sample in solution, accountable for a mixture of all conformational states, and the static AlphaFold2 prediction is not unexpected. Ent1 fulfills these criteria for which structural prediction is not possible, highlighting the limitations of prediction algorithms. As all the member of the Epsins family, the C-terminus of Ent1 contains a large IDR, which has been subject of several studies given this region is functionally relevant containing several motifs for clathrin binding (Clathrin-box sLiM), biquitin, and other adaptors (NPF motifs), and for its contribution for CME at high tension (Zeno et al., 2021; Joseph et al., 2020).

Secondly, even when structural models can be predicted with high reliability, they represent just a snapshot of the protein, revealing just one of its conformations. In contrast, proteins suffer from dynamics, and they commonly experience conformational changes that are essential to their function, its regulation, or part of their native state. All these conformations are captured and averaged in the experimental data acquired in solution, like in SAXS. A good example of this can be found in membrane transporters, whose structure can be predicted with certain accuracy but often in one of the conformations of their transport cycle (Alamo et al., 2022). Therefore, these prediction algorithms provide of a static picture of a dynamic molecule which the bulk experimental techniques capture and the disagreement between the experimental data and the predicted model arises from these dynamics. A plausible approach to overcome this limitation when some prior information is available regarding the protein domains could be to generate several models in different conformations and use multiple models to fit the experimental data. With these considerations in view, it is clear that the flexible CLC and mid-coat adaptor datasets yield a poor fitting of the SAXS data into

the predicted models.

6.2.2 Sla2: A flexible and dynamic actin regulator

In line with the flexibility observed by SAXS, the cryoEM map determined for Ct-Sla2 also raises the issue of flexibility during 3D volume reconstruction. In the two samples that led to a trustworthy 3D reconstruction (although at low resolution), the density from the maps could only be assigned to the C-terminus of the protein (as a dimer, including the last part of the long coiled-coil domain, the 5 α -helical bundle and the THATCH domain). It is clear that the region between the N-terminal ANTH domain and the coiled coil is the most flexible and disordered of the protein, from the disordered prediction software IUPred and from the AlphaFold2 predictions. Therefore, this extremely large flexibility could prevent particle alignment and structure determination, and just the C-terminus observed could be aligned properly. Another option (as mentioned in the results) is that the protein is degraded during grid preparation by harsh interactions with the air-water interface.

It is noteworthy that samples containing ENTH and PIP₂ (in an attempt to obtain the full length adaptor complex) yield a different oligomeric state, where a trimer of dimers is solved in presence of the binding partners of Sla2. Given that the presence of these partners is the only parameter modified during sample preparation and that they are known to oligomerize with the ANTH domain of Sla2, it is tempting to speculate that the map corresponds partially to a Sla2-ENTH-PIP₂ oligomer. However, density is only present for the C-terminus of Sla2 molecules, and no information regarding the position or oligomeric state of this sample could be obtained from the cryoEM data. Nevertheless, the fitting of the AF2 model shows that the C-terminus in this oligomeric state is adopting a "closed" conformation, in where the proposed actin residues of the THATCH domain are not exposed for binding. Interestingly, AF2 brings a prediction of the C-terminus in an open conformation upon inclusion in the model of the very C-terminal latch helix. The role of regulatory helices has been debated in other actin binding proteins such as TALIN (Gingras et al., 2008), therefore raising the hypothesis of a regulatory role of this helix for Sla2 as well. A structure of Sla2 bound to actin filaments would enlighten what is the truly open and bound state of the protein.

Finally, the recent *in situ* detection of the mammalian homologue of Sla2, Hip1R,

in situ (Serwas et al., 2022) exemplifies how the combination of the strengths from structural techniques and modelling tools can open the door for the determination of *in-situ* cellular structures to understand these systems essential for several cellular functions in their native environment.

6.2.3 Sla2 and CLC binding

The communication between mid-coat adaptors and clathrin as a template for vesicle budding is essential during endocytosis. Sla2 (and Hip1R in mammals) is known to bind to Clathrin Light Chain, and previous molecular biology studies have proposed a regulatory role for CLC over Sla2 and its capability to bind to actin (Newpher, Lemon, 2006).

The interaction between CLC and Sla2, previously characterised in the mammalian system (Biancospino et al., 2019), was also studied here using SEC-SAXS and ITC. SAXS data showed that CLC behaves in solution as an extremely flexible protein, and that upon binding to Sla2 coil-coil region, its flexibility is decreased. This suggests that binding of its partners decreases the conformational space explored by CLC in solution. It could be hypothesized that the interaction between Sla2 and CLC causes partial refolding of one of the components, given the disordered regions present in CLC. There are several examples of proteins which refold upon binding to other interaction partners, and a possible way to follow this refolding would be the study of the evolution of secondary structure elements by CD or NMR techniques. The interaction between Sla2 and CLC is in the low micromolar range for both constructs used, and it is similar to the one reported for Hip1R and CLCb (Biancospino et al., 2019). The structure of the coiled-coil domain of Hip1R containing crucial residues for the binding of CLC suggests that CLC should bind to this structured region (Ybe et al., 2007). The low resolution SAXS model obtained together with the SAXS model of the Sla2 coiled-coil and CLC in solution confirms that the topology of the complex is elongated, and shows just a few contacts between the densities assigned to the two components of the complex in the yeast system as well. However, no further information can be interpolated given the limited resolution of this technique. Further experiments to determine the role of CLC binding to Sla2 will be required using structural techniques and potentially set ups where the binding to actin is regulated.

6.3 Interactions of clathrin with SLiMs accross species

The NTD of CHC is a hub for the network of protein-protein interactions that build the endocytic coat. The multiple binding sites present in the NTD of clathrin raise the question regarding the specificity of the binding to the different boxes, their redundancy and the possibility of a hierarchy of adaptors binding to clathrin.

In this work, it has been shown by X-ray crystallography and by computational methods (AlphaFold2) that the structure of the CHC NTD of the thermophilic fungi *C. thermophilum* is extremely conserved from higher eukaryotes (Haar ter et al., 2002; Miele et al., 2004), including a high degree of conservation in the different binding sites, also known as boxes. Given the platform for the binding of different adaptors to the different boxes is largely conserved, the functional regulation of the different boxes must be given by the sequences of the motifs that bind deferentially to the different boxes.

Epsin is one of the main players during membrane internalization, and remarkably, in *C. thermophilum*, the sequence for its "Clathrin box" motif is replaced by a sequence more similar to the Arrestin motif in humans. This change, however, does not prevent the protein from binding to the clathrin box, as it was during the AF2 predictions. Moreover, the binding experiments with Ent1 full length and CHC NTD showed that the affinity of the interaction is similar than the one reported for the arrestin peptides from other species. On the other hand, comparing the affinity of the peptide from *C. thermophilum* containing a "Clathrin-box" motif, yields a numerally lower K_D . However, it should be taken into account that the techniques used to measure these two systems are different: nanoDSF and MST. The second important difference is that the MST experiments were performed using full length Ent1, in contrast with the short soluble peptide used at high concentrations for nanoDSF experiments. The presence of the rest of the protein during the binding assays could modulate the affinity reported in our binding experiments, in this case towards the low micromolar range compared to a high micromolar K_D obtained by nanoDSF. The third important consideration of these values is that the dissociation constants are calculated at different temperatures, since Isothermal Analysis requieres the calculation of this value based on the fraction of protein unfolded at a temperature around the melting temperature (which in the case

of Ct CHC NTD is around 62 °C). Therefore, this value of K_D needs to be compared with the K_D obtained at standard temperature of 25 °C at which the MST experiments with the full length protein was performed.

These binding experiments confirm that both motifs, the "Clathrin box" and the Arrestin motif bind to CHC NTD in *C. thermophilum*. However, information regarding the real number of binding sites, and the actual binding site for each peptide only comes from the AF2 predictions, with the above discussed limitations. A way forward to unravel whether the binding of the two motifs aligns with the pattern observed for the motifs in higher eukaryotes would be to obtain crystal structures of clathrin in complex with peptides containing these motifs which can answer this question by direct visualization of the adaptor peptides bound to clathrin.

7. Outlook

In summary, the work presented here builds on the previous knowledge to provide the mechanism of membrane anchoring of mid-coat adaptors to the plasma membrane during CME. ANTH and ENTH domains can assemble in a fast and coordinated way into their hetero-tetrameric functional unit, stabilized by shared PIP₂ molecules. These tetramers can give rise to different assemblies depending on the lipid environment and contribute to the membrane remodelling process occurring during endocytosis. The synergy achieved by the structural properties of ENTH α 0 helices, combined with the lipid clamp of Sla2 ANTH domains makes the complex a strong membrane anchor relying on shared PIP₂ molecules in several protein interfaces. Thus, the combination of these two elements transforms the monomeric low-affinity (micromolar K_D) interaction with phospholipids (Smith et al., 2017; Ford et al., 2001, 2002) into a nanomolar interaction (Skruzny et al., 2015; Garcia-Alai et al., 2018) provided by a highly organized protein-lipid-protein complex. This multimeric membrane anchor is then essential for membrane invagination in organisms and conditions where cells where endocytosis is challenged by high membrane tension or turgor pressure.

Beyond the dimension of protein-protein interactions described in the first part of this work, the results obtained for Sla2 full-length C-terminal domain open some interesting questions for future research regarding the regulation of its activity as an actin regulator during CME. The different oligomeric states of Sla2 obtained in different conditions highlight that this adaptor is capable of larger oligomerization similarly to the ANTH oligomerization together with ENTH domains. However, with the current data available for full-length Sla2, the dependance of PIP₂ and of ENTH interactions this oligomerization is only speculative at this stage, since these components were not resolved in the cryoEM maps.

Furthermore, the differences observed between structural predictions of the full length protein and the experimental data rise questions regarding the role of the last C-terminal α -helix of Sla2 (the latch) and of the 5- α -helical bundle in the regulation for actin binding of this adaptor. In order to study the role of these different domains

present in Sla2 C-terminus, different Sla2 constructs (Figure) have been produced, and future biophysical studies will be performed in order to assess the effect of these different Sla2 domains in actin binding, and propose a detailed molecular model of the regulation of the binding of Sla2 to actin by these structural components and by clathrin.

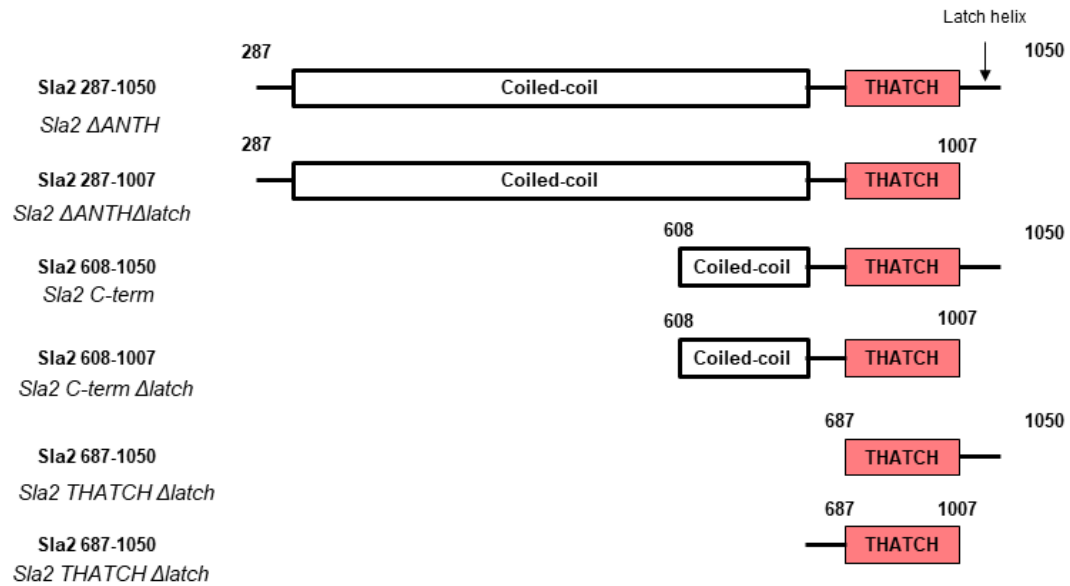


Figure 7.1: Sla2 constructs that will be used for biophysical binding studies to actin.

8. Materials and Methods

8.1 Materials

8.1.1 Chemicals used in this work

Table 8.1: Chemicals used in this work

Name	Supplier	Catalogue Number
1,4-dithiothreitol (DTT), >99%	Roth	3483-12-3
Agarose SERVA for DNA electrophoresis	Serva	11404.07
Albumin, from Bovine Serum (BSA)	Sigma-Aldrich	A7906
Chloramphenicol	Roth	3886,3
Chloroform, >= 99.8% for analysis	Sigma-Aldrich	288306
Complete EDTA-free protease inhibitor	Roche	04 693 132 001
D(+) Sucrose	Roth	4621.1
EDTA Tetrasodi- umsalt 86-88%	Roth	3619.1
Ethanol >=99,8%	Roth	9065,3
Ethidium Bromide	Roth	HP471
HEPES, Pufferan >99,5%, p.a.	Roth	7365-45-9
Hydrochloric acid 32%	Roth	X896.1
Imidazole, >99%, p.a	Roth	X998.4
Isopropyl- β -d- thiogalactopyranoside (IPTG)	Roth	2316.4
Kanamycin sulfate	Roth	T832.4
LB Agar (Lennox)	Roth	X965.1
LB Broth Low Salt Granulated	Melford	GL1703
LDS Sample Buffer (4x), NuPAGE	Novex	NP0008
Magnesium chloride hexahydrate, >99%, ACS	Roth	2189.1
Nickel(II)chloride hexahydrate	Roth	4489.2
Pentane	Merck	60089
Potassium chloride, >99,5%, p.a., ACS, ISO	Roth	6781.1
SDS Pellets	Roth	CN 30.3
Sekusept Plus	Ecolab	104372E

Table 8.2: Chemicals used in this work- continued

Name	Supplier	Catalogue Number
Sodium chloride, >99,5%, p.a., ACS, ISO	Roth	3957.2
Sodium hydroxide, pellets, >99%, p.a., ISO	Roth	6771
TB powder	Melford	T1510-1000.0
TRIS hydrochloride, Pufferan, >99%, p.a.	Roth	9090.3
Tris(2-carboxyethyl)phosphine hy- drochloride (TCEP)	Soltec Bio Science	M115
TRIS, Pufferan, >99,9%, Ultra Qualitaet	Roth	5429.3

8.1.2 Lipids used in this work

Table 8.3: Lipids used in this work

Lipid name	Cat.	Supplier
di-C ₈ -PI(4,5)P ₂	P-4508	Echelon
DOPC (18:1 (Δ_9 -Cis) PC)	850375	Avanti Polar lipids
DOPS (18:1 PS)	840035	Avanti Polar lipids
PIP2 (08:0 PI(4,5)P ₂)	85185 840046	Avanti Polar lipids
14:0 Liss Rhod PE	810517	Avanti Polar lipids

8.1.3 Molecular Biology Reagents

Table 8.4: Molecular Biology Reagents used in this work

Reagent	Provider and Cat.
Monarch miniprep kit	New England Biolabs
Nucleospin gel and PCR clean up kit	Machinery Nagel
Cutsmart buffer	New England Biolabs

8.1.4 Enzymes used in this work

8.1.5 Enzymes used in this work

Enzyme	Provider and Cat.
AgeI-HF	R3552S
DpnI	R0176S
Nco-I HF	R3193S
HindIII-HF	R3104S
BamHI-HF	R3136S
T4 DNA Ligase (and T4 DNA Ligase Buffer 10x)	M0202S
XhoI	R0146S
2X Green Phu-Sso7d mix	
40 mM Tris pH 8.8	
4 mM MgCl ₂	
120 mM KCl	
20 mM (NH ₄) ₂ SO ₄	
0.02 mM EDTA	EMBL
0.2 % TritonX-100	Heidelberg
8 % Glycerol	
0,005 % Xylene Cyanol FF	
0,05 % Orange G	
0,4 mM dNTPs	
0,04 U/μL Phu-Sso7d Polymerase	

8.1.6 Consumables used in this work

Table 8.5: Consumables used in this work

Name	Supplier	Catalogue Number
Gene Ruler 1 kb DNA ladder	ThermoFisher	SM0311
Instant Blue (coomassie based staining solution)	Expedeon ISB	
Loading Dye Purple NuPAGE™ 4 to 12%, Bis-Tris, 1.0–1.5 mm, Mini Protein Gels	New England Biolabs	B7024S
PageRuler™ Un- stained Protein Ladder	ThermoFisher Scientific	NP0323PK2
PageRuler™ Plus Prestained Protein Ladder, 10 to 250 kDa	ThermoFisher Scientific	26614
Mix & Go! E. coli Transformation kit	Zymo research	26619
Ni-NTA agarose beads	Invitrogen	T3001
PC Membranes 0.2µm	Avanti® Polar Lipids	R901-15
PC Membranes 0.1µm	Avanti® Polar Lipids	610006
Extruder Set Without Holder/Heating Block	Avanti® Polar Lipids	610005
Filter supports	Avanti® Polar Lipids	610023
Novex NuPAGE LDS Sample Buffer	ThermoFisher	610014
Prometheus NT.48		NP0008
Standard grade nan- oDSF capillaries	Nanotemper	PK002
Spectra/Por 6 Dialysis Tubing 2 kD 38mm 33ft	Repligen	132625
15 u-Slide 2 well co-culture	Ibidi	210810/7

Table 8.6: Consumables used in this work - continued

Name	Supplier	Catalogue Number
Filter Papers	Whatman	1001-090
Amicon Ultra -15 10K Centridu- gal Filter Devices	Merck	UFC901024
Amicon [®] Ultra-15 Centrifugal Filter Unit – 10 kDa cut-off	Merck	UFC801024
Amicon [®] Ultra-15 Centrifugal Filters – 30 kDa cut off	Merck	UFC903024
Amicon [®] Ultra-4 Centrifugal Filter Unit	Merck	UFC800324
Amicon [®] Ultra-0.5 Centrifugal Filter Unit	Merck	UFC500396
Zeba [™] Spin Desalt- ing Columns, 7K MWCO, 0.5 mL	ThermoFisher	89883
Greiner CELLSTAR [®] 96 well plates flat bottom clear wells	Sigma-Aldrich	M0812-100EA
BugBuster Protein extraction reagents	Merck	70584-M
Sealing film PARAFILM [®]	Roth	CNP8.1
Syringe filter, Filtropur S, PES, pore size: 0.45 μm , for clear filtration	Starsted	83.1826

8.1.7 Equipment used in this work

Table 8.7: Equipment used in this work

Name	Supplier
AnalytikJena UVP Chemstudio	AnalytikJena
Agilent 1260 with autosampler and fraction collector	Agilent
ÄKTA Pure with F9C fraction collector	Cytivia
Analytical scale	Sartorius
Avanti JXB-26 Centrifuge	Beckmann Coulter
Centrifuge 5424 R	Eppendorf
Centrifuge 5810 R	Eppendorf
Electrophoresis chamber for SDS gels	Invitrogen
EmulsiFlex-C3 homogenizer	Aventin
Freezer -20 °C	Liebherr
Freezer -80 °C	Eppendorf
Fridge 4 °C	Liebherr
Fume hood	Waldner
JLA 25.50 rotor for Avanti JXB-26 centrifuge	Beckmann Coulter
JLA 8.100 rotor for Avanti JXB-26 centrifuge	Beckmann Coulter
Microwave	Severin
MilliQ machine	Millipore
nanodrop 2000c	Thermoscientific
Magnetic stirr plate	Roth
Nanotemper Prometheus NT.48	Nanotemper
New Brunswick™ Innova® 42 Incubator Shaker	Eppendorf
New Brunswick™ Innova® 44 Incubator Shaker	Eppendorf
Octet RED96 System	Molecular Devices
PCR Master cycler	Eppendorf
pH meter	Toledo
Power Supply	Consort
Rock imager	Formulatrix
Rotating wheel	Stuart
Scales	Sartorius

8.1.8 Cell strains used in this work

Table 8.8: Equipment used in this work - continued

Name	Supplier
Superdex [®] 200 HiLoad 16/600 pg	Cytivia
Superdex [®] 200 Increase 10/300	Cytivia
Superose 6 Increase 10/300	Cytivia
Superose 6 Increase 3.2/300	Cytivia
Scorpion Screen Builder ARI-arts	Robbins Instruments
Glass bottles	Schott Duran [®]
Heating waterbath	VWR
MiniSpin [®] centrifuge	Eppendorf
MiniStar Microcentrifuge	VWR
Vortex	Scientific Industries
Shaking platform Edward	Bühler GmbH
Sonicator waterbath	Elmasonic
Cell culture Erlenmeyer flasks	Schott Duran [®]
1 L (1000 mL) Polypropylene Bot- tle Assembly for JLA-8.1000 rotor	Beckman Coulter C31597
50 mL, Polypropylene Bot- tle with Cap Assembly, 29 x 104mm for JA 25.50 rotor	Beckman Coulter 361694

Table 8.9: Cell strains used in this work

Strain	Description	Application	Antibiotic Resistance	Source
DH5 α	F- ϕ 80dlacZ Δ M15 Δ (lacZYA-argF) U169 recA1 endA1 tonA hsdR17 (rK-, mK+) phoA supE44 λ -thi-1 gyrA96 relA1	T1 Phage- resistant, general purpose cloning, plasmid propagation		Life Technologies
BL21(DE3)	deficient in lon and ompT proteases	general purpose expression host		EMBL Hamburg
C41(DE3)	deficient in lon and ompT proteases; ATPase mutant	Enhances the expression of membrane proteins		EMBL Hamburg
BL21 pLysS GOLD	deficient in lon and ompT proteases, pLysS plasmid	high- stringency expression host	Cam	Novagen

8.1.9 Media used in this work

LB medium

- 10 g/L tryptone
- 5 g/L yeast extract
- 5 g/L NaCl

TB medium

- 12 g/L tryptone
- 24 g/L yeast extract
- 9.4 g/L K₂HPO₄
- 2.2 g/L KH₂PO₄
- 8 mL/L glycerol

LB-Agar

- 15 g/L agar
- 10 g/L tryptone
- 5 g/L yeast extract
- 5 g/L NaCl

8.1.10 Buffers used in this work

Buffer A Nickel

- 20 mM Tris pH 7.5
- 500 mM NaCl
- 12.5 mM Imidazol

Buffer B Nickel

- 20 mM Tris pH 7.5
- 500 mM NaCl
- 250 mM Imidazol

Dialysis Buffer

- 20 mM Tris pH 7.5
- 200 mM NaCl
- 1 mM DTT

SEC Buffer

- 20 mM Tris pH 7.5

- 250 mM NaCl
- 0.5 mM TECP
- 20 mM Tris, pH 8.0 • 250 mM NaCl • 0.5 mM TECP ITC Buffer
 - 20 mM Tris pH 7.5
 - 150 mM NaCl
 - 2.5% glycerol

Sla2 Buffer

- 100 mM NaPO₄
- 150 mM NaCl
- 100 mM NaPO₄ • 150 mM NaCl CD Buffer
 - 10 mM NaP, pH 8.0
 - 50 mM KCl

Liposome Buffer

- 20 mM HEPES pH 7.5
- 100 mM KCl

GUVS buffer

- 200 mM Sucrose

CtCHC NTD Buffer

- 20 mM Tris pH 7.5
- 150 mM NaCl
- 2.5% glycerol

PEPTIDE BUFFER

- 20 mM Tris pH 9
- 150 mM NaCl
- 0.5 mM TCEP

8.1.11 Computational resources used in this work

- Inkscape 0.92.4 (5da689c313, 2019-01-14) <https://www.inkscape.org>
- Microsoft Word <https://www.microsoft.com/en-ww/microsoft-365/word>
- Overleaf <https://www.overleaf.com/project>
- BioRender <https://biorender.com/>
- ChimeraX version 1.4.dev202201060033 (2022-01-06)
- Pymol (version 2.2.2, <https://pymol.org/2/>)

- BioIcons <https://bioicons.com/>
- R RStudio 2022.02.3 Build 492
- Uniprot database <https://www.uniprot.org/>
- ProtParam (Expasy, <https://web.expasy.org/protparam/>)
- Clustal Omega <https://www.ebi.ac.uk/Tools/msa/clustalo/>
- RELION (versions 3.1 and 4.0)
- cryoSPARC (version v3.3.2)
- AlphaFold2 (Jumper et al., 2021)
- CollabFold https://colab.research.google.com/github/sokrypton/ColabFold/blob/main/batch/AlphaFold2_batch.ipynb

8.2 Methods

8.2.1 Molecular biology

8.2.1.1 PCR and site directed mutagenesis

Polymerase Chain Reaction (PCR) is a molecular biology technique used to amplify a fragment of DNA with a specific sequence. In short, two sets of single stranded DNA fragments with a specific sequence at the edges of the target sequence, called primers, are designed (Table 8.10) and used in a sequential reaction. The reaction mixture consists of dNTPs (10 mM), 0.5 μ M of each primer, 1 ng of template DNA (containing the sequence to be amplified) and 1 Unit of Phusion DNA polymerase/50 μ L of PCR reaction. This reaction mixture was prepared either following the manufacturer guidelines for the Phusion[®] DNA polymerase and dNTPs (New England Biolabs) or by using a stock of 2x Green Phu-Sso7d mix prepared by the EMBL Protein Production Core Facility (Heidelberg, Germany, Table 8.1.5 for details) to which the primers and template DNA were added at the desired final concentrations.

The reaction consists of the following steps: an initial DNA denaturation (1 minute at 98 °C); a short second DNA denaturation (30 seconds at at 98 °C), in which the two strands of the DNA are denatured; an annealing step of the primers, where the primers hybridize with their target sequence in the template DNA (30 seconds at 62 °C); and elongation, where the polymerase synthesizes the complementary chain to the template DNA (at 72 °C, time adjusted depending on the length of the sequence to be amplified, calculated at a synthesis rate of 30 s/kb). These last three steps were repeated for 25-30 cycles. A final elongation step is included in the reaction (10 minutes at 72 °C) before storing the PCR product at 4 °C before further use.

8.2.1.2 Site-directed mutagenesis (Quickchange)

For the insertion of point mutations into recombinant plasmids, primers containing the mutated sequence with flanking regions were designed (Table 8.11). Then, a plasmid containing the inserted gene of interest was used as template and the whole plasmid was amplified by PCR using a long elongation time of X minutes. The template vector, which does not contain the desired mutation, is then digested using DpnI, a restriction

Table 8.10: Primers used to generate different constructs

Primer name	Primer	sequence
Sequencing primer Sla2	Gtagacggccttgcacacggc	
Forward Yeast CLC	CCCCATGGGGATGAGCGAAAAATTCC	
Reverse Yeast CLC	CCGGATCCTTATTACGCGCCCG	
Yeast Ent1 FL Fwd	GGCCATGGGGATGTCGAAACAATTTGTTAGATCTGC	
Yeast Ent1 FL Rev	GGGGATCCTCATCAATCTAAATCAATTAGAGTATATCCCC	
Sla2 cc217 fwd	GACCcatggccGGTGACGCTGCTCTGCAGCCCTTGAAAG	
Sla2 cc287 fwd	GACCcatggccCCGGCACGGACTCCAACACCAACACCACC	
Sla2 cc328 fwd	GACCcatggccGACCAGGCTTTATTGCAGCAATATGAC	
Sla2 cc rev HindIII	GGCAAGCTTTTATCAGTCAACACGTAAGTGTTT	
Sla2 GFP	CTGAATCTATTCTGGACATgccACCGGTCTGTTGCTGGAAC	
Ent1-GFP	cgcagatctaacaattgtttcgacatgccaccggtctgttgcggaacacgtc	
CtSla2-GFP	cgcagatgtccaggctacgggtggtcgccatgccaccggtctgttgcggaac	
CtSla2-GFP rev	GAGCCTAGGAATAATGAGGAGAACCATCG	
GFP rev	gccgatccccctcctcttgtagctgattttacgc	

enzyme that digest the methylated DNA used as template for the PCR reaction (Fisher, Pei, 1997). Finally, the PCR product was transformed into chemically competent *E. coli* DH5 α cells.

8.2.1.3 Plasmid Transformation

Recombinant plasmids containing sequences of interest were transformed into *E. coli* cells using the following protocol. Chemically competent cells were prepared using the commercial kit “Mix Go! *E. coli* Transformation” kit (Zymo research, CAT T3001). 50 ng of DNA were incubated with 50 μ L of chemically competent cells on ice. After the incubation time, a heat shock was performed for 30 seconds on a hot bath at 42 $^{\circ}$ C, and immediately after cells were allowed to recover for 2 minutes on ice. Then, 900 μ L of LB medium was added to the cells and they were incubated at 37 $^{\circ}$ C shaking speed of 180 r.p.m. for 1 hour. Finally, cells were plated into an LB-Agar plate supplemented with the antibiotic present in the newly transformed plasmid to allow selection of correctly transformed cells.

8.2.2 Protein Production

All proteins were produced in *E. coli* under the IPTG inducible system. An overnight liquid pre-culture was cultured over night by picking a colony from an LB-Agar plate and putting it into liquid LB medium supplemented with the corresponding antibiotic. Briefly, *E. coli* liquid cultures were grown in 2L flasks using 800-1000 mL of

Table 8.11: Primers used to generate ANTH and ENTH mutants

Primer name	Primer sequence
ENTH F52 53A	GAAAAGCTACGACAGCGCAGACgcgGAGATCATGGAC ATGCTGGAC
ENTH F52 53A rc	GTCCAGCATGTCCATGATCTCgcccGTCTGCGCTGTC GTAGCTTTTC
ENTH E54A D57 60A	CTACGACAGCGCAGACTTCTTTGcGATCATGGcgATGC TGGcgAAACGCCTGAACGACAAAGGC
ENTH E54A D57 60A rc	GCCTTTGTCGTTTCAGGCGTTTcgCCAGCATcgCCATG ATCgCAAAGAAGTCTGCGCTGTCGTAG
ENTH E97A N98A	GAAAACGTGTGTACTGTGGTGCCGTGcGgCGTGTA CATCATCAAACCCTG
ENTH E97A N98A rc	CAGGGTTTTGATGATGTACAGcgcCgCACGGCACC ACAGTACACAGTTTTTC
ENTH Y100R	GTACTGTGGTGCCGTGAGAACCTGcgtATCAT CAAACCCTGAAAGAG
ENTH Y100R rc	CTCTTTTCAGGGTTTTGATGATagCAGGTTCT CACGGCACACAGTAC
ENTH F5A L12A V13A	ccatggGATCCATGTCTAAACAGgcgGTGCGTTCCGCGAAA AACgcGGcGAAAGGTTATTCCTCTACCCAGGTAC
ENTH F5A L12A V13A rc	GTACCTGGGTAGAGGAATAACCTTTcGcCGcGTTTTTCGCG GAACGCACcgcCTGTTTAGACATGGATCccatgg
ANTH M1A	cagggcgccatggGATCCgcgAGCCGTATCGATTCTGAC CTGCAG
ANTH M1A rc	CTGCAGGTCAGAATCGATACGGCTcgcGGATCccatg ggcctg
ANTH S6A K10A	catggGATCCATGAGCCGTATCGATgCgGACCTGCAGgcg GCGCTCAAAAAAGCCTGTTCCGTTG
ANTH S6A K10A rc	CAACGGAACAGGCTTTTTTTGAGCGCcgCCTGCAGGT CcGcATCGATACGGCTCATGGATCccatg
ANTH Q9A K10A	CCATGAGCCGTATCGATTCTGACCTGgcgccCGCTCAA AAAAGCCTGTTCCGTTGAGG
ANTH Q9A K10A rc	CCTCAACGGAACAGGCTTTTTTTGAGCGCggccgcCA GGTCAGAATCGATACGGCTCATGG
ANTH K13D	GATTCTGACCTGCAGAAAGCGCTCgatAAAGCCTGTTCC GTTGAGGAAACCG
ANTH K13D rc	CGGTTTCCTCAACGGAACAGGCTTTatcGAGCGCT TTCTGCAGGTCAGAATC
ANTH A15D	CCTGCAGAAAGCGCTCAAAAAgatTGTTCGGTTGAGGA AACCGCAC
ANTH A15D rc	GTGCGGTTTCCTCAACGGAACAatcTTTTTTGAGC GCTTTCTGCAGG
ANTH R3A I4A	ctttatcttcagggcgccatggGATCCATGAGCgcg ccGATTCTGACCTGCAGAAAGCGCTC
ANTH R3A I4A rc	GAGCGCTTTCTGCAGGTCAGAATCggccgcGCT CATGGATCccatggcgccctgaaaataaag
ANTH D37R	GTGCATGCATTGTGTACACCTGGcgtCACCAGTCTAGCAAA GCTGTCTTC
ANTH D37R rc	GAAGACAGCTTTGCTAGACTGGTGacgCCAGGTGTAC ACAATGCATGCAC

liquid media inoculated with 10 mL of the over-night pre-culture at 37 °C shaking at 220 r.p.m. until the OD₆₀₀ reached values between 0.8 and 1. Induction was performed with the addition of IPTG at different temperatures for different times depending on

Table 8.12: Primers used to generate ANTH and ENTH mutants - continued

Primer name	Primer sequence
ANTH dY247L248	GTTTTACGCGGATTGCTCCTCTGTGAAAACCAC GCTGGTTACCATTCCAAAACCTGC
ANTH dY247L248 rc	GCAGTTTTGGAATGGTAACCAGCGTGGTTTTCA CAGAGGAGCAATCCGCGTAAAAC
ANTH K10 13 14A	GCCGTATCGATTCTGACCTGCAGgccGCGCTCg ccgCGCCTGTTCCGTTGAGGAAACCCGCACCG
ANTH K10 13 14A rc	CGGTGCGGTTTTCTCAACGGAACAGGCcg cggc- GAGGCGcggcCTGCAGGTCAGAATCGATACGGC
ANTH K10 13 14D	GCCGTATCGATTCTGACCTGCAGgacGCGCTCgat gacGCCTGTTCCGTTGAGGAAACCCGCACCG
ANTH K10 13 14D rc	CGGTGCGGTTTTCTCAACGGAACAGGCgt catc- GAGGCGgtcCTGCAGGTCAGAATCGATACGGC
ENTH _Q 20A	CCTGGTGAAAGGTTATTCTCTACCgcgGTACTGGTTTCGTA ACGCAACCTCTAAC
ENTH Q20A rc	GTTAGAGGTTGCGTTACGAACCAGTACcgcGGTAGAG GAATAACCTTTCACCAGG
ENTH E97A	CGAAAACCTGTGTACTGTGGTGCCGTGcGAACCTGTAC ATCATCAAACCCCTGAAAGAG
ENTH E97A rc	CTCTTTCAGGGTTTTGATGATGTACAGGTTTCgC ACGGCACACAGTACACAGTTTTTCG
ENTH N98A	GCTCCGAAAACCTGTGTACTGTGGTGCCGTGAGgcgCT GTACATCATCAAACCCCTGAAAG
ENTH N98A rc	CTTTCAGGGTTTTGATGATGTACAGcgcCTCAC GGCACACAGTACACAGTTTTTC GGAGC
ANTH D37R H38A	GCATGCATTGTGTACACCTGGcgtgcCCA GTCTAGCAAAGCTGTCTTCAC
ANTH D37R H38A rc	GTGAAGACAGCTTTGCTAGACTGGgcaag CCAGGTGTACACAATGCATGC
ANTH K10D K13D	CTGACCTGCAGgacGCGCTCgatAAAGCC TGTTCGTTGAGGAAACCG
ANTH _K 10D _K 13D _{r,c}	CGGTTTTCTCAACGGAACAGGCTTTatcG AGCGCgtcCTGCAGGTCAG
ANTH _K 14D	CTGACCTGCAGAAAGCGCTCAAAgacGCCTGTTCCGT TGAGGAAACCCG
ANTH K14D rc	GCGGTTTTCTCAACGGAACAGGCgtcTTTGAGC GCTTCTGCAGGTCAG
ANTH _R 3A	cagggcgccatggGATCCATGAGCgcgATCGATTCTG ACCTGCAGAAAGC
ANTH R3A rc	GCTTCTGCAGGTCAGAATCGATcgcGCTCAT GGATCccatggcgccctg
ANTH R177E R178E	CTTTGCGTCTATTCAGTCCGAAgaagaa AACACTGAGTGCAAATCTCTGC CC
ANTH R177E R178E rc	GGCAGAGATTTTGCACCTCAGTGT TttcttcTTCGGACTGAATAGAC GCAAAG
ANTH S100A	CTGGGTGCGTGTACACTCTGGCGGTgcgAGCTA TAGCAAACCTGATCCGCG
ANTH S100A rc	CGCGGATCAGTTTGCTATAGCTcgcACCGCCA GAGTGACACGACCCAG
ANTH E57R	GAAAACCTCTGCCGCTGGCAAACGACcgtGTGCAGCT GTTCAAATGCTGATC
ANTH E57R rc	GATCAGCATTTTGAACAGCTGCACacgGTCGT TTGCCAGCGGCAGAGTTTTTC

the construct expressed (Table 8.13). After induction, cells were harvested by centrifugation using the JL-8.100 rotor and the Avanti JXN-86 centrifuge at 4000 x g for 30 minutes at 4 °C. Cell pellets were stored at -20 °C or used immediately after production for subsequent protein purification.

Table 8.13: Expression conditions of different proteins

Construct	Expression strain	[IPTG] (mM)	Time (h)	Temperature (°C)
ANTH	<i>E. coli</i> <i>BL21(DE3)</i>	0.2	4	37
ENTH	<i>E. coli</i> <i>BL21(DE3)</i>	0.2	4	37
CtEnt1	<i>E. coli</i> <i>BL21(DE3)</i>	1	16	12
CtSla2	<i>E. coli</i> <i>C41</i>	0.5	16	18
Sla2 coil coil 432-767	<i>E. coli</i> <i>BL21</i> <i>pLysS GOLD</i>	0.2	16	20
Sla2 coil coil 296-767	<i>E. coli</i> <i>BL21</i> <i>pLysS GOLD</i>	0.2	16	20
CLC	<i>E. coli</i> <i>BL21(DE3)</i>	0.2	16	20

8.2.3 Protein Purification

Cell pellets were re-suspended in Lysis buffer (20 mM Tris pH 7.5, 200 mM NaCl, 0.05% Tween-20, 0.5 mM MgCl₂, 1.4 mM TCEP) supplemented with 400 U DNase I and complete EDTA-free protease inhibitor cocktail (Roche) using a ratio of 3 mL of Lysis buffer per gram of cell pellet. Cells were disrupted using the Emulsiflex(EmulsiFlex-C3 (Aventin)) at a pressure of 15000 psi three times. The cell lysate was cleared by centrifugation at 17000 r.p.m. for 45 minutes at 4 °C using the JA 25-50 rotor in the Avanti JXN-86 centrifuge. The supernatant was then filtered using 0.45 µm filters (Starsted, cat 83.1826) and proteins purified by IMAC using Ni-NTA Agarose beads (Invitrogen, Cat R90110), 2 mL of beads packed in a column and equilibrated with Buffer A (20 mM Tris pH 7.5, 500 mM NaCl, 12.5 mM Imidazole). After loading the supernatant, the column was washed 50 ml Buffer A. The protein was then eluted with 9 ml of Buffer B (20 mM Tris pH 7.5, 500 mM NaCl, 250 mM Imidazol) in 1 mL fractions. Fractions 2-9 were pooled together into a dialysis membrane (SpectraPor) and dialysed against 4L of Dialysis buffer (20 mM Tris pH 7.5, 200 mM NaCl, 1 mM DTT) at 4 °C dialyzing in presence of 1 aliquot of TEV at 1 mg/ml over-night. The next

day, the dialysis was loaded into the Ni-NTA and the flow-through (FT) containing the cleaved protein was collected. Then, the Ni-NTA beads were washed with approximately the same volume of Buffer A and the flow-through was collected as the “Wash” fraction. The FT and the Wash were concentrated to a volume of around 1 ml using 10 KDa cut off Amicon[®] Ultra-15 centrifugal filter units (Merk). The concentrated samples were then injected into a Size Exclusion Chromatography column (e.g. HiLoad 16/600 Superdex 200 column) equilibrated in SEC Buffer (50 mM Tris pH 8, 150 mM NaCl, 1 mM DTT) using an AEKTA Pure (Cytivia). Fractions corresponding to the elution peaks were analysed by SDS-PAGE and pulled together and concentrated using concentrators of the appropriate cut-off for each protein. Proteins were aliquoted in 50-200 μ L aliquots and flash frozen with liquid Nitrogen and stored at -80 °C.

8.2.4 Protein Characterization

8.2.4.1 nano Differential scanning fluorimetry (nanoDSF)

nano-Differential Scanning Fluorimetry (nanoDSF) follows the intrinsic fluorescence of Tryptophan (Trp) residues upon thermal denaturation. The fluorescence of Trp residues changes depending on the environment (Teale, Weber, 1957), with the maximum on the emission spectra from Tryptophan residues shifting from 330 nm to 350 nm depending on the hydrophobicity of its environment, which upon thermal denaturation yields a transition from which the melting temperature (T_m) of a sample can be calculated. The main advantage of this technique against conventional Thermofluor is the lack of external dyes for detection of melting temperatures. On the other hand, if there are no Trp residues or if they are already exposed to the solvent, there will be no observable transition. Therefore, the quality of the signal is protein-dependent. In cases where the fluorescence signal might be unclear, the static scattering signal can also be followed, as a proxy for the aggregation of sample. Following this signal, one can obtain the Temperature of aggregation (T_{agg}).

For nanoDSF experiments, proteins were diluted to a concentration that gave the recommended number of counts between 2000-20000 (usually around 30 μ M). Measurements were performed using a Prometheus NT.48 (NanoTemper Technologies, München, Germany) controlled by PR.ThermControl (version 2.1.2). 10 μ L of sam-

ple were loaded into the nanoDSF Grade High Sensitivity Capillaries (Nanotemper) and the samples were warmed up from 20 to 95 °C at a speed of 1 °C/minute and the change in fluorescence at 330 and 350 nm was followed along with the static scattering over time. For each sample, 3 capillaries were used. The T_m of each sample was calculated using the MoltenProt module from the publicly available server from the Sample Preparation and Characterization Facility at EMBL Hamburg: <https://spc.embl-hamburg.de/app/moltenprot> (Burastero et al., 2021). For cases where samples were compared, the difference between T_m is reported as ΔT_m .

The scattering signal recorded (back-scattering mode) was used as a stability reporter for the AENTH samples, where the mid aggregation point, T_{agg} , corresponds to the inflexion points in the scattering curves of the first transitions observed upon heating (T_{agg} = mid-aggregation temperature obtained from scattering curves). ΔT_{agg} was calculated in the same way as done for ΔT_m : $\Delta T_{agg} = T_{agg} \text{ mutant} - T_{agg} \text{ wild-type}$.

8.2.4.2 Circular Dichroism

Circular Dichroism (CD) is a non-destructive spectroscopic technique based on the differential interaction of chiral chromophores with left and right circularly polarized light. Given the chirality of the peptide bond, CD spectra in the far UV region (180-240 nm) can inform about the secondary structure content of proteins (Kelly, Price, 2000). By comparison with samples of known secondary structure, it is possible to deconvolute the proportion of alpha-helical, beta-sheet or random coil within a sample. For CD measurements, samples were buffer exchanged by dialysis into CD Buffer (10 mM NaP buffer pH 8 and 150 mM KCl) using the dialysis method with a membrane of 3 kDa cut off in order to reduce the signal at lower wavelengths coming from the buffer. CD measurements were acquired using a Chiarascan VX (Applied Photophysics Ltd, United Kingdom) and Quartz cuvettes of 0.5 mm optic pass. The equipment was purged prior to measurements with Nitrogen as indicated by the manufacturer. Spectra for air and for buffer were recorded for subtraction of the background signal. 250 μ L of sample at a suitable concentration (usually between 0.5-1.5 mg/ml) was used for each measurement. The most suitable concentration was determined by looking at the photomultiplier counts and a concentration with an Absorbance below 2 at all wavelengths was selected.

CD spectra were deconvoluted to obtain the proportions of secondary structure for each spectra using CAPITO (Wiedemann et al., 2013).

8.2.4.3 Dynamic Light Scattering

Dynamic Light Scattering (DLS) is a common quality control technique that is used to check for the presence of large macromolecular aggregates into the samples. The technique is based on the scattering of molecules in solution, which is measured at an angle (usually 90°) during very short intervals of times. The scattering signal is recorded over time. From these signal, an auto-correlation function is generated with the following formula:

$$g^2(q; t) = \frac{\langle I(t)I(t + t) \rangle}{\langle I(t)^2 \rangle}$$

where $g^2(q; \tau)$ is the autocorrelation function at a particular wave vector, q , and delay time, τ , and I is the intensity.

As the difference in scattering depends on the diffusion speed of the particle in solution, the correlation times are related to the size of the particles. The relationship between the size of a particle and their diffusion speed is given by the Stokes-Einstein equation:

$$R_h = \frac{kT}{6p\eta D}$$

where R_h is the hydrodynamic radius, D is the translational diffusion coefficient, k is Boltzmann's constant, T is temperature in K, and η is the solvent viscosity.

For this work, measurements were performed using a DynaPro Nanostar device (Wyatt Technology Corporation) and data processed with Dynamics v.7 software. Proteins were used at a final concentration of 30 μ M. Samples in presence of PIP₂ were incubated overnight at 4 °C. After incubation, samples were centrifuged at 13200 x g for 10 minutes at 4 °C prior to measurements using 4 μ L plastic cuvettes (Wyatt Technology Corporation). Measurements were performed using 10 μ L of sample and the final curve was obtained using the average of 30 acquisitions over 5 s. If aggregates were present after centrifugation, samples were filtered using Durapore[®] 0.22 μ m Membrane

Filters from (Millipore®)

The standard way of analyzing the autocorrelation function obtained from the sample is employing the so-called method of cumulants (Koppel, 1972) and the DynaPro Nanostar device provides with results from fitting the data with the cumulants method and a smoothed distribution.

8.2.4.4 Mass Photometry

Mass Photometry is a single molecule technique that allows the detection of molecules upon their landing onto a glass surface. This interferometric scattering microscopy method measures the size molecules by detecting the contrast generated by the particle upon landing to microscope cover slide (Cole et al., 2017; Young et al., 2018). It is possible to measure the molecular weight of the sample of interest by correlating the contrast with a known standard with greater accuracy than other techniques such as DLS, as this technique is shape-independent.

Mass Photometry measurements were acquired on a commercial Refeyn OneMP mass photometer using the programs controlled with the software Acquire MP v2.5.0 (Refeyn Ltd.). For measurements, 1 μ M stock solutions of the protein/complexes were prepared using the measurement buffer and the device was focused automatically using 18 μ L of buffer. Then, 2 μ L of buffer were added and mixed and the measurement was recorded for 1 minute. The masses were calculated from a calibration curve using the Native Protein marker (NativeMarker Unstained Protein Standard, Invitrogen, LC0725). Dilutions were adjusted when the number of counts was higher than the one recommended by the manufacturer. The data was then analysed using the Discover MP v2.5.0 software.

8.2.5 Binding Assays

8.2.5.1 Biolayer interferometry

Bio-Layer Interferometry (BLI) is a biophysical technique that allows to measure binding kinetics between two molecules. Briefly, one of the interaction partners (usually referred as the ligand and the analyte) is immobilized in a sensor (e.g. by binding of Ni-NTA sensors to a His-tagged protein). After this loading step, the sensor is intro-

duced in a well containing the partner protein and the association of the two molecules is recoded over time, as a change in thickness from the sensor surface upon interaction with light due to the change of the interference patterns (Abdiche et al., 2008). BLI measurements were performed using an Octet RED96 instrument and Ni-NTA biosensors (ForteBio). Protein solutions were centrifuged for 10 minutes at 10,000 rpm at 4 °C before the experiment to remove possible aggregates. Protein concentrations of these stock solutions were determined after centrifugation by the absorbance at 280 nm with a NanoDrop1000. Prior to the experiment, the biosensors were equilibrated in buffer I (50 mM Tris, pH 8; 125 mM NaCl and 0.05% BSA) for 10 minutes. Binding between His-tagged ANTH and ENTH from *Chaetomium thermophilum* was measured in the presence of 170 n-Dodecyl- β -D-Maltoside (DDM) and 50 PIP₂ in buffer I (buffer II). Prior attempts to use PIP₂ (225 without DDM) resulted in unspecific binding of ENTH to the biosensor. The experiments were performed at 25°C with a shaking speed of 1000 rpm. An evaporation cover was used throughout the experiment.

Kinetic assays were performed in black, flat-bottom polypropylene 96 well plates (Greiner bio-one, item no. 655201) using 200 μ l in each well. The kinetic assay consisted of 4 steps: 300 s equilibration in buffer I (baseline I), 300 s loading (3.75 μ M His-tagged ANTH in buffer I), 300 s equilibration in buffer II (baseline II), 600 s ENTH association (0.25 μ M ENTH in buffer II), 1200 s dissociation in buffer II. To test for unspecific binding, a kinetic assay without loading His-tagged ANTH was used as control.

Data were visualized and analyzed with self-written Python scripts using the Python packages Numpy, Matplotlib and Scipy (Hunter, 2007; Oliphant, 2010; Walt van der et al., 2011; Virtanen et al., 2020). Association and dissociation were fit with a bi-exponential function yielding a pair of two k_{obs} and k_{diss} , each.

8.2.5.2 Isothermal titration Calorimetry (ITC)

Isothermal Titration Calorimetry (ITC) measures the difference in heat over time upon titration of one of the components into the sample cell compared to the reference cell. The power necessary to keep the heat constant in both cells is recorded over time and the signal is integrated in order to obtain a binding curve that informs about the K_D and the thermodynamic parameters of the interactions (Wiseman et al., 1989).

ITC was employed to measure protein-protein interactions between Sla2 Δ THATCH

or Sla2 435-767 and CLC. ITC experiments were performed at 25 °C using an MicroCal PEAQ-ITC (Malvern) controlled by MicroCal PEAQ-ITC Control Software 1.1.0.1262. A sample of CLC at 300 uM was titrated into a cell containing a sample of Sla2 at 30 uM in the sample ITC Buffer. As run of Buffer into Buffer and CLC into Buffer were performed as controls to discard effects coming from the dilution of CLC or the buffer contributing to the signal. Fittings were performed using MicroCal PEAQ-ITC Analysis Software 1.1.0.1262 number and NITPIC v 1.2.7 (Scheuermann, Brautigam, 2015).

8.2.5.3 Microscale thermophoresis

Microscale thermophoresis was used to study the binding between CHC NTD and Ent1. Briefly, a titration of CHC NTD was performed into labelled Ent1. MST curves were acquired with a Nanotemper Monolith NT.LabelFree (Nanotemper) using the MO.Control v1.6 acquisition software and Monolith NT.LabelFree capillaries. 16 different CtCHC MTD concentrations (serial dilution with a factor of 2) in the range between 5 mM and 0.15 μ M were used for each measurement. For the MST experiment the IR laser power was set to 20% and the UV laser power to 1%. In total, two independent measurements were done plus an additional repeat.

The regions for F_{norm} determination were 1–0 s for “cold” and 1-2 s for “hot”. For each curve F_{norm} was calculated as the ratio between the mean values in the “hot” and “cold” region. In the final step, F_{norm} was fitted to a 1:1 binding model using the ThermoAffinity software available at eSPC (Burastero et al., 2021).

8.2.6 Small Angle X-ray Scattering

Small angle X-ray scattering (SAXS) is a structural technique that provides information about biomolecules in solution. SAXS can help to understand the flexibility and the compactness of the molecule in study, as well as their overall structural parameters (to a limited resolution) of the sample size and shape in solution. SAXS is based in the momentum transfer of the samples in solution, defined by the following equation:

$$s=4\pi \sin(\vartheta)/\lambda$$

In order to obtain enough contrast, the solvent (buffer) must be subtracted as it accounts for a large proportion of the scattering signal. For this reason, the buffer must

be perfectly matched to the one in which the sample is in.

8.2.6.1 SAXS batch measurements

The SAXS data presented in this work were collected using the P12 beamline (EMBL P12, PETRA III, DESY, Germany) (Blanchet et al., 2015) with a PILATUS 6M pixel detector (DECTRIS, Switzerland) (20×0.1 s frames). For batch measurements, typically a dilution series of the protein, protein complex, or protein-lipid complex was prepared using the buffer from the last purification step of the proteins in order to avoid buffer miss matched. In case when this was not available, proteins were dialysed over-night into fresh buffer and the dialysis buffer was used for the dilution series and as the sample buffer. Samples were flown through a capillary and data acquired at 20 °C. The sample-to- detector distance was 3.0 m, covering a range of momentum transfer $0.01 \leq s \leq 0.72 \text{ \AA}^{-1}$ ($s = 4\pi \sin\theta/\lambda$). In most cases, data Frame comparison showed no detectable radiation damage.

Data from the detector were normalized, averaged, buffer subtracted, and placed on an absolute scale that is relative to water, according to standard procedures using the automatic pipeline implemented in P12. All data manipulations were performed using PRIMUSqt and the ATSAS software package (Blanchet et al., 2015; Petoukhov et al., 2012). The forward scattering $I(0)$ and radius of gyration, R_g were determined from Guinier analysis: $I(s) = I(0)\exp(-(sR_g)^2/3)$. The indirect Fourier transform method was applied using the program GNOM (Svergun, 1992) to obtain the distance distribution function $p(r)$ and the maximum particle dimensions D_{max} . From the distance distribution function, low-resolution ab-initio 3D models were generated using DAMMIF (Franke, Svergun, 2009).

8.2.6.2 SEC-SAXS

When the samples studied using SAXS correspond to not homogeneous samples such as protein complexes, SEC-SAXS experiments were performed. Samples were concentrated to between 5 and 10 mg/ml and 50 μ L injected the size exclusion chromatography column previously equilibrated in the same buffer. For SEC-SAXS data analysis, CHROMIX (Panjkovich, Svergun, 2018) was used to select the regions corresponding to the sample and to the buffer. Once the curve for each peak was selected,

the curves were processed using the same tools than the batch ones.

8.2.6.3 Stopped-flow time-resolved SAXS (SF-TR-SAXS) data collection and analysis

A stopped flow mixer (SFM 400, Bio-logic, Seyssinet-Pariset, France) equipped with a quartz capillary (0.8 mm inner diameter) was used as the sample delivery system at the SAXS beamline P12 (EMBL, PETRA III, DESY, Germany)(Josts et al., 2020). The device was used to rapidly mix equimolar ratios of ANTH and ENTH domains at 2 mg/ml both in the presence of 200 μ M PIP₂ with a dead time of 5 milliseconds (ms).

SAXS curves were recorded with an EIGER X 4M detector at a distance of 3 m from the sample position using different time delays (0 ms, 400 ms, 800 ms, 1200 ms). These curves were collected in series spanning 600 ms and with a 200 ms overlap between each series. Each series contained spectra at 60 time points (10 ms spacing).

All SAXS curves were solvent subtracted (buffer and PIP₂ lipid) and used in the q -range between 0.01 and 2.9 nm⁻¹ for further analysis. SVD of the buffer-subtracted SAXS curves was performed to obtain the number of components that contribute to the data using self-written Python code containing the modules Numpy, Scipy and Scikit-learn (done in cooperation with Stephan Niebling). To minimize the possible impact of beam-induced radiation damage, the 10 first frames (timepoints) of each round were selected for further analysis. SVD using just 10 frames showed that the data could be described by two main components, whose contribution decreased and increased over time (monomers and complex formation, Figure 10.10).

DAMMIX (Konarev, Svergun, 2018) was used to study the evolution from monomers to 16-mers an equilibrium in the TR-SF-SAXS data accounting for a possible intermediate and to obtain the ab initio model of the intermediate component.

8.2.7 Mass Spectrometry

8.2.7.1 MALDI-ToF

Matrix-Assisted Laser Desorption/Ionization (MALDI) was performed using purified proteins to confirm their identity by accurate identification of their molecular weight. The samples were detected with a Time of Flight (ToF) detector.

Briefly, a stock solution of protein at 4 μM was prepared in water, and mixed with the Maxtrix and 0.1% TFA using a 1:1:1 ratio. Then, between 0.5-1 μL were spotted onto the metal plate and dried on air for 30 minutes before laser ionization. The molecular weight of the samples was calculated from a reference calibration using Protein Standards (PSII).

8.2.7.2 Native Mass Spectrometry

Native Mass Spectrometry (NMS) allows the study of intact non-covalent protein and protein-lipid complexes. Briefly, molecules are ionized into the gas phase and their intact molecular masses can be detected extremely accurately with the remaining tertiary and quaternary properties, which allows to obtain information regarding oligomeric assemblies such as number of ligands bound and sub-units arrangement within the complex.

For electrospray ionization (ESI) of the samples used in this work, borosilicate nano-electrospray capillaries (Thermo Scientific) were prepared in-house using a P-97 micropipette puller (Sutter Instrument Co.), and coated with palladium/gold in a Polaron SC7620 sputter coater (Quorum Technologies). Native mass spectrometry measurements were done using an Orbitrap Q Exactive Plus UHMR (Thermo Scientific) operated in positive ion mode. Proteins were buffer-exchanged using one or two consecutive Zeba spin desalting columns (Thermo Scientific) into 300 mM ammonium acetate, 1 mM DTT, pH 8. 1 mg di- C_8 -PI(4,5) P_2 (as a sodium salt) dissolved in water was added to a mixture of ANTH and ENTH proteins (1:1 molar ratio) to form the complex at a final concentration of 10 μM monomeric proteins and 60 or 200 μM PIP2. Instrument settings were 1.5-1.6 kV capillary voltage, -150 V in source trapping, HCD was off and the AGC target set to 3×10^6 with a maximum inject time of 300 ms. The trapping gas pressure (ratio) was 8, the mass range was 2000 – 20000 m/z and the resolution set to 6,250. Raw data were processed and analyzed using UniDec (Marty et al., 2015).

8.2.8 Cryogenic Electron Microscopy

8.2.8.1 Negative Staining

Negative staining EM was performed using previously described EM protocols. Samples were diluted in SEC buffer at a concentration of around 100 µg/ml. For samples containing PIP₂, the dilution was performed in buffer containing PIP₂. Then, 3 µL of sample were applied to a glow-discharged, carbon coated copper grid. Grids were prepared in-house and glow discharged for 30 s in a Pelco easiGlow™ (Ted Pella) at 0.39 mbar and 12 mA. The sample was incubated on the grid for 30 s, then blotted and the grid was washed with ddH₂O three times and stained with 2% uranyl acetate twice for 60 s each. Excess stain was blotted off and the grid was dried. Grids were imaged using a Talos 120 kV or a Technai F20 microscope equipped with a Ceta (CMOS CCD) camera (FEI/Thermo Scientific).

8.2.8.2 Single Particle Analysis cryoEM

8.2.8.3 Grid preparation

ANTH and ENTH at a concentration of 100 µM were pre-incubated in 200 µM PIP₂ in buffer containing 20mM Tris pH 8.0, 250 mM NaCl and 1 mM DTT for 3 h at room temperature. Then, the solutions were mixed 1:1 to generate the AENTH complex and left on ice for at least 1 h. For cryo-EM grid preparation, Quantifoil 300 mesh Cu R 1.2/1.3 holey carbon grids were glow-discharged in a Cressington 208 carbon coater at 10 mA and 0.1 mbar air pressure for 30 s. The complex was diluted to 10 µM ANTH/ENTH (monomer) in buffer containing 200 µM PIP₂ and 3 µL was then applied to the grid and vitrified using a Vitrobot™ mark IV (FEI/Thermo Scientific) with a blot force of 6 and a blot time of 6 s. The relative humidity (RH) was 90% and temperature 5-6 °C. Liquid ethane was used as the cryogen.

8.2.8.4 Data processing

8.2.8.5 ANTH-ENTH complex

Cryo-EM data were collected on a Titan Krios (FEI/Thermo Scientific) at the Astbury Biostructure Laboratory using a Falcon III direct electron detector operating

in integrating mode. The main data acquisition parameters for the wildtype dataset (A_8E_8) are listed in Table 5.5. Processing of the A_8E_8 data was done by David Klebl using RELION 3 (Zivanov et al., 2018) and cryoSPARC v2: Micrographs were corrected for beam-induced motion using MotionCor2 (Zheng et al., 2017) and the contrast transfer function (CTF) was estimated using Gctf (Zhang et al., 2016), in RELION. Particles were picked initially using the general model in crYOLO (Wagner et al., 2019) to generate 2D classes and a 3D reconstruction in RELION. The model was then trained to pick A_8E_8 particles. Using the trained model, 195,536 particles were picked from 7990 micrographs. A subset of these was used to generate an initial model and all particles were subjected to 3D classification to remove ‘bad’ particles. 96,664 particles were taken forward to refinement in C1 and D2 symmetry. Bayesian polishing (Zivanov et al., 2019) and beamtilt estimation were applied and a 2D classification step was performed on the polished particles to give a final selection of 79,414 particles, leading to a resolution of 4.1 Å (D2 symmetry). Non-uniform refinement in cryoSPARC v2 (Punjani et al., 2020) was used to further improve the resolution to 3.9 Å and the final reconstruction was sharpened with a B-factor of 200.

8.2.8.6 Model building of the ANTH-ENTH-PIP₂ complex

Model building of the ANTH-ENTH-PIP₂ was done by David Klebl. Sla2 ANTH domain crystal structure from *Chaetomium thermophilum* (PDB: 5007) and the crystal structure of the ENTH domain from *S. cerevisiae* (PDB: 5ONF) were used as initial models for rigid-body docking into the cryo-EM map of the A_8E_8 complex using Chimera and manually adjusted in Coot (Emsley et al., 2010). The A_2E_2 tetramer, which was the asymmetric unit was then iteratively refined in Coot and ISOLDE (Croll, 2018). In total, 20 PIP₂ ligands were identified and placed in the model in Coot. Ligand coordinates and restraints were generated, symmetry applied and validation performed using tools in PHENIX 1.17 (Liebschner et al., 2019). For comparison with the previously published structure of ANTH-ENTH on lipid tubules, the atomic model for the A_2E_2 tetramer was docked into a subvolume of the EMD-2896 map and then flexibly fitted using adaptive distance restraints in ISOLDE. Cryo-EM maps and atomic models were visualized using ChimeraX.

8.2.8.7 Sla2 C-terminus

Cryo-EM movies were collected at the cryoEM Core Facility in CSSB Hamburg a Titan Krios (Thermo Fisher Scientific) equipped with a K3 camera and BioQuantum energy filter (Gatan) set to 15 eV using EPU (Thermo Fisher Scientific) at a nominal magnification of $\times 105,000$ and a physical pixel size of 0.85 Å, with a 70- μm C2 aperture at a dose rate of 15 e/pixel per second. A total dose of 65 e/Å² was collected with 3 s exposure as movies of 48 frames. Micrographs were corrected for beam-induced motion using Relion's own Implementation of MotionCor2. Contrast transfer function parameters were calculated using CTFFIND4 (Rohou, Grigorieff, 2015). Data was processed using RELION 4.0 . 942 particles were picked manually and used to train Topaz, in RELION. Then, particles were picked using a trained model and were subjected to multiple rounds of 2D classification in RELION. After removal of duplicates and particle selection, 35171 particles were selected and used for an ab-initio 3D reconstruction. Then, particles were used for a Refinement job type in Non-uniform refinement in cryoSPARC v3.3.2 was used to further improve the resolution to 5.96 Å and the final reconstruction was sharpened with a B-factor of 523. The processing pipeline is indicated in Figure 8.1.

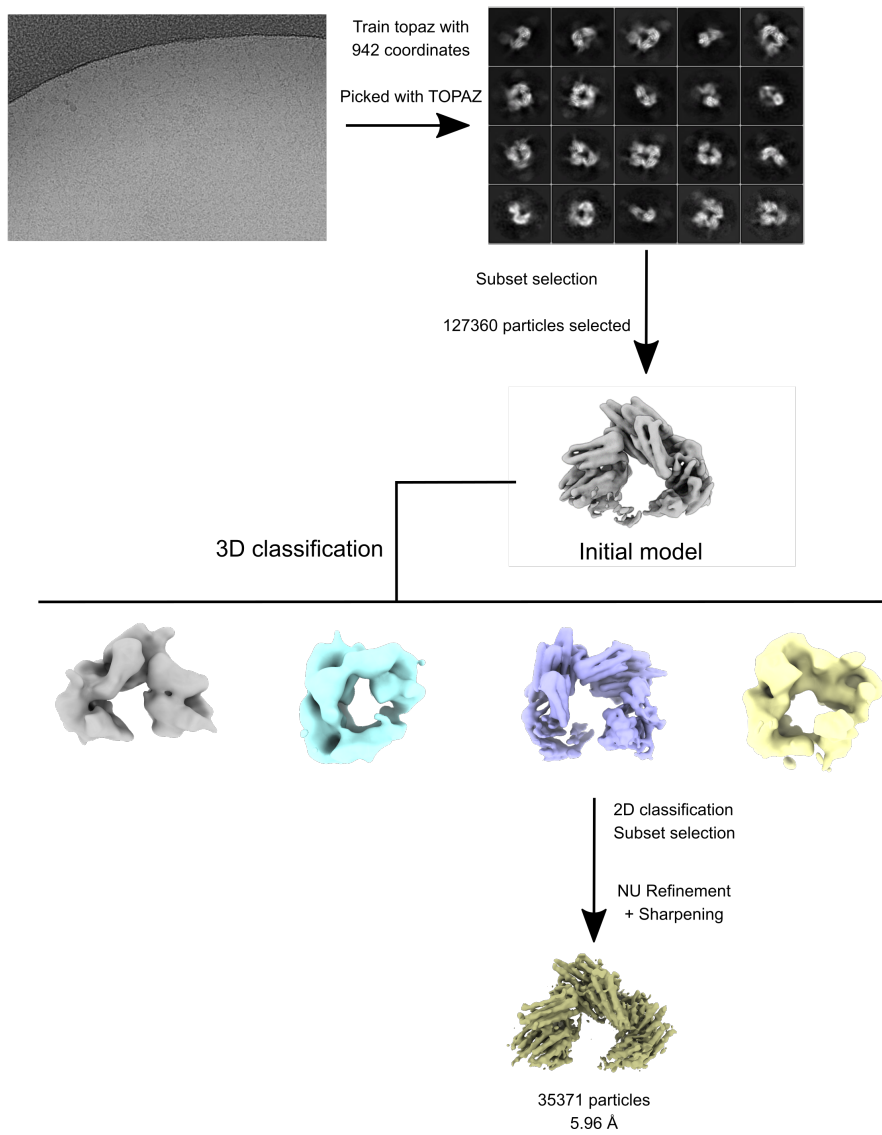


Figure 8.1: Processing pipeline for the structure of the C-terminus of Sla2

8.2.9 X-ray crystallography

For crystal trials, CtCHC NTD was concentrated to 10 mg/mL. Before setting up crystallization plates, protein samples were centrifuged (13,000 xg, 30 min, 4 °C) to remove any aggregates. Crystallization plates were set-up using a Mosquito-LCP robot (STP Labtech) dispensing three ratios of protein-to-reservoir of 200:100 nL, 150:150 nL and 100:200 nL into an Swisssci-96plate (Molecular Dimensions). Plates were incubated at 19 °C, while being imaged by a RockImager system (Formulatrix).

The structure of *C. thermophilum* CHC NTD was solved by molecular replacement using MOLREP, with a search model of the predicted structure by AlphaFold2. The structure was refined with REFMAC and manually rebuilt with Coot, and the statistics are reported in Table 5.14. The stereochemistry was checked with Molprobity, indicating good overall geometry with only 0.4% of the residues in disallowed regions of the Ramachandran plot. Structure diagrams were prepared with ChimeraX (Goddard et al., 2018).

8.2.10 Membrane deformation assays

8.2.10.1 LUVs preparation

Large unilamellar vesicles (LUVs) were prepared by extrusion. Lipids (76 mol% DOPC, 16 mol% DOPS, 8 mol% porcine brain PI(4,5)P2) were mixed in 2:1 Chloroform/Methanol to give a total lipid weight of 1.8 mg. The solvent was evaporated under a stream of nitrogen gas and the lipid film dried in vacuum. Lipids were resuspended in 183 μ L buffer (20mM Tris pH 8.0, 250 mM NaCl and 1 mM DTT) to give a total lipid concentration of 10 mg/mL. After 5 freeze/thaw cycles, the suspension was passed through a 100 nm polycarbonate membrane 21 times in an extruder (Avanti Mini-Extruder).

To form AENTH tubules, ANTH, ENTH and PIP₂-containing LUVs were mixed at final concentrations of 2 μ M ANTH, 2 μ M ENTH and 0.1 mg/mL lipids in 20mM Tris pH 8.0, 250 mM NaCl and 1 mM DTT. The mixture was incubated at room temperature for 90 s.

The samples were observed by negative staining as described in the negative staining section.

8.2.10.2 GUVs preparation

GUVs were prepared following the classical electroformation protocol (Vollmer et al., 2015). Briefly, the lipid mixture (76 mol% DOPC, 16 mol% DOPS, 8 mol% 08:0 PI(4,5)P₂) dissolved in chloroform at concentration 1.25 mg/ml was mixed with 0.1% of 14:0 Liss Rhod PE and spread over two Pt nets and dried for 1 hour in vacuum. Then, a sucrose solution with the same osmolarity as the experimental buffer was added and a voltage of 220 V at an alternating frequency of 10 Hz was applied to the Pt nets using electrodes for 2 hours. Later, the frequency was lowered to 2 Hz for 30 minutes. GUVs were allowed to settle for 30 minutes and observed using a Leica SP8 confocal microscope equipped with a white light laser and a 63 x NA 1.4 oil immersion objective.

8.2.10.3 Fluorescence Microscopy

To study the membrane deformation effects of ANTH and ENTH domains, both proteins were added at a final concentration of 1 μ M to GUVs, with either ANTH or ENTH tagged with GFP. Z-stacks were acquired for each sample and three independent experiments from 3 different GUV preparations were performed.

9. References

- Abdiche Yasmina, Malashock Dan, Pinkerton Alanna, Pons Jaume.* Determining kinetics and affinities of protein interactions using a parallel real-time label-free biosensor, the Octet // Analytical Biochemistry. 2008. 377, 2. 209–217.
- Abella Marc, Andruck Lynell, Malengo Gabriele, Skruzny Michal.* Actin-generated force applied during endocytosis measured by Sla2-based FRET tension sensors // Developmental Cell. 2021. 56, 17. 2419–2426.e4.
- Aguilar Rubén C., Longhi Silvia A., Shaw Jonathan D., Yeh Lan Yu, Kim Sean, Schön Arne, Freire Ernesto, Hsu Ariel, McCormick William K., Watson Hadiya A., Wendland Beverly.* Epsin N-terminal homology domains perform an essential function regulating Cdc42 through binding Cdc42 GTPase-activating proteins // Proceedings of the National Academy of Sciences of the United States of America. 2006. 103, 11. 4116–4121.
- Akamatsu Matthew, Vasan Ritvik, Serwas Daniel, Ferrin Michael, Rangamani Padmini, Drubin David G.* Principles of self-organization and load adaptation by the actin cytoskeleton during clathrin-mediated endocytosis // eLife. 2020. 9. 1–58.
- Alamo Diego, Sala Davide, Mchaourab Hassane S, Meiler Jens.* Sampling alternative conformational states of transporters and receptors with AlphaFold2 // eLife. 2022. 11, e75751. 1–12.
- Amlacher Stefan, Sarges Phillip, Flemming Dirk, Noort Vera Van, Kunze Ruth, Devos Damien P, Arumugam Manimozhiyan, Bork Peer, Hurt Ed.* Insight into Structure and Assembly of the Nuclear Pore Complex by Utilizing the Genome of a Eukaryotic Thermophile // Cell. 2011. 146, 2. 277–289.
- Avinoam Ori, Schorb Martin, Beese Carsten J., Briggs John A.G., Kaksonen Marko.* Endocytic sites mature by continuous bending and remodeling of the clathrin coat // Science. 2015. 348, 6241. 1369–1372.
- Baek Minkyung, DiMaio Frank, Anishchenko Ivan, Dauparas Justas, Ovchinnikov Sergey, Lee Gyu Rie, Wang Jue, Cong Qian, Kinch Lisa N., Dustin Schaeffer R., Millán Claudia, Park Hahnbeom, Adams Carson, Glassman Caleb R., DeGiovanni Andy, Pereira Jose H., Rodrigues Andria V., Van Dijk Alberdina A., Ebrecht Ana C., Opperman Diederik J., Sagmeister Theo, Buhlheller Christoph, Pavkov-Keller Tea, Rathinaswamy Manoj K., Dalwadi Udit,*

- Yip Calvin K., Burke John E., Christopher Garcia K., Grishin Nick V., Adams Paul D., Read Randy J., Baker David.* Accurate prediction of protein structures and interactions using a three-track neural network // *Science*. 2021. 373, 6557. 871–876.
- Baskin Jeremy M., Wu Xudong, Christiano Romain, Oh Michael S., Schauder Curtis M., Gazerro Elisabetta, Messa Mirko, Baldassari Simona, Assereto Stefania, Biancheri Roberta, Zara Federico, Minetti Carlo, Raimondi Andrea, Simons Mikael, Walther Tobias C., Reinisch Karin M., De Camilli Pietro.* The leukodystrophy protein FAM126A (hyccin) regulates PtdIns(4)P synthesis at the plasma membrane // *Nature Cell Biology*. 2016. 18, 1. 132–138.
- Biancospino Matteo, Buel Gwen R., Niño Carlos A., Maspero Elena, Perrotolo Rossella Scottodi, Raimondi Andrea, Redlingshöfer Lisa, Weber Janine, Brodsky Frances M., Walters Kylie J., Polo Simona.* Clathrin light chain A drives selective myosin VI recruitment to clathrin-coated pits under membrane tension // *Nature Communications*. 2019. 10, 1.
- Blanchet Clement E., Spilotros Alessandro, Schwemmer Frank, Graewert Melissa A., Kikhney Alexey, Jeffries Cy M., Franke Daniel, Mark Daniel, Zengerle Roland, Cipriani Florent, Fiedler Stefan, Roessle Manfred, Svergun Dmitri I.* Versatile sample environments and automation for biological solution X-ray scattering experiments at the P12 beamline (PETRA III, DESY) // *Journal of Applied Crystallography*. 2015. 48. 431–443.
- Boettner Douglas R, Friesen Helena, Andrews Brenda, Lemmon Sandra K.* Clathrin light chain directs endocytosis by influencing the binding of the yeast Hip1R homologue, Sla2, to F-actin // *Molecular Biology of the Cell*. 2011. 22, 19. 3699–3714.
- Brach Thorsten, Godlee Camilla, Moeller-Hansen Iben, Boeke Dominik, Kaksonen Marko.* The initiation of clathrin-mediated endocytosis is mechanistically highly flexible // *Current Biology*. 2014. 24, 5. 548–554.
- Brett Tom J., Legendre-Guillemain Valerie, McPherson Peter S., Fremont Daved H.* Structural definition of the F-actin-binding THATCH domain from HIP1R // *Nature Structural and Molecular Biology*. 2006. 13, 2. 121–130.
- Bucher Delia, Frey Felix, Sochacki Kem A., Kummer Susann, Bergeest Jan Philip, Godinez William J., Kräusslich Hans Georg, Rohr Karl, Taraska Justin W., Schwarz Ulrich S., Boulant Steeve.* Clathrin-Adaptor ratio and membrane tension regulate the flat-to-curved transition of the clathrin coat during endocytosis // *Nature Communications*. 2018. 9, 1109. 1109.

- Burastero Osvaldo, Niebling Stephan, Defelipe Lucas A., Günther Christian, Struve Angelica, Garcia Alai Maria M.* eSPC: An online data-analysis platform for molecular biophysics // *Acta Crystallographica Section D: Structural Biology*. 2021. 77. 1241–1250.
- Busch David J., Houser Justin R., Hayden Carl C., Sherman Michael B., Lafer Eileen M., Stachowiak Jeanne C.* Intrinsically disordered proteins drive membrane curvature // *Nature Communications*. 2015. 6. 1–11.
- Campelo Felix, McMahon Harvey T., Kozlov Michael M.* The hydrophobic insertion mechanism of membrane curvature generation by proteins // *Biophysical Journal*. 2008. 95, 5. 2325–2339.
- Carragher B, Cheng Y, Frost A, Glaeser R. M., Lander G. C., Nogales E., Wang H. W.* Current outcomes when optimizing ‘standard’ sample preparation for single-particle cryo-EM // *Journal of Microscopy*. 2019. 276, 1. 39–45.
- Chen Hong, Fre Silvia, Slepnev Vladimir I., Capua Maria R, Takei Kohji, Butler Margaret H., Di Fiori Pier P., DeCamilli Pietro.* Epsin is an EH-domain-binding protein implicated in clathrin-mediated endocytosis // *Nature*. 1998. 394. 793–797.
- Cocucci Emanuele, Aguet François, Boulant Steeve, Kirchhausen Tom.* The first five seconds in the life of a clathrin-coated pit // *Cell*. 2012. 150, 3. 495–507.
- Cole Daniel, Young Gavin, Weigel Alexander, Sebesta Aleksandar, Kukura Philipp.* Label-Free Single-Molecule Imaging with Numerical-Aperture-Shaped Interferometric Scattering Microscopy // *ACS Photonics*. 2017. 4, 2. 211–216.
- Croll Tristan Ian.* ISOLDE: A physically realistic environment for model building into low-resolution electron-density maps // *Acta Crystallographica Section D: Structural Biology*. 2018. 74, 6. 519–530.
- Dannhauser Philip N., Ungewickell Ernst J.* Reconstitution of clathrin-coated bud and vesicle formation with minimal components // *Nature Cell Biology*. 2012. 14, 6. 634–639.
- Day Kasey J., Stachowiak Jeanne C.* Biophysical forces in membrane bending and traffic // *Current Opinion in Cell Biology*. 2020. 65. 72–77.
- Di Paolo Gilbert, De Camilli Pietro.* Phosphoinositides in cell regulation and membrane dynamics // *Nature*. 2006. 443, 7112. 651–657.
- Doherty Gary J., McMahon Harvey T.* Mechanisms of endocytosis // *Annual Review of Biochemistry*. 2009. 78. 857–902.

- Edeling Melissa A., Mishra Sanjay K., Keyel Peter A., Steinhauser Amie L., Collins Brett M., Roth Robyn, Heuser John E., Owen David J., Traub Linton M.* Molecular switches involving the AP-2 β 2 appendage regulate endocytic cargo selection and clathrin coat assembly // *Developmental Cell*. 2006. 10, 3. 329–342.
- Emsley P., Lohkamp B., Scott W. G., Cowtan K.* Features and development of Coot // *Acta Crystallographica Section D: Biological Crystallography*. 2010. 66, 4. 486–501.
- The actin-binding protein Hip1R associates with clathrin during early stages of endocytosis and promotes clathrin assembly in vitro. // . 2001. 154, 6. 1209–1223.
- Fisher C. L., Pei G. K.* Modification of a PCR- Based Site-Directed Mutagenesis Method // *Benchmarks*. 1997. 23, 4.
- Foley Kevin, Boguslavsky Shlomit, Klip Amira.* Endocytosis, recycling, and regulated exocytosis of glucose transporter 4 // *Biochemistry*. 2011. 50, 15. 3048–3061.
- Ford M. G.J., Pearse B. M.F., Higgins M. K., Vallis Y., Owen D. J., Gibson A., Hopkins C. R., Evans P. R., McMahon H. T.* Simultaneous binding of PtdIns (4,5) P 2 and clathrin by AP180 in the nucleation of clathrin lattices on membranes // *Science*. 2001. 291, 5506. 1051–1055.
- Ford Marijn G.J., Mills Ian G., Peter Brian J., Vallis Yvonne, Praefcke Gerrit J.K., Evans Philip R., McMahon Harvey T.* Curvature of clathrin-coated pits driven by epsin // *Nature*. 2002. 419, 6905. 361–366.
- Fotin Alexander, Cheng Yifan, Grigorieff Nikolaus, Walz Thomas, Harrison Stephen C., Kirchhausen Tomas.* Structure of an auxilin-bound clathrin coat and its implications for the mechanism of uncoating // *Nature*. 2004a. 432, 7017. 649–653.
- Fotin Alexander, Cheng Yifan, Sliz Piotr, Grigorieff Nikolaus, Harrison Stephen C, Kirchhausen Tomas, Walz Thomas.* Molecular model for a complete clathrin lattice from electron cryomicroscopy // *Nature*. 2004b. 432, 7017. 573–579.
- Franke Daniel, Svergun Dmitri I.* DAMMIF, a program for rapid ab-initio shape determination in small-angle scattering // *Journal of Applied Crystallography*. 2009. 42, 2. 342–346.
- Frost Adam, Perera Rushika, Roux Aurélien, Spasov Krashimir, Destaing Olivier, Engelman Edward H., Camilli Pietro De, Unger Vinzenz M.* Structural Basis of Membrane Invagination by F-BAR Domains // *Cell*. 2008. 807–817.
- Garcia-Alai Maria M., Heidemann Johannes, Skruzny Michal, Gieras Anna, Mertens Haydyn D.T., Svergun Dmitri I., Kaksonen Marko, Utrecht Charlotte, Meijers Rob.* Epsin and

- Sla2 form assemblies through phospholipid interfaces // *Nature Communications*. 2018. 9, 1. 1–13.
- Gingras Alexandre R, Bate Neil, Goult Benjamin T, Hazelwood Larnele, Canestrelli Ilona, Grossmann J. Günter, Liu Hong Jun, Putz Nicholas S.M., Roberts Gordon C.K., Volkmann Niels, Hanein Dorit, Barsukov Igor L, Critchley David R.* The structure of the C-terminal actin-binding domain of talin // *EMBO Journal*. 2008. 27, 2. 458–469.
- Goddard Thomas D., Huang Conrad C., Meng Elaine C., Pettersen Eric F., Couch Gregory S., Morris John H., Ferrin Thomas E.* UCSF ChimeraX: Meeting modern challenges in visualization and analysis // *Protein Science*. 2018. 27, 1. 14–25.
- Goldstein Joseph L, Anderson Richard G W, Brown Michael S.* Coated pits, coated vesicles, and receptor-mediated endocytosis // *Nature*. 1979. 279, June. 679–685.
- Graham Stephen C, Honing S., Ungewickell Ernst J, Kelly Bernard T, Liska Nicole, Dannhauser Philip N, Owen David J.* AP2 controls clathrin polymerization with a membrane-activated switch // *Science*. 2014. 345, 6195. 459–463.
- Haar E. ter, Harrison S. C., Kirchhausen T.* Peptide-in-groove interactions link target proteins to the beta -propeller of clathrin // *Proceedings of the National Academy of Sciences*. 2002. 97, 3. 1096–1100.
- Haucke Volker, Kozlov Michael M.* Membrane remodeling in clathrin-mediated endocytosis // *Journal of Cell Science*. 2018. 131, 17. 1–10.
- He Kangmin, Marsland Robert, Upadhyayula Srigokul, Song Eli, Dang Song, Capraro Benjamin R, Wang Weiming, Skillern Wesley, Gaudin Raphael, Ma Minghe, Kirchhausen Tom.* Dynamics of phosphoinositide conversion in clathrin-mediated endocytic traffic // *Nature*. 2017. 552, 7685. 410–414.
- Heidemann Johannes, Kölbl Knut, Konijnenberg Albert, Van Dyck Jeroen, Garcia-Alai Maria, Meijers Rob, Sobott Frank, Utrecht Charlotte.* Further insights from structural mass spectrometry into endocytosis adaptor protein assemblies // *International Journal of Mass Spectrometry*. 2020. 447. 1–9.
- Hom Robert A., Vora Mohsin, Regner Maryann, Subach Oksana M., Cho Wonhwa, Verkhusha Vladislav V., Stahelin Robert V., Kutateladze Tatiana G.* pH-dependent Binding of the Epsin ENTH Domain and the AP180 ANTH Domain to PI(4,5)P2-containing Bilayers // *Journal of Molecular Biology*. 2007. 373, 2. 412–423.

- Houser Justin R., Cho Hyun Woo, Hayden Carl C., Yang Noel X., Wang Liping, Lafer Eileen M., Thirumalai D., Stachowiak Jeanne C.* Molecular Mechanisms of Steric Pressure Generation and Membrane Remodeling by Intrinsically Disordered Proteins // *Biophysical Journal*. 2022. 1–14.
- Hunter John D.* Matplotlib: A 2D graphis environment // *Computing in Science Engineering*. 2007. 9. 90–95.
- Itoh T., Koshiba S., Kigawa T., Kikuchi A., Yokoyama S., Takenawa T.* Role of the ENTH domain in phosphatidylinositol-4,5-bisphosphate binding and endocytosis // *Science*. 2001. 291, 5506. 1047–1051.
- Joseph Jophin G., Osorio Carlos, Yee Vivian, Agrawal Ashutosh, Liu Allen P.* Complimentary action of structured and unstructured domains of epsin supports clathrin-mediated endocytosis at high tension // *Communications Biology*. 2020. 3, 1. 1–16.
- Josts Inokentij, Gao Yunyun, Monteiro Diana C.F., Niebling Stephan, Nitsche Julius, Veith Katharina, Grüwert Tobias W., Blanchet Clement E., Schroer Martin A., Huse Nils, Pearson Arwen R., Svergun Dmitri I., Tidow Henning.* Structural Kinetics of MsbA Investigated by Stopped-Flow Time-Resolved Small-Angle X-Ray Scattering // *Structure*. 2020. 28, 3. 348–354.e3.
- Jumper John, Evans Richard, Pritzel Alexander, Green Tim, Figurnov Michael, Ronneberger Olaf, Tunyasuvunakool Kathryn, Bates Russ, Žídek Augustin, Potapenko Anna, Bridgland Alex, Meyer Clemens, Kohl Simon A.A., Ballard Andrew J., Cowie Andrew, Romera-Paredes Bernardino, Nikolov Stanislav, Jain Rishub, Adler Jonas, Back Trevor, Petersen Stig, Reiman David, Clancy Ellen, Zielinski Michal, Steinegger Martin, Pacholska Michalina, Berghammer Tamas, Bodenstein Sebastian, Silver David, Vinyals Oriol, Senior Andrew W., Kavukcuoglu Koray, Kohli Pushmeet, Hassabis Demis.* Highly accurate protein structure prediction with AlphaFold // *Nature*. 2021. 596, 7873. 583–589.
- Kaksonen Marko, Roux Aurélien.* Mechanisms of clathrin-mediated endocytosis // *Nature Reviews Molecular Cell Biology*. 2018. 19. 313–326.
- Kaksonen Marko, Sun Yidi, Drubin David G.* A Pathway for Association of Receptors, Adaptors, and Actin during Endocytic Internalization // *Cell*. 2003. 115, 4. 475–487.
- Kalthoff Christoph, Alves Jürgen, Urbanke Claus, Knorr Ruth, Ungewickell Ernst J.* Unusual structural organization of the endocytic proteins AP180 and epsin 1 // *Journal of Biological Chemistry*. 2002. 277, 10. 8209–8216.

- Kang Dong Soo, Kern Ronald C, Puthenveedu Manojkumar A, Zastrow Mark von, Williams John C, Benovic Jeffrey L.* Structure of an arrestin2-clathrin complex reveals a novel clathrin binding domain that modulates receptor trafficking // *Journal of Biological Chemistry*. 2009. 284, 43. 29860–29872.
- Kelly S.M. M M, Price N.C. C C.* The use of circular dichroism in the investigation of protein structure and function. // *Current protein peptide science*. 2000. 1, 4. 349–84.
- Kirchhausen Tom, Owen David, Harrison Stephen C.* Molecular Structure, Function, and Dynamics of Clathrin-Mediated Membrane Traffic // *Cold Spring Harb Perspect Biol*. 2014. 6, a016725.
- Klebl David P., White Howard D., Sobott Frank, Muench Stephen P.* On-grid and in-flow mixing for time-resolved cryo-EM // *Acta Crystallographica Section D: Structural Biology*. 2021. 77. 1233–1240.
- Konarev Petr V., Svergun Dmitri I.* Direct shape determination of intermediates in evolving macromolecular solutions from small-angle scattering data // *IUCrJ*. 2018. 5. 402–409.
- Konarev Petr V., Volkov Vladimir V., Sokolova Anna V., Koch Michel H.J., Svergun Dmitri I.* PRIMUS: A Windows PC-based system for small-angle scattering data analysis // *Journal of Applied Crystallography*. 2003. 36, 5. 1277–1282.
- Koppel Dennis E.* Analysis of Macromolecular Polydispersity in Intensity Correlation Spectroscopy : The Method of Cumulants // *The Journal of Chemical Physics*. 1972. 57, December 1972. 4814–4820.
- Koutun Oleksiy, Dickson Veronica Kane, Kelly Bernard T., Owen David J., Briggs John A.G.* Architecture of the AP2/clathrin coat on the membranes of clathrin-coated vesicles // *Science Advances*. 2020. 6, 30. 1–10.
- Kozlov Michael M., Campelo Felix, Liska Nicole, Chernomordik Leonid V., Marrink Siewert J., McMahon Harvey T.* Mechanisms shaping cell membranes // *Current Opinion in Cell Biology*. 2014. 29, 1. 53–60.
- Kozlov Michael M, Taraska Justin W.* Generation of nanoscopic membrane curvature for membrane trafficking. 2022.
- Kukulski Wanda, Picco Andrea, Specht Tanja, Briggs John A.G., Kaksonen Marko.* Clathrin modulates vesicle scission, but not invagination shape, in yeast endocytosis // *eLife*. 2016. 5, JUN2016. 1–10.

- Kukulski Wanda, Schorb Martin, Kaksonen Marko, Briggs John A G.* Plasma membrane reshaping during endocytosis is revealed by time-resolved electron tomography // *Cell*. 2012. 150, 3. 508–520.
- Kumar Manjeet, Michael Sushama, Alvarado-Valverde Jesús, McRossed D Sign@száros Bálint, Sámano-Sánchez Hugo, Zeke András, Dobson Laszlo, Lazar Tamas, Örd Mihkel, Nagpal Anurag, Farahi Nazanin, Käser Melanie, Kraleti Ramya, Davey Norman E., Pancsa Rita, Chemes Lucía B., Gibson Toby J.* The Eukaryotic Linear Motif resource: 2022 release // *Nucleic Acids Research*. 2022. 50, D1. D497–D508.
- Kweon Dae Hyuk, Shin Yeon Kyun, Shin Jae Yoon, Lee Jong Hwa, Lee Jung Bok, Seo Jin Ho, Kim Yong Sung.* Membrane topology of helix 0 of the epsin N-terminal homology domain // *Molecules and Cells*. 2006. 21, 3. 428–435.
- Lacy Michael M., Ma Rui, Ravindra Neal G., Berro Julien.* Molecular mechanisms of force production in clathrin-mediated endocytosis // *FEBS Letters*. 2018. 592, 21. 3586–3605.
- Lai Chun-liang, Jao Christine C, Lyman Edward, Gallop Jennifer L, Peter Brian J, McMahon Harvey T, Langen Ralf, Voth Gregory A.* Membrane Binding and Self-Association of the Epsin N-Terminal Homology Domain // *Journal of Molecular Biology*. 2012. 423, 5. 800–817.
- Legendre-Guillemain Valerie, Metzler Martina, Lemaire Jean Francois, Philie Jacynthe, Gan Lu, Hayden Michael R., McPherson Peter S.* Huntingtin Interacting Protein 1 (HIP1) regulates clathrin assembly through direct binding to the regulatory region of the clathrin light chain // *Journal of Biological Chemistry*. 2005. 280, 7. 6101–6108.
- Liebschner Dorothee, Afonine Pavel V., Baker Matthew L., Bunkoczi Gábor, Chen Vincent B., Croll Tristan I., Hintze Bradley, Hung Li Wei, Jain Swati, McCoy Airlie J., Moriarty Nigel W., Oeffner Robert D., Poon Billy K., Prisant Michael G., Read Randy J., Richardson Jane S., Richardson David C., Sammito Massimo D., Sobolev Oleg V., Stockwell Duncan H., Terwilliger Thomas C., Urzhumtsev Alexandre G., Videau Lizbeth L., Williams Christopher J., Adams Paul D.* Macromolecular structure determination using X-rays, neutrons and electrons: Recent developments in Phenix // *Acta Crystallographica Section D: Structural Biology*. 2019. 75. 861–877.
- Lizarrondo Javier, Klebl David P., Niebling Stephan, Abella Marc, Schroer Martin A., Mertens Haydyn D.T., Veith Katharina, Thuenauer Roland, Svergun Dmitri I., Skruzny Michal, Sobott Frank, Muench Stephen P., Garcia-Alai Maria M.* Structure of the endocytic adaptor

- complex reveals the basis for efficient membrane anchoring during clathrin-mediated endocytosis // *Nature Communications*. 2021. 12, 1.
- Lu Rebecca, Drubin David G., Sun Yidi*. Clathrin-mediated endocytosis in budding yeast at a glance // *Journal of Cell Science*. 2016. 129, 8. 1531–1536.
- Marsh M.* The Structural Era of Endocytosis // *Science*. 2002. 285, 5425. 215–220.
- Marty Michael T., Baldwin Andrew J., Marklund Erik G., Hochberg Georg K.A., Benesch Justin L.P., Robinson Carol V.* Bayesian deconvolution of mass and ion mobility spectra: From binary interactions to polydisperse ensembles // *Analytical Chemistry*. 2015. 87, 8. 4370–4376.
- McCann Richard O., Craig Susan W.* The I LWEQ module : a conserved sequence that signifies F-actin binding in functionally diverse proteins from yeast to mammals // *Proceedings of the National Academy of Sciences of the United States of America*. 1997. 94, May. 5679–5684.
- McMahon H. T., Boucrot E.* Membrane curvature at a glance // *Journal of Cell Science*. 2015. 128, 6. 1065–1070.
- Merrifield Christien J., Kaksonen Marko.* Endocytic Accessory Factors and Regulation Clathrin-Mediated Endocytosis // *Cold Spring Harbor Perspectives in Biology*. 2014. 6, 11. 1–16.
- Messa Mirko, Fernández-Busnadiego Rubén, Sun Elizabeth Wen, Chen Hong, Czapla Heather, Wrasman Kristie, Wu Yumei, Ko Genevieve, Ross Theodora, Wendland Beverly, De Camilli Pietro.* Epsin deficiency impairs endocytosis by stalling the actin-dependent invagination of endocytic clathrin-coated pits // *eLife*. 2014. 3, August2014. 1–25.
- Mettlen Marcel, Chen Ping-hung, Srinivasan Saipraveen, Danuser Gaudenz, Schmid Sandra L.* Regulation of Clathrin-Mediated Endocytosis // *Annual review of biochemistry*. 2018. 87, April. 871–96.
- Meyer Arne, Dierks Karsten, Hussein Rana, Brillet Karl.* Systematic analysis of protein – detergent complexes applying dynamic light scattering to optimize solutions for crystallization trials // *research communications*. 2015. F71. 75–81.
- Miele Adriana E, Watson Peter J, Evans Philip R, Traub Linton M, Owen David J.* Two distinct interaction motifs in amphiphysin bind two independent sites on the clathrin terminal domain β -propeller // *Nature Structural and Molecular Biology*. 2004. 11, 3. 242–248.
- Miller Sharon E., Mathiasen Signe, Bright Nicholas A., Pierre Fabienne, Kelly Bernard T., Kladt Nikolay, Schauss Astrid, Merrifield Christien J., Stamou Dimitrios, Höning Stefan,*

- Owen David J.* CALM Regulates Clathrin-Coated Vesicle Size and Maturation by Directly Sensing and Driving Membrane Curvature // *Developmental Cell*. 2015. 33, 2. 163–175.
- Morris Kyle L, Jones Joseph R, Halebian Mary, Wu Shenping, Baker Michael, Armache Jean Paul, Avila Ibarra Amaurys, Sessions Richard B, Cameron Alexander D, Cheng Yi-fan, Smith Corinne J.* Cryo-EM of multiple cage architectures reveals a universal mode of clathrin self-assembly // *Nature Structural and Molecular Biology*. 2019. 26, 10. 890–898.
- Moulay Gilles, Lainé Jeanne, Lemaitre Mégane, Nakamori Masayuki, Nishino Ichizo, Caillol Ghislaine, Mamchaoui Kamel, Julien Laura, Dingli Florent, Loew Damarys, Bitoun Marc, Leterrier Christophe, Furling Denis, Vassilopoulos Stéphane.* Alternative splicing of clathrin heavy chain contributes to the switch from coated pits to plaques // *Journal of Cell Biology*. 2020. 219, 9.
- Muenzner Julia, Traub Linton M., Kelly Bernard T., Graham Stephen C.* Cellular and viral peptides bind multiple sites on the N-terminal domain of clathrin // *Traffic*. 2017. 18, 1. 44–57.
- Mund Markus, Beek Johannes Albertus van der, Deschamps Joran, Dmitrieff Serge, Monster Jooske Louiser, Picco Andrea, Nédélec François, Kaksonen Marko, Ries Jonas.* Systematic Nanoscale Analysis of Endocytosis Links Efficient Vesicle Formation to Patterned Actin Nucleation // *Cell*. 2018. 174. 884–896.
- Mund Markus, Tschanz Aline, Wu Yu-le, Frey Felix, Mehl Johanna L, Kaksonen Marko, Avinoam Ori, Schwarz Ulrich S., Ries Jonas.* Superresolution microscopy reveals partial pre-assembly and subsequent bending of the clathrin coat during endocytosis // *bioRxiv*. 2022.
- Nakatsu Fubito, Perera Rushika M., Lucast Louise, Zoncu Roberto, Domin Jan, Gertler Frank B., Toomre Derek, De Camilli Pietro.* The inositol 5-phosphatase SHIP2 regulates endocytic clathrin-coated pit dynamics // *Journal of Cell Biology*. 2010. 190, 3. 307–315.
- Nawara Tomasz J, Ii Yancey D Williams, Rao Tejeshwar C, Hu Yuesong, Sztul Elizabeth, Salaita Khalid, Mattheyses Alexa L.* Imaging vesicle formation dynamics supports the flexible model of clathrin-mediated endocytosis // *Nature Communications*. 2022. 13, 1732.
- Newpher Thomas M., Lemmon Sandra K.* Clathrin is important for normal actin dynamics and progression of Sla2p-containing patches during endocytosis in yeast // *Traffic*. 2006. 7, 5. 574–588.
- Niu Qian, Ybe Joel A.* Crystal Structure at 2.8 Å of Huntingtin-Interacting Protein 1 (HIP1) Coiled-Coil Domain Reveals a Charged Surface Suitable for HIP1 Protein Interactor (HIPPI) // *Journal of Molecular Biology*. 2008. 375, 5. 1197–1205.

- Oliphant Travis E.* Guide to NumPy // Methods. 2010. 1. 378.
- Panjekovich Alejandro, Svergun Dmitri I.* CHROMIXS: Automatic and interactive analysis of chromatography-coupled small-angle X-ray scattering data // Bioinformatics. 2018. 34, 11. 1944–1946.
- Paraan Mohammadreza, Mendez Joshua, Sharum Savanna, Kurtin Danielle, He Huan, Stagg Scott M.* The structures of natively assembled clathrin-coated vesicles // Science Advances. 2020. 6, 30.
- Park Sang Yoon, Guo Xiaoli.* Adaptor protein complexes and intracellular transport // Bio-science Reports. 2014. 34, 4. 381–390.
- Partlow Edward A, Cannon Kevin S, Hollopeter Gunther, Baker Richard W.* Structural basis of an endocytic checkpoint that primes the AP2 clathrin adaptor for cargo internalization // Nature Structural and Molecular Biology. 2022. 29, April.
- Payne Gregory S., Baker David, Van Tuinen E., Schekman R.* Protein transport to the vacuole and receptor-mediated endocytosis by clathrin heavy chain-deficient yeast // Journal of Cell Biology. 1988. 106, 5. 1453–1461.
- Pearse B. M.F.* Clathrin: A unique protein associated with intracellular transfer of membrane by coated vesicles // Proceedings of the National Academy of Sciences of the United States of America. 1976. 73, 4. 1255–1259.
- Pearse Barbara M.F.* Coated vesicles from pig brain: Purification and biochemical characterization // Journal of Molecular Biology. 1975. 97, 1. 93–98.
- Petoukhov Maxim V., Franke Daniel, Shkumatov Alexander V., Tria Giancarlo, Kikhney Alexey G., Gajda Michal, Gorba Christian, Mertens Haydyn D.T., Konarev Petr V., Svergun Dmitri I.* New developments in the ATSAS program package for small-angle scattering data analysis // Journal of Applied Crystallography. 2012. 45, 2. 342–350.
- Punjani Ali, Zhang Haowei, Fleet David J.* Non-uniform refinement: adaptive regularization improves single-particle cryo-EM reconstruction // Nature Methods. 2020. 17, 12. 1214–1221.
- Redlingshöfer Lisa, McLeod Faye, Camus Marine, Chen Yu, Burden Jemima, Palomer Ernest, Briant Kit, Dannhauser Philip, Salinas Patricia, Brodsky Frances.* Clathrin light chain diversity regulates budding efficiency in vitro and synaptic vesicle formation in vivo // PNAS. 2019.

- Rennick Joshua J., Johnston Angus P.R., Parton Robert G.* Key principles and methods for studying the endocytosis of biological and nanoparticle therapeutics // *Nature Nanotechnology*. 2021. 16, 3. 266–276.
- Rohou Alexis, Grigorieff Nikolaus.* CTFFIND4: Fast and accurate defocus estimation from electron micrographs // *Journal of Structural Biology*. 2015. 192, 2. 216–221.
- Saheki Yasunori, De Camilli Pietro.* Synaptic vesicle endocytosis // *Cold Spring Harb Perspect Biol*. 2012. 4, a005645.
- Scheuermann Thomas H., Brautigam Chad A.* High-precision, automated integration of multiple isothermal titration calorimetric thermograms: New features of NITPIC // *Methods*. 2015. 76. 87–98.
- Schmid Eva M., Ford Marijn G.J., Burtey Anne, Praefcke Gerrit J.K., Peak-Chew Sew Yeu, Mills Ian G., Benmerah Alexandre, McMahon Harvey T.* Role of the AP2 β -appendage hub in recruiting partners for clathrin-coated vesicle assembly // *PLoS Biology*. 2006. 4, 9. 1532–1548.
- Schöneberg Johannes, Lehmann Martin, Ullrich Alexander, Posor York, Lo Wen Ting, Lichtner Gregor, Schmoranzler Jan, Haucke Volker, Noé Frank.* Lipid-mediated PX-BAR domain recruitment couples local membrane constriction to endocytic vesicle fission // *Nature Communications*. 2017. 8, May.
- Scott Brandon L., Sochacki Kem A., Low-Nam Shalini T., Bailey Elizabeth M., Luu Quoc Ahn, Hor Amy, Dickey Andrea M., Smith Steve, Kerkvliet Jason G., Taraska Justin W., Hoppe Adam D.* Membrane bending occurs at all stages of clathrincoat assembly and defines endocytic dynamics // *Nature Communications*. 2018. 9, 1. 419.
- Serwas Daniel, Akamatsu Matthew, Moayed Amir, Vegesna Karthik, Vasan Ritvik, Hill Jennifer M., Schöneberg Johannes, Davies Karen M., Rangamani Padmini, Drubin David G.* Mechanistic insights into actin force generation during vesicle formation from cryo-electron tomography // *Developmental Cell*. 2022. 57, 9. 1132–1145.e5.
- Skrzyny M., Brach T., Ciuffa R., Rybina S., Wachsmuth M., Kaksonen M.* Molecular basis for coupling the plasma membrane to the actin cytoskeleton during clathrin-mediated endocytosis // *Proceedings of the National Academy of Sciences U. S. A.* 2012. 109, 38. E2533–E2542.
- Skrzyny Michal, Desfosses Ambroise, Prinz Simone, Dodonova Svetlana O., Gieras Anna, Utrecht Charlotte, Jakobi Arjen J., Abella Marc, Hagen Wim J.H., Schulz Joachim, Meijers Rob, Rybin Vladimir, Briggs John A.G., Sachse Carsten, Kaksonen Marko.* An Organized

- Co-assembly of Clathrin Adaptors Is Essential for Endocytosis // *Developmental Cell*. 2015. 33, 2. 150–162.
- Smith Sarah M, Baker Michael, Halebian Mary, Smith Corinne J.* Weak Molecular Interactions in Clathrin-Mediated Endocytosis // *Frontiers in Molecular Biosciences*. 2017. 4, November. 72.
- Smith Sarah M, Smith Corinne J.* Capturing the mechanics of clathrin-mediated endocytosis // *Current Opinion in Structural Biology*. 2022. 75. 102427.
- Sochacki Kem A., Taraska Justin W.* From Flat to Curved Clathrin: Controlling a Plastic Ratchet // *Trends in Cell Biology*. 2019. 29, 3. 241–256.
- Stachowiak Jeanne C., Schmid Eva M., Ryan Christopher J., Ann Hyoung Sook, Sasaki Darryl Y., Sherman Michael B., Geissler Phillip L., Fletcher Daniel A., Hayden Carl C.* Membrane bending by protein-protein crowding // *Nature Cell Biology*. 2012. 14, 9. 944–949.
- Sun Yidi, Drubin David G.* The functions of anionic phospholipids during clathrin-mediated endocytosis site initiation and vesicle formation // *Journal of Cell Science*. 2012. 125, 24. 6157–6165.
- Svergun D. I.* Determination of the regularization parameter in indirect-transform methods using perceptual criteria // *Journal of Applied Crystallography*. 1992. 25, pt 4. 495–503.
- Szymanska Monika, Fosdahl Anne Marthe, Raiborg Camilla, Dietrich Markus, Liestøl Knut, Stang Espen, Bertelsen Vibeke.* Interaction with epsin 1 regulates the constitutive clathrin-dependent internalization of ErbB3 // *Biochimica et Biophysica Acta - Molecular Cell Research*. 2016. 1863, 6. 1179–1188.
- Teale F W J, Weber G.* Ultraviolet fluorescence of the aromatic amino acids // *Biochemical Journal*. mar 1957. 65, 3. 476–482.
- Thieman James R., Mishra Sanjay K., Ling Kun, Doray Balraj, Anderson Richard A., Traub Linton M.* Clathrin regulates the association of PIPKI γ 661 with the AP-2 adaptor β 2 Appendage // *Journal of Biological Chemistry*. 2009. 284, 20. 13924–13939.
- Traub Linton M., Bonifacino Juan S.* Cargo recognition in clathrin-mediated endocytosis // *Cold Spring Harbor Perspectives in Biology*. 2013. 5, 11. 1–23.
- Ungewickell Ernst, Branton Daniel.* Assembly units of clathrin coats // *Nature*. 1981. 289, 5796. 420–422.

Vigers G. P., Crowther R. A., Pearse B. M. Location of the 100 kd-50 kd accessory proteins in clathrin coats. // *The EMBO journal*. 1986. 5, 9. 2079–2085.

Virtanen Pauli, Gommers Ralf, Oliphant Travis E., Haberland Matt, Reddy Tyler, Cournapeau David, Burovski Eugeni, Peterson Pearu, Weckesser Warren, Bright Jonathan, Walt Stéfan J. van der, Brett Matthew, Wilson Joshua, Millman K. Jarrod, Mayorov Nikolay, Nelson Andrew R.J., Jones Eric, Kern Robert, Larson Eric, Carey C. J., Polat İlhan, Feng Yu, Moore Eric W., VanderPlas Jake, Laxalde Denis, Perktold Josef, Cimrman Robert, Henriksen Ian, Quintero E. A., Harris Charles R., Archibald Anne M., Ribeiro Antônio H., Pedregosa Fabian, Mulbregt Paul van, Vijaykumar Aditya, Bardelli Alessandro Pietro, Rothberg Alex, Hilboll Andreas, Kloeckner Andreas, Scopatz Anthony, Lee Antony, Rokem Ariel, Woods C. Nathan, Fulton Chad, Masson Charles, Häggström Christian, Fitzgerald Clark, Nicholson David A., Hagen David R., Pasechnik Dmitrii V., Olivetti Emanuele, Martin Eric, Wieser Eric, Silva Fabrice, Lenders Felix, Wilhelm Florian, Young G., Price Gavin A., Ingold Gert Ludwig, Allen Gregory E., Lee Gregory R., Audren Hervé, Probst Irvin, Dietrich Jörg P., Silterra Jacob, Webber James T., Slavič Janko, Nothman Joel, Buchner Johannes, Kulick Johannes, Schönberger Johannes L., de Miranda Cardoso José Vinícius, Reimer Joscha, Harrington Joseph, Rodríguez Juan Luis Cano, Nunez-Iglesias Juan, Kuczynski Justin, Tritz Kevin, Thoma Martin, Newville Matthew, Kümmerer Matthias, Bolingbroke Maximilian, Tartre Michael, Pak Mikhail, Smith Nathaniel J., Nowaczyk Nikolai, Shebanov Nikolay, Pavlyk Oleksandr, Brodtkorb Per A., Lee Perry, McGibbon Robert T., Feldbauer Roman, Lewis Sam, Tygier Sam, Sievert Scott, Vigna Sebastiano, Peterson Stefan, More Surhud, Pudlik Tadeusz, Oshima Takuya, Pingel Thomas J., Robitaille Thomas P., Spura Thomas, Jones Thouis R., Cera Tim, Leslie Tim, Zito Tiziano, Krauss Tom, Upadhyay Utkarsh, Halchenko Yaroslav O., Vázquez-Baeza Yoshiki. SciPy 1.0: fundamental algorithms for scientific computing in Python // *Nature Methods*. 2020. 17, 3. 261–272.

Vollmer Benjamin, Lorenz Michael, Moreno-Andrés Daniel, Bodenhöfer Mona, De Magistris Paola, Astrinidis Susanne Adina, Schooley Allana, Flötenmeyer Matthias, Leptihn Sebastian, Antonin Wolfram. Nup153 Recruits the Nup107-160 Complex to the Inner Nuclear Membrane for Interphasic Nuclear Pore Complex Assembly // *Developmental Cell*. 2015. 33, 6. 717–728.

Wagner Thorsten, Merino Felipe, Stabrin Markus, Moriya Toshio, Antoni Claudia, Apelbaum Amir, Hagel Philine, Sitsel Oleg, Raisch Tobias, Prumbaum Daniel, Quentin Dennis, Roderer Daniel, Tacke Sebastian, Siebolds Birte, Schubert Evelyn, Shaikh Tanvir R, Lill Pascal, Gatsogiannis Christos, Raunser Stefan. SPHIRE-crYOLO is a fast and accurate fully automated particle picker for cryo-EM // *Communications Biology*. 2019. 2, 1. 1–13.

- Walt Stéfan J. van der, Colbert S. Chris, Varoquaux Gael.* The NumPy Array: A Structure for Efficient Numerical Computation // *Computing in Science Engineering*. 2011. 13, 2. 22–30.
- Wendland Beverly, Steece Katharine E, Emr Scott D.* Yeast epsins contain an essential N-terminal ENTH domain, bind clathrin and are required for endocytosis // *EMBO Journal*. 1999. 18, 16. 4383–4393.
- Wiedemann Christoph, Bellstedt Peter, Görlach Matthias.* CAPITO - A web server-based analysis and plotting tool for circular dichroism data // *Bioinformatics*. 2013. 29, 14. 1750–1757.
- Wilbur Jeremy D, Chen Chih-ying, Manalo Venus, Hwang Peter K, Fletterick Robert J, Brodsky Frances M.* Actin Binding by Hip1 (Huntingtin-interacting Protein 1) and Hip1R (Hip1-related Protein) Is Regulated by Clathrin // *Journal of Biological Chemistry*. 2008. 283, 47. 32870 –32879.
- Willox Anna K, Royle Stephen J.* Functional analysis of interaction sites on the N-terminal domain of clathrin heavy chain // *Traffic*. 2012. 13, 1. 70–81.
- Wiseman Thomas, Williston Samuel, Brandts John F, Lin Lung Nan.* Rapid measurement of binding constants and heats of binding using a new titration calorimeter // *Analytical Biochemistry*. 1989. 179, 1. 131–137.
- Xing Yi, Böcking Till, Wolf Matthias, Grigorieff Nikolaus, Kirchhausen Tomas, Harrison Stephen C.* Structure of clathrin coat with bound Hsc70 and auxilin: Mechanism of Hsc70-facilitated disassembly // *EMBO Journal*. 2010. 29, 3. 655–665.
- Yang Shirley, Cope M. Jamie T.V., Drubin David G.* S1a2p is associated with the yeast cortical actin cytoskeleton via redundant localization signals // *Molecular Biology of the Cell*. 1999. 10, 7. 2265–2283.
- Ybe Joel A., Greene Barrie, Liu Shu Hui, Pley Ursula, Parham Peter, Brodsky Frances M.* Clathrin self-assembly is regulated by three light-chain residues controlling the formation of critical salt bridges // *EMBO Journal*. 1998. 17, 5. 1297–1303.
- Ybe Joel A., Mishra Sanjay, Helms Stephen, Nix Jay.* Crystal Structure at 2.8 Å of the DLLRKN-containing Coiled-coil Domain of Huntingtin-interacting Protein 1 (HIP1) Reveals a Surface Suitable for Clathrin Light Chain Binding // *Journal of Molecular Biology*. 2007. 367, 1. 8–15.
- Yoon Youngdae, Tong Jiansong, Lee Park Joo, Albanese Alexandra, Bhardwaj Nitin, Källberg Morten, Digman Michelle A., Lu Hui, Gratton Enrico, Shin Yeon Kyun, Cho Wonhwa.*

Molecular basis of the potent membrane-remodeling activity of the epsin 1 N-terminal homology domain // *Journal of Biological Chemistry*. 2010. 285, 1. 531–540.

Young Gavin, Hundt Nikolas, Cole Daniel, Fineberg Adam, Andrecka Joanna, Tyler Andrew, Olerinyova Anna, Ansari Ayla, Marklund Erik G., Collier Miranda P., Chandler Shane A., Tkachenko Olga, Allen Joel, Crispin Max, Billington Neil, Takagi Yasuharu, Sellers James R., Eichmann Cédric, Selenko Philipp, Frey Lukas, Riek Roland, Galpin Martin R., Struwe Weston B., Benesch Justin L.P., Kukura Philipp. Quantitative mass imaging of single biological macromolecules // *Science*. 2018. 360, 6387. 423–427.

Zeno Wade F., Hochfelder Jacob B., Thatte Ajay S., Wang Liping, Gadok Avinash K., Hayden Carl C., Lafer Eileen M., Stachowiak Jeanne C. Clathrin senses membrane curvature // *Biophysical Journal*. 2021. 120, 5. 818–828.

Zhang Fan, Song Yang, Ebrahimi Mohammad, Niu Liwen, Teng Maikun, Li Xu. Structural and functional insight into the N-terminal domain of the clathrin adaptor Ent5 from *Saccharomyces cerevisiae* // *Biochemical and Biophysical Research Communications*. 2016. 477, 4. 786–793.

Zheng Shawn Q, Palovcak Eugene, Armache Jean Paul, Verba Kliment A, Cheng Yifan, Agard David A. MotionCor2: Anisotropic correction of beam-induced motion for improved cryo-electron microscopy. 2017. 331–332.

Zhuo Yue, Cano Kristin E, Wang Liping, Ilangovan Udayar, Hinck Andrew P, Sousa Rui, Lafer Eileen M. Nuclear Magnetic Resonance Structural Mapping Reveals Promiscuous Interactions between Clathrin-Box Motif Sequences and the N - Terminal Domain of the Clathrin Heavy Chain // *Biochemistry*. 2015. 54. 2571–2580.

Zivanov Jasenko, Nakane Takanori, Forsberg Björn O., Kimanius Dari, Hagen Wim J.H., Lindahl Erik, Scheres Sjors H.W. New tools for automated high-resolution cryo-EM structure determination in RELION-3 // *eLife*. 2018. 7. 1–22.

Zivanov Jasenko, Nakane Takanori, Scheres Sjors H.W. A Bayesian approach to beam-induced motion correction in cryo-EM single-particle analysis // *IUCrJ*. 2019. 6. 5–17.

10. Appendix

10.1 Appendix 1

10.1.1 ANTH-ENTH system

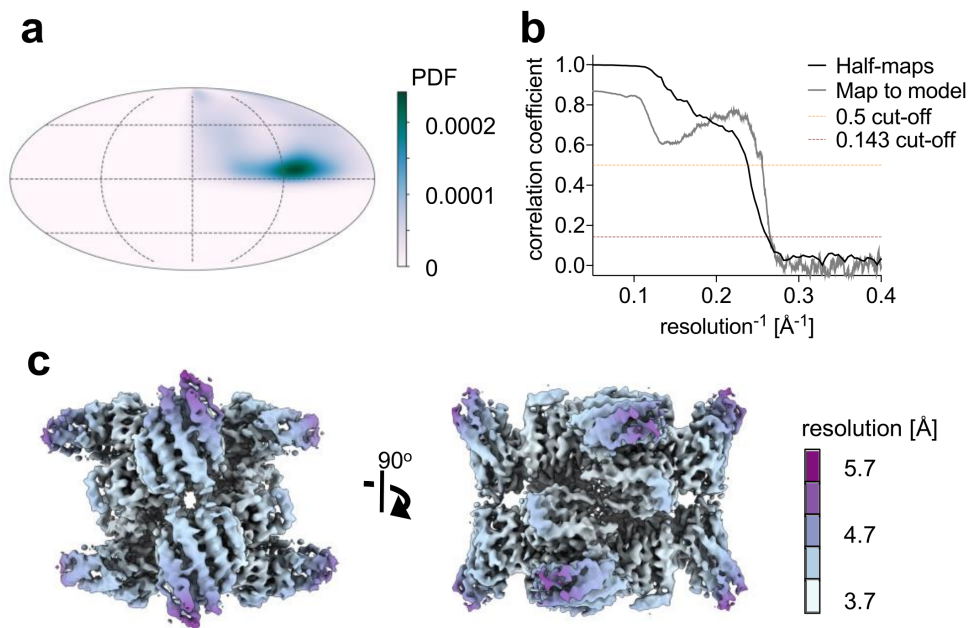


Figure 10.1: **Cryo-EM reconstruction parameters for the 16-mer ANTH-ENTH complex.** **a.** Angular distribution (PDF = Probability density function). **b.** Fourier Shell Correlation (FSC) curves and **c.** local resolution for the ANTH-ENTH 16-mer complex.

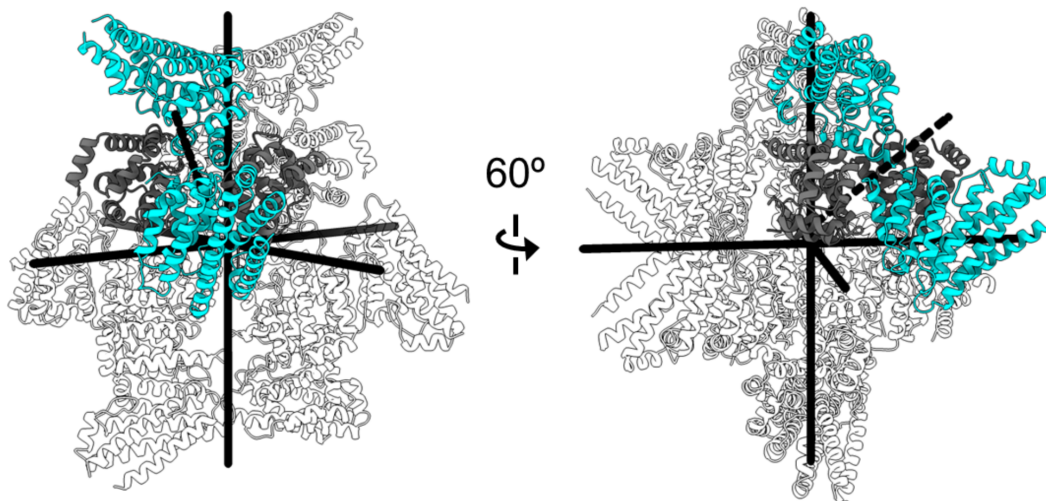


Figure 10.2: **Symmetry of the 16-mer ANTH-ENTH complex.**

Structure of 16-mer AENTH (A_8E_8) complex with symmetry axes indicated by black solid lines. ANTH and ENTH subunits of one asymmetric unit (tetramer) are shown in cyan and grey, respectively. The pseudo-2fold axis within the tetramer is shown as dashed black line.

Table 10.1: Data collection and processing parameters for the ANTH-ENTH 12-mer assembly (ANTH WT, ENTH F5A/L12A/V13A).

Data collection and processing	
Magnification	$\times 75,000$
Voltage (kV)	300
Electron exposure ($e^-/\text{\AA}^2$)	72.6
Defocus range (μm)	-1.5 to -4.2
Pixel size (\AA)	1.065
Symmetry imposed	D3
Initial particle images (no.)	142,399
Final particle images (no.)	16,206
Map resolution (\AA)	7.4
FSC threshold	0.143
Map resolution range (\AA)	6.8 to 9.9

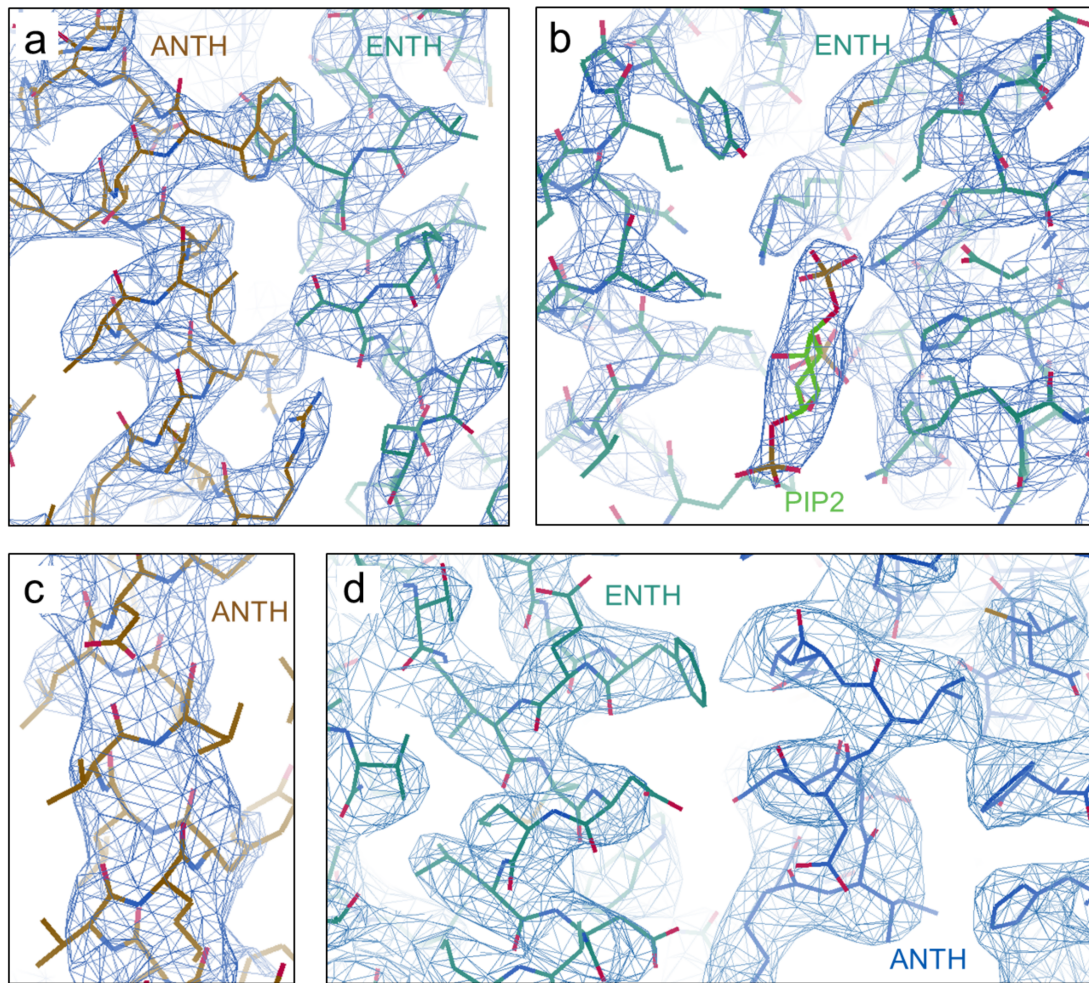


Figure 10.3: **Representative EM densities in the cryoEM model of the 16-mer.**
a. Well-resolved central alpha-helical parts of the ANTH-ENTH complex. **b.** One of the PIP₂-binding sites between two ENTH domains **c.** Lower resolution at the periphery of the complex in the last alpha helix of the ANTH domain and **(d)** the ANTH-ENTH interface 2.

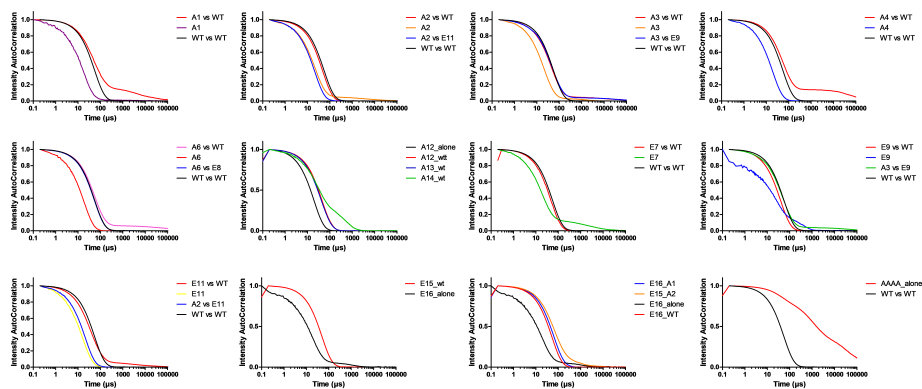


Figure 10.4: **DLS data for the ANTH/ENTH mutants and complexes.**

For all of them, the monomeric data and the complex with its wild-type counterpart is represented. In some cases, combinations of mutants are represented too. The mutants A5 and E8 are not shown since these mutants modified the thermal stability of the complexes making them more sensitive domains. E17 data are not shown as we could not get enough sample for the experiments. AAAAA mutant shows severe aggregation.

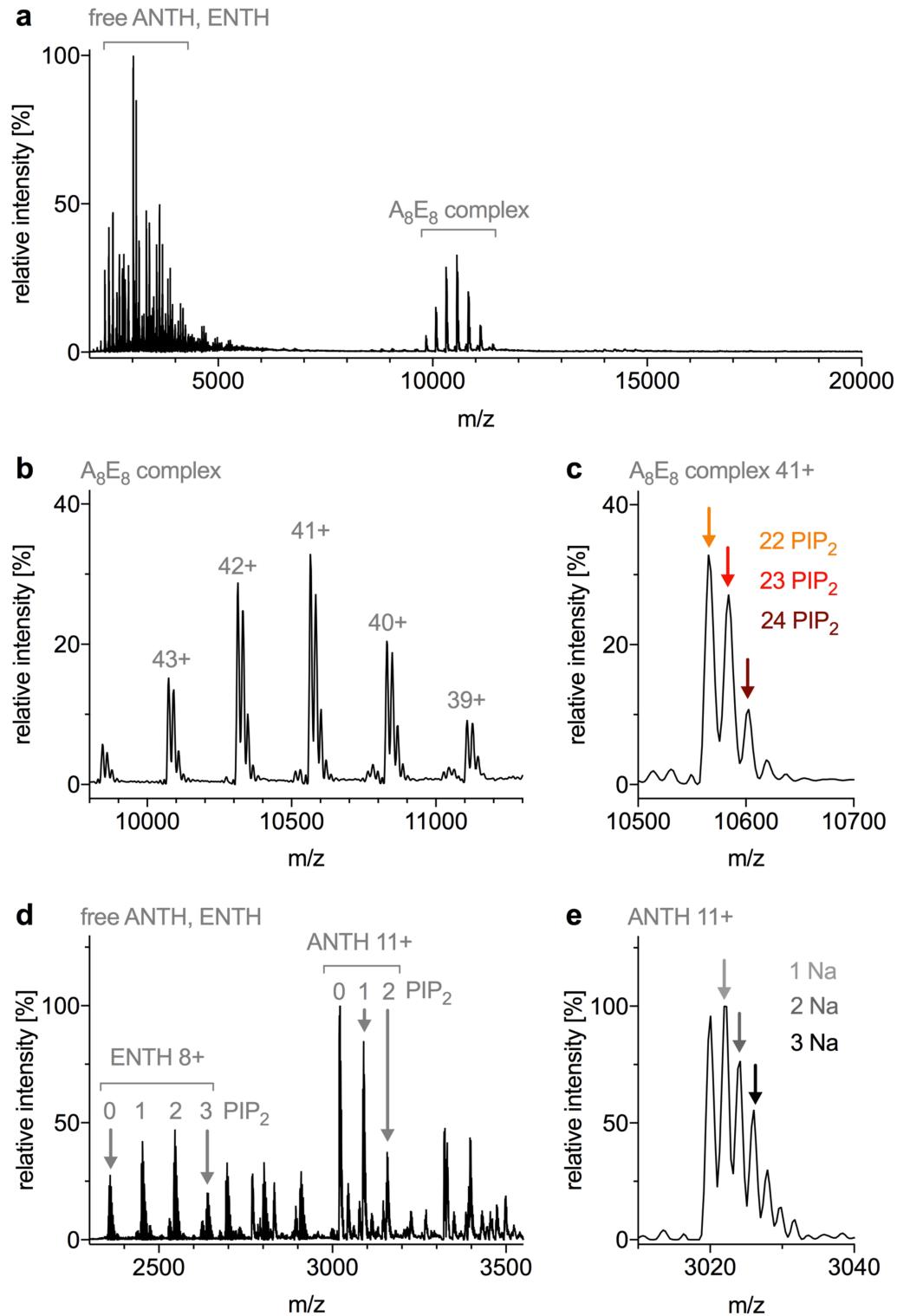


Figure 10.5: Native MS of the ANTH-ENTH WT complex in the presence of 60 μM PIP_2 . **a.** Full m/z range of the spectrum. The presence of free ANTH and ENTH is observed at low m/z while the complex appears around 10500 m/z . **b.** Charge state distribution of the A_8E_8 ANTH/ENTH complex with individual charge states labelled **c.** Close up of the 41⁺ charge state of the A_8E_8 8:8 ANTH/ENTH complex showing different numbers of PIP_2 molecules bound to the complex (22, 23 and 24 are clearly distinguishable). **d.** Close up of the spectrum at lower m/z where ENTH bound to 0-3 PIP_2 molecules and ANTH bound to 0-2 PIP_2 molecules can be observed. **e.** Peak fine structure of the ANTH (no PIP_2) 11+ charge state shows adducts with 1, 2 and 3 Na^+ molecules.

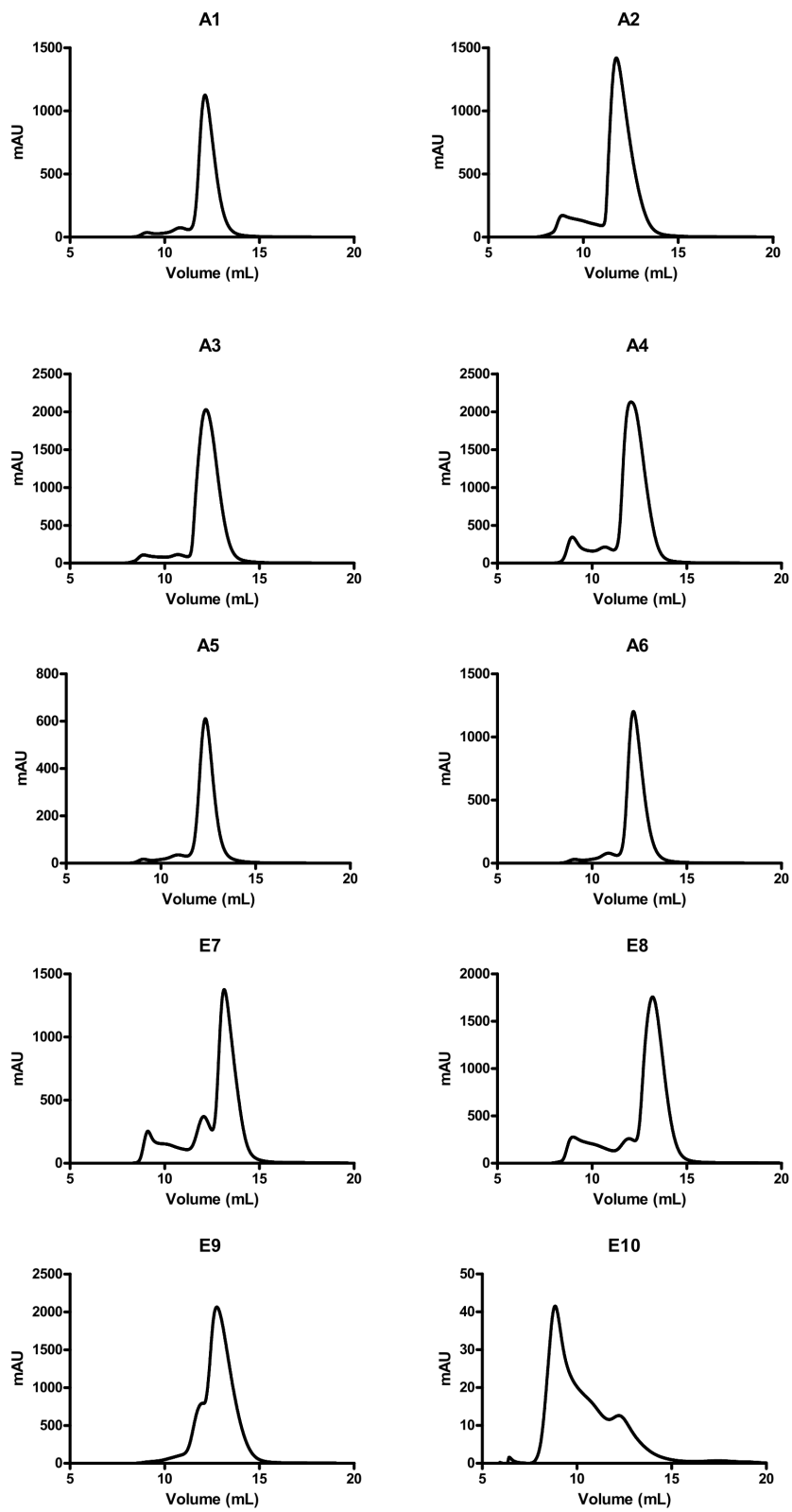


Figure 10.6: SEC profiles from different ANTH and ENTH mutants

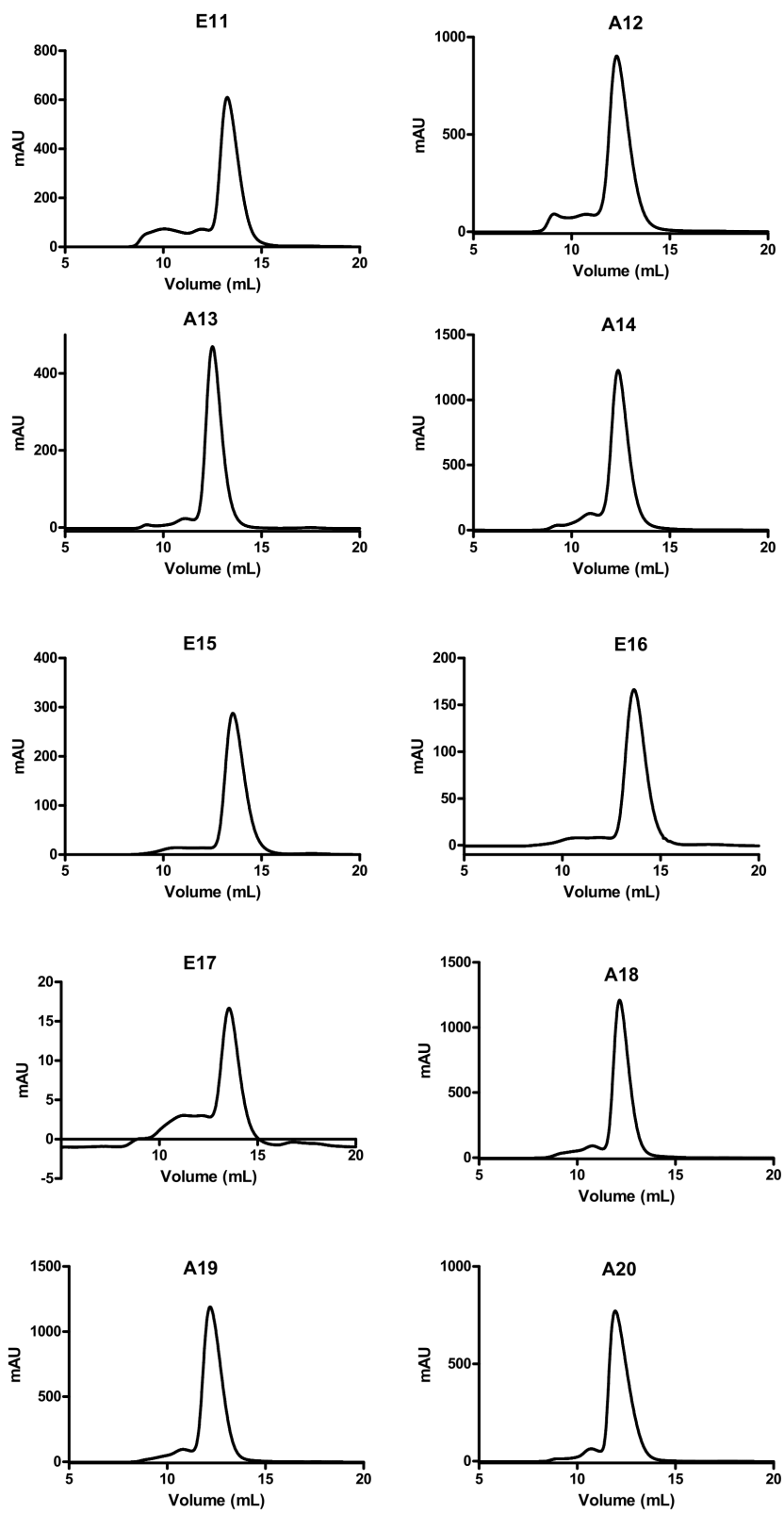


Figure 10.7: SEC profiles from different ANTH and ENTH mutants

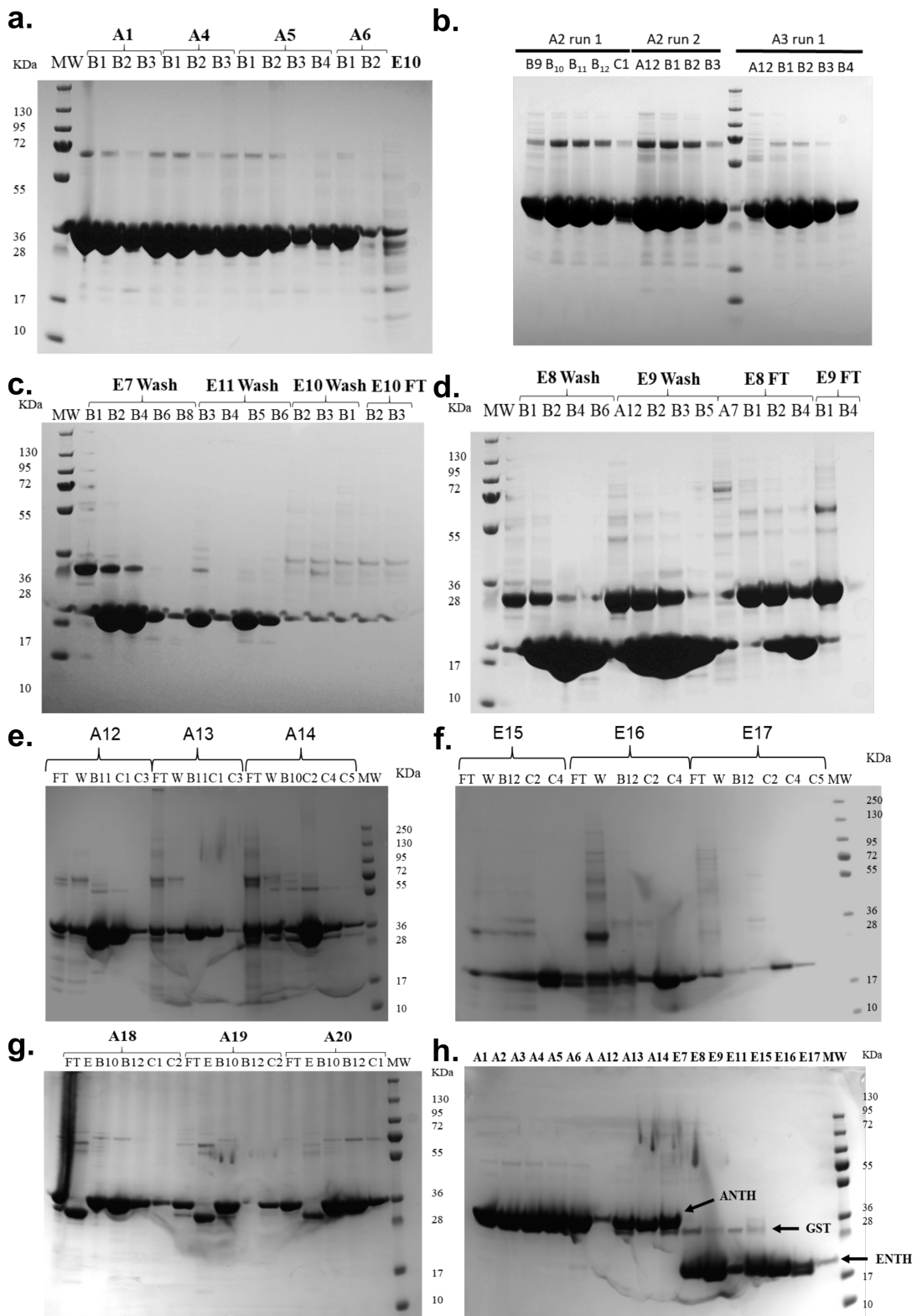


Figure 10.8: SDS-PAGE analysis of ANTH and ENTH mutants purified.

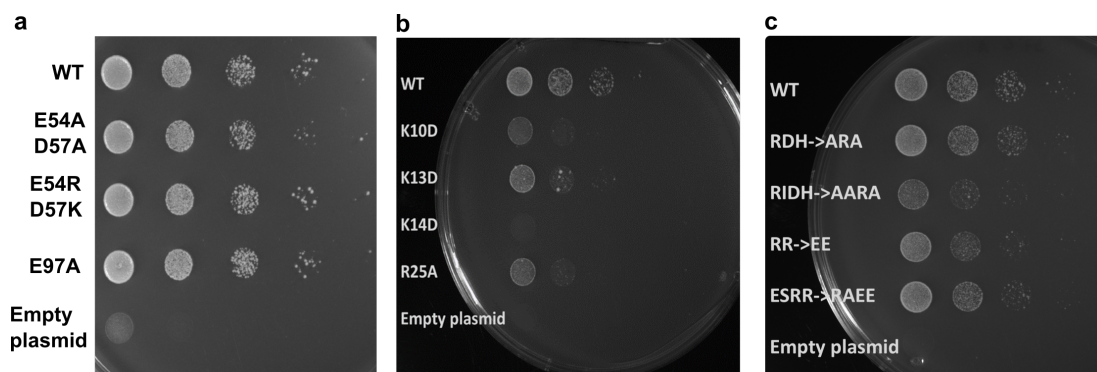


Figure 10.9: **Growth defects of selected mutants affecting the ANTH-ENTH interface 2 and the ANTH-ANTH interface.**

ANTH wt and ENTH wt domains or indicated interface mutants were expressed after depletion or deletion of endogenous Ent1 and Sla2 proteins, respectively. Cell growth was analysed after plating 10-fold serial dilution of cells on SD-Ura plates and incubation for 3 days at 37 °C. **a.** Mutation of negatively charged residues ENTH E54 and D57 does not introduce a growth defect. **b.** Mutation of single ANTH positively charged residues K10, K13, K14 and R25 impair cell growth. **c.** Growth of mutants of the ANTH-ANTH interface (RDH- \rightarrow ARA, R3A/D37R/H38A, RIDH- \rightarrow AARA, R3A/I4A/D37R/H38A) and the ANTH loop 175-183 (RR- \rightarrow EE, R178E/E178E, ESRR- \rightarrow RAEE, E57R/S100A/R178E/E178E). These growth assays were performed as part of a collaboration by Michal Skruzny and Marc Abella from the MPI for Terrestrial microbiology

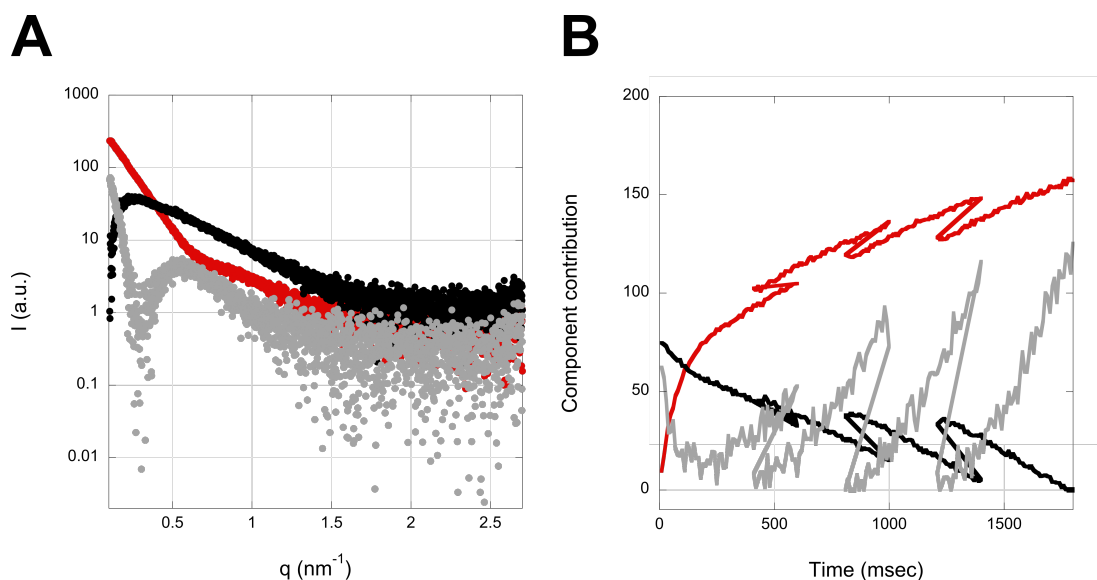


Figure 10.10: **SVD analysis of SF-TR-SAXS.**

a. SVD analysis of the full dataset revealed 3 components present. **b.** SAXS spectra of the three components. **c.** Component contribution over time of the SVD analysis using the full dataset. **d.** SVD analysis of the dataset using the first 10 points after beam exposure reveals two major components. **e.** SAXS spectra of the three first components. **f.** Component contributions over time of the SVD analysis using the first 10 points after beam exposure.

Table 10.2: Native MS of ANTH and ENTH mutants

Sample	m/z range	MWs obtained (Da)	Species	Number of PIP ₂ bound to the complex
ANTH Q9A/K10A + ENTH WT	8000-12000	324500	ANTH ₆ :ENTH ₆	16
		325300		17
		432200	ANTH ₈ :ENTH ₈	21
		433000		22
ANTH K10D/K13D + ENTH WT	8000 - 12000	433020	ANTH ₈ :ENTH ₈	22
		433770		23
ANTH K14D + ENTH WT	9000-12000	432960	ANTH ₈ :ENTH ₈	22
		433760		23
ANTH WT + ENTH E54A/D57A	13000-19000	292700	ANTH ₅ :ENTH ₆	18
		293380		19
		294150		20
	8000-12000	294880		21
		325840	ANTH ₆ :ENTH ₆	18
		326570		19
		327330		20
		328080		21
		436590	ANTH ₈ :ENTH ₈	27
		5000-8000	148020	ANTH ₂ :ENTH ₄
148770		9		
149520		10		
ENTH F5A/L12A + ANTH WT	8000-12000	325000	ANTH ₆ :ENTH ₆	17
		325800		18
		326600		19
		327400		20
		328000		21
		432600	ANTH ₈ :ENTH ₈	21
	13000-20000	432800		22
		434200		23
		291800	ANTH ₅ :ENTH ₆	17
		292600		18
293400		19		

Table 10.3: Oligomeric states with different number of PIP₂ molecules bound. The cells marked in black are species detectable for the corresponding mutants

Oligomeric Species	Hexamer					Octamer			2ANTH:4ENTH				3ANTH:4ENTH						
	N of PIP ₂	14	15	16	17	18	19	20	21	22	23	6	7	8	9	10	9	10	
WT												x	x						
ANTH	M1A								x	x									
	K13D											x	x						
	Q9A/ K10A			x	x							x	x						
	DDD																		
	K14D													x	x				
	AA			x	x	x	x												
ENTH	K10D/ K13D													x	x				
	F5A/I12A			x	x	x	x					x	x	x					
	E54A/ D57A					x	x	x	x						x	x	x		
	Y100R E97A											x	x	x					
Combinations	ANTH M1A + ENTH E97A											x	x	x					
	ANTH Q9A/ K10A + ENTH F5A/ I12A		x	x	x	x													
	ANTH Q9/K10 ENTH E54A/D57A														x	x	x		
	ANTH Q9A/K10A + ENTH Y100R																		
	ANTH K10R/K13R + ENTH E54A/D57A																		
	AA + ENTH E54A/D57A														x	x	x	x	
	ANTH Q9/K10 + ENTH E54A/D57A															x	x	x	x

10.1.2 Full lengths chapter

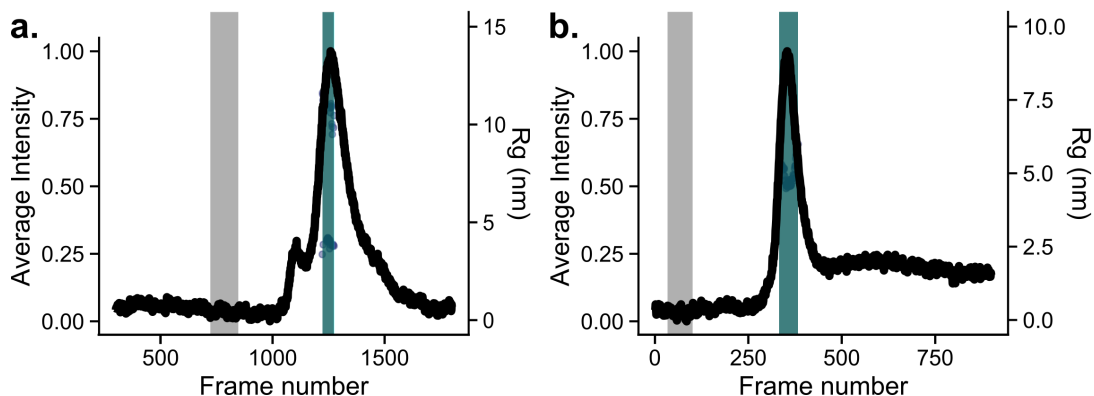


Figure 10.11: **Intensity profiles from SEC-SAXS for CtSla2 and CtEnt1**

a and b. SEC-SAXS intensity profiles acquired. The R_G for the selected points in the regions highlighted in green are also indicated in the right y-axis. The region selected as buffer is highlighted in grey.

Table 10.4: Secondary structure content derived from the CD data

Protein name	Alpha-helix	Beta-sheet	Random coil
Sla2 cc 432-767	0.7	0.2	0.11
Sla2 cc 296-767	0.69	0.23	0.08
Sc CLC full-length	0.57	0.07	0.35
Sla2 432-767 and CLC	0.18	0.13	0.66
CtEnt1	0.12	0.31	0.56

Table 10.5: Data collection and processing parameters for the C-terminus of CtSla2

Data collection and processing	
Magnification	$\times 105,000$
Voltage (kV)	300
Electron exposure ($e^- / \text{\AA}^2$)	65.6
Defocus range (μm)	-1.6 to -2.6
Pixel size (\AA)	0.85
Symmetry imposed	none
Initial particle images (no.)	127360
Final particle images (no.)	35371
Map resolution (\AA)	5.96
FSC threshold	0.143
Map resolution range (\AA)	6.8 to 9.9

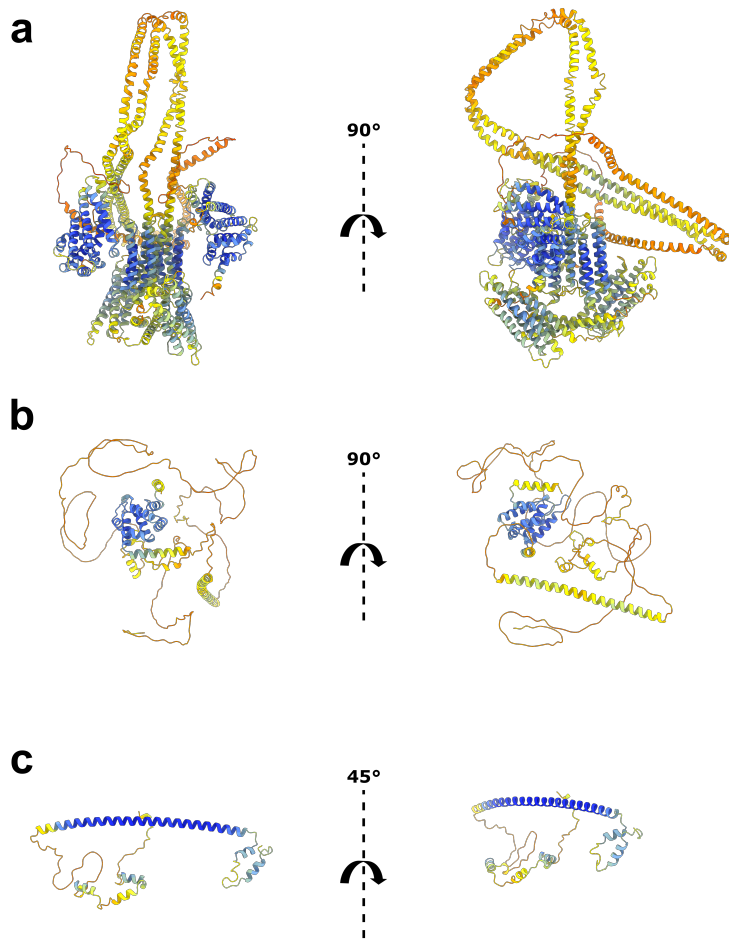


Figure 10.12: AlphaFold predictions of CtSla2 dimer (a), CtEnt1 (b) and yeast CLC (c).

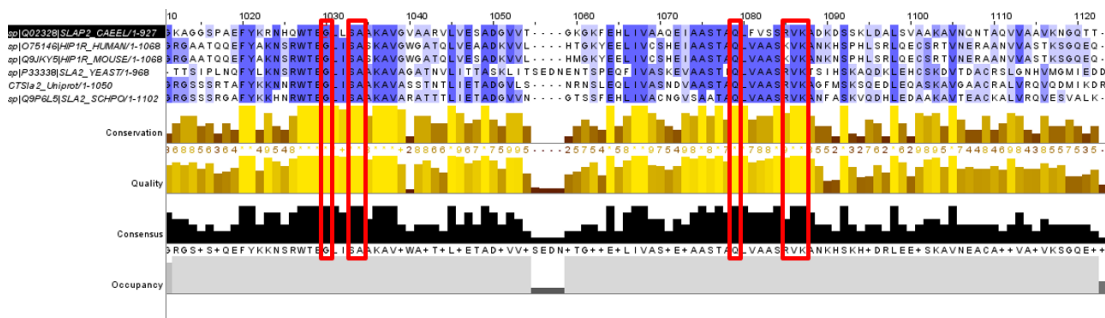


Figure 10.13: Multiple sequence alignment of Sla2 binding residues. The actin binding residues are marked in red

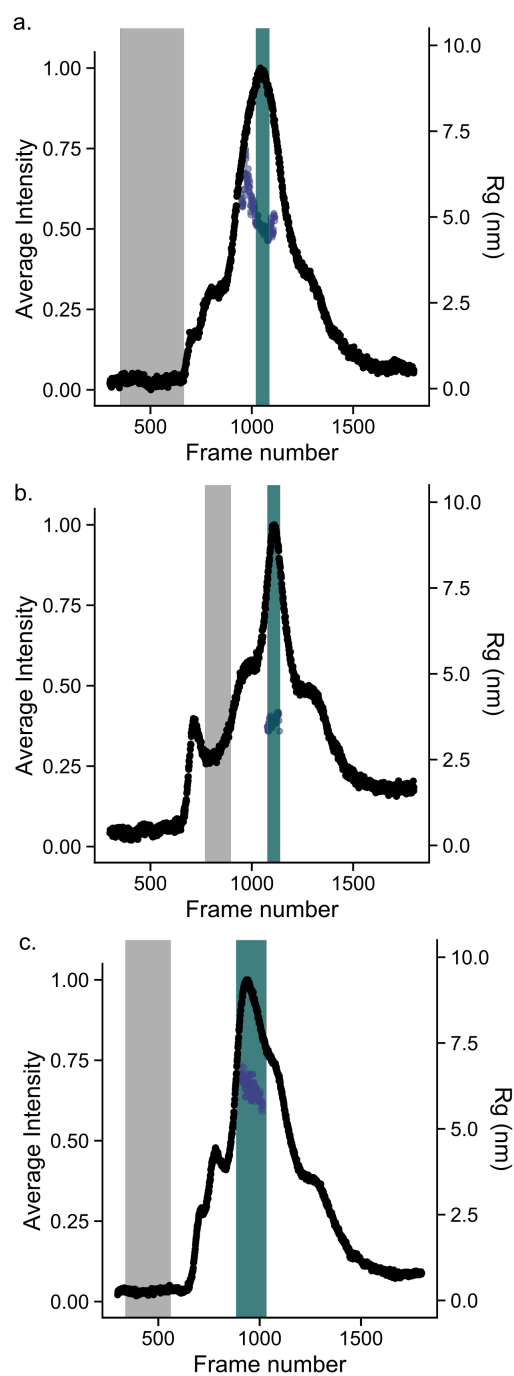


Figure 10.14: Intensity plots of SEC-SAXS runs for CLC, Sla2 coil-coil and the complex between the two.

a. CLC. b. Sla2 coil-coil. c. CLC-Sla2 coil-coil complex. The regions selected as buffer were chosen automatically with CHROMIX and are shadowed in grey. The regions corresponding to the sample are shadowed in green and the R_G values for the corresponding plots is also plotted in the right y-axis.

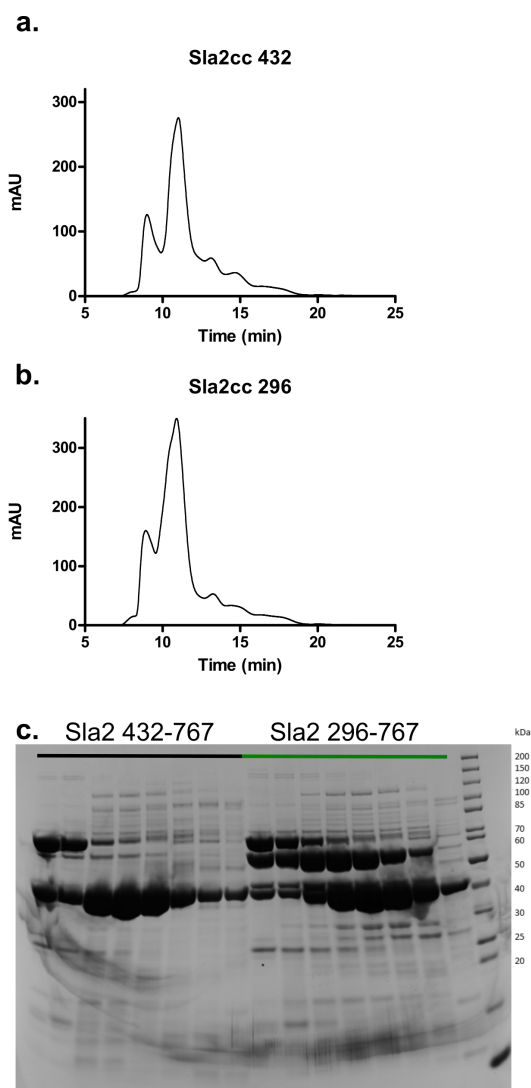


Figure 10.15: **Purification of Sla2 coil-coil constructs**

a. Chromatogram for Sla2 432-767 **b.** Chromatogram for Sla2 296-767 **c.** SDS-PAGE analysis of the peak fractions for both constructs.

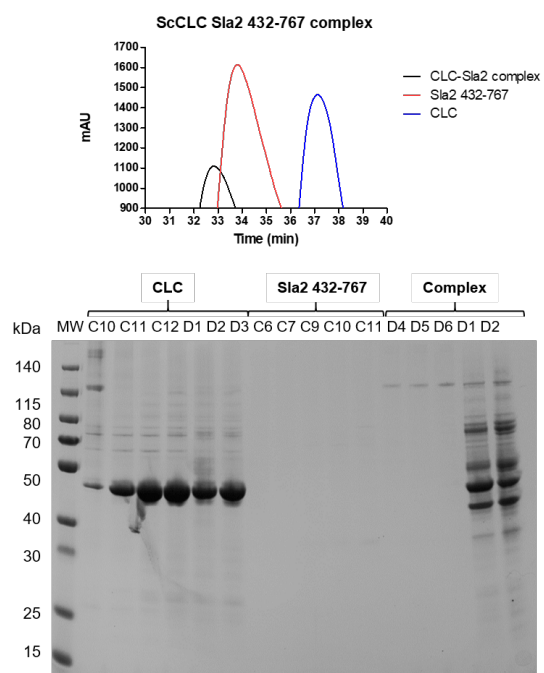


Figure 10.16: **SEC runs of Sla2 coil-coil, CLC and the complex between the two.** In the gel below, fractions corresponding to the top of the CLC and complex peaks can be seen.

10.1.3 Ct CHC NTD structure

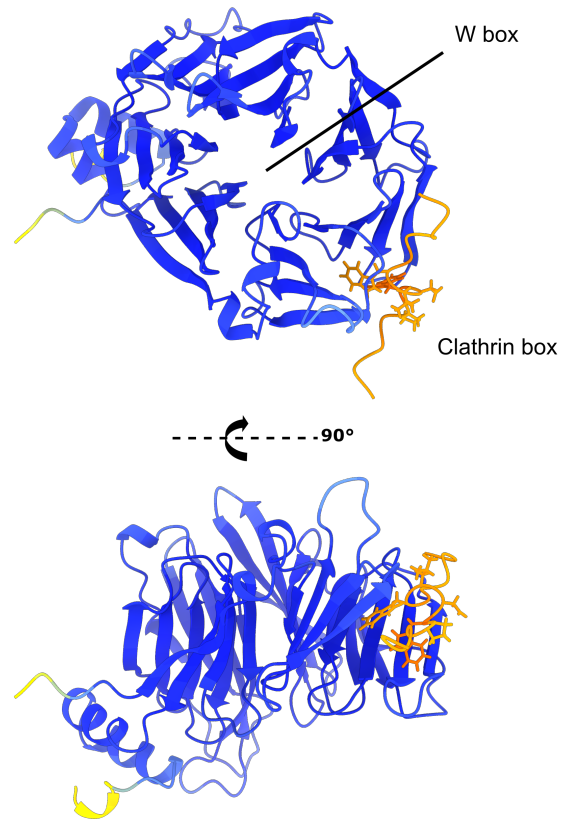


Figure 10.17: AlphaFold prediction of an W-box peptide into Ct CHC NTD

Table 10.6: Summary of proteins used in this work

Construct	MW (KDa)	Extinction coefficient (M^{-1} cm^{-1})	pI	Accession ID
His-CtANTH	32.03	37485	7.34	XP_006691708.1
CtANTH	29.03	34505	8.36	XP_006691708.1
His-CtENTH	21.17	32430	8.89	XP_006694659.1
CtENTH	18.17	29450	9.32	XP_006694659.1
Sc His- GST-ANTH	62.05	79230	6.28	P33338
Sc ANTH	33.21	29130	6.23	P33338
Sc His-GST -ENTH	47.69	68675	7.66	Q12518
Sc ENTH	18.85	18.575	9.21	Q12518
Sc His-GST Sla2 full length 1 - 968	138.16	117870	5.51	P33338
Sla2 full length 1 - 968	109.32	67270	5.27	P33338
Sc His-GST- Sla2dTHATCH 1 - 767	116.1	107775	5.47	P33338
Sla2dTHATCH 1 - 767	87.26	57675	5.19	P33338
Sc CLC full length	26531.54	13980	4.31	P17891
CtEnt1 full length	65907.95	52830	6.17	XP_006694659.1
CtEnt1-His	68.32	54320	6.17	XP_006694659.1
CtSla2 full length	118.65	79105	5.68	XP_006691708.1
CtCHC NTD 1-363	40.5	39670	6.26	XP_006697553.1
Sla2 cc 432-767	38.6	20065	4.68	P33338
Sla2 cc 296-767	53.9	28545	4.77	P33338

10.1.4 List of hazardous substances

Table 10.7: List of hazardous substances. For more information, check the ‘Regulation (EC)No 1272/2008’ of the European Agency for Safety and Health at Work.

Name	GHS pictogram	GHS hazardous statements (H)	GHS precautionary statements (P)
1,4-dithiothreitol	GHS07	302, 315, 319, 335	P261 - P301 + P312 - P302 + P352 - P305 + P351 + P338 - P280 - P332 + P313 - P337 + P313
2-Propanol	GHS02, GHS07	225-319-336	210-233-240-241-242-305+351+335
Ampicillin disodium salt	GHS08	317, 334	261, 280, 342+331
Calcium chloride	GHS07	319	264-280-305+351+338-337+313
Chloramphenicol	GHS08	H318-H351-H361fd	P202 P280 P305+P351+P338 P308+P313
cOmplete™ Protease Inhibitor Cocktail	GHS05	314	260, 280, 301+330+331, 303+361+353, 304+340+310,305+351 +338+310
EDTA Tetrasodium-salt	GHS07, GHS08	319, 332, 373	280, 304+340-312, 305+351+338-337+313
Ethanol	GHS02, GHS07	225, 319	210, 233,240, 241, 242, 305+351+338, 403+223
Ethidium Bromide	GHS06,GHS08	302, 330, 341	206, 281, 284, 310
GelGreen Nucleic Acid Gel Stain	GHS07	227	210, 280, 403+233, 501
Hydrochloric acid	GHS05, GHS07	290, 314, 335	234, 261, 271, 280, 303+361+353, 304+340+310, 305+351+338
Imidazole	GHS05,GHS07,GHS08	302, 314, 360D	260, 280, 301+330+331, 303+361+353, 305+351+338, 304+340+310
InstantBlue™	GHS05	290, 315, 319,	P234 P264 P280 P302 + P352 P305 + P351 + P338 P332 + P313
Kanamycin sulfate	GHS07	360, 372	201, 260, 280, 264, 314, 202, 308+313
MES	GHS07	315, 319, 335	261, 305+351+338
Nickel(II)chloride hexahydrate	GHS06,GHS08,GHS09	301+331-315-317-334-341-350i-360D-372-410i	P270 P273 P280 P304+P340 P310i
Pentane	GHS02, GHS07, GHS08, GHS09	225, 304, 336, 411	210, 233,240, 273, 301+310, 331
SDS	GHS02, GHS05, GHS07	302, 315, 318, 335, 412	P273 P280 P302+P352 P305+P351+P338 P312
Sekusept Plus	GHS05,GHS07,GHS09	302+332, 314, 400	273, 280, 303+361+353, 305+351+338, 310
Sodium hydroxide	GHS05	290, 314	P233 P280 P303+P361+P353 P305+P351+P338 P310

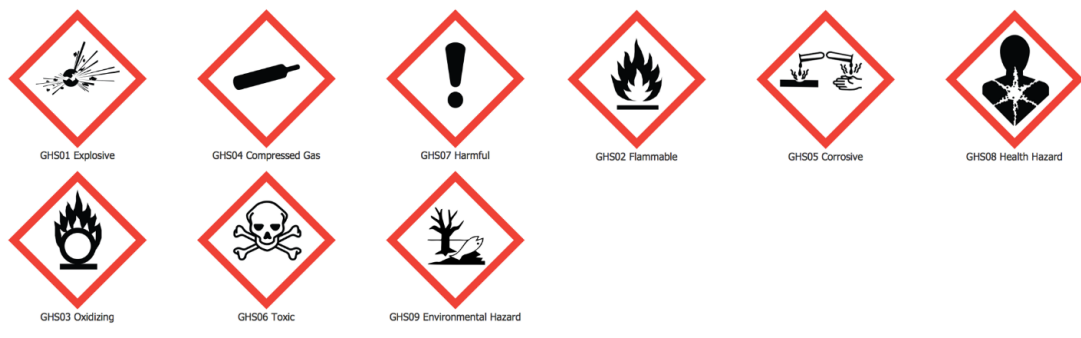


Figure 10.18: GSH symbols

11. Acknowledgements

This doctoral dissertation is the result of a long journey over the last four years, which has been possible thanks to many people who have walked with me for at least part of it. This PhD experience has definitely shaped me and my scientific thinking, and has made me a big part who I am now.

First and foremost, I would like to start by thanking my PhD supervisor, Dr. Maria Garcia-Alai, for giving me the great opportunity to join her research Team. Her door was always open for all my questions and she was always ready to listen to me and to support me when I needed it; and most importantly, has taught me how to become a good scientist. Her guidance and careful advice have been extremely important to me through this time, and I am extremely grateful for having her as my supervisor.

Second, I would like to thank all the members of my group, present and past, and for being such a fantastic team of scientists, and beyond science, of people. Angelica, Christian, David, Stephan, Katha, Osva, Fede, Janina, Niklas, George and Lucas: thank you for being there. Their company throughout these years has been an absolute pleasure. All the fun times in the lab and outside have made this an unforgettable journey and a great experience, which I will always remember. You all helped me since Day 1 to achieve this point, and have been an incredible support for me. I need to thank particularly Katha, Stephan and Lucas, who have been a massive support for bringing this project forward, have taught me a lot of lessons and have made me enjoy doing science together.

I would also like to thank to my collaborators, Frank Sobott and Stephen Muench from the University of Leeds, and specially David Klebl, who has been a major force for driving this project forward. I also want to thank Michal Skruzny and Marc Abella, who have taught me the best values of collaborative science and how great team work is a game-changer for complex scientific challenges.

I would like to thank my Thesis Advisory Committee members, Christian Loew, Jonas Ries and Daniel Wilson, for their support through this years and their great advice during the TAC meetings regarding the challenges these projects brought and their support.

I also would like to thank everyone at the P12, P13 and P14 beamlines; and the CSSB cryoEM facility (specially Clement, Cy, Hayden, Isabel and Carolin Seuring), for making this such a excellent place to work. In spite of all complains, hic-cups with the microscopes or beamlines down, you are always there to support and make sure that experiments can be performed. I would also like to thank all the people involved in the Administration at EMBL

Hamburg, specially Margret and Huong, who make our life much easier by dealing with all the arduous administrative tasks; and to the whole Wetlab team, for keeping the wetlab up and running, working behinds the scenes to maintain all the equipment.

I also want to thank the EMBL Graduate Office for funding through the EMBL International PhD programme, and I also want to heart-fully say thank you to all the great and fantastic people that I have met in this institute and who have accompanied my through this PhD journey, specially Anna, Alberto, Gilberto, Jesus, Lucia, Karolina, Charlie, Agata, Wolfi, Christina, Fergus, Alex, Brice, Guillermo, Irene, Sofia, Sara... and to many others who also embarked into this adventure that Fall of 2018 in Heidelberg.

I would like to thank everyone from the Kosinski and Loew groups who we share the space in CSSB, and in particular Maxime and Lenka, for their great support, the scientific discussions and for enriching this journey in positive things along with the science. I could not imagine doing it again without all of you.

I also want to thank my friends back home, who wherever I might be and no matter how long I have not seen, always bring their smiles and those very refreshing laughs and great moments, which have been extremely important to me during this time. And I also would like to thank my friends here in Hamburg (including the Soup for Scientists), who have transformed the rainy Hanseatic Stadt in a great place that I will surely miss in my next adventures.

This thesis is also for Joseba, to whom I am extremely thankful for all his support throughout the years, and for Rosa and Julio, who always made me feel like at home, encouraged me and motivated me to achieve my goals.

And finally, this PhD thesis is also for my Family, because in spite of being far they always feel close, and because they are that really strong pilar in my life who is always there, constantly supporting all my endeavours. Without them, probably most of the work I have accomplished through these years would not be there.

To all of you, and to everyone who has walked a bit of this journey with me...

THANK YOU

GRACIAS

DANKE

ESKERRIK ASKO

Declaration of Oath

I hereby declare on oath that this doctoral dissertation is written independently and solely by my own based on the original work of my PhD and has not been used other than the acknowledged resources and aids. The submitted written version corresponds to the version on the electronic storage medium. I declare that the present dissertation was prepared maintaining the Rules of Good Scientific Practice of the German research Foundation and it has never been submitted in the present form or similar to any other University or board of examiners.

Date: 07/10/2022

Signature:

A handwritten signature in blue ink, appearing to read 'Janice L', with a horizontal line underneath.

Hiermit versichere ich an Eides statt, die vorliegende Dissertation selbst verfasst und keine anderen als die angegebenen Hilfsmittel benutzt zu haben. Die eingereichte schriftliche Fassung entspricht der auf dem elektronischen Speichermedium. Ich versichere, dass diese Dissertation nicht in einem früheren Promotionsverfahren eingereicht wurde.

Unterschrift

Datum: 07/10/2022